國立台灣大學理學院化學所

碩士論文

Department of Chemistry

College of Science

National Taiwan University

Master's Thesis

製備高品質氮化鉭光陽極於光電化學之應用

Fabrication of High-Quality Ta_3N_5 Photoanode for Photoelectrochemical Application

張家維

Chia-Wei Chang

指導教授：姜昌明 博士

Advisor: Chang-Ming Jiang Ph. D.

中華民國 113 年 7 月

July 2024

doi:10.6342/NTU202403464

國立臺灣大學碩士學位論文
口試委員會審定書

NTU Master Thesis
Oral Defense Approval Form

製備高品質氮化鉭光陽極於光電化學之應用

Fabrication of High-Quality Ta_3N_5 Photoanode for Photoelectrochemical Application

本論文係 張家維 君（學號 R10223221）在國立臺灣大學化學系完成之碩士學位論文，於民國 113 年 07 月 24 日承下列考試委員審查通過及口試及格，特此證明。

The student Chia-Wei Chang (student no. R10223221) enrolled in the Master Program of the Department of Chemistry, NTU has satisfactorily passed the oral defense on 2024/07/24 with the approval of all committee members as follows.

口試委員 (Committee Members)：

姜 浩 明 （簽名 Signature）

（指導教授 Advisor）

系主任、所長 （簽章）

(Dept./Institute Chair's Signature and Seal)

doi:10.6342/NTU202403464

Acknowledgments

本論文能夠順利產出首先我最感謝的是我的指導老師─姜昌明教授，最要謝謝老師的事情莫過於在實驗室草創初期就願意賭一把收留來自完全不同領域、沒有化學相關背景的化生組學生加入實驗室。然後也願意讓我待在實驗室在沒什麼產出的情況下到第三年，待在實驗室的三年間大概是我在台大的旅程中最充實、學到最多東西的一段日子，也從老師您的身上學習到學術嚴謹的態度以及面對事情好的處事方法，這些肯定都會對我的未來有著比起好成績更重要的影響。除了做人處事及研究態度，對於我的研究，老師願意放心的讓我去嘗試所有可能性，並跟我討論相關數據，也對我產出這份論文有很大的幫助，當然能夠完成這份英文論文也必須謝謝老師您願意花時間逐字閱讀並給予相當多的建議與改進方法，我才能夠寫出一份能夠讓我自己滿意的作品，這個部分真的是麻煩老師了。除了我的指導教授，我第二位想要感謝的人是陳浩銘教授，雖然和教授沒緣，沒有實際與教授有過討論機會，教授也因為龍門計畫無辦法擔任我的口試委員，但教授願意慷慨借出各類儀器，對於完成我的論文也是有非常大的幫助。除了兩位教授，我也非常感謝台灣布魯克的林博士願意幾乎是每兩週就讓我過去使用 D8-Discover 量測我的樣品，若是沒有這些解析度夠好的 XRD 量測，我是絕對沒辦法完成我的研究，可能也真的要畢不了業打包回家了。我還要感謝擔任口委的王迪彥教授、廖衛斯教授、本來預計擔任口委的陳俊顯教授及 Jeffrey Farrell 教授。口試時王老師提出的問題，也讓我有了很多反思的機會可以從平常沒有想到的方面去思考，現在想起來很多提問我還可以答得更好，請老師擔任口委讓我受益良多。同樣的，廖老師在口試時對我提出的問題，對於不同材料間的比較，也是我之前覺得只要把我眼下的東西做好而沒有深入去思考過的，除此之外，從廖老師給我的建議中，就能聽出廖老師是有把我的論文仔細看完，所以才能提出一些格式上改了又改但還是忽略的部分。對於無緣擔任口委的陳俊顯教授，我還是想感謝一開始教授願意在繁忙的公務中排開時間來參加甚至沒上過任何一堂教授的課的學生的口試，覺得如果這次能有陳老師來擔任口試委員，我一定能在電化學上面獲得更多想像不到的見解。若沒有 Farrell 教授讓我們自由使用可見光光譜儀，我最後對異質接面的研究就只能是紙上談兵，完全無法完成這篇論文中我認為是最精華的部分。

doi:10.6342/NTU202403464

當然，除了感謝教授們的幫助，實驗室的同學們也對我完成這份論文有很多的幫助，雖然在研究上我做的項目和實驗室的其他同學有很大的差異，對於解釋上大家比較沒辦法直覺性的幫上忙，但大家憶起集思廣益的過程，也讓我可以去理解自己思考上的盲點，這對我來說是非常重要、有幫助的。在寫論文跟做實驗很煩燥的時候也是有大家跟我講一堆有的沒的幹話我才有辦法度過一直撞牆的痛苦期。

最後，感謝我的家人們不論在經濟上、精神上提供的一切幫助與支持，女朋友的陪伴與體諒，還有要謝謝我自己的毅力讓我撐下來，連續兩年半包含假日幾乎每天都去學校做實驗生產數據待到半夜才回家，這個過程中真的是犧牲了太多東西，但現在回想起來我還是不會後悔做了這些。

來讀化學研究所真的是我從來沒有想過，意料之外的一步，從零開始重新學習新的東西真的好難，所以說我能完成這個碩士學位真的需要感謝太多的人了，能夠完成這個碩士學位都是歸功於大家的幫助。

doi:10.6342/NTU202403464

中文摘要

光電化學 (PEC) 水分解利用半導體材料將太陽能用以分解水轉換為氫氣，是一個有前景的能量儲存方式。在過渡金屬氮化物中，五氮化三鉭 (Ta_3N_5) 因其比過度金屬氧化物 (Transition metal oxides, TMOs) 好的載子傳輸性質、約 2.1 電子伏特的能隙及合適進行水氧化反應之能帶位置而成為有前景的光陽極候選材料，其理論太陽能轉氫氣之效率 (solar-to-hydrogen efficiency, STH) 可以達到 15.9%。近期的研究中，雖然 Ta_3N_5 光陽極系統的效率也已經趨近理論值所預期，但其缺點是因大量使用鉭金屬所導致的較差的材料使用效率。因此，本研究中利用矽基板作為導電層以磁控反應濺鍍法 (reactive magnetron sputtering) 合成介穩態三氮化二鉭 (Ta_2N_3) 作為前驅物，並將前驅物以氨氣燒結合成 Ta_3N_5 光陽極。首先，本研究利用氨氣燒結之溫度調控表面缺陷含量，特別是在 Ta_3N_5 能帶結構中做為電子電洞複合中心的晶格中的氮空缺 (N_V) 及低價態的鉭陽離子 (Ta^{3+}) 可在燒結溫度 820°C 並持溫三小時的情況下在表面消除。除此之外，使用 Ta_2N_3 而非 Ta_2O_5 作為 Ta_3N_5 製備之前驅物優點便在於，以 Ta_2N_3 作為前驅物時會在薄膜塊材之相組成中引進低價態的氮化鉭族群如 Ta_2N 及 Ta_5N_6，這些低價態的氮化鉭族群可以有效的增加 Ta_3N_5 光陽極的載子傳輸性質。在黃血鹽 ($K_4[FeCN_6]$) 作為電洞捕捉劑 (hole scavenger) 存在於電解液中時，沉積在高度砷參雜之 n 型矽 (111) 基材上生長之 Ta_3N_5 光陽極有著最好的光電化學活性，其光電流密度可達 3.86 mA/cm^2，並表現出對可逆氫電極 0.48 伏 (V_{RHE}) 之起始電位，這樣的表現優於使用其他參雜及方向之矽基材系統。這樣的差異最主要來自於使用不同參雜及不同方向性之矽基材時其與 Ta_3N_5 之異質接面的差異造成，並可用光電化學阻抗譜 (photoelectrochemical impedance spectroscopy, PEIS) 分析驗證其造成之光電化學活性差異。沉積在磷參雜之 n 型矽 (100) 基材上之 Ta_3N_5 光陽極會因兩個半導體材料相接形成之 n-n 異質接面 (n-n heterojunction)，而產生光生電子電洞堆積在 n-n 異質接面之間，產生大量的漏電流消耗光生載子並降低可獲得的光電流密度。本研究之結果近一步驗證了藉由更改氮化前驅物及使用矽基板作為導電層可以完整地建立一個更有效利用鉭金屬的光陽極合成平台，並可以做為之後以矽基板作為導電層時進一步改善光電化學活性的基礎。

doi:10.6342/NTU202403464

關鍵字：光電化學水分解、五氮化三鉭光陽極、過渡金屬氮化物、磁控反應濺鍍

doi:10.6342/NTU202403464

Abstract

Photoelectrochemical (PEC) energy conversion is a promising pathway to store excess energy in the form of chemical fuels. Ta_3N_5 represents a promising photoanode candidate owing to its better charge transport properties compared to transition metal oxides (TMOs), theoretical its ~ 2.1 eV band gap, suitable band energetics for oxygen evolution reaction (OER), and a theoretical solar-to-hydrogen (STH) efficiency of 15.9%. As far, as the Ta_3N_5-based photoanode system has almost achieved its theoretical limitation but with the outcome of inefficient material usage caused by the massive usage of tantalum metal. Herein, Ta_3N_5 thin films were fabricated on n^+-Si(111) substrate through nitridation of the metastable Ta_2N_3 films synthesized via reactive magnetron sputtering. To begin with, the surface composition, especially, the deep-trap sates in the Ta_3N_5 system, namely nitrogen-vacancy (V_N), and low-valence Ta cations (Ta^{3+}) can be effectively tuned by precisely controlling annealing temperature. A defect-free surface composition can be achieved by annealing at 820°C for 3 hours. Aside from the surface composition, the incorporation of Ta_2N_3 as a nitridation precursor can effectively introduce low-valence Ta_2N and Ta_5N_6 content in the bulk composition that facilitates the carrier transport of Ta_3N_5 photoanode system compared to Ta_3N_5 fabricated from Ta_2O_5. In the presence of $K_4[Fe(CN)_6]$ as a hole scavenger, the Ta_3N_5/n^+-Si(111) photoanode demonstrated an onset potential at 0.48 V_{RHE} and 3.86 mA/cm^2 photocurrent density at 1.23 V_{RHE}, outperforming comparable films grown on the other two substrates. Such differences in PEC performance were attributed to the heterojunction between Ta_3N_5 and Si and verified by photoelectrochemical impedance spectroscopy (PEIS). This heterojunction dominated the carrier dynamics as the leakage current across the heterojunction would consume the photogenerated holes and consequently diminish the photocurrent density. The present study

doi:10.6342/NTU202403464

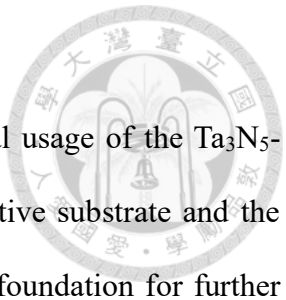

reveals the importance of constructing a platform for efficient material usage of the Ta_3N_5-based photoanode system via the incorporation of silicon as a conductive substrate and the metastable Ta_2N_3 as nitridation precursor films, which can serve as a foundation for further improvement of the PEC performance of silicon-based Ta_3N_5 photoanode system.

Keywords: Photoelectrochemical Water Splitting, Ta_3N_5 Photoanode, Transition Metal Nitride, Reactive Magnetron Sputtering

doi:10.6342/NTU202403464

Table of Contents

doi:10.6342/NTU202403464

doi:10.6342/NTU202403464

doi:10.6342/NTU202403464

List of Abbreviations

AC	Alternative current
BSE	Backscattered electron
BnOH	Benzyl alcohol
CA	Chronoamperometry
CBM	Conduction band minimum
CL	Cathodoluminescence
CO_2RR	CO_2 reduction reaction
CPE	Constant phase element
CV	Cyclic voltammetry
DC	Direct current
DoS	Density of state
DRS	Diffuse reflectance spectroscopy
EBSD	Electron backscattering diffraction
FE	Faradaic efficiency
FWHM	Full width of the half maximum
GIXRD	Grazing incident X-ray diffraction
HER	Hydrogen evolution reaction
ICSD	Inorganic crystal structure database
LA	Longitudinal acoustic
LSV	Linear sweep voltammetry
OCP	Open circuit potential
OER	Oxygen evolution reaction
PCC	Pyridinium chlorochromate
PEC	Photoelectrochemical

doi:10.6342/NTU202403464

PES	Photoelectron spectroscopy
PEIS	Photoelectrochemical impedance spectroscopy
PXRD	Powder X-ray diffraction
PVD	Physical vapor deposition
RBS	Rutherford backscattering spectroscopy
RE	Reference electrode
RF	Radio-frequency
RGA	Residual gas analysis
RHE	Reversible hydrogen electrode
SE	Secondary electron
SEI	Secondary electron image
SEM	Scanning electron microscopy
SHE	Standard hydrogen electrode
SIMS	Secondary ion mass spectroscopy
TA	Transverse acoustic
TBAP	Tetrabutylammonium perchlorate
UPS	Ultra-violet photoelectron spectroscopy
UV-Vis	Ultraviolet-visible
VBM	Valance band maximum
WE	Working electrode
XPS	X-ray photoelectron spectroscopy
XRD	X-ray diffraction

doi:10.6342/NTU202403464

List of Figures

doi:10.6342/NTU202403464

doi:10.6342/NTU202403464

doi:10.6342/NTU202403464

doi:10.6342/NTU202403464

doi:10.6342/NTU202403464

List of Table

doi:10.6342/NTU202403464

Chapter 1. Introduction

1.1 Motivation

Metal nitrides are a fascinating class of materials, possessing unique properties such as high melting points, refractivity, and mechanical hardness, making them the focus of significant research interest over the past decades.[1] They have applications in light-emitting diodes, ceramic coatings, superconductors, and photocatalysts.[2] For example, radio-frequency (RF) transistors based on semiconducting GaN are becoming an important part of the 5G telecommunication technology.[3] However, our understanding and technological development of metal nitrides lag behind that of metal oxides, primarily due to the lower availability of nitride materials. For instance, the number of nitride compounds listed in the Inorganic Crystal Structure Database (ICSD) is about ten times fewer than oxide compounds.[2]

Among researched metal nitrides, Ta_3N_5 is a promising candidate for photoelectrochemical (PEC) water splitting to provide renewable energy due to its approximately 2.1 eV band gap and suitable band energetics for the oxygen evolution reaction (OER), boasting a theoretical solar-to-hydrogen efficiency of 15.9%.[4-7] Despite its potential, the performance of Ta_3N_5-based photoelectrodes has nearly reached its optimal value, but at the expense of high material usage of tantalum metal.[7] Traditionally, Ta_3N_5 photoanodes are fabricated by direct nitridation of Ta_2O_5 in an ammonia atmosphere, highlighting the difficulty of direct fabrication of nitrogen-rich metal nitride. Although nitrogen is the most abundant element on Earth and plays a vital role in organic and biological systems, nitride synthesis is challenging due to the chemical stability of N_2, which has a high bond enthalpy (964 kJ/mol) and ionization energy (1505 kJ/mol).[8] Consequently, synthesizing nitrides typically requires extreme reaction conditions.[9]

doi:10.6342/NTU202403464

Additionally, oxygen- and water-free environments are necessary to prevent the formation of oxynitride phases, further complicating the synthesis process.[8, 10, 11]

The Ta_2O_5 precursor can be obtained by several methods, including direct oxidation of tantalum foil and reactive sputtering of tantalum oxide on metal foils. However, regardless of the method, a relatively thick layer of Ta_3N_5 after conversion, about 0.5 to 1 μm, is required to achieve a higher photocurrent density and better performance. For commercial purposes, reducing the dependence on expensive tantalum metals is essential. Using a commercial silicon wafer as a conductive substrate can further reduce costs significantly.

As a result, this thesis primarily focuses on developing and characterizing Ta_3N_5 photoanodes deposited on silicon wafers, prepared using Ta_2N_3 as the nitridation precursor synthesized via reactive magnetron sputtering. The optimization of Ta_2N_3 was examined by carefully tuning the deposition parameters of reactive sputtering, followed by optimizing an ammonia annealing process conducted with a tube furnace through the examination of each annealing parameter.

The rest of **Chapter 1** briefly introduces photoelectrochemical water splitting, and transition metal nitrides, particularly tantalum nitride. In **Chapter 2**, necessary background information for characterization and experimental methods is introduced. **Chapter 3** details the optimized conditions of Ta_2N_3 as nitridation precursors, including the influence of each deposition parameter on the final crystallinity and phase composition of this nitridation precursor. Additionally, the characterization of Ta_3N_5 converted from Ta_2N_3 precursors is provided in the latter half of this chapter. **Chapter 4** mainly focuses on the PEC performance of Ta_3N_5 photoanodes constructed in **Chapter 3**, and a detailed explanation of the performance differences is made by combining the characterization achieved in **Chapter 3**. **Chapter 5** includes the Ta_3N_5 converted from

doi:10.6342/NTU202403464

other precursors also fabricated with reactive magnetron sputtering, including doping Ta_2N_3 films with oxygen and directly using Ta_2O_5 as a precursor. This chapter aims to reference how our newly developed Ta_3N_5 photoanode system can outperform Ta_3N_5 converted from Ta_2O_5, which is the most common strategy used in research articles. Finally, in **Chapter 6**, we examine the water-splitting performance of Ta_3N_5 photoanodes with or without a $NiFeO_x$ co-catalyst deposited through spin-coating procedures.

These findings offer significant insights into the integration of transition nitride-based photoelectrodes with commercial silicon wafers and lay the foundation for further improvements in PEC performance with similar systems. Overall, this research advances the understanding and efficiency of Ta_3N_5 photoanodes, contributing to the development of more effective and sustainable photoelectrochemical systems.

1.2 Photoelectrochemical Energy Conversion

PEC energy conversion using semiconductor materials is a promising way to convert excess solar energy into renewable chemical fuels via redox reactions — usually, hydrogen evolution reaction (HER), OER, CO_2 reduction reaction (CO_2RR), etc. This thesis emphasizes on the generation of hydrogen and oxygen via solar-driven water splitting, though the same fundamental principles are also applicable for CO_2RR, with differences in the redox potential and product selectivity.[12] Contrary to electrochemical water splitting, which requires high overpotential to overcome the energy barrier of the redox reaction, the band gap of semiconductors offers an alternative route for reaction to reduce the electrical energy exerted into the system upon light illumination.

doi:10.6342/NTU202403464

1.2.1 Photoelectrochemical Water Splitting

For overall water splitting at the standard condition (pH = 0), the anodic side consists of reactions involving the transfer of four electrons into the (photo)electrode, or transfer of four holes in order to produce one oxygen molecule; on the other side, to compensate for the excess electrons in the system a cathodic reaction for the reduction of protons into hydrogen gas takes place.[13] However, for most semiconductors, the acidic condition with pH = 0 is too harsh to operate; instead, the neutral or basic conditions are preferred for operational stability. As a result, the reversible hydrogen electrode (RHE) scale is used to describe the potentials of HER and OER. By the Nernst equation, the standard redox potential in the standard hydrogen electrode (SHE) scale could be converted into potential with respect to the RHE scale:[14]

Anodic: $H_2O + 2h^+ \rightarrow 2H^+ + \frac{1}{2}O_2$ $E^0_{oxi.} = -1.23\ V\ (vs.SHE)$ (1.1)

Cathodic: $2H^+ + 2e^- \rightarrow H_2$ $E^0_{red.} = 0.00\ V\ (vs.SHE)$ (1.2)

Overall: $H_2O \rightarrow H_2 + \frac{1}{2}O_2$ $\Delta E = -1.23\ V\ (vs.SHE)$ (1.3)

Nernst Equation: $E\ (vs.RHE) = E_{read}(vs.SHE) + E^0_{ref} + 0.0591 \times pH$ (1.4)

1.2.2 Configurations of PEC Energy Conversion Devices

Typically, a three-electrode PEC system consists of a photoelectrode, an electrolyte, a metallic counter electrode, and a reference electrode. As demonstrated in **Figure 1.1a**, the semiconductor-electrolyte junction forms after aligning the Fermi level with the electrochemical potential of the chemical reaction of interest. A space charge region, also known as the depletion region, would appear near the junction and give rise to a built-in electric field.

doi:10.6342/NTU202403464

Next, light illumination generates excess carriers in the form of electron-hole pairs. These excess carriers would be separated respectively toward the surface of the photoelectrode and the external circuit owing to the electric field established in the depletion region. While the minority carrier drifts toward the surface, the majority carrier moves in the opposite direction into the external circuit. The excess carriers generated after illumination create quasi-Fermi levels for electrons and holes ($E_{F,n}$, $E_{F,p}$), and the difference between electron and hole quasi-Fermi levels is dominated by the number of excess minority carriers. The decrease in onset potential is also related to the difference in electron and hole quasi-Fermi levels; that is, the higher the difference it is, the photovoltage becomes larger.

The above-mentioned single photoelectrode PEC system, as shown in **Figure 1.1a**, would typically still need an external bias to drive oxidation reactions since the photovoltage generated by absorbing the solar spectrum isn't enough. To achieve unassisted overall water splitting without an external bias, a tandem configuration of a PEC cell would be used as shown in **Figure 1.1b**, where both electrodes are semiconductors. This is meant to utilize the semiconductor-electrolyte junctions on both sides, and the sum of anodic and cathodic photovoltages must be larger than the overall energy difference of water splitting plus the unavoidable overpotentials. This thesis emphasizes the single photoelectrode system for the oxygen evolution reaction, and the detailed PEC setup will be further elaborated on in **Chapter 2**.

doi:10.6342/NTU202403464

1.2.3 Selection Criteria for Photoelectrode Material

Selecting a suitable photoelectrode material is based on several criteria, depending on the type of PEC configuration, whether single or tandem. Important parameters include the band alignment with the desired half-reaction potential, the size of the band gap, and the carrier mobility.

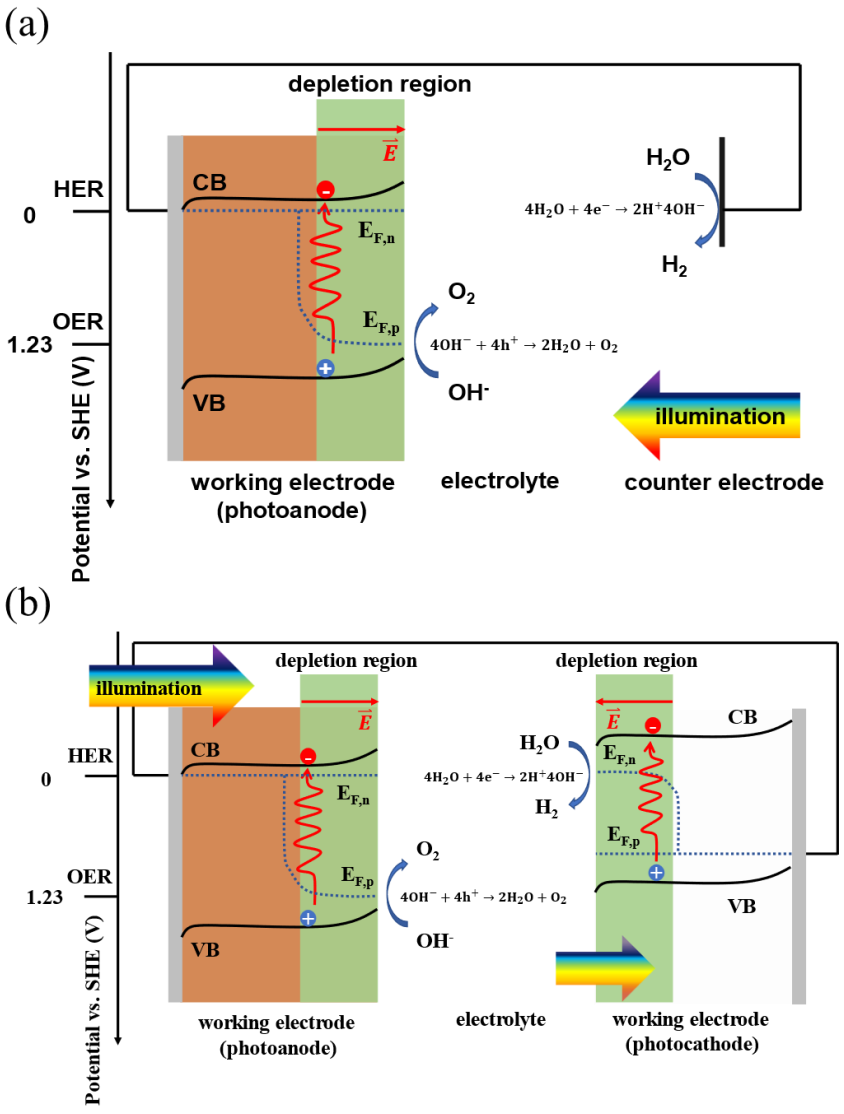

Figure 1.1 Schematic illustration of (a) a single photoelectrode setup with a photoanode and a metallic cathode, and (b) a tandem photoanode-photocathode configuration.

doi:10.6342/NTU202403464

First, the band bending of the semiconductors at the semiconductor-electrolyte junction, whether upward or downward, determines the reaction it can drive. For an oxidation reaction, an n-type semiconductor should be used, while a p-type semiconductor is needed for reduction reactions. As a result, for PEC water-splitting, n-type semiconductors should be used as the photoanode, and p-type semiconductors should be used as the photocathode.

The valence band edges of photoanodes must be deeper than the redox potential of the desired reaction, ensuring that the surface-collected holes have sufficient driving force. Similarly, the conduction band edges of photocathodes must be higher than the respective reduction potential. The frequently used photoelectrodes for PEC water-splitting are summarized in **Figure 1.2** with energy relative to the HER, and OER potential at pH 0. Typically, a metal oxide semiconductor has a CBM position lower than HER potential which is not suitable for PEC water reduction.

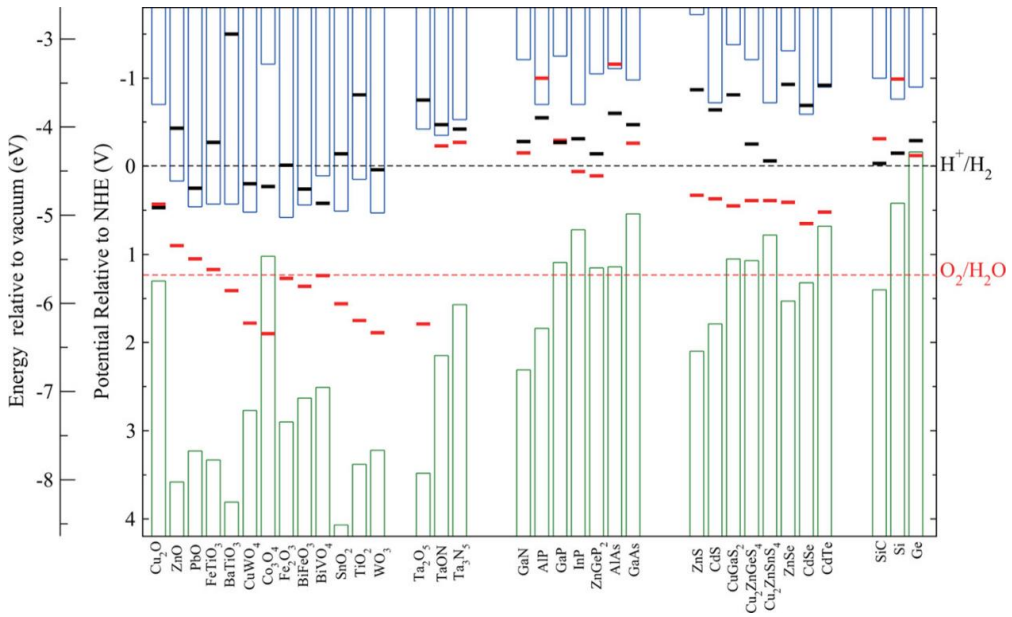

Figure 1.2 Summary of semiconductor conduction band (blue) and valance band (red) positions at pH = 0 relative to the redox potential of water oxidation and reduction.[15]

doi:10.6342/NTU202403464

According to the Shockley-Queisser limit, a single photovoltaic cell with a band gap of 1.35 eV can achieve a maximum conversion efficiency of 33.16% under illumination of AM 1.5G simulated solar spectrum.[16] This is because a semiconductor can only absorb photons with energy higher than its band gap energy. However, this energy cannot be fully converted to output power; only the energy difference between the quasi-Fermi level of electrons and holes can be utilized.

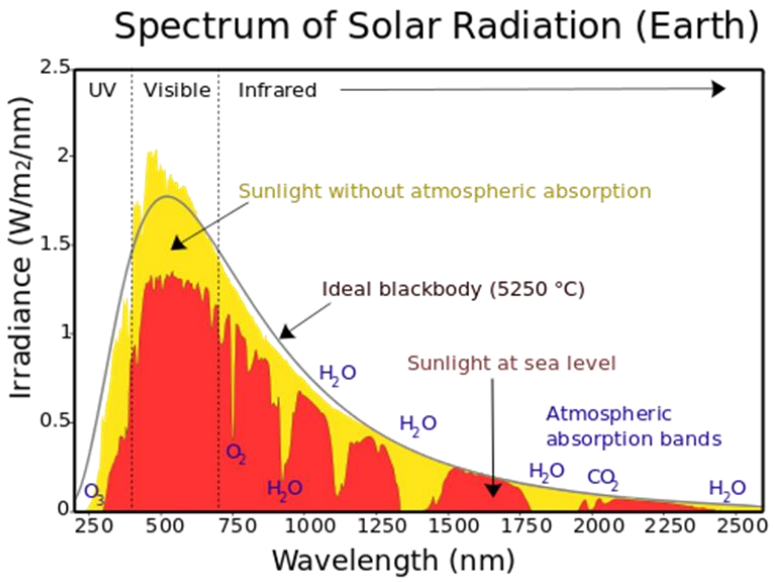

Figure 1.3 Solar spectrum showing the incident power versus wavelength in outer space and on the Earth's surface. The solid curve is the ideal blackbody spectrum.[17]

Additionally, the solar spectrum shown in **Figure 1.3** reveals that most high-energy photons are scattered or absorbed while traveling through the atmosphere. At the same time, the low-energy part of the solar spectrum is absorbed by molecules such as water and oxygen gas. As a result, visible light has the highest irradiation on Earth. Although semiconductors with larger band gaps can produce larger photovoltages, the low irradiation leads to a low photocurrent density. Conversely, if the band gap is too small, the semiconductors would deliver insufficient photovoltage. Therefore, the

doi:10.6342/NTU202403464

efficiency of a photoelectrode is significantly affected by the band gap energy of the material. For solar water splitting, a single semiconductor typically requires a minimal band gap of at least 2 eV. This provides the 1.23 eV needed for the reaction and the catalytic overpotentials necessary to drive the overall reaction in the forward direction.[18] The charge transport properties, stability for operations, and the surface-active sites for desired redox reactions should also be considered when selecting photoelectrodes. In most research, transition metal oxides are used as photoelectrodes due to their good stability, facile fabrication methods, and low fabrication costs. However, the charge transport properties of transition metal oxides are extremely low due to the formation of small polarons caused by electron-phonon coupling, and their ionic properties result in high effective masses of carriers traveling through alternating deep potential wells. Oxide-based photoelectrode materials, such as hematite (Fe_2O_3), bismuth vanadate ($BiVO_4$), and delafossite ($CuFeO_2$), all suffer from this low carrier mobility problem.[19-23] On the other hand, compound semiconductors with less electronegativity difference, such as metal nitrides, selenides, and phosphides, often exhibit better carrier mobility and better conversion efficiency, though they suffer from corrosion issues in aqueous solutions, which necessitates conformal protective layers.[24] To date, the perfect photoelectrode material has not yet been found, and nitride semiconductors garnered lots of attention as possible candidate photoelectrode and photocatalytic material. Nitride-based semiconductors are expected to exhibit advantageous optoelectronic properties such as smaller optical band gaps, higher charge carrier mobilities, and defect tolerance than comparable oxide semiconductors.[4, 25-27]

doi:10.6342/NTU202403464

1.3 Transition Metal Nitride

Transition metal nitrides are a relatively unexplored but fascinating class of inorganic compounds with diverse properties that make them promising candidates in various fields, including integrated circuits, photovoltaics, superconductors, and catalysts.[28-34] Despite being among the most abundant elements in the atmosphere, almost no natural nitride minerals are observed due to the chemical stability of nitrogen molecules, which have extremely stable triple bonds.

1.3.1 Advantages of Nitrides

The moderate electronegativity of nitrogen atoms gives nitrides a mixed covalent/ionic bonding character. Compared to other pnictides used for solar energy conversion, such as GaAs and InP, nitride materials are more ionic, allowing better tolerance to structural defects.

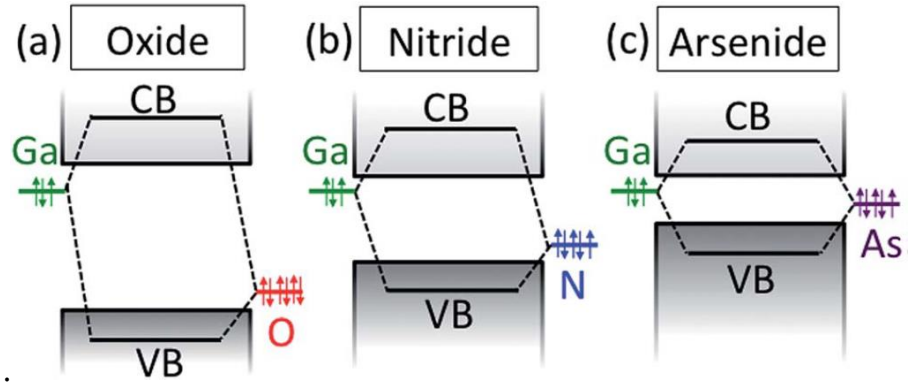

Figure 1.4 Schematic representation of chemical bonding in Ga-based semiconducting (a) oxides, (b) nitrides, and (c) arsenides, showing how nitrides tend to have intermediate energy of the valence band compared to the more ionic oxides and the more covalent pnictides.[26]

doi:10.6342/NTU202403464

This tolerance arises because the constituent atomic orbitals in ionic compounds lie closer to the band edges than in covalent compounds, making defect states resulting from broken atomic bonds shallower as shown in **Figure 1.4**.

In contrast to oxides, nitrides are more covalent due to the higher position of N 2p orbitals compared to O 2p orbitals. The lower energy difference between the N 2p levels and the electronic states of metal elements, along with the resulting hybridization, typically leads to better charge-transport properties and higher valence band positions, thus lower band gap compared to oxides used in photovoltaic and photoelectrochemical applications.

Additionally, the electronic structure of metal nitrides varies significantly depending on the nitrogen content, giving rise to properties ranging from metallic to semiconducting. Mononitrides are usually metallic with excellent electrical conductivities due to the partially occupied metal d states. Conversely, nitrogen-rich compounds with cations in their highest oxidation states exhibit semiconducting properties because of the energy gap separating the N 2p states from the unoccupied metal d states. Therefore, transition metal nitrides represent a versatile and promising chemical space from which new functional materials can be developed, showcasing a broad range of electronic properties that can be tailored for specific applications.

1.3.2 Challenges in Nitride Synthesis

Metal nitrides are scientifically intriguing due to their relatively unexplored nature. Despite theoretical predictions of hundreds of stable binary and ternary nitrides, the experimentally discovered nitrides remain limited.[2, 9, 35-37] This limitation arises from the thermodynamically unfavorable formation of nitrides, which have lower formation enthalpies compared to oxides.[26, 38] This metastability of nitride species originates from

doi:10.6342/NTU202403464

the extremely low chemical potential of nitrogen, which means that forming nitrogen-rich metal nitrides requires slightly higher energy than the ground state energy. Consequently, metals tend to oxidize in the presence of oxygen, making it difficult to form pure-phase nitrides and often resulting in nitrogen-deficient nitrides with cations in lower oxidation states. As a result, the experimental synthesis of nitrides requires an oxygen-free environment.

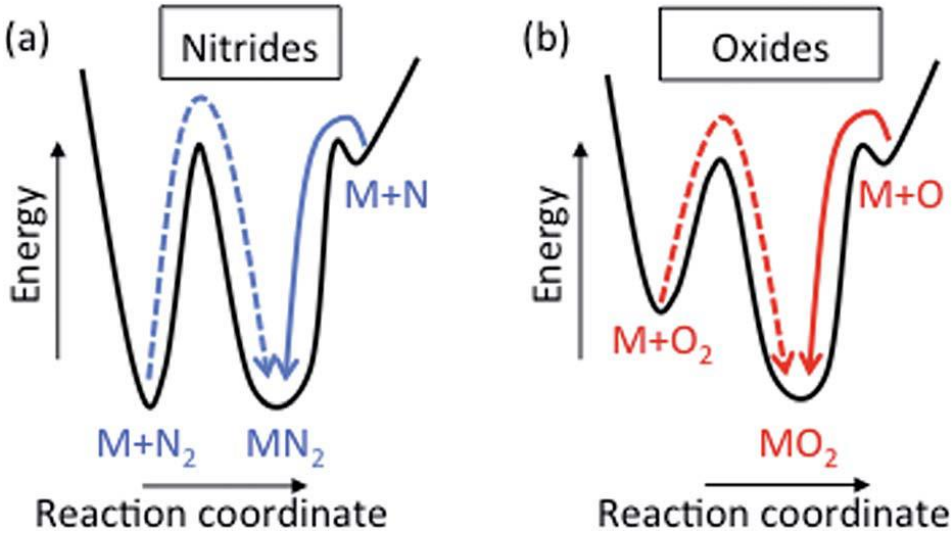

Figure 1.5 Generalized potential energy landscape for the synthesis of (a) nitrides and (b) oxides, showing a larger kinetic barrier for the synthesis of nitrides from an N_2 molecule, but the same barrier if a N atom is used.[26]

However, the instability of metal nitrides is primarily due to the extremely low chemical potential of nitrogen molecules, rather than the metal-nitrogen bonding energies. Once nitrides are successfully synthesized, the metal-nitrogen bonds can be as strong as or stronger than metal-oxygen bonds, rendering the nitride species kinetically stable in the absence of oxygen, as illustrated in **Figure 1.5**. This stability can be achieved by the formation of a native oxide layer on the surface of nitride species, which acts as a barrier against further deterioration by oxygen.

doi:10.6342/NTU202403464

1.3.3 Synthesis Strategies

The formation of metastable nitrides instead of thermodynamically favorable phases requires "constrained equilibrium" conditions, where the latter's formation is kinetically inhibited. Given that nitrogen gas is relatively stable under ambient conditions due to its high bond enthalpy (964 kJ/mol) and ionization energy (1505 kJ/mol), a better approach to the synthesis of metastable nitride is to raise the chemical potential of nitrogen.[8, 9, 26] This makes the stability of metastable nitrogen possible, as illustrated by the convex hull diagrams in **Figure 1.6**. Here, the convex hull is connected by the thermodynamically stable phases, and the points above the hull represent the unstable species of that compound that will easily decompose into the thermodynamically favorable phase. Constrained conditions disable the formation of thermodynamically stable nitrogen gas, and a new convex hull should be drawn with respect to the elevated chemical potential of atomic nitrogen, making the synthesis of metastable nitrides possible.

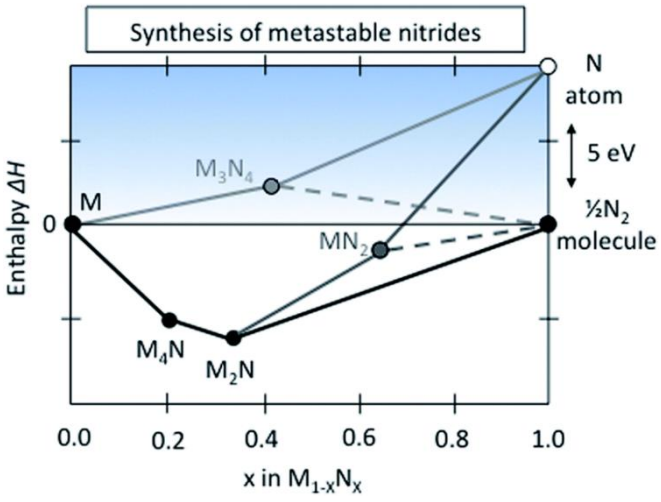

Figure 1.6 The "convex hull" diagram of the thermodynamically stable nitrides and unstable nitrides concerning the molecular nitrogen N_2.

doi:10.6342/NTU202403464

Several ways can be used to increase the chemical potential of nitrogen. One method involves using nitrogen precursors that are not strongly bound, such as ammonia and azides, instead of N_2. Ammonia (NH_3) is usually utilized as a nitrogen source combined with high temperatures to convert metal oxides to their corresponding nitrides.[38] while using ammonia as a nitrogen source, the chemical potential of nitrogen can be increased by +0.46 eV/N compared to the standard state.[9] For example, the synthesis of Ta_3N_5 often involves the ammonia annealing of Ta_2O_5 at high temperatures.[39] Azide precursors decompose with thermal treatment, generating highly reactive nitrogen atoms for nitride synthesis:[40]

$$N_{3(g)}^{-} \rightarrow N_{2(g)} + N + e^{-} \quad (1.5)$$

Another method employs high pressure and high temperature to overcome the chemically inert nature of N_2 and elevate its chemical potential above its standard state.[41] This approach has led to the synthesis of several metastable nitrides, including Ti_3N_4 and Zr_3N_4.[42, 43] However, this technique is generally limited to lab-scale synthesis and lacks the ability to scale up for larger production.

Additionally, reactive atomic nitrogen can be generated from nitrogen plasma via the reactive sputtering process.[44-46] The chemical potential of nitrogen can have extreme levitation by the incorporation of nitrogen plasma. Several metastable nitrides have been established via this method, including $LaWN_3$, $CeWN_3$, and $ZnTiN_2$.[47-49] It should be noted that the formation of metastable nitride usually requires a lower temperature environment to prevent the formation of gaseous N_2 or transformation to equilibrium phases.[50] Reactive magnetron sputtering is a key technique applied in this thesis. Detailed background information on this technique will be introduced in **Chapter 2**, and the experimental results regarding sputtering will be further discussed in **Chapter 3**.

doi:10.6342/NTU202403464

1.4 Tantalum Nitride as Photoanode

The phase diagram of the tantalum nitride (Ta-N) system is complicated, with the nitrogen content x of tantalum nitride varying from 0.41 to 1.67 when represented as TaN_x.[51-53] We summarize the known phases of the Ta-N system in the order of nitrogen content in **Table 1.1**.

Table 1.1 Overview of known tantalum nitride phases. Adapted from Ref.[54]

Phase	Crystal Structure	Composition	Density (g/cm^3)
γ-phase, β-Ta_2N	hcp of Ta	$TaN_{0.41-0.5}$	
ε-phase	hexagonal, B35 CoSn-type	TaN	
δ-phase	FCC, B1 NaCl-type	$TaN_{0.8-1.4}$	13.1
θ-phase	hexagonal, Bn WC-type	$TaN_{1-1.08}$	
Ta_5N_6	hexagonal	Ta_5N_6	
Ta_4N_5	tetragonal	Ta_4N_5	
Ta_2N_3	orthorhombic, tetragonal, cubic bixbyite-type	Ta_2N_3	13.42[55] 11.33
Ta_3N_5	orthorhombic, Fe_2TiO_5-type	Ta_3N_5	9.75

1.4.1 TaN

Tantalum nitrides with low nitrogen content are intrinsically metallic with excellent electrical conductivities, including 3 TaN phases as well as Ta_2N. These mononitrides can be easily fabricated via reactive magnetron sputtering.

doi:10.6342/NTU202403464

Their chemical resistance and mechanical stability make them popular in integrated circuit-related industries, serving as excellent copper diffusion barriers, particularly the δ-TaN phase.[51, 56, 57]

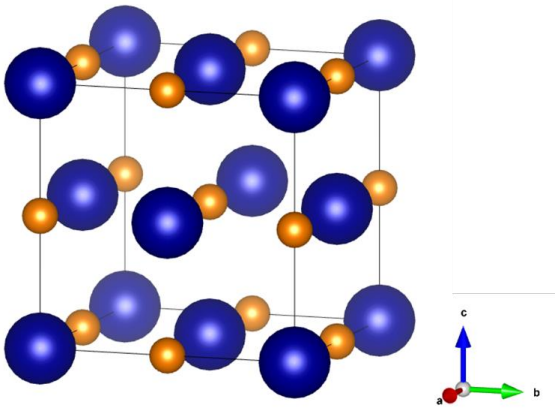

Figure 1.7 Crystal structure of δ-TaN obtained from ICSD-CollCode180957.

1.4.2 Ta_2N_3

A relatively nitrogen-rich phase in the Ta-N system is Ta_2N_3. Although first reported in 1968, this compound has been sporadically explored. The lattice structure of bixbyite-Ta_2N_3 can be found in **Figure 1.8**. It is considered an order-defective variant of the CaF_2 structure. The Ta atoms stack in the same face-centered cubic (fcc) manner as the Ca atoms in CaF_2, but unlike the 8-fold coordinated Ca, each Ta is surrounded by only six N atoms, with two corners of a Ta-centered cube remaining unoccupied. For 25% of the Ta atoms, the surrounding N atoms occupy all but two body diagonal corners. For the other 75% of the Ta atoms, the surrounding N atoms are located on all but two face diagonal sites. To share the unoccupied corner sites between the two types of Ta atoms, a 2×2×2 cubic supercell is constructed. Other compounds with the same bixbyite structure include C-Y_2O_3, In_2O_3, and U_2N_3.

doi:10.6342/NTU202403464

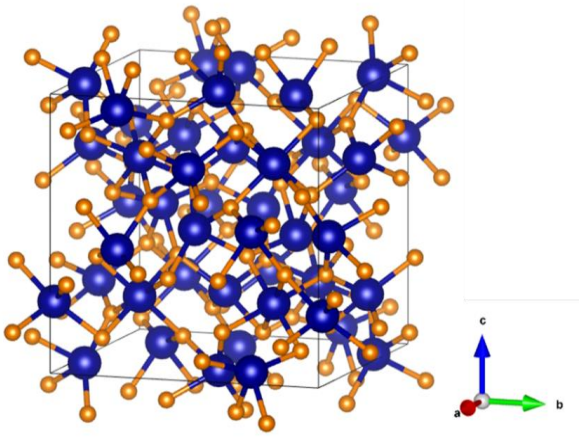

Figure 1.8 Crystal Structure of Bixbyite-Ta_2N_3 revised using VASTA according to the structure of $ZrTaN_3$.[58]

The first reported Ta_2N_3 phase was by the research group of Coyne *et al.* in 1968, prepared by sputtering a Ta target with pure nitrogen gas.[52] They assigned the strong X-ray peaks to the cubic FCC structure with a lattice constant of a = 5.047 Å. However, there was almost no research on this Ta-N phase after its first appearance. Coyne *et al.* reported the semiconductor nature of bixbyite Ta_2N_3, evidenced by the temperature-dependent electric resistivity, and an optical band gap between 1.95 and 2.6 eV: [52]

$$\rho = \rho_0 \cdot \exp\left(\Delta E / kT\right) \tag{1.6}$$

They claim that ΔE depends on the sputter deposition conditions and film thickness.

In 2004, another research group reported the fabrication of the Ta_2N_3 phase with plasma-enhanced CVD, assigning it to the bixbyite structure due to several weak diffraction peaks from the 2×2×2 superstructure.[54] The lattice constant was determined to

doi:10.6342/NTU202403464

be 9.8205 Å. Additionally, contrary to Coyne *et al.*, they report the metallic properties of Ta_2N_3.[54]

In 2016, Salamon *et al.* prepared a bixbyite Ta_2N_3 phase by reactive sputtering with a slightly larger lattice constant of about 9.84 to 9.88 Å.[51] They reported an optical band gap of about 2.0 eV but described the material as a degenerate semiconductor based on ab initio calculations.[51]

For Ta_2N_3, the excess electrons in the conduction band are not provided by external doping but by Ta itself. The formal oxidation state of Ta is +4.5, indicating that for every two Ta atoms, there is one electron left in the Ta 5d orbitals. Consequently, even though an internal band gap separates the N 2p states from the Ta 5d states, the bottom of the conduction band is filled with the remaining Ta 5d electrons. Optical transitions from the valence band to the conduction band are still possible but require more energy than suggested by the band gap, as electrons can only be excited into the unoccupied states above the Fermi level. Therefore, the optical band gap appears larger than the actual band gap; this effect is known as the Burstein-Moss shift.[59]

Fifty-three years after the first research article about Ta_2N_3, Jiang *et al.* reported the synthesis of metastable Ta_2N_3 by reactive sputtering with slight oxygen incorporation.[60] The incorporation of oxygen effectively stabilized the oxidation states of Ta. However, the oxygen content in the as-deposited films hampered the electric conductivity of Ta_2N_3 films, which could be eliminated by post-annealing under an NH_3 atmosphere, producing high-quality Ta_2N_3 and increasing conductivity by up to seven orders of magnitude. It was not until their report, combining experimental and computational results, that stoichiometric Ta_2N_3 was first characterized as a degenerate semiconductor with an optical band gap of about 1.9 eV.

doi:10.6342/NTU202403464

Aside from the cubic bixbyite Ta_2N_3 phase, the orthorhombic phase of η-Ta_2N_3 was synthesized by the high-pressure-high-temperature method.[55] Another phase, tetragonal Ta_2N_3, was predicted to be metastable by first-principle calculations and would undergo a phase transformation to η-Ta_2N_3 at 7.7 GPa.[61, 62]

1.4.3 Ta_3N_5

The most nitrogen-rich phase in the Ta-N system is Ta_3N_5. Ta_3N_5 is a semiconductor with a distinct red color, and its resistivity ranges from 10^{-2} to 10^{0} Ω·cm depending on the fabrication method.[63] It behaves diamagnetically.[64] The crystal structure of Ta_3N_5, shown in **Figure 1.9**, is orthorhombic with the space group Cmcm, characterized by the refinement of time-of-flight neutron diffraction.[65] Every Ta atom is six-fold coordinated by N and every N atom is connected to 3 or 4 Ta atoms. The lattice parameters are a = 3.8862 Å, b = 10.2118 Å, and c= 10.2624 Å. It has a pseudobrookite (Fe_2TiO_5)-like structure.

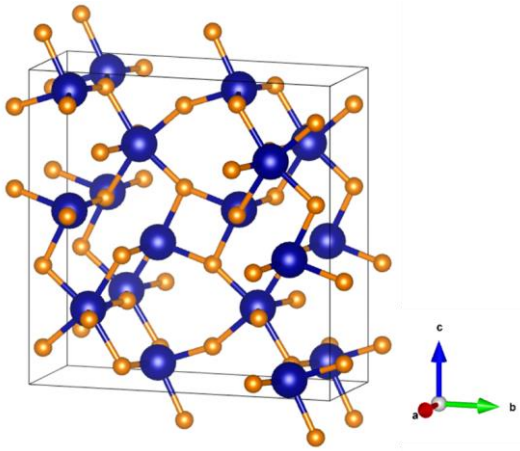

Figure 1.9 Crystal structure of Cmcm-Ta_3N_5 obtained from ICSD-CollCode66533.

doi:10.6342/NTU202403464

The oxidation state of Ta cations in Ta_3N_5 reaches the highest oxidation state of +5, suggesting that the Ta 5d orbital is empty. According to theoretical computations, the conduction band of Ta_3N_5 consists mainly of empty Ta 5d orbitals, while the valence band consists solely of contributions from N 2p orbitals.[66, 67] Similar cases are observed in Ta_2O_5 and TaON, where the conduction band also comprises empty 5d orbitals. In Ta_2O_5, the valence band consists only of O 2p orbitals, whereas, in TaON, it includes both O 2p and N 2p orbitals.[4, 25, 68] The energetic diagram shown in **Figure 1.10** illustrates that the valence band position shifts upward when oxygen is replaced by nitrogen due to the higher energy level of N 2p compared to O 2p, leading to a reduction in the band gap.

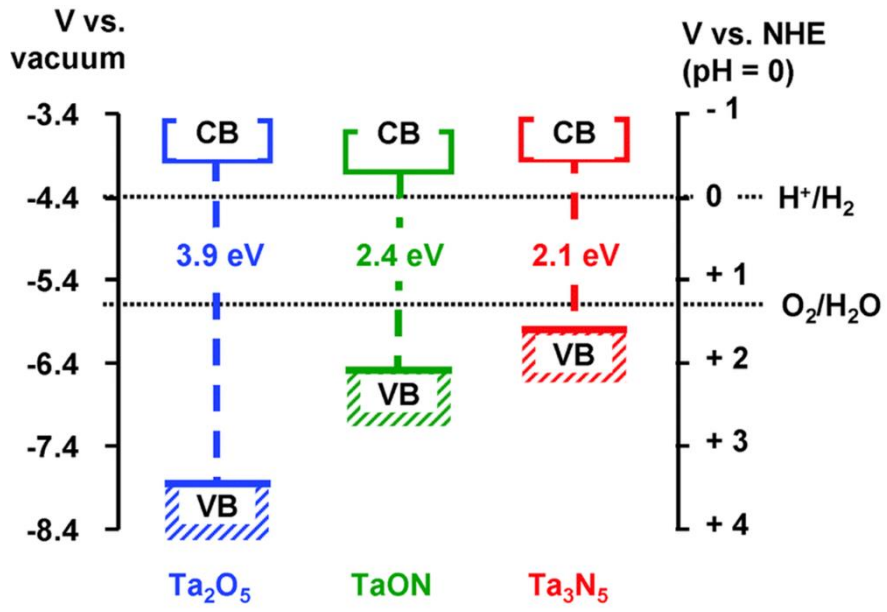

Figure 1.10 Band edge energetics of Ta_2O_5, TaON, and Ta_3N_5.[5]

According to the energetic positions in **Figure 1.10**, the valence and conduction bands of Ta_3N_5 straddle the oxygen and hydrogen evolution potentials. The 2.1 eV optical band gap of Ta_3N_5 enables efficient utilization of the solar spectrum in the visible region, which has the strongest radiation.[4-6] Additionally, the enhanced charge transport properties are due to the intrinsic properties of nitride. Based on its band gap, Ta_3N_5 is

doi:10.6342/NTU202403464

predicted to have a maximum solar-to-hydrogen efficiency of 15.9% with the highest current density output of 12.9 mA/cm².[7] Consequently, Ta_3N_5 is recognized as a promising candidate for photoelectrochemical energy conversion, particularly water splitting for green energy production, and has been extensively researched.

The fabrication of Ta_3N_5 typically involves annealing of the oxide precursor, Ta_2O_5, at temperatures between 800°C and 1000°C for several hours under an ammonia atmosphere.[34, 69-75] This method maintains the highest oxidation state of Ta cations in the Ta_3N_5 system. Some research also utilizes Ta metal precursors for the nitridation process.[33, 63, 76-80] Recently, platforms for direct synthesis via reactive sputtering have also been discussed.[81-84] However, the direct formation of the Ta_3N_5 phase with reactive sputtering is still challenged owing to the difficulty of increasing the oxidation state of Ta cations with nitrogen plasma directly.

1.4.4 Challenges of Ta_3N_5-based Photoelectrode

Despite being a promising photoelectrode, the PEC performance of Ta_3N_5 is hindered by its poor charge separation efficiency due to intrinsic defects, including oxygen impurities (O_N), nitrogen vacancies (N_V), and low-valence tantalum species (Ta^{3+}), as shown in **Figure 1.11**.[85-88] Oxygen impurities act as electron donor states, serving as n-type dopants that increase the carrier concentration of Ta_3N_5. However, nitrogen vacancies and low-valence tantalum species form deep defect states that trap carriers and facilitate recombination. Additionally, the surface of Ta_3N_5 lacks active sites for heterogeneous catalytic reactions and suffers from severe photo-corrosions, further deteriorating its performance.[89-91] Strategies to improve Ta_3N_5 performance include nanostructuring, integration of co-catalysts, and the introduction of extrinsic dopants, as summarized in **Table 1.2**.[92-96]

doi:10.6342/NTU202403464

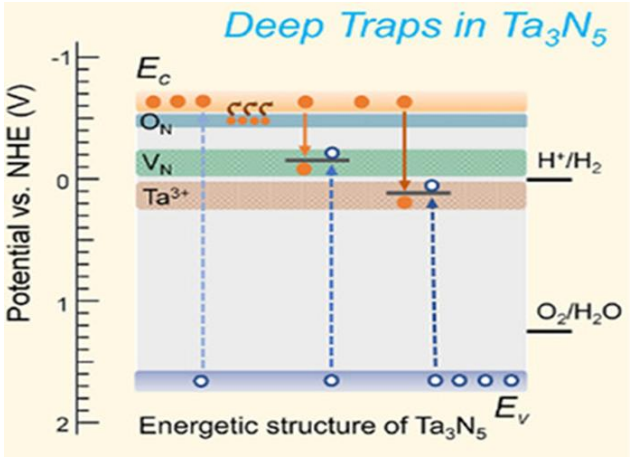

Figure 1.11 Energetic structure of Ta_3N_5 with its energetic position of defect states.[34]

To date, the Ta_3N_5 photoanode system has nearly reached its theoretical limits. However, closer examination of the conductive substrate and film thickness reveals that achieving such performance often involves extensive use of expensive and rare tantalum and niobium. Most research employs Ta foil or Nb foil as the conductive layer, depositing a thick layer (roughly 500 nm to 1 μm) of Ta_2O_5 via e-beam evaporation or reactive sputtering. This approach seems inefficient regarding material usage.

Tantalum metal is primarily purified from columbite-tantalite, an oxide mineral containing iron, manganese, niobium, and tantalum. The tantalum content in columbite-tantalite varies from 30% to 50%, depending on niobium content. Despite purification reaching 99.9%, tantalum's price remains high, at approximately 200,000 dollars per ton. Additionally, columbite-tantalite sources are mainly in South America, Australia, China, Russia, and Central Africa. Brazil and China dominate tantalum production, with significant recent production in the Democratic Republic of the Congo, often potentially associated with civil unrest and wars.

Given these factors, efficient use of tantalum is necessary for the potential commercialization of Ta_3N_5-based photoelectrodes. Mass production of Ta_3N_5-based

doi:10.6342/NTU202403464

photoanodes for green energy production faces challenges due to the high cost of tantalum and the ethical concerns surrounding its mining. An alternative conductive layer, such as silicon wafers, should be considered. Silicon wafers have mature processing procedures, are cheaper, and are easily integrated into current markets. Integrating Ta_3N_5 with silicon substrates has been investigated, with nanostructuring needed to enhance performance but potentially increasing production costs.[97, 98]

This thesis addresses the challenge of inefficient material usage in Ta_3N_5-based photoanodes by developing a new silicon-based Ta_3N_5 photoelectrode platform. Instead of using thick Ta_2O_5 as a nitridation precursor, a new nitride-based precursor, Ta_2N_3, is constructed via reactive sputtering. This approach enables a thin layer (about 100 nm) of Ta_3N_5 photoanodes to achieve superior PEC performance. Detailed findings will be elaborated on in **Chapters 4** and **Chapter 5**.

doi:10.6342/NTU202403464

Table 1.2 PEC performance of Ta_3N_5 photoanodes underwent different treatments from 2013 to 2024.

Group	Co-catalyst	Photoanode	Thickness (nm)	Substrate	J (mA/cm^2) @ 1.23 V_{RHE}
Kawase *et. al.*[99]	NiFeOx	Ta_3N_5	Nanorods	Ta	7.1
Kwon *et. al.*[69]	N:CoFeOx	Ta_3N_5/NbNx*	600	n-Si(100)	9.27
Pihosh *et. al.*[100]	NiFeCoOx	Ta_3N_5	NRs	Ta	10.96
Pihosh *et. al.*[101]	NiFeCoOx	Ta_3N_5	NRs	GaN/Al_2O_3	10.8
Higashi *et. al.*[80]	NiFeOx	Ta_3N_5	1000	Quartz	6.0
Wang *et. al.*[102]	NiFeOx	Ta_3N_5	>1000	Ta	9.8
Fu *et. al.*[70]	NiCoFe-Bi	In:GaN/Ta_3N_5/Mg:GaN	700	Nb	7.5
Xiao *et. al.*[71]	NiCoFe-Bi	La: Ta_3N_5/g-Mg: Ta_3N_5	650	Nb	8.51
Kawase *et. al.*[79]	IrOx	Ta_3N_5	800-900	Si:GaN/ Al_2O_3	3.0
Higashi *et. al.*[78]	NiFeOx	Ta_3N_5	800	Si:GaN/ Al_2O_3	7.4
Kawase *et. al.*[34, 63]	NiFeOx	Ta_3N_5	850	Quartz	5.1

doi:10.6342/NTU202403464

Table 1.2 (continued) PEC performance of Ta_3N_5 photoanodes underwent different treatments from 2013 to 2024.

Group	Co-catalyst	Photoanode	Thickness (nm)	Substrate	J (mA/cm^2) @ 1.23 V_{RHE}
Fu *et. al.*[34]	NiCoFe-Bi	Ta_3N_5	800	Nb	7.3
Xiao *et. al.*[72]	NiCoFe-Bi	g-Mg: Ta_3N_5	550	Nb	8.5
Higashi *et. al.*[76]	NiFeOx	Ta_3N_5	900	Quartz	6.0
Nurlaela *et. al.*[103]	CoPi	TaOx/ Ta_3N_5/Ta_3N_5+Ta_2N	900	Ta	8.1
Higashi *et. al.*[33]	NiFeOx	Ta_3N_5	500	Si:GaN/ Al_2O_3	6.3
Haleem *et. al.*[104]	Ni:CoFeOx	Ta_3N_5	>1000	Ta	5.3
Zhong *et. al.*[73]	CoPi	GaN/ Ta_3N_5	570	Ta	8.0
He *et. al.*[90]	NiFeOOH	Ta_3N_5	Nanotubes	Ta	6.3
Wang *et. al.*[74]	Co(OH)x	Ta_3N_5/TaxNy	Nanotubes	Ta	6.3
Liu *et. al.*[7]	Ni(OH)x	Fh/TiOx/ Ta_3N_5	>1000	Ta	12.1
Li *et. al.*[75]	CoPi	Ba: Ta_3N_5	Nanotubes	Ta	6.7

doi:10.6342/NTU202403464

1.4.5 Advantages of Ta_3N_5 over Oxide-Based Photoanodes

This section compares Ta_3N_5 photoanodes with other oxide-based photoanodes. First, we summarize the theoretical photocurrent density of various photoanode materials at V = 1.23 V vs. RHE under AM 1.5G solar irradiation in **Table 1.3**. Additionally, **Table 1.4** provides an overview of the photocurrent density achieved by these oxide-based photoanode materials for water splitting over the past three years. As discussed in **Section 1.2.3**, materials with larger band gaps tend to have lower theoretical photocurrent densities due to the wavelength-dependent irradiance intensity of the solar spectrum.

Table 1.3 Theoretical photocurrent density of different photoanode materials. Adapted from Ref.[7, 105]

Photoanode	**Band gap (eV)**	**Theoretical photocurrent density (mA/cm^2) @ 1.23 V_{RHE}**
Ta_3N_5	2.1	12.9
Fe_2O_3	2.1	12.5
$BiVO_4$	2.4	7.5
WO_3	2.7	4.8

One of the primary advantages of Ta_3N_5 photoanode over oxide-based counterparts is their higher theoretical photocurrent density, attributable to its moderate band gap. For example, hematite (Fe_2O_3) theoretically offers a photocurrent density of approximately 12.5 mA/cm² at V = 1.23 V vs. RHE. However, in practice, hematite photoanodes typically achieve only 3−5 mA/cm² at this potential, as shown in **Table 1.4**. Despite having a theoretical photocurrent density comparable to Ta_3N_5, the best-reported photocurrent density for hematite is around 5.1 mA/cm² at V = 1.23 V vs. RHE. This

doi:10.6342/NTU202403464

discrepancy is primarily due to hematite's short hole diffusion length (2−4 nm) and poor charge transport properties, leading to significant charge recombination.[106] Consequently, strategies like heteroatom doping and nanostructuring are often employed in hematite systems to mitigate recombination and improve charge extraction.[107]

In contrast, Ta_3N_5 photoanodes offer superior charge transport properties and longer hole diffusion lengths compared to oxide materials like hematite. Another extensively studied material is bismuth vanadate ($BiVO_4$), which has a theoretical photocurrent density of approximately 7.5 mA/cm² at V = 1.23 V vs. RHE due to its larger band gap. $BiVO_4$ photoanodes face challenges with short electron diffusion lengths (10 nm) and poor charge transport properties due to small polaron formation, both of which contribute to significant charge recombination.[108-110] These issues can be partially resolved by back-side illumination to enhance electron injection and by doping or creating vacancies in the lattice to improve charge transport. Although $BiVO_4$ photoanodes have nearly reached their theoretical limit, with the highest reported photocurrent density of 6.4 mA/cm² at V = 1.23 V vs. RHE, their stability remains a challenge due to photo-corrosion caused by hole accumulation and sluggish oxygen evolution reaction (OER) kinetics.[111]

Thus, Ta_3N_5 photoanodes are a more promising option than $BiVO_4$ photoanodes, offering higher theoretical photocurrent density, better charge transport properties, and improved stability for OER.

Tungsten trioxide (WO_3) is another promising photoanode material that has garnered significant attention due to its high electron mobility and longer hole diffusion length of approximately 150 nm, which is notably better than many other oxide-based semiconductors.[112, 113] However, WO_3 as a photoanode faces challenges due to its large

doi:10.6342/NTU202403464

band gap of about 2.7 eV, which limits its ability to efficiently absorb sunlight, resulting in a lower theoretical photocurrent density of about 4.8 mA/cm² at V = 1.23 V vs. RHE.

Additionally, WO_3 photoanodes suffer from severe charge recombination issues, primarily due to the presence of surface defects.[114, 115] To address these limitations, various strategies have been employed, including doping to enhance light absorption, surface passivation to reduce recombination, and the creation of heterojunctions, such as the $WO_3/BiVO_4$ structure, to improve photocurrent density.[116-119] Despite these efforts and the inherent advantages WO_3 has over other oxide-based photoanodes, the combination of severe charge transport issues and a large band gap significantly hinders its overall performance as a photoanode material.

doi:10.6342/NTU202403464

Table 1.4 PEC performance of different oxide-based photoanode materials.

Group	Co-catalyst	Photoanode	Treatment	J (mA/cm^2) @ 1.23 V_{RHE}
Liu *et. al.*[120]	NiCoFe-Bi	CuSCN/$BiVO_4$	Heterojunction	5.6
Pei *et. al.*[121]	NiFeLDH	$BiVO_4$	Gradient VO_4 vacancy	5.07
Zhang *et. al.*[122]	NiOOH	Co_3O_4/$BiVO_4$	Heterojunction	6.4
Liu *et. al.*[123]	X	VO_x/$BiVO_4$	Heterojunction	6.29
Zhang *et. al.*[124]	N:$NiFeO_x$	$BiVO_4$	Co-catalyst engineering	6.4
Park *et. al.*[125]	$NiFe(OH)_x$	Ge:Ti:Sn:Fe_2O_3	Doping/Nanostructuring	5.1
Chaule *et. al.*[126]	$NiFeO_x$	Al:Ti:Fe_2O_3	Doping/Nanostructuring	4.0
Kang *et. al.*[127]	$NiFeO_x$	P:Sn:Fe_2O_3	Doping	4.30
Yoon *et. al.*[128]	$NiFeO_x$	Ti:Si:Fe_2O_3	Doping	4.30
Zhang *et. al.*[129]	$NiFe(OH)_x$	Ta:Fe_2O_3/Fe_2O_3	Doping/Nanostructuring/ Homojunction	3.22
Kong *et. al.*[130]	FeNiOOH	WO_3	Nanostructuring/ O vacancy control	3.21
Nomellini *et. al.*[131]	Using scavengers	$BiVO_4$/WO_3	Nanostructuring/ Heterojunction	1.3
Wang *et. al.*[132]	TiO_x	WO_3	Passivation/Heterojunction	1.67

doi:10.6342/NTU202403464

Chapter 2. Experimental Method

This chapter focuses on the preparation and analyzing procedures of tantalum nitride thin films. **Chapter 2.1** introduces the working principles of the reactive magnetron sputtering apparatus employed in this work. **Chapters 2.2 - 2.6** discuss various structural, morphological, and optical characterization methods. Finally, details of the photoelectrochemical measurements, including the direct current (DC) and alternative current (AC) methods are presented in **Chapters 2.7 - 2.8**.

2.1 Reactive Magnetron Sputtering

Sputtering is a form of physical vapor deposition (PVD) technique employed to prepare a diverse range of functional materials, including metals, semiconductors, and insulators. This technique has been used to deposit thin films with specific mechanical, chemical, optical, or electrical properties. For instance, titanium nitride (TiN) can be deposited by sputtering as a wear-resistant coating on the knives to improve durability. Additionally, tantalum mono-nitride (TaN) serves as a crucial diffusion barrier for Cu in semiconductor manufacturing. The applications of the sputtering process extend to various aspects of everyday life, playing a pivotal role in producing high-quality films with diverse applications. The main difference between sputtering and other PVD techniques, like electron beam evaporation and thermal evaporation, lies in its utilization of dense plasma; this plasma derives from the ionization of inert gas, such as argon, and directly acts on the sputtering target to knock atoms out, in contrast to the high temperatures required by the evaporation techniques.

doi:10.6342/NTU202403464

In addition to argon, reactive gases such as O_2 and N_2 can also be introduced into the process chamber to deposit compound semiconductors, such as oxide or nitride, from metallic targets, which is referred to as reactive sputtering. However, the introduction of reactive gas may lead to target poisoning, which can be mitigated by using pulsed-DC or radio-frequency (RF) power supplies. Moreover, magnetron sputtering utilizes a set of strong magnets to spatially confine the plasma near the target surface and hence increases the deposition rate while reducing the consumption of high-purity inert gases. The mechanism and apparatus configurations of various sputter deposition methods will be further addressed and discussed in the following sections.

2.1.1 Physics of Sputtering Process

Plasma is defined as a quasi-neutral gas of charged particles exhibiting collective behavior. A quasi-neutral gas means that the electron density (n_e) within the plasma approximates the ion density (n_i) times the electrical charge of the ion (Z):

$$n_e \cong Z \cdot n_i \tag{2.1}$$

On the other hand, the collective behavior connotes that the local disturbance of equilibrium can strongly influence other parts of plasma due to the strong $1/r$ Coulomb potential. The imbalance of net charge, either increasing or decreasing the charge density (ρ), would be immediately reflected by the Gauss law to cause fluctuation in the electric field (E):

$$\nabla E = \rho/\epsilon_0 \tag{2.2}$$

doi:10.6342/NTU202403464

Concurrently, the moving ions and electrons, which respectively have velocities v_i and v_e, give rise to a current density (J) and the induction of a magnetic field B owing to Amperes' law:

$$J = q(Zn_i v_i - n_e v_e) \tag{2.3}$$

$$\nabla \times B = \mu_0 J \tag{2.4}$$

Here, ϵ_0, μ_0, and q represent vacuum permittivity, vacuum permeability, and elementary charge, respectively. The internal electric and magnetic fields strongly determine the dynamic of plasma. The plasma density usually refers to the electron density or the degree of ionization (α) defined as:

$$\alpha = \frac{n_e}{n_e + n_n} \tag{2.5}$$

in which n_n is the density of neutral species. The degree of ionization is strongly affected by the type of plasma generated.

To fulfill the quasi-neutrality of plasma, the electrons and ions would adjust their local charge distribution in response to the disturbance. The large mass difference between ions and electrons leads to nonequilibrium electron and ion motions. A positive 'test charge' placed in the middle of plasma induces the redistribution of charges, thus building up a potential that shields the test charge, as shown in **Figure 2.1**. Such a Debye shielding sheath brings about two important parameters: Debye length (λ_D) and plasma parameter (g), both of which will be derived briefly in the next paragraphs.[133]

doi:10.6342/NTU202403464

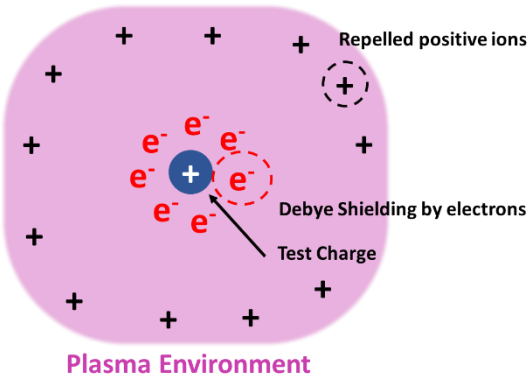

Figure 2.1 Formation of Debye shielding sheath to screen the test charge that is placed in the plasma environment.

As in **Figure 2.1**, assuming a positive charge is placed in the plasma. The electrons in the plasma would be attracted toward the test charge while the positive ions are repelled. After thermal equilibrium ($T_e = T_i$), the kinetic energy of electrons and ions can be represented by the electron temperature:

$$\frac{1}{2}m_e v_e^2 = \frac{1}{2}m_i v_i^2 = \frac{3}{2}k_B T_e \tag{2.6}$$

$$\frac{v_i}{v_e} = \left(\frac{m_e}{m_i}\right)^{1/2} = \left(\frac{m_e}{A \cdot m_p}\right)^{1/2} \tag{2.7}$$

in which k_B, A, and m_p are Boltzmann constant, proton number and proton mass, respectively. Given the large mass difference between electrons and ions, the ions are almost stationary from the electron's perspective. Considering the ion density (n_i) is approximately constant, it can be represented by the mass density (ρ_m) and the Avogadro constant (N_v). The electron density (n_e) will be the function of ion density and the potential $\phi(r)$ created by the positive charge placed in the plasma.

doi:10.6342/NTU202403464

$$n_e = n_i \exp\left(e\phi/k_B T_e\right) \tag{2.8}$$

Using Poisson's equation in (2.9), the potential can be solved, and so can the Debye length in the unit of cm:

$$\nabla^2 \phi = -\frac{\rho}{\epsilon_0} = -\frac{q}{\epsilon_0}(n_i - n_e) \tag{2.9}$$

$$\phi = \frac{1}{4\pi\epsilon_0} \cdot \frac{\exp(-r/\lambda_D)}{r} \tag{2.10}$$

$$\lambda_D = \left(\frac{\epsilon_0 k_B T_e}{e^2 n_e}\right)^{1/2} \tag{2.11}$$

Where the electron temperature has a unit of electronvolts, and the electron density is in the unit of cm^{-3}.

Debye length is a fundamental property of plasma that measures the net electrostatic effect in a solution and how far its electrostatic effect persists. Within Debye length, the charges are increasingly electrically screened and the electrostatic potential decreases exponentially. It depends on the plasma temperature and the density. For an ideal plasma, the Debye sphere includes many particles and the discussion of collective properties is meaningful. Plasma parameter (g) is another way to describe plasma.

$$N_D = n_e \frac{4\pi}{3} \lambda_D^3 \tag{2.12}$$

$$g = 4\pi n_e \lambda_D^3 \tag{2.13}$$

Plasma temperature measured in Kelvin or electronvolts therefore can be used to calculate the Debye Length and Plasma parameter for the control of plasma for material

doi:10.6342/NTU202403464

processing, which usually represents the temperature of electrons and is usually in the range of thousands of Kelvins when field emission is utilized.

Plasma can only be created by ionization. There are several ways to ignite a plasma: by collisions of fast electrons or neutrons with atoms, photoionization by electromagnetic radiation, and through the electric breakdown in the strong electric field.[134] The latter are categorized as field ionization, which is the same mechanism as plasma formation for the sputtering process. The concept of field ionization can be known from the field strength (E_a) required to kick an electron away from an atom. The electric field strength at the Bohr radius (α_B) can be used as the threshold for the ionization for target material by the introduction of atomic intensity (I_a).

$$\alpha_B = \frac{\hbar^2}{m_e^2} = 5.3 \times 10^{-10}\ (m) \tag{2.14}$$

$$E_a = \frac{e}{4\pi\epsilon_0 \alpha_B^2} \cong 5.1 \times 10^9\ (V \cdot m^{-1}) \tag{2.15}$$

$$I_a = \frac{\epsilon_0 \cdot c \cdot E_a^2}{2} \cong 3.51 \times 10^{20}\ (W \cdot m^{-2}) \tag{2.16}$$

Plasma ignition in the sputtering process uses field ionization by a strong direct current voltage applied across the two electrodes, causing electric breakdown of the inert sputtering gas in low pressure. First, electrons are ionized near the cathode and then accelerated away by the negative bias applied to the cathode. After gaining sufficient kinetic energies, these electrons can collide with the neutral gas atoms and generate another electron through impact ionization. The newly generated electrons then keep ionizing the other gas molecules, forming a cascade reaction to the dense plasma formation.

doi:10.6342/NTU202403464

$$e^- + Ar \rightarrow 2e^- + Ar^+ \quad (2.17)$$

Meanwhile, the ionized Ar^+ ions are attracted and accelerated toward the cathode with their kinetic energy increasing. These energetic ions bombard the sputtering target and transfer energy to the target atoms, ejecting them out from the surface. This linear collision cascade reaction is illustrated in **Figure 2.2**.[135]

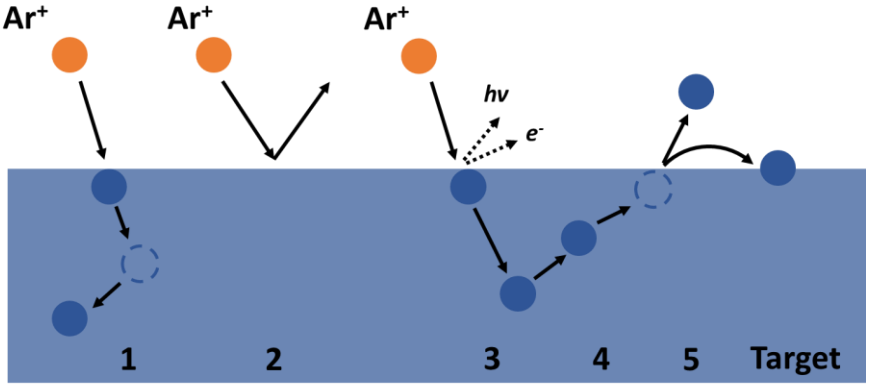

Figure 2.2 The trajectory of the target atom on the surface after energetic collision by the sputtering gas ions: (1) displacement, (2) back scattering, (3) photon or secondary electron emission, (4) collision cascade, and (5) sputtering or re-deposition.

As illustrated in **Figure 2.2**, a linear cascade occurs when target atoms are displaced due to the implantation of energetic ions. This initial displacement causes the recoil of neighboring atoms. Suppose these recoiled atoms acquire kinetic energy greater than the surface binding energy of the target. In that case, they may either be ejected as neutral target atoms or escape directly as target ions. The ejected ions would have enough kinetic energy to be deposited on the substrate some distance from the target. Conversely, the positively charged ions would also be re-deposited on the cathode.

doi:10.6342/NTU202403464

To describe the rate of target erosion by the sputtering process, the sputtering yield (Y) is defined by:

$$Y = \frac{number\ of\ emitted\ particles}{number\ of\ incident\ particles} \tag{2.18}$$

The sputtering yield, usually with a value in the range of 0.5 to 2.0, depends on the structure and composition of the target, the incident current, the applied voltage, and the incident angle. Detailed influences of these parameters are beyond the scope of this thesis.

Another important quantity is the deposition rate, which is proportional to the sputtering yield but is more dependent on the deposition process pressure that dictates the electron mean free path. At lower process pressures, the electron mean free path is extended, leading to the formation of plasma far away from the target. This increases the probability of Ar^+ not reaching the target surface with efficient kinetic energy, resulting in a low deposition rate. On the other hand, the mean free path becomes shorter at extremely high process pressures, and collisions between ionized plasma gas become more prevalent. The collisions between ions or neutral gas atoms/molecules consume the energy for the sputtering of target atoms and hence reduce the deposition rate. Therefore, there exists an optimal range of process pressure for maximizing the deposition rate.

2.1.2 Magnetron Sputtering

In the typical sputtering process, the chamber would first be evacuated to a high vacuum, not only to avoid contaminations from residual gases such as moisture but also to increase the mean free path of electrons, the latter of which is closely related to the

doi:10.6342/NTU202403464

mechanism of sputtering. To ignite the plasma, a high voltage is applied between the cathode, usually a metal target, and the anode, commonly connected to the chamber as electric ground. The high voltage ionizes the sputtering gas introduced into the chamber, and the formation of plasma is the consequence of the cascade process of ionization.

To facilitate more energetic collisions without changing the properties of the target material, the sputtering gas is usually chosen to be an inert gas with a high molecular weight such as argon and xenon. However, with the simplest configuration of sputtering, as mentioned in the previous section, the usage of sputtering gas would be difficult to control and the deposition rate is strongly affected by the pressure of the chamber. If the pressure is too low, then it's difficult to ignite the plasma due to the deficiency of electrons for the cascade reaction, leading to a decrease in the ionization rate and the deposition rate of the target material on the substrate.

If higher pressure of sputtering gas is applied to compensate for this problem, the upcoming issues include the rapid consumption of expensive sputtering gas, which usually should have a purity of 99.9999%. Additionally, the high plasma temperature may damage the deposited film.

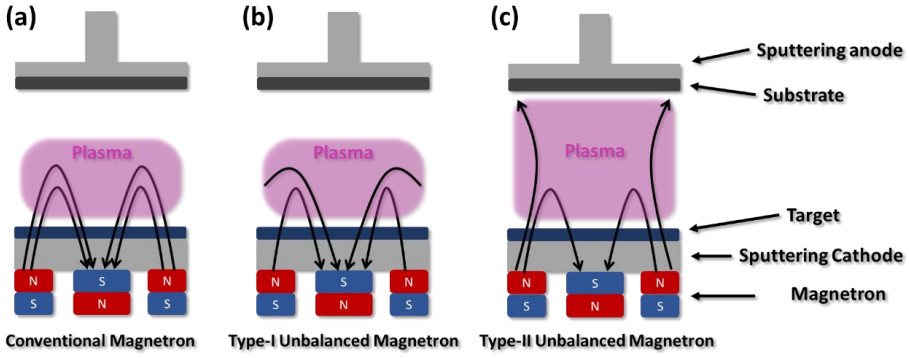

Figure 2.3 Different Configuration of Magnetron sputtering: (a) conventional setup of magnetron, (b) type-I unbalanced magnetron, and (c) type-II unbalanced magnetron.[136]

doi:10.6342/NTU202403464

Magnetron sputtering was developed to overcome the limitations of the traditional sputtering process by incorporating strong magnets underneath the sputtering target. The magnets are arranged so that one pole is positioned at the central axis of the target, while the second pole is formed by a ring of magnets around the outer edge of the target (**Figure 2.3**). This configuration allows the magnetic field to restrict the motion of secondary electrons to the vicinity of the target surface, and facilitates the formation of denser plasma without excess consumption of sputtering gas, leading to an increased deposition rate through enhanced collisions between ionized gas molecules and target materials. Furthermore, it helps mitigate the potential damage caused by the direct impact of these secondary electrons on the substrate or growing films. In this setup, the plasma typically extends to approximately 60 mm from the target surface. and films grown in this region are strongly influenced by ion bombardments. However, when the substrate is placed away from that region, the low plasma density dominates, resulting in a lower deposition rate and film quality. This conventional setup of magnetron sputtering is known as balanced magnetron sputtering (**Figure 2.3a**).

On the other hand, unbalanced magnetron sputtering involves a magnetron composed of magnets with different strengths, allowing some magnetic lines to be directed toward the substrate. In this case, the plasma is not confined near the target but slightly extends to the substrate region. The ions can be extracted from the plasma without requiring additional negative bias applied to the substrate. Consequently, within the same target-to-substrate distance, which is greater than 60 mm, unbalanced magnetron sputtering provides a higher deposition rate than conventional magnetron sputtering (**Figure 2.3b** & **Figure 2.3c)**. The advantages of unbalanced magnetron sputtering include achieving an adequate deposition rate at a greater target-to-substrate distance.

doi:10.6342/NTU202403464

This capability allows for the implantation of multiple cathodes in the same magnetron sputtering system, enabling a more diverse film composition via the co-sputtering process.

The sputtering process described above is suitable for depositing high-quality and uniform conducting materials, typically metals. However, for the deposition of insulating or semiconducting compound materials, two methods are commonly employed: reactive magnetron sputtering of the metal target and the direct usage of insulating or semiconducting compound targets. In the reactive magnetron sputtering process, chemically reactive gases (such as O_2 or N_2) with controlled partial pressure are introduced into the chamber in addition to the inert gas. The chemical potentials of these reactive gases are elevated due to plasma formation, which can facilitate the formation of the metastable phases.

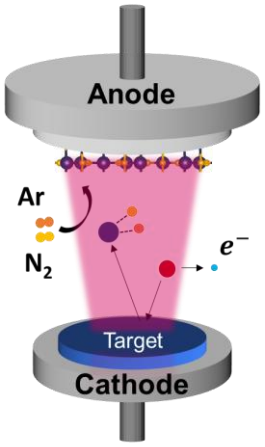

Figure 2.4 Schematic illustration of the reactive sputtering process.

The detailed mechanism of reactive magnetron sputtering is still a subject of debate. The formation of compounds on the target surface may be sputtered by the plasma and then deposited on the substrate. The process is similar to the unbalanced magnetron sputtering process, with the key difference being the sputtering of a compound target (on the surface of the metal target) rather than just a metal target. In addition, the reactive gases may react with the ejected target materials in the process environment.

doi:10.6342/NTU202403464

The advantage of using reactive magnetron sputtering over the direct usage of a compound target lies in the controllability of partial pressure, which allows for composition tuning on the deposited materials. Additionally, cleaning a metal target is generally easier than cleaning a semiconducting or insulating target. Both methods, however, face challenges such as low deposition rates, target poisoning, and arcing of the target material.[137, 138] These issues stem from the non-conducting nature of the targets, leading to a deficiency of charges to compensate for the lost positive charged sputtered atoms. This charging phenomenon can hinder the ejection of target molecules from the surface, as the strong electric field shields collision from the plasma.

To address these challenges, two solutions are commonly employed: radio-frequency (RF) magnetron sputtering and pulsed-DC magnetron sputtering. Both methods involve alternative switching of positive and negative bias applied on the sputtering target, allowing for the continuation of the sputtering process without altering deposition parameters or succumbing to target poisoning.

In the RF sputtering process, a 13.56 MHz radio frequency power supply is utilized, meaning the bias switching happens at this frequency.[139] On the positive potential cycle, a positive bias attracts the electrons in the plasma to dissipate the positive charges accumulated during sputtering. In the negative portion of the cycle, a negative potential is applied to sustain the sputtering process. However, RF magnetron sputtering is known for its complex setup and high cost.

Alternatively, pulsed-DC magnetron sputtering employs a pulsed direct circuit power supply.[140] In this approach, the sputtering process operates at the normal operation voltage during the pulsed-on period. This period is limited to control surface charging and prevent arcing. During the pulsed-off period, the applied potential is raised to the opposite sign compared to the pulsed-on period with the applied potential raised slightly higher

doi:10.6342/NTU202403464

(~20-30%), attracting electrons in the plasma to dissipate the positive charges. This method offers advantages such as a simpler setup, direct installation in magnetron sputtering systems without major modifications, and a more cost-effective solution compared to RF magnetron sputtering.

2.1.3 Deposition Apparatus

The sputtering deposition system used in this work is a custom-built co-sputtering system. It consists of a process chamber and a load-lock chamber, both can be evacuated and kept under a high vacuum of approximately 2×10^{-7} Torr. The load-lock chamber is used to transfer the sample into or out of the process chamber to avoid contaminating the process chamber (**Figure 2.5b**). The load-lock chamber is approximately $250 \times 250 \times 200$ mm^3 in volume and made of SUS304L stainless steel; it is equipped with a quartz window and the inner surface is electropolished for minimizing out-gassing. The chamber is evacuated first to roughly 8×10^{-2} Torr by a dry scroll pump (ACP15, Pfeiffer GmbH) with the ability to evacuate 233 L/min, and then switched to a 260 L/min turbo pump (Hipace 300, Pfeiffer GmbH) to reach the high vacuum condition below 3×10^{-7} Torr for sample transfer. The pressure is measured by a full range (750 to 10^{-10} Torr) cold cathode gauge (PTR91, Pfeiffer GmbH), a Pirani gauge (TTR91, Pfeiffer GmbH) with a pressure range from 750 to 5×10^{-4} Torr, and an ATM sensor (ZSW40, SMC Japan) with a pressure range from 750 to 10^{-2} Torr.

The process chamber, which I would denote as the main chamber afterward, is approximately $500 \times 500 \times 500$ mm^3 in volume and made of SUS304L stainless steel (**Figure 2.5a**). It is also equipped with a quartz window covered by a retractable shutter, and the inner surface is electropolished. The chamber is evacuated first to roughly 8×10^{-2} Torr by a 400 L/min dry scroll pump (ACP28, Pfeiffer GmbH), and then

doi:10.6342/NTU202403464

switched to a 685 L/min turbo pump (Hipace 700, Pfeiffer GmbH) with the ability to evacuate to reach the high vacuum condition for below 5×10^{-8} Torr. The pressure is measured by a full range (750 to 10^{-10} Torr) cold cathode gauge (PTR91, Pfeiffer GmbH), a Pirani gauge (TTR91, Pfeiffer GmbH) with a pressure range from 750 Torr to 5×10^{-4} Torr, and an ATM sensor (ZSW40, SMC Japan) with a pressure range from 750 Torr to 10^{-2} Torr.

On the bottom of the main chamber, there are four 2"-diameter sputtering cathodes (L200A01FM, MEIVAC U.S.A) mounted with an incline angle of about 30 degrees pointing toward the substrate holder. Each sputtering target is covered by a mechanical shutter. In this work, only one of the sputtering cathodes is used, and it is installed with a 6 mm thick Ta target (99.99 wt%, Ultimate Material Technology). The sputtering cathodes are electrically connected to a pulsed DC power supply (DC4001, MEIVAC U.S.A) with a maximum output power of 1 kW and the shortest pulsed time of 1 μs.

The substrate holder that can accommodate a 3"-diameter wafer is situated at approximately 30 cm above the sputtering targets, facing the downward direction to reduce particle contamination (**Figure 2.5c**). The substrate holder is equipped with a shutter and a resistive heater (SU-300-HH, MEIVAC U.S.A) on the backside. The rotation of substrate can be set between 5 to 25 rpm to provide a more even temperature distribution and better film homogeneity without the shadowing effect. A 300 W RF power supply (R301-MKII, Seren USA) is connected to the substrate holder for plasma generation for substrate cleaning; this RF power supply is equipped with an auto-matching box to maximize the bias generated on the substrate holder in case of any power loss by impedance non-matching problems.

During the deposition, the gases, such as Ar, N_2, and O_2 (99.9999%, Shenyi Gas Co.), are introduced into the main chamber and the gas flow rates, which is in the unit of

doi:10.6342/NTU202403464

standard cubic centimeter per minute (sccm), are controlled by mass flow controllers (1179C, MKS U.S.A). The process pressure is adjusted by a butterfly valve, and the feedback control is done by measuring the process pressure with a Baratron gauge (626C, MKS U.S.A) to fulfill the stability of the process condition. A water chiller (KW-12PTS-D, KauKan Industries) with a maximum cooling capacity of 3000 kcal is used for the cooling of the system, especially the target cathodes, to avoid issues regarding target debonding.

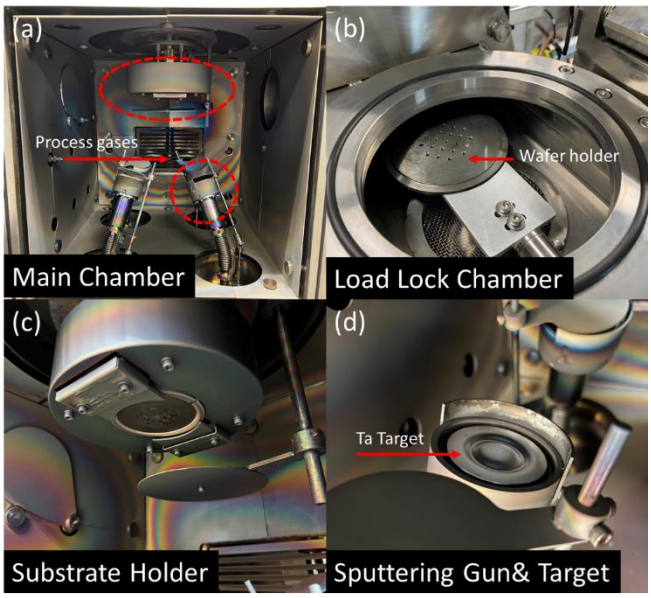

Figure 2.5 Image taken of (a) the sputtering main chamber, (b) the load lock chamber, (c) the substrate holder, and (d) the sputtering gun& target.

doi:10.6342/NTU202403464

2.2 Structure Characterization

2.2.1 X-ray Diffraction

X-ray diffraction (XRD) is a non-destructive technique capable of determining the structural properties of crystalline materials. No special sample pre-treatments are required for basic measurements. Crystal structure, grain orientation, and film thickness can be obtained depending on measurement conditions and the samples used in the measurement, such as films or powder. Usually, Bragg's law is used to describe the diffraction event with a specific set of periodic lattice planes. Herein, we will discuss the principle of X-ray diffraction and divide it into different aspects: the definition of lattice, the diffraction of high-energy photons, and the experimental setup of X-ray diffractometry for different measurement conditions.

Crystalline materials have a periodic arrangement of planes or atoms that cannot be directly observed with the naked eye. Hence, the smallest repeating unit, a unit cell, is defined as the building block of the structure. A three-dimensional unit cell is constructed by the volume with defined edge lengths (a, b, c) and the angles between edges (α, β, γ). A unit cell can be categorized into 7 different crystal systems with 14 different lattice types (**Figure 2.6**).[141] Miller indices with syntax (*hkl*) are used as a coordinate system to describe the planes in the crystal lattice. These syntaxes (*hkl*) represent a lattice plane intercepting the 3 axes at point (a/*h*, b/*k*, c/*l*). It turned out to be more useful for structure analysis to specify the orientation of a plane by Miller indices.

doi:10.6342/NTU202403464

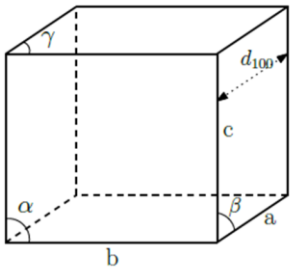

System	# of lattice	Parameters
Triclinic	1	$a \neq b \neq c; \alpha \neq \beta \neq \gamma$
Monoclinic	2	$a \neq b \neq c; \alpha = \gamma = 90° \neq \beta$
Orthorhombic	4	$a \neq b \neq c; \alpha = \beta = \gamma = 90°$
Tetragonal	2	$a = b \neq c; \alpha = \beta = \gamma = 90°$
Cubic	3	$a = b = c; \alpha = \beta = \gamma = 90°$
Trigonal	1	$a = b = c; \alpha = \beta = \gamma < 120°, \neq 90°$
Hexagonal	1	$a = b \neq c; \alpha = \beta = 90°; \gamma = 90°$

Figure 2.6 Schematic of a unit cell and all the Bravais lattice types in three dimensions.

Considering a crystalline material with a periodic electron density of $\rho(r)$, the electron density can be represented by the Fourier series with a set of vectors G that is invariant under all crystal translations leading to the invariance of crystal, where ρ_n is the Fourier coefficient of the series.

$$\rho(r) = \sum_n \rho_n \exp(i \cdot G \cdot r) \tag{2.19}$$

We would define G as the reciprocal lattice vectors of which the constituted basis are orthogonal to the basis of the lattice vector r and fulfill the equations below:

$$G = h \cdot b_1 + k \cdot b_2 + l \cdot b_3 \tag{2.20}$$

$$r = v \cdot a_1 + m \cdot a_2 + s \cdot a_3 \tag{2.21}$$

$$b_i \cdot a_j = 2\pi\delta_{ij} \tag{2.22}$$

Assuming an incident radiation in the form of a plane wave with amplitude $A(r,t)$ interacts with the material and the outgoing wave has an amplitude $A'(r,t)$. The wavevectors of the incoming and outgoing beams are k and k', respectively, and define $K = k - k'$.

doi:10.6342/NTU202403464

$$A(r,t) = A_0 \cdot \exp\left[-i \cdot (r - R) \cdot k - i \cdot \omega \cdot t\right] \tag{2.23}$$

$$A'(r,t) = A_0 \cdot \exp\left(\mathrm{R'k'} - \mathrm{Rk}\right) \cdot \exp\left(-2i \cdot \omega \cdot t\right) \cdot \int \rho(\mathrm{r}) \cdot \exp\left[-i \cdot (K) \cdot r\right] dV \tag{2.24}$$

The measured intensity $I(K)$ can be obtained from the squared modulus of the amplitude $A'(r,t)$, with $\rho(\mathrm{r})$ substitute into the equation.

$$I(K) \propto \left| \sum_n \rho_\mathrm{n} \int \exp[i \cdot (G - K) \cdot r] dV \right|^2 \tag{2.25}$$

$$\sum_n \rho_\mathrm{n} \int \exp[i \cdot G \cdot r] \cdot \exp[-i \cdot K \cdot r] dV = \sum_n \rho_\mathrm{n} \delta_{GK} \tag{2.26}$$

From the Fourier analysis of this measured intensity, this function can only get the solution when $G = K$. The implication is that diffraction would happen only when the scattering vector is equal to a specific set of reciprocal lattice vectors. When considering the elastic scattering of high-energy photons with the lattice, the energy and the momentum of the photon are therefore conserved, which leads to the fact that the magnitude of k should be equal to that of k' but in opposite directions.

$$G = k - k' = K \tag{2.27}$$

We can derive the diffraction condition above by squaring the above equation with substituting the identity that k^2 should equal to k'^2.

doi:10.6342/NTU202403464

$$2k \cdot G + G^2 = 0 \tag{2.28}$$

By substituting $-G$ into the equation, the diffraction condition can finally be achieved. This diffraction condition is another representation of Bragg's law we are familiar with.

$$2k \cdot G = G^2 \tag{2.29}$$

Recall that for a specific reciprocal lattice vector G, the coefficient of that vector satisfies the diffraction conditions is the same as the coefficient of Miller indices. Substituting the distance between parallel lattice planes, d, and the value of the wavevector, k, into the equation leads to Bragg's condition with $n = 1$, where θ is the angle between the incident beam and the crystal plane:

$$d = \frac{2\pi}{|G|} \tag{2.30}$$

$$k = \frac{2\pi}{\lambda} \tag{2.31}$$

The integers *hkl* define the specific reciprocal lattice vector G are not necessarily identical to the indices of an actual crystal plane, because *hkl* may contain a common factor n, representing a smaller spacing between the same set of lattice planes. Therefore, Bragg's condition can be obtained.

$$2dsin\theta = n\lambda \tag{2.32}$$

doi:10.6342/NTU202403464

The discussion above for Bragg's condition only considers the contribution of the lattice plane but does not consider the contribution of the basis inside the lattice. The atoms in the lattice would cause the interference of the diffracted beams because of the different electron density distribution. Here, we can consider the effect of atoms by re-visits the measured intensity under diffraction condition $K = G$ without substituting $\rho(\mathrm{r})$. We can denote the contribution of the final intensity to some structural factor F caused by the atoms inside the lattice.

$$I(K) \propto \left| \int \rho(\mathrm{r}) \cdot \exp[-i \cdot G \cdot r] dV \right|^2 \propto F^2 \tag{2.33}$$

The electron density $\rho(\mathrm{r})$ can be constructed by the superposition of the electron density function of ρ_j associated with each atom j of the cell.

$$\rho(\mathrm{r}) = \sum_{j}^{s} \rho_\mathrm{j}(\mathrm{r} - \mathrm{r_j}) \tag{2.34}$$

The structure factor, F, can be obtained by substituting the electron density.

$$\mathrm{F} = \int \sum_{j} \rho_\mathrm{j}(\mathrm{r} - \mathrm{r_j}) \cdot \exp[-i \cdot G \cdot r] dV \tag{2.35}$$

By substitute $l = \mathrm{r} - \mathrm{r_j}$ into the equation, we can construct the atomic form factor and obtain the structure factor of the basis.

doi:10.6342/NTU202403464

$$f_j = \int \rho_j(l) \cdot \exp[-i \cdot G \cdot r_j] dV \quad (2.36)$$

$$F = \sum_j f_j \cdot \exp[-i \cdot G \cdot r_j] \quad (2.37)$$

Some diffraction planes are forbidden in the diffractogram because the structure factor would go to zero under these diffraction conditions as indicated by the $G \cdot r_j$ in equation (2.37). Besides, for the same crystal system with differently constituted atoms, the final peak intensity would also differ because the electron density is different shown by the f_j term in equation (2.37).

A basic X-ray diffractometer setup usually consists of 5 major components: an X-ray source, the incident optical system, a goniometer, the receiving optical system, and the detector. Four axes are generally presented in the diffractometer: the ω axis (sample rotation), φ axis (in-plane rotation), χ axis (tilting axis), and 2θ axis (scanning detector) To precisely control the angle of the X-ray source and detector relative to the sample stage, a goniometer is used with both the source and detector mounted on it. The incident angle of the X-ray beam with respect to the sample surface is defined as ω, and the angle enclosed by the incident beam and the diffracted beam is denoted as 2θ (**Figure 2.7**). For different kinds of samples, such as polycrystalline powder, polycrystalline films, or epitaxial thin films with a well-defined growth orientation, different measurement conditions should be used to extract the desired structural information.

When performing a $2\theta/\omega$ scan under a Bragg Brentano geometry with a polycrystalline powder, only the out-of-plane information, that is, the diffraction plane parallel to the sample surface can be obtained. Nevertheless, since the powder has a fully random orientation with equal weight, there will always be crystal orientation pointing out-of-plane direction to satisfy Bragg's condition under this measurement condition. The

doi:10.6342/NTU202403464

formation of Debye-Scherrer rings in the reciprocal space guarantees the detection of each orientation just by the $2\theta/\omega$ scan mode, also known as Bragg Brentano mode.

The out-of-plane information can be achieved by both symmetric and asymmetric configurations. Symmetric measurement condition was conducted by concurrently moving the x-ray source and the detector with the incident angle $\omega = 2\theta/2$, this measurement mode is the same as $2\theta/\omega$ scan under a Bragg Brentano geometry. Since a $2\theta/\omega$ scan mode only supports the detection of out-of-plane information parallel to the sample surface, it would be specifically useful to determine the orientation of the deposited sample with a preferred orientation presented. On the other hand, an asymmetric measurement with a fixed small incident angle ω with scanning 2θ under grazing incident geometry is more useful for the measurement of polycrystalline thin film, this measurement condition is also known as grazing incidence X-ray diffraction (GIXRD, **Figure 2.7**).

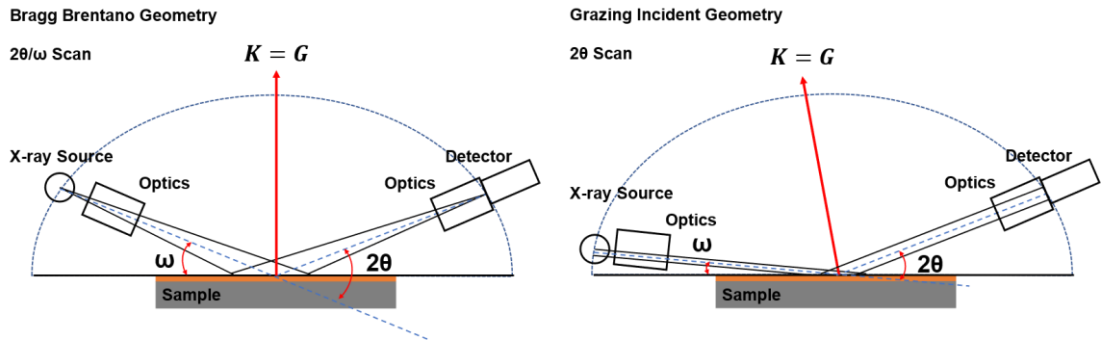

Figure 2.7 XRD measurement configuration for out-of-plane diffraction planes: Bragg-Brentano geometry utilizes symmetric measurement, and grazing incident geometry is under asymmetric measurement mode.

The penetration depths of X-rays under symmetric and asymmetric configurations are quite different. For the $2\theta/\omega$ scan mode, the penetration depth of the X-ray is deeper

doi:10.6342/NTU202403464

at large diffraction angles, so the signal from the substrate would dominate. When measuring a sample having lower crystallinity, the background level would be extremely large and the signal-to-noise ratio is significantly reduced. On the other hand, the 2θ scan mode has a shallower X-ray penetration depth, which would suppress the signal from the substrate and highlight the signal from the sample. As a result, the GIXRD measurement is said to be more surface-sensitive than the $2\theta/\omega$ scan mode.

In this thesis, Bruker D8 Discover was used for XRD measurements. A rotating anode provides a high photon flux at the Cu $K_\alpha = 1.5406$ Å wavelength. For the GIXRD measurements, the incident angle was set as 0.5° and the diffraction angle spanned from 15° to 70° with 0.04° step size and 1 second/step accumulation time. For Bragg Brentano measurements, the diffraction angle spanned from 15° to 50° with 0.04° step size and 1 second/step accumulation time.

2.2.2 Raman Spectroscopy

When light interacts with a material, several trajectories of light-matter interaction can occur: transmission, scattering, or absorption. If the material is transparent and does not absorb in the visible region of the electromagnetic spectrum, nearly all the light is transmitted. A fraction of light might be elastically scattered by the material, causing Rayleigh scattering without energy loss of scattered photons. Small fractions of light may undergo inelastic scattering by the material, resulting in energy gain or loss of scattered photons, leading to the anti-Stokes and the Stokes shifts in the spectrum, respectively. Raman scattering can be interpreted from two different perspectives: quantum physics and classical electromagnetism.

From the quantum theory perspective, the interaction of photons with molecules or materials leads to the formation of a photon-molecule complex that creates a virtual

doi:10.6342/NTU202403464

state (**Figure 2.8**). The relaxation of electrons from the virtual level back to the original vibrational energy level ($v = 0$) leads to the emitted photon having the same energy, which is thought of as elastic scattering without energy loss. This relaxation corresponds to the Rayleigh scattering process of light. Raman scattering, including Stokes shift and anti-Stokes shift, can be thought of as the relaxation from the virtual state to other vibrational states. At room temperature, most of the population of electrons lies on the vibrational ground state ($v = 0$), after excitation to the virtual state, the relaxation of electrons to the vibrational excited states ($v = 1,2, \ldots$) leads to the energy loss of emitted photons. The inelastically scattered signal appears as a Stokes shift, which is thermodynamically favorable due to the Boltzmann distribution among vibrational levels. For the anti-Stokes shift, the energy gain after relaxation from the virtual state is derived from the excitation of electrons from the excited vibrational state ($v = 1,2, \ldots$) and relaxation to the ground state of the vibrational energy level ($v = 0$). The Stokes shift would be the dominant signal instead of the anti-Stokes shift due to the relative population of molecules at room temperature.

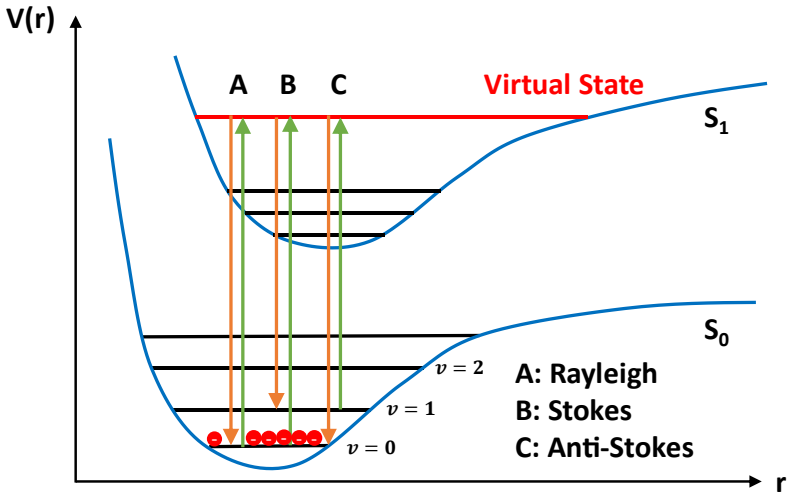

Figure 2.8 Raman scattering scheme of elastic or inelastic process.

doi:10.6342/NTU202403464

The other explanation of Raman scattering is the change in polarizability (α) of the molecule by the electromagnetic field (E). The electric field causes the deformation of charge distribution with the formation of induced dipole moment (μ_i). The magnitude of μ_i depends on the intensity of the electric field and the polarizability of the molecule. When a molecule is subjected to the irradiation of frequency v_i, the time-varying electric field can be expressed as below, which causes a time-dependent dipole moment.

$$\mu_i = \alpha \cdot E \tag{2.38}$$

$$E = E_0 sin(2\pi v_i t) \tag{2.39}$$

If the molecule itself undergoes some motion like vibration or rotation, which would change the polarizability periodically, then the induced dipole moment is superimposed by the vibrational or rotational oscillation. Considering a vibration mode of frequency v_0, the polarizability can be expressed as the superposition of polarizability in the equilibrium position, α_0, and polarizability caused by varying polarizability during vibration, β:

$$\alpha = \alpha_0 + \beta Sin(2\pi v_0 t) \tag{2.40}$$

The induced dipole moment can be derived by substituting the electric field and polarizability into equation (2.38). It can be expressed into three different components using trigonometric relations:

$$\mu_i = \alpha_0 E_0 sin(2\pi v_i t) + \frac{1}{2}\beta E_0 cos[2\pi(v_i - v_0)t] \tag{2.41}$$

doi:10.6342/NTU202403464

$$+\frac{1}{2}\beta E_0 cos[2\pi(v_i + v_0)t]$$

The first component oscillates at the same frequency as the incident light, representing the Rayleigh scattering. The other two components oscillate at frequencies of $v_i - v_0$ and $v_i + v_0$, respectively. These two frequencies represent the Raman scattering, with the lower frequency as the Stokes line and the higher frequency representing the anti-Stokes line. The existence of Raman lines depends on β, the change of polarizability with respect to the vibration. Therefore, for a vibrational or rotational mode to be Raman active, a change of polarizability is required. In crystalline solids, the polarizability changes associated with lattice vibration can also be probed, but only the phonon modes near the Γ-point in the first Brillouin zone are detectable.

In this thesis, Raman spectra were acquired using a micro-Raman setup (UniDRON-A, UniNanoTech, Korea). A 532 nm green laser with 1.1W power was used as the excitation source, while a monochromator (Kymera 193i, Andor) was used to analyze the light. A charge-coupled device camera (iVac316) was used to acquire the spectra. Each spectrum was accumulated over 30 frames, each integrated for 5 seconds.

2.3 Ultraviolet-Visible Spectroscopy

In semiconductors, the excitation of an electron from the valence band to the conduction band occurs when a photon with energy equal or larger than the bandgap energy is absorbed. This process provides valuable insights into the electronic structure of material. For thin film samples, optical characterization techniques are used to analyze the proportions of light emitted, reflected, transmitted, or absorbed during interaction with the material. The optical properties of a material are typically described by the dispersion relation of the refractive index (n) and the extinction coefficient (κ).

doi:10.6342/NTU202403464

The refractive index measures the speed of light in a medium relative to its speed in a vacuum. This index is influenced by the relative permittivity (ε_r) and relative magnetic permittivity (μ_r). Understanding these properties helps in characterizing the optical behavior of thin films and the efficiency of photon absorption, which is crucial for applications such as photovoltaics and optoelectronics.

$$n = \frac{c}{v} = \sqrt{\varepsilon_r \cdot \mu_r} \tag{2.42}$$

The extinction coefficient quantifies the amount of energy absorbed by a medium when light passes through it. In the case of a non-magnetic medium, μ_r can be considered as 1, simplifying the relationship between optical properties and dielectric properties as described by Maxwell's equations. This simplification facilitates the analysis of how materials interact with light, aiding in the characterization of their optical behavior and absorption properties. The absorption of light in a medium is characterized by considering a complex refractive index, $\tilde{n}$:

$$\tilde{n} = n + i\kappa = \sqrt{\varepsilon_1 + i\varepsilon_2} \tag{2.43}$$

The real part and the imaginary part of $\tilde{n}$ can be related by the Kramers-Kronig relationship. Once the imaginary or real part of the complex refractive index is known over a wide frequency range, the other can be determined by the Kramers-Kronig relationship.

doi:10.6342/NTU202403464

Assuming an incident electric field with a plane wave approximation in the x-direction, the transmitted electric field experiences a decrease in amplitude due to energy loss incurred by the material. The intensity of the transmitted light, which is proportional to the square of the electric field, is thus indicative of the absorption of light and can be related to the extinction coefficient.

$$E_T = E_0 \cdot \exp\left[\mathrm{i}(\tilde{n}kx - \omega t)\right] = E_0 \cdot e^{n\kappa x} \cdot \exp\left[\mathrm{i}(nkx - \omega t)\right] \tag{2.44}$$

$$I_T = |E_T|^2 \cdot e^{\frac{2\kappa\omega}{c}x} = e^{-\alpha x} \cdot |E_T|^2 \tag{2.45}$$

$$\alpha = \frac{2\kappa\omega}{c} = \frac{4\pi \cdot \kappa}{\lambda} \tag{2.46}$$

The absorption coefficient (α) describes the wavelength-dependent absorption associated with the extinction coefficient. Sources of optical absorption in semiconductors include free-carrier absorption, impurity absorption related to dopants and lattice defects, and inter-band absorption involving the generation of electron-hole pairs.

Conventional ultraviolet-visible (UV-Vis) spectroscopy, based on Beer-Lambert's law, is typically employed to determine α using the transmission spectra. However, for accurate determination of material absorption, the contribution of reflection must also be considered. The fractions of absorbed (A), reflected (R), and transmitted (T) light should sum up to 1 under the assumption of no luminescence occurring post-photon absorption. The absorption coefficient of a material can be calculated using the transmittance and reflectance of the film once the film thickness, d, is known.

doi:10.6342/NTU202403464

$$\frac{I(\lambda)}{I_0(\lambda)} = \exp(A) = \exp(-\alpha d) \tag{2.47}$$

$$1 - A = R + T \tag{2.48}$$

$$A = -\log(R + T) = -\alpha d \tag{2.49}$$

The bandgap (E_g) of a semiconductor can then be determined through Tauc analysis using equation (2.50), assuming both the valence and conduction bands are parabolic. Here, h is the Planck constant and B is a proportionality constant.

$$(\alpha h\nu)^{1/\gamma} = B(h\nu - E_g) \tag{2.50}$$

The empirical exponent γ in the Tauc equation represents the types of transition:[142]

$$\gamma = \begin{cases} 1/2 & direct\ allow\ transition \\ 3/2 & direct \text{ forbidden } transition \\ 2 & indirect\ allow\ transition \\ 3 & indirect\ forbidden\ transition \end{cases} \tag{2.51}$$

In this thesis, UV-Vis spectra were acquired using a JASCO V-770 spectrometer between 250 to 1000 nm with a 0.5 nm step size. A quartz substrate served as the reference for transmission measurements, while an aluminum mirror served as the reference for reflectivity measurements. Both transmission and reflection spectra were obtained using a 5° incident angle relative to the surface normal vector.

doi:10.6342/NTU202403464

2.4 Photoelectron Spectroscopy

The main principle of photoelectron spectroscopy is the photoelectric effect.[143-146] Incident photons with energy larger than the ionization threshold are used to eject photoelectrons with the entire energy transfer occurring on a time scale of roughly 10 attoseconds. To analyze the photoelectron ejected from the material, the ultra-high vacuum chamber is needed to ensure a sufficiently long mean-free path of low-energy photoelectrons, as well as to keep the surface clean. Since the electron would have an energy-dependent inelastic mean free path inside the material, even though the penetration depth of photons may reach micrometer scale, photoelectrons with useful information only comes from the region 1 - 4 nm from the surface, according to the incident photon energy and the universal curve of the electron mean free path (**Figure 2.9**). As a result, photoelectron spectroscopy is said to be a surface-sensitive technique. Besides, the acquirable information from the material using photoelectron spectroscopy depends strongly on the incident photon energy, such as ultraviolet or soft X-ray photons, which will be discussed in the following sections.

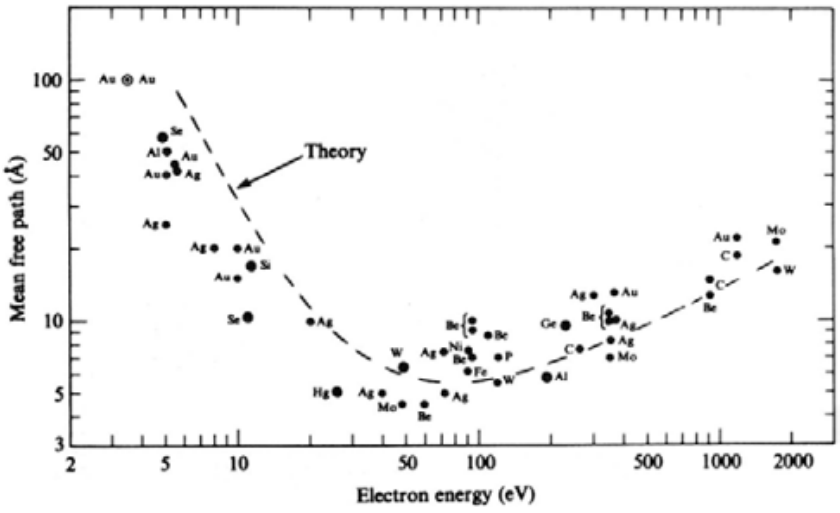

Figure 2.9 The universal curve for electron inelastic mean free path.[147]

doi:10.6342/NTU202403464

2.4.1 X-ray Photoelectron Spectroscopy

The absorption of X-ray photons can trigger 3 different trajectories: X-ray fluorescence, ionization with photoelectron emission, and the Auger process when considering elastic scattering without energy loss. The fluorescence channel is more prevalent for heavier elements while the Auger process dominates for lighter elements. In the X-ray photoelectron spectroscopy setup, the photoelectron emission from the material is the main signal for acquisition with some Auger electrons also present for the analysis. The core-level electron can be ionized by the X-ray photons after overcoming the work function of the material and the binding energy of that state, so the measured kinetic energy would strongly depend on the binding energy of the state such that differentiation between elements would be straightforward. Another information that can be obtained by XPS analysis is the chemical state of materials because the change in the chemical environment will induce the re-arrangement of valance electrons to optimize the shielding of the core nuclei charges, so the core level electron would feel different potential that causes the binding energy change within chemical environment, usually higher oxidation state would increase the binding energy of that element.

The determination of the binding energy of core-level electrons can be done by considering energy conservation before and after ionization:

$$h\upsilon = E_k + E_{BE} + \phi \tag{2.52}$$

In which $h\upsilon$ is the photon energy, E_{BE} is the binding energy, and ϕ is the work function of materials if referencing the energy to the vacuum level. However, energy referencing with respect to the vacuum level would cause some difficulty in determining the binding energy trends inside the material, because the work function is affected by surface

doi:10.6342/NTU202403464

contamination. Therefore, the Fermi level is usually used as the referencing level instead. Especially, the measurement would be conducted by aligning the Fermi level of the electron analyzer that has a known value with that of the material to precisely determine the binding energy of that material.

For semiconducting or insulating materials, charge referencing is also required to determine peak position before discussing chemical shift even if the spectrometer is well calibrated because the production of photoelectrons also causes sample charging. Several ways are used for charge referencing, and the most common way is referencing the binding energy of the C 1s level of adventitious carbon-containing molecules to 284.8 eV. However, this is a scientifically incorrect method since the binding energy of adventitious carbon would vary with the surface work function.[148] It would be better to determine the chemical state by the modified Auger parameters, which calculate the difference between each chemical state concerning the Auger transition to cancel the effect of charging.[149, 150] However, this is typically difficult to conduct because of the low Auger electron intensities. The other way to do the energy referencing is to deposit Au clusters on the sample surface to serve as a known reference point. However, the conductivity of Au depends strongly on the cluster size and sometimes causes insufficient charging dissipation if the cluster size is too small. Besides, the electron reflection is severe so the photoelectron yield would be reduced for the buried material.

Usually, soft X-rays obtained from the Al K-alpha line with an energy of 1486.7 eV or the Mg K-alpha line with an energy of 1253.7 eV are used as the ionization photon source after monochromatizating; the acquisition depth is roughly 1-3 nm while using a soft X-ray source. The Cr K-alpha line with an energy of 5419 eV is usually employed as the hard X-ray photon source that can achieve a deeper acquisition depth of about 5 - 8

doi:10.6342/NTU202403464

nm. Varying the incident X-ray energy can acquire the information from different sampling depths.

In this thesis, XPS was measured by a ULVAC PHI 500 Versa Probe apparatus equipped with an Al K-alpha photon source and an electron flooding gun for charge compensation. The energy referencing of the spectrum was done by referencing the main peak in the C 1s spectrum to the adventitious carbon with a binding energy of 284.8 eV. All the XPS spectra were fitted with a Shirley background and a mixed Gaussian-Lorentz peak profile GL(30) by CasaXPS.

2.4.2 Ultraviolet Photoelectron Spectroscopy

When using UV photons with energies not as high as X-ray photons, only valance electrons can be ionized. Information such as valence band density of states (DOS) and work function can be easily obtained. Even using an X-ray photon can also ionize valance electrons but the interaction cross-section of an X-ray photon with valance electrons is low due to the large energy difference. On the other hand, a UV photon source can better give the fine structure of DOS in the valance band. A helium discharge lamp with emission from the He I-alpha line with an energy of 21.22 eV or the He II-alpha line with an energy of 40.81 eV was used for ultraviolet photoelectron spectroscopy (UPS). The ejected photoelectrons from the deeper regions of the films need to travel longer distances to escape, often resulting in significant energy loss. This energy loss can lead to the formation of secondary electrons, which increase noise in the signal. Furthermore, since the binding energy is larger, the kinetic energy of the photoelectrons is lower, causing the density-of-states information to be distorted. This distortion occurs because the secondary electrons are generated by the random energy loss of photoelectrons as they escape from the material. Therefore, a sample bias is applied to the material to ensure the extraction

doi:10.6342/NTU202403464

of low-energy photoelectrons. The work function can be obtained by the secondary electron cut-off when it is plotted with respect to the Fermi level and the position of the valance band maximum can be obtained by the Fermi-edge cut-off at the low binding energy side:

$$\phi = h\upsilon - E_{cut-off} \tag{2.53}$$

In this thesis, UPS was measured by a ULVAC PHI 500 Versa Probe apparatus using He I-alpha line with an energy of 21.22 eV and an electron flooding gun for charge compensation. A 5 V sample bias was applied to ensure the extraction of low-energy photoelectrons.

2.5 Scanning Electron Microscopy

A Scanning electron microscope (SEM) uses a focused electron beam to create highly magnified images, enabling detailed characterization of surface morphology, subsurface structures, and cross-sectional features at a microscopic level. To ensure that the electron beam is not distorted by collisions with gas molecules, a high-vacuum environment is necessary, which also extends the electron mean free path.

Electron sources in SEM can vary, including thermal emission from a tungsten filament, a LaB_6 single crystal with a sharp tip, and field emission from a tungsten sharp tip in a strong electric field. The emitted electrons are initially accelerated and focused by an extractor lens using high voltage (typically 5 - 20 kV) to achieve a high-brightness electron beam. These accelerated electrons then pass through a column equipped with Einzel-type electrostatic condenser lenses, which further focus and align the beam with the zone axis. Electrostatic lenses are preferred over electromagnetic lenses to avoid the

doi:10.6342/NTU202403464

spiral motion of charged particles, which can increase image aberration. A set of quadrupole deflectors, known as the stigmator, is used to minimize image aberration. These deflectors also scan the sample surface for imaging.

Once the electron beam leaves the focus column, it interacts with the specimen's surface, generating various signals described by the interaction volume (**Figure 2.10**): backscattered electrons (BSEs), secondary electrons (SEs), Bremsstrahlung, characteristic X-rays, Auger electrons, and cathodoluminescence (CL). For SEM imaging, BSEs and SEs are the primary signals detected. BSEs result from Rutherford backscattering and possess higher kinetic energy comparable to the incident electrons. In contrast, SEs are generated through inelastic processes where energy from more energetic electrons ionizes the specimen, resulting in much lower kinetic energy (~50 eV). Due to their short inelastic mean free path, SE images are more surface-sensitive. Meanwhile, BSE images provide Z-contrast, meaning the contrast in BSE images includes elemental information based on atomic number differences.

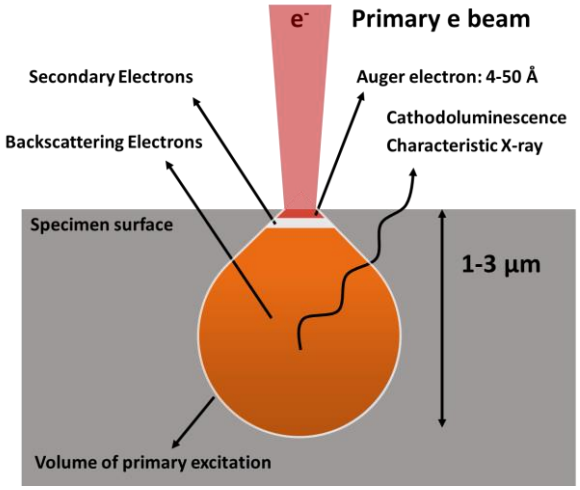

Figure 2.10 The interaction volume excited by the accelerated electron beam with various interactions between electron and specimen: backscattered electrons (BSEs), secondary electrons (SEs), Bremsstrahlung, characteristic X-rays, Auger electrons, and Cathodoluminescence (CL).

doi:10.6342/NTU202403464

The interaction volume in SEM, which is significantly influenced by the accelerating voltage, plays a crucial role in determining the resolution of the images. At high accelerating voltages, the interaction volume is larger, enabling secondary electrons from deeper regions within the specimen to be ejected. This results in a mix of surface and subsurface signals, potentially obscuring the true surface morphology. Despite this, high voltages can stabilize the scanning deflector, leading to a common misconception that higher accelerating voltages always produce better resolution. Conversely, lower accelerating voltages result in a smaller interaction volume, thereby producing secondary electrons predominantly from the surface region. This enhances surface sensitivity and potentially provides better resolution of surface features. However, the use of low accelerating voltages can compromise the precision of the scanning coil, which may result in less optimal resolution if the instrument is not specifically designed for low-voltage operation.

In this work, SEM images were acquired in secondary electron image (SEI) mode using a JEOL JSM-7600 and an cold field emission Hitachi SU8220 apparatus. The accelerating voltage was set to 10.0 kV, and the working distance was varied depending on the specific specimens. For top-view SEM images, the samples were cut into 5×5 mm^2 pieces and directly attached to the sample holder using double-sided carbon tape. For cross-sectional SEM images, the samples were also freshly cut into 5×5 mm^2 pieces, with the freshly cut facet mounted on the sample holder by using double-sided carbon tape. To prevent the charging of the specimens due to secondary emission, a thin gold layer, roughly 1-3 nm, was coated on the sample surface using a sputter coater.

doi:10.6342/NTU202403464

2.6 Photoelectrochemical Characterization

Electrochemical measurements were done with a Zennium Pro potentiostat (Zahner-Elektrik GmbH & Co. KG, Germany). The electrolyte consisted of 0.1 M potassium ferrocyanide ($K_4[Fe(CN)_6]\cdot 3H_2O$, CAS:14459-95-1, Thermo scientific) as a hole scavenger in 0.1 M sodium phosphate buffer (Na_2HPO_4, CAS:7558-79-4, Sigma-Aldrich; $Na_3PO_4\cdot 12H_2O$, CAS:10101-89-0, Thermo Scientific) with a pH value of 12.3. The electrochemical measurements were conducted using a three-electrode configuration in a custom-built photoelectrochemical cell (GINGEN technology, Taiwan). The reference (RE) and counter electrodes (CE)were Hg/HgO in 1 M NaOH (RE-61AP, ALS, Japan) and a platinum plate, respectively. For illuminated measurements, a AM 1.5 G solar simulator (LSH-7320, Newport, USA) was used as the light source at 1 sun intensity (100 mW/cm^2). Before each measurement, a series of measurements was performed as pretreatment: (1) application of –0.4 V versus RE to the working electrode (WE) under a dark environment for 2 minutes, (2) relaxation for 3 minutes, followed by 4 minutes of illumination, then another relaxation period in the dark under open circuit conditions, and (3) a linear sweep voltammetry scan from -0.85 V to 0.7 V versus reference electrode with a scan rate of 100 mV/s and a sampling frequency of 0.1 seconds per point.

2.6.1 Linear Sweep Voltammetry

Linear sweep voltammetry (LSV) is a technique that involves scanning the potential linearly in either the cathodic or anodic direction to measure the resulting current response, akin to I-V characterization in electronic circuits. The final current measured in the system is contributed by both the Faradaic and non-Faradaic currents. Faradaic current results from a redox reaction with electron transfer, where the kinetic of the redox reaction

doi:10.6342/NTU202403464

at the electrode surface and the output current can be described by the Butler-Volmer equation (2.54) and the Nernst-Planck equation (2.57):

$$I = I_0[\frac{C_0(0,t)}{C_0^*}\exp\left(\frac{-\alpha nF\eta}{RT}\right) - \frac{C_R(0,t)}{C_R^*}\exp\left(\frac{(1-\alpha)nF\eta}{RT}\right)] \tag{2.54}$$

$$I = I_0[\exp\left(\frac{-\alpha nF\eta}{RT}\right) - \exp\left(\frac{(1-\alpha)nF\eta}{RT}\right)] \tag{2.55}$$

$$\begin{aligned} I_0 &= nFAk_0C_0^*\exp\left(\frac{-\alpha nF}{RT}(E_{eq}-E^0)\right) \\ &= nFAk_0C_R^*\exp\left(\frac{(1-\alpha)nF}{RT}(E_{eq}-E^0)\right) \end{aligned} \tag{2.56}$$

Here, I_0 is the exchange current at the equilibrium potential, and $C_0(0,t)$ and C_0^* are the time-dependent reductant concentration near the electrode surface and the bulk reductant concentration, respectively. $C_R(0,t)$ and C_R^* are the time-dependent oxidant concentration near the electrode surface and the bulk oxidant concentration, respectively. α is the charge transfer coefficient describing the stiffness and symmetry of the potential energy surface of reactants, n is the number of electrons transferred in the overall electrochemical reaction, and E_{eq} is the equilibrium potential. E^0 is the standard redox potential, k_0 is the equilibrium rate constant, and η is the overpotential that describes the difference between the applied potential and the equilibrium potential. F is the Faraday constant, R is the ideal gas constant, and T is the absolute temperature.

According to the Butler-Volmer equation, the current exhibits an exponential growth with increasing potential once a certain potential threshold, known as the overpotential, is exceeded, assuming that the effects of mass transport of reactants to the electrode are negligible. The overpotential, also referred to as the onset potential, can be defined as the intercept on the potential axis by extrapolating the rising current.

doi:10.6342/NTU202403464

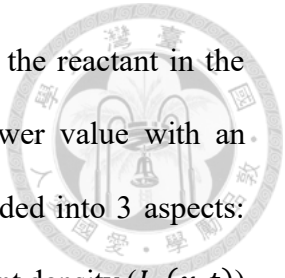

However, when considering the mass transport properties of the reactant in the electrolyte, the current will reach a plateau or even drop to a lower value with an increasing potential scan. The mass transport properties can be divided into 3 aspects: diffusion, migration, and convection of reactants with the output current density ($J_O(x,t)$) described by the Nernst-Planck equation:

$$J_A(x,t) = -D_A \frac{\partial C_A(x,t)}{\partial x} - Z_A \frac{F}{RT} D_A C_A(x,t) \frac{\partial \phi(x,t)}{\partial x} + C_A(x,t) v(x,t) \qquad (2.57)$$

Where D_A is the diffusion constant of reactant species A, Z_A is the valance of reactant species A, $\phi(x,t)$ is the electric field generated by the applied potential on the electrode surface, and $v(x,t)$ is the flow velocity.

$$I_{lim} = nFSD_A \frac{C_A^*}{\delta} \qquad (2.58)$$

S is the active surface area of the electrode for redox reaction, C_A^* is the bulk concentration of reactant A in the solution, and δ is the distance from the electrode surface that the reactant concentration is equal to the bulk concentration.

Diffusion occurs due to the concentration gradient across the electrode surface to the bulk of the solution, leading to a limiting current (I_{lim}) related to the reactant concentration. Migration, resulting from charged reactants moving along the electric field created by the applied potential, impacts the final current density based on the reactant's charge and the applied bias. For instance, the migration current can increase, decrease, or remain unaffected depending on whether the reduction reaction involves cations, anions,

doi:10.6342/NTU202403464

or uncharged molecules, respectively. The migration current can be minimized by adding supporting electrolytes.

Finally, convection helps the transportation of reactants to the electrode surface, ensuring a uniform concentration in the solution. This can lead to overestimated current densities. To eliminate the effect of convection, a laminar flow parallel to the electrode surface, achieved by proper rotation (e.g., using a rotating disk electrode system) or controlled stirring, ensures that only diffusion of reactants plays a significant or rate-limiting role during the redox reaction.

Both migration and convection currents can be considered non-Faradaic currents since no redox reaction occurs. Another source of non-Faradaic current is the charging of the double-layer capacitance, which increases with the potential sweep rate. Assuming a double-layer capacitance (C_{dl}) behaves as an ideal parallel capacitance, the charging current (I_{dl}) responds accordingly. Thus, whether a redox reaction occurs or not, an increasing sweep rate in either direction will result in a larger charging current:

$$I_{dl} = C_{dl}\frac{dV}{dt} \tag{2.59}$$

In this study, linear sweep voltammetry was performed within a potential window ranging from –0.65 to 0.7 V versus the reference electrode, both in dark and light conditions. The scan rate was 50 mV/s, with a sampling frequency of 0.1 seconds per point.

doi:10.6342/NTU202403464

2.6.2 Chronoamperometry

Chronoamperometry (CA) is a technique that involves applying a constant potential between the working electrode (WE) and the reference electrode (RE) to measure the evolution current with time. The current response for a diffusion-controlled redox reaction can be described by the Cottrell equation, which is derived from Fick's second law of diffusion combined with the Laplace transform:

$$I(t) = \frac{nFAC_A^* D_A^{1/2}}{(\pi t)^{1/2}} \tag{2.60}$$

According to the Cottrell equation, plotting $I(t) \cdot t^{1/2}$ against t should yield a horizontal line if the reaction is purely diffusion-controlled. If the plot deviates from this horizontal line, it suggests that the electrochemical reaction is not solely controlled by diffusion but may involve multi-step reactions. Therefore, a CA diagram can help identify the type of reaction occurring.

Additionally, assuming the current response in the CA diagram is entirely Faradaic, the total charge consumed by the reactant can be calculated by integrating the area under the current-time curve. This allows for quantitative analysis of the redox reaction products.

2.7 Electrochemical Impedance Spectroscopy

Basic electrochemical measurements were conducted using a DC configuration, where both the voltage and corresponding current are independent of time. While DC measurements provide valuable information such as current density, overpotential, and Tafel slope, they offer limited insights into carrier dynamics within both electrochemical and photoelectrochemical systems.

doi:10.6342/NTU202403464

In contrast, an AC configuration provides more detailed information about carrier dynamics due to its time-varying properties, which introduce a built-in perturbation to the electrochemical system. To better describe the time-varying potential in AC measurements, parameters such as angular frequency (ω) and phase shift (φ) are introduced, utilizing a phasor domain to formulate these properties:

$$V = A\cos(\omega t + \varphi)\ ;\ I = A\cos(\omega t + \varphi') \tag{2.61}$$

$$\mathrm{A}\cos(\omega t + \varphi) = \mathrm{Re}[\mathrm{A}\,\mathrm{e}^{j(\omega t+\varphi)}] \tag{2.62}$$

2.7.1 Impedance of Electronic Components in AC Configuration

Ohm's law describes the current response of conductors when a potential is applied across them in a DC configuration. In an AC configuration, Ohm's law is generalized to define impedance (Z), which combines resistance (R) and reactance (X):

$$Z = \frac{V_{AC}(t)}{I_{AC}(t)} = |Z|\exp\big(j \cdot Arg(z)\big) = R + jX \tag{2.63}$$

Resistance, the real part of impedance, represents the energy dissipated from the input potential, leading to an exponential decay in amplitude. Reactance, the imaginary part of impedance, represents the energy stored in the electronic components, which is later released to contribute to the current. To analyze the impedance of basic electronic elements such as resistors, capacitors, and inductors, consider a time-varying applied potential $V(t) = V_0 e^{j\omega t}$. The impedance of a resistor remains unchanged from the DC configuration since there is no phase shift between the current and voltage across the resistor.

doi:10.6342/NTU202403464

$$Z_{resistance} = \frac{V_{AC}}{I_{AC}} = R \tag{2.64}$$

For a capacitor, using the definition of capacitance, we observe a phase shift. A capacitor contributes only reactance to the impedance, causing a phase shift of $\pi/2$ for the voltage relative to the current:

$$\mathrm{I(t)} = \frac{\mathrm{dQ}}{\mathrm{dt}} = C\frac{dV}{dt} = C \cdot j\omega V_0 e^{j\omega t} \tag{2.65}$$

$$Z_{capacitance} = \frac{V_{AC}}{I_{AC}} = \frac{V_0 e^{j\omega t}}{Cj\omega V_0 e^{j\omega t}} = \frac{V_0 e^{j\omega t}}{C\omega V_0 e^{j(\omega t + 0.5\pi)}} = \frac{1}{j\omega C} \tag{2.66}$$

Applying Faraday's law of induction to an inductor, we understand that the electromotive force generated opposes the change in magnetic flux. The inductance contributes only to the imaginary part of the impedance, resulting in a phase lag of $\pi/2$ for the current compared to the applied voltage. This phase relationship underscores the role of inductors in creating a time-varying potential response.

$$V = L\frac{dI}{dt} \tag{2.67}$$

$$Z_{inductance} = \frac{V_{AC}}{I_{AC}} = \frac{j\omega L V_0 e^{j\omega t}}{V_0 e^{j\omega t}} = \frac{V_0 e^{j\omega t}}{V_0 e^{j(\omega t - 0.5\pi)}} = j\omega L \tag{2.68}$$

2.7.2 Electrochemical Equivalent Circuit Components

To better understand an electrochemical system subjected to AC perturbation measurement, we utilize an equivalent circuit model to simplify the complex phenomena

doi:10.6342/NTU202403464

observed during impedance analysis. The components of this model include series resistance (R_s), charge transfer resistance (R_{ct}), double-layer capacitance (C_{dl}), constant phase element (CPE), and Warburg impedance (Z_w). While a simplified Randles circuit was introduced earlier, a more generalized Randles circuit is employed to evaluate systems considering reactant diffusion (**Figure 2.11**).[151] The contributions of each component in the Randles circuit are discussed in detail below.

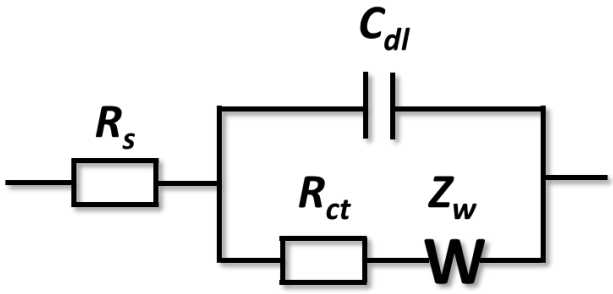

,

Figure 2.11 Randles circuit served as the commonly used equivalent circuit in electrochemical and photoelectrochemical systems while considering the mass transport effects of reactants with each electronic component: series resistance (R_s), charge transfer resistance (R_{ct}), double-layer capacitance (C_{dl}), and Warburg impedance (Z_w).

Series resistance (R_s) represents the resistance encountered by ions drifting in the electrolyte, facilitating a closed circuit. This resistance is often referred to as the "iR-drop" in electrochemistry, as it is responsible for the voltage drop due to ionic mobility in the bulk solution under an applied potential:

$$R_s = \frac{l}{\kappa A} \tag{2.69}$$

doi:10.6342/NTU202403464

where l is the distance between the working electrode and the reference electrode, κ is the ionic conductivity, and A is the limiting cross-section area of the solution passing the current.

Charge transfer resistance (R_{ct}) is associated with the kinetics of the electrochemical process occurring at the electrode surface. It is described by the Butler-Volmer equation, particularly under conditions of small overpotential.

$$R_{ct} = \frac{RT}{nFI_0} \tag{2.70}$$

Double-layer capacitance (C_{dl}) arises from the formation of an ionic or polarized molecular double layer at the electrode surface when immersed in an electrolyte solution. Applying a voltage within the diffusion layer causes additional counter-charge migration, leading to increased charging and an expanded double layer:

$$C_{dl} = \epsilon \frac{A}{d} \tag{2.71}$$

where ϵ is the dielectric constant of electrode material, A is the geometrical area of the electrode surface, and d is the thickness of the electrode material.

The constant phase element (CPE) accounts for the non-ideal behavior of capacitors, considering factors like inhomogeneous reaction rates, non-uniform ionic current distribution, inconsistent thickness or chemical composition, and surface roughness. In semiconductor systems, CPE also describes the rectifying characteristics of semiconductor junctions. These factors can cause the electrode resistance to increase as the frequency decreases:

doi:10.6342/NTU202403464

$$Z_{CPE} = \frac{1}{C(j\omega)^n} \tag{2.72}$$

In equation (2.72), n is called the constant phase, which is an empirical value that makes this capacitance have a certain resistance factor. It is obvious that the $j\omega$ term gives the capacitor pure reactance behavior, but with the constant phase, the 90° phase will result in an impedance with an argument less than 90°.

Warburg impedance (Z_w) reflects the ionic perturbation of reacting species, particularly significant at low frequencies. As the concentration gradient builds up under an applied voltage, it will relax or reverse direction when the voltage changes, with the time constant of this process increasing as the frequency approaches zero. The Warburg coefficient (σ) measures the efficiency of reactant mass transfer.

$$Z_w = \frac{\sigma}{\sqrt{\omega}}(1 - j) \tag{2.73}$$

$$\sigma = \frac{RT}{\sqrt{2}n^2F^2A}\left(\frac{1}{D_0^{1/2}C_0(x,t)} + \frac{1}{D_R^{1/2}C_R(x,t)}\right) \tag{2.74}$$

In this study, EIS measurements were conducted with a potential window scanned from –0.60 to 0.60 V versus RE in 100 mV increments, using a perturbation bias of 20 mV. The frequency scan ranged from 1 kHz to 200 kHz and then back to 0.8 Hz, with 10 accumulation cycles above and 4 cycles below 66 Hz. A quiet time of 70 seconds was maintained between each scan to allow the double-layer capacitance to stabilize.

doi:10.6342/NTU202403464

Chapter 3. Establishing and Optimization of Ta_3N_5 Growth Condition

This chapter primarily focuses on using Ta_2N_3 as a nitridation precursor for Ta_3N_5 synthesis. **Chapter 3.1** details the sputter deposition procedure of Ta_2N_3 and examines the influence of each deposition parameter on the Ta_2N_3 films. **Chapter 3.2** addresses the importance of reproducibility, with particular emphasis on the main chamber conditions and their influence on the as-deposited films.

In **Chapter 3.3**, the optimized condition of Ta_2N_3 thin films, combining the best conditions obtained in **Chapter 3.1** and the reproducibility factors from **Chapter 3.2**, is characterized in terms of structural, elemental, and optical properties. From **Chapter 3.4** to **Chapter 3.5**, the nitridation process and the establishment of Ta_3N_5 via post-ammonia annealing are discussed. **Chapter 3.4** outlines the detailed experimental methods used and addresses the influence of each annealing parameter on the final crystallinity and phase composition of Ta_3N_5 thin films. In **Chapter 3.5**, the characterization of optimized Ta_3N_5 thin films is conducted, including structural, elemental, valence electronic, and optical properties. The detailed electrochemical performance will be presented in **Chapter 4**.

doi:10.6342/NTU202403464

3.1 Deposition Procedure of Metastable Ta_2N_3 as Nitridation Precursor

Double sides polished quartz substrate (Gredmann), n-Si wafer (phosphorus-doped, R ~ 1-10 ohm-cm, PCA) with the out-of-plane orientation of (100), n^+-Si wafers (arsenic-doped, R ~ 0.001-0.005 ohm-cm, El-Cat Inc.) with the out-of-plane orientation of (100) and n^+-Si wafer (Arsenic doping, R ~ 0.001-0.005 ohm-cm, PCA) with the out-of-plane orientation of (111) were used as the substrate for this thesis. Before each deposition, the quartz substrate was cleaned with detergent mixed with deionized water for 10 minutes and dried in an oven set at 80°C. Subsequently, the substrate was cleaned with acetone (analytical grade, Supelco) and then isopropanol (analytical grade, Supelco) for 10 minutes. All the cleaning processes were conducted with an ultrasonic sonicator (Elmasonic P, Elma) with a frequency set at 37 Hz. Finally, the quartz substrate was cleaned by a UV-Ozone cleaner (Model 24, Jelight) for 10 minutes to get rid of organic residuals. On the other hand, Si wafers underwent cleaning solely with an N_2 air gun to remove adhesion contaminants and prevent oxide formation.

After the cleaning process, the substrate was securely attached to the substrate holder and then introduced into the load lock chamber. The load lock chamber was evacuated until it reached a pressure of 3×10^{-7} Torr, then the substrate holder was transferred into the main chamber for the sputter deposition process. Typically, after the transfer to the main chamber, an additional 10 minutes were allocated to ensure the stability of pressure before initiating the deposition. The substrate holder was configured with a rotational speed of 10 rpm and heated at a ramp rate of 10°C/sec until it reached the 500°C target temperature. To guarantee thermal equilibrium at the substrate holder, the deposition process was initiated 10 minutes after the target temperature was attained.

doi:10.6342/NTU202403464

Typically, the base pressure of the main chamber should be maintained below 3×10^{-7} Torr at room temperature and 5×10^{-7} Torr at elevated temperatures.

Figure 3.1 Image taken during different periods of the sputtering process.

The deposition process was divided into three distinct phases: cleaning and conditioning, pre-deposition, and deposition. During the cleaning and conditioning period (**Figure 3.1a** & **Figure 3.1b**), Ar gas was introduced into the main chamber at a 40 sccm flow rate, with the process pressure maintained at 9 mTorr. The substrate shutter was then opened, and a 50W RF power was applied on the substrate to ignite the Ar plasma, aimed at removing organic contaminants and native oxide from the substrate surface. This condition was sustained for 10 minutes. Following the substrate cleaning, the substrate shutter was closed, and the target shutter was opened. A DC power of 60W was applied to the Ta target to ignite the Ar plasma for target cleaning and chamber conditioning for another 10 minutes. The gas flow and process pressure remained constant during this phase.

The pre-deposition phase commenced after these cleaning processes. The DC power applied to the Ta target was changed to the desired value, and the pulsed DC mode was activated with 100 kHz frequency and a 1 μs reverse time, which is equivalent to a 99% duty cycle. Subsequently, the reactive gas(es) was introduced, with the Ar flow rate adjusted to the specified value. The target shutter remained open while and the substrate

doi:10.6342/NTU202403464

shutter remained closed in the target conditioning phase (**Figure 3.1c**). This phase would last for 10 minutes, allowing the voltage and current applied to the target to reach a steady state. The actual deposition period commenced after the substrate shutter was opened (**Figure 3.1d**). Upon completion of the deposition, the heater was promptly turned off, followed by discontinuing the supply of oxygen, nitrogen, and then Ar. The substrate shutter would remain open after the deposition. The deposited film would be transferred out for further use once it had cooled down to room temperature.

In the process of reactive magnetron sputtering, a multitude of parameters play crucial roles. These factors encompass the gas atmosphere, deposition temperature, duration, applied power to the target, process pressure, and more. Each variable significantly impacts the characteristics of resulting films, including their phase, stoichiometry, and crystallinity. The pursuit of high-quality films demands the identification of an optimal combination of deposition parameters. To achieve this objective, a systematic approach was adopted, wherein each parameter's influence was individually assessed and fine-tuned stepwise.

All samples used for GIXRD measurements in this section were deposited on quartz substrates. The selection of quartz is based not only on its widespread availability and mechanical durability but also on its compatibility with optical measurements. For SEM measurements, n^+-Si(111) wafers were utilized for the deposition in this section.

3.1.1 Influence of Gas Atmosphere

The chemical composition and crystallinity of as-deposited tantalum nitride (TaN_x) films were found to be strongly dependent on the composition of the sputtering atmosphere, which consists of Ar and reactive gases (N_2 and O_2). When the deposition temperature was set at 500°C with the working pressure at 5 mTorr and the flow rate of

doi:10.6342/NTU202403464

Ar was kept constant at 20 sccm, adjusting the flow rate of N_2 led to significant variations in the resulting phases and chemical composition. This dependence was indicated by the GIXRD measurements, as shown in **Figure 3.2**. When an extremely low flow rate of N_2 (5 sccm) was applied, the as-deposited film exhibited diffraction peaks at 2θ = 36.12°, 42.12°, and 60.84°. These are characteristic peaks for the cubic δ-TaN phase, albeit with a slight shift to higher angles compared to their theoretical values. The cubic δ-TaN phase is metallic, which gave the as-deposited films on quartz a silverish appearance.[152]

Increasing the N_2 flow to a moderate 30 sccm rate resulted in a different phase in the Ta-N system. Instead of the metallic δ-TaN phase, a metastable bixbyite-Ta_2N_3 phase was indicated by the diffraction peak at 2θ = 31.20°. However, a strong amorphous background was also observed between 2θ = 30 - 40°, suggesting a relatively poor crystallinity of the deposited Ta_2N_3 films. The metastable bixbyite-Ta_2N_3 phase is known as a degenerate n-type semiconductor with a brownish color.[60]

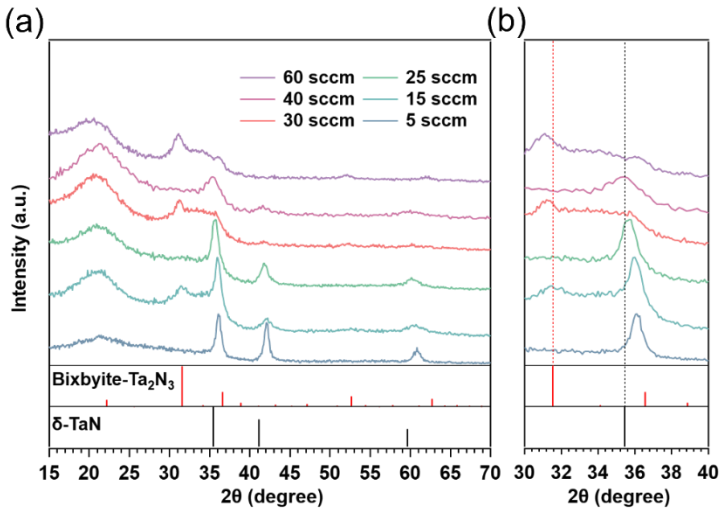

Figure 3.2 (a) The GIXRD patterns measured from TaN_x films deposited with varying N_2 flow rates. (b) The enlarged view of 2θ = 30 - 40°. The reference of δ-TaN was obtained from ICSD-colloid180957.

doi:10.6342/NTU202403464

When the N_2 flow rate was increased to 40 sccm, the Ta_2N_3 phase disappeared, and only the δ-TaN phase was observed. Further increasing the N_2 flow rate to 60 sccm resulted in deposited films in the bixbyite-Ta_2N_3 phase but also with a strong amorphous background.

No obvious trend was observed in the formation of the metastable Ta_2N_3 phase, which can be attributed to poor control of the residual oxygen content in the process chamber. It is crucial to control the residual content in the process chamber for the formation of the Ta_2N_3 phase. This issue will be further addressed in the following section. Nevertheless, the increased flow rate of N_2 with fixed Ar flow rate and process pressure indicated a higher concentration of N_2, enabling the elevation of the chemical potential of nitrogen in the plasma state and the efficient formation of metastable Ta_2N_3.[153] The limit potential for accessing metastable Ta-N species was reached approximately at an N_2 flow rate of 30 sccm.

Another significant effect of increasing the nitrogen flow rate was the variation of nitrogen content within the deposited films. Films deposited with a nitrogen flow rate of 5 sccm exhibited a peak shift towards higher angles, indicating a smaller unit cell size compared to the theoretical value of δ-TaN. However, increasing the nitrogen flow rate to values below 30 sccm resulted in diffraction peaks shifting back toward the theoretical value (**Figure 3.2b**), indicating an increase in nitrogen content. This trend continued when the nitrogen flow rate exceeded 30 sccm, with the diffraction peaks shifting towards lower angles compared to the theoretical value of the bixbyite-Ta_2N_3 phase, suggesting more nitrogen occupying interstitial sites within the unit cell of the bixbyite-Ta_2N_3 phase.[60]

One drawback of increasing the flow rate of reactive gas is the reduced deposition rate. Increasing the flow rate of reactive gases would decrease the concentration of sputtering gas when the working pressure is fixed, thus slowing the deposition procedure.

doi:10.6342/NTU202403464

As seen in the cross-sectional SEM images (**Figure 3.3**), film thickness decreased dramatically with increasing nitrogen flow rate from ~ 100 nm (5 sccm) to 20 nm (60 sccm) with deposition time fixed at 1 hour. To obtain a metastable Ta_2N_3 phase with a reasonable deposition rate, the nitrogen flow rate was fixed at 30 sccm for the remaining experiments.

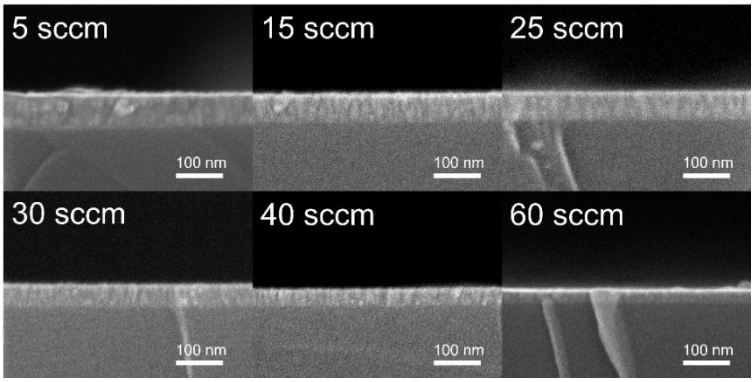

Figure 3.3 Cross-sectional SEM images for TaN_x films deposited with different N_2 flow rates.

3.1.2 Influence of Deposition Temperature

The substrate temperature significantly influences the properties of thin films produced through sputtering, impacting both crystallinity and surface morphology. The sputtering process can be broadly divided into two key aspects: the impact of active bombardment by sputtered atoms and the diffusion of adsorbed atoms across the substrate's surface. The former is primarily influenced by the kinetic energy of the sputtered atoms, akin to the power exerted on the target material, while the latter can be linked to the temperature of the substrate. At temperatures below 300°C, the as-deposited TaN_x films exhibited an amorphous structure, as indicated by the board peak around 2θ = 30 - 35° in GIXRD measurement (**Figure 3.4**). This resulted from constraints in the

doi:10.6342/NTU202403464

deposition process, where the diffusion of adsorbed atoms was limited, and the bombardment of the sputtered atom dominated.

As the substrate temperature rose to 500℃, both lateral and vertical diffusion of adsorbed atoms became significantly enhanced, leading to the gradual formation of crystalline structure. The sample deposited at 500℃ exhibited a diffraction peak at 2θ = 31.53° in the GIXRD measurement (**Figure 3.4**), and can be identified with the metastable bixbyite Ta_2N_3 phase. However, a broad peak was also observed in the diffractogram, too, which indicated the sample was still majorly amorphous.

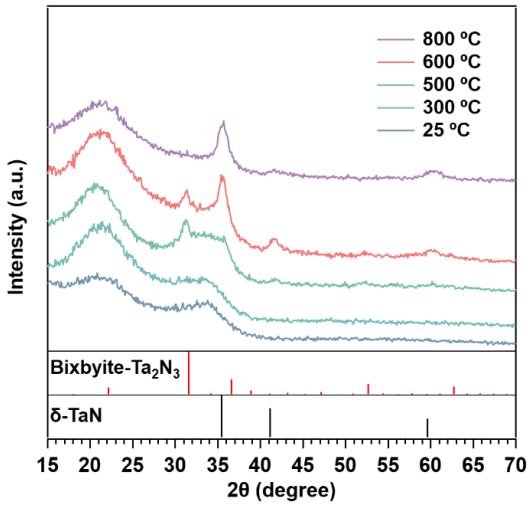

Figure 3.4 The GIXRD patterns measured from TaN_x films deposited at varying temperatures. The reference of δ-TaN was obtained from ICSD-colloid180957.

As the deposition temperature further increased to 600℃, a mixture of the metastable bixbyite Ta_2N_3 phase and stable δ-TaN phase appeared. The newly observed diffraction peak at 2θ = 35.65° could be assigned to the δ-TaN phase in the GIXRD measurement (**Figure 3.4**). This can be attributed to the metastable property of Ta_2N_3, leading to the desorption of nitrogen with increasing deposition temperature.

doi:10.6342/NTU202403464

In extremely high temperatures about 800℃, the metastable Ta_2N_3 phase completely decomposed into TaN, accompanied by the desorption of nitrogen atoms. The diffractogram provided evidence of this transformation for the complete disappearance of the signal of bixbyite-Ta_2N_3 at $2\theta = 31.53°$ and the only observation for all peaks characterized for the structure of δ-TaN phase (**Figure 3.4**). To consistently obtain a pure phase of metastable Ta_2N_3, the deposition temperature was fixed at 500℃ for subsequent experiments.

3.1.3 Influence of Deposition Time

When employing magnetron sputtering under constant working pressure and sputtering power, the deposition rate is mainly governed by the configuration of the instrument. Factors such as the incident angle and the distance between the substrate and target can influence the deposition rate of the thin film profoundly.

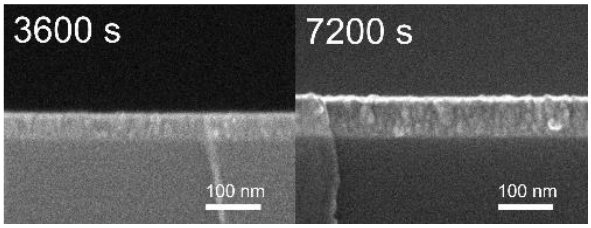

Figure 3.5 Cross-sectional SEM images for TaN_x films deposited with different dwell times.

With a dwell time of 1 hour, the resulting film was relatively thin, approximately 41nm (**Figure 3.5**). The sample still exhibited a strong amorphous nature as indicated by the board peak around $2\theta = 30 - 35°$ in GIXRD measurement (**Figure 3.6**). Some crystalline Ta_2N_3 phase could still be observed at a diffraction peak at $2\theta = 31.53°$ even though the crystallinity is relatively low and almost suppressed by the amorphous quartz

doi:10.6342/NTU202403464

substrate. Conducting measurements using both GIXRD and PXRD revealed a relatively low peak-to-background ratio, often causing the diffractogram to be overshadowed by the substrate signal. This presented challenges in characterizing the structure of the synthesized film.

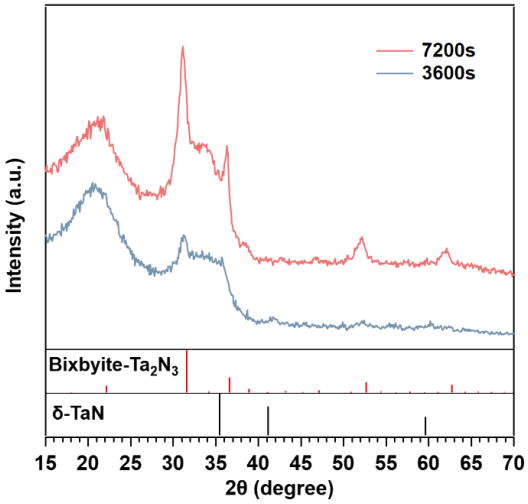

Figure 3.6 The GIXRD patterns measured from TaN_x films deposited with varying dwell time. The reference of δ-TaN was obtained from ICSD-colloid180957.

To address these challenges, increasing the deposition time from 1 hour to 2 hours yielded a thicker film, approximately 70 nm in thickness (**Figure 3.5**). A relatively clear columnar growth structure could also be observed, which is the classical growth mode for sputtering deposition described by the structure zone model.[154, 155] This adjustment provided a more robust signal for detecting the presence of the bixbyite Ta_2N_3 phase. Additionally, the sample exhibited improved crystallinity, as evidenced by the higher diffraction peak intensities at $2\theta = 31.53°$ and $36.82°$ under the same GIXRD measurement configuration (**Figure 3.6**). Furthermore, the appearance of other diffraction peaks underscored the enhanced crystallinity of the Ta_2N_3 phase just by the increase of the film thickness. Therefore, the deposition dwell time was set to 2 hours, maintaining the previously determined optimal value for further optimization.

doi:10.6342/NTU202403464

3.1.4 Influence of Sputtering Power

As mentioned previously, the sputtering process is greatly influenced by the power applied to the target. When the power is relatively low, such as at 10W and 30W, the sputtered atom wouldn't get enough kinetic energy after being ejected by the argon ions. Consequently, the resulting films exhibited little sputtering yield and formed an extremely thin layer of material that cannot be detected by either GIXRD measurement or cross-sectional SEM (**Figure 3.7** & **Figure 3.8**).

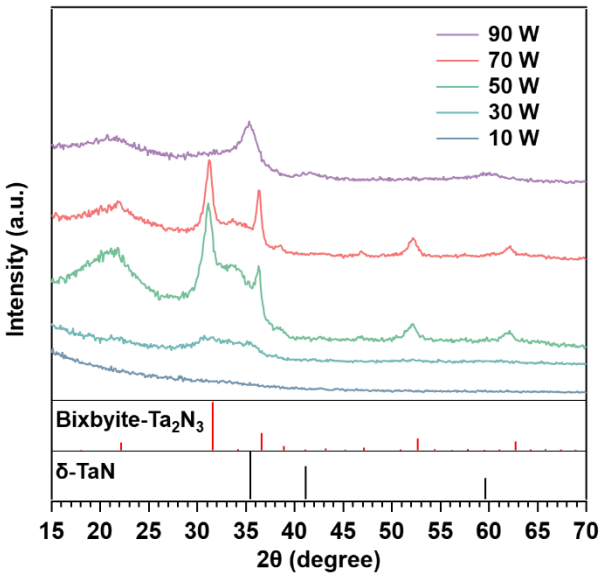

Figure 3.7 The GIXRD patterns measured from TaN_x films deposited with varying sputtering power. The reference of δ-TaN was obtained from ICSD-colloid180957.

When increasing the applied power to 50W, the kinetic energy of sputtered atoms increased, and the number of ejected ions survived this process. This, combined with the unbalanced configuration created by the introduction of a nitrogen gas atmosphere, facilitates the formation of the metastable transition metal nitride species, such as bixbyite Ta_2N_3 as indicated by the diffraction peak at $2\theta = 31.53°$. However, some amorphous

doi:10.6342/NTU202403464

natures were also observed in the formation of the board peak around 2θ = 30 - 35°. SEM revealed a relatively thick film with approximately 60 nm thickness (**Figure 3.8**).

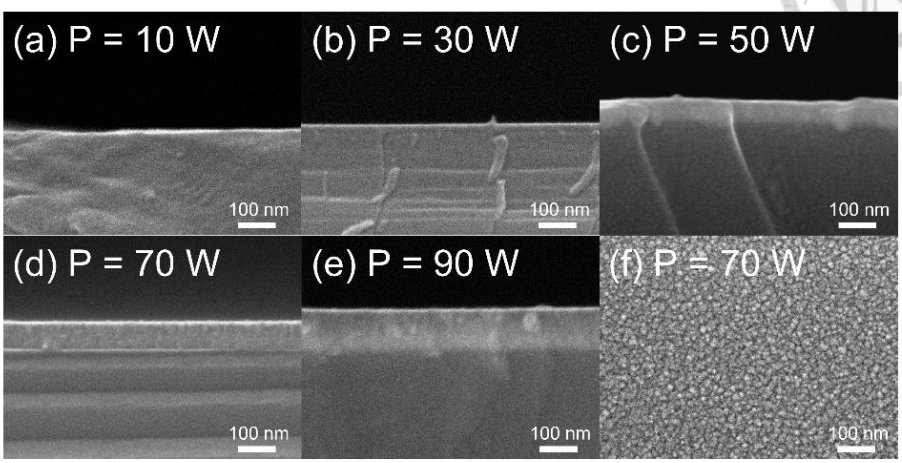

Figure 3.8 Cross-sectional SEM images for TaN_x films deposited with different dwell times.

When considering an increase in the power applied to the target, it's essential to first ascertain the bonding type of the target material. For target materials that are brittle or not easy to process, bonding to copper using indium solder is needed. As a result, caution is required as higher power leads to elevated temperatures on the target surface. Indium solder typically has a temperature tolerance limit of approximately 200℃, and exceeding this threshold can result in the target debonding from the back contact. Therefore, it's advisable to verify the bonding type before adjusting the power settings.

Tantalum targets, in contrast to materials like tungsten, are typically not bonded to the cooper back-contact due to their relatively soft nature. This allows for the application of power exceeding 60W for a 2-inch target. When the power is increased to 70W a greater number of atoms ejected from the target, resulting in a thicker film measuring approximately 75 nm in thickness (**Figure 3.8**). The increased film thickness has a positive effect on its crystallinity, and only minor amorphous domains are observed, as confirmed by the diffractogram. The top-view SEM image of the as-deposited film

doi:10.6342/NTU202403464

with an applied power of 70W revealed the typical morphology of sputtering deposition, with densely packed small grains (**Figure 3.8f**).

However, when the target power was elevated to 90W, the impact of sputtered atom bombardment on the films became increasingly pronounced. While higher power did result in thicker films within the same dwell time, the increasing kinetic energy intensified the effects of the active bombardment. As a consequence, nitrogen desorption becomes noticeable, and the complete decomposition of bixbyite Ta_2N_3 into δ-TaN is observed, evidenced by the complete disappearance of the signal of bixbyite-Ta_2N_3 at $2\theta = 31.53°$ and the only observation for all peaks characterized for the δ-TaN phase.

To clarify, there may be some discrepancies when comparing the film thicknesses obtained with different deposition times. In **Section 3.2.3**, a power of 50W was used; however, in **Figure 3.5**, the film thickness achieved with a 2-hour deposition dwell time (~ 80 nm) differed from that observed here in **Figure 3.8c** (~ 65 nm). This discrepancy can be attributed to the properties of the sputtering target itself. The sputtering yield tends to improve with target usage when the same power is applied initially, but then gradually decreases after reaching a critical (power*time) threshold, which varies depending on the target material. Nevertheless, to achieve optimal crystallinity of the Ta_2N_3 phase, a power of 70W was deemed necessary, which also resulted in improved film thickness for subsequent applications.

3.1.5 Influence of Process Pressure

Even though not prominently emphasized previously, the process pressure also wields significant influence on the deposited films. Process pressure in conjunction with the applied power on the target governs the frequency of scattering events that happen as ejected atoms traverse the path and adhere to the substrate. Consequently, when the

doi:10.6342/NTU202403464

deposition temperature was set at 500°C with the nitrogen-to-argon ratio fixed at 1.5, a higher process pressure introduced more gas molecules into the sputter chamber, elevating the likelihood of sputtered atoms colliding with these molecules. This process effectively reduces the kinetic energy of the sputtered atoms, resulting in less active bombardment of atoms onto the film.

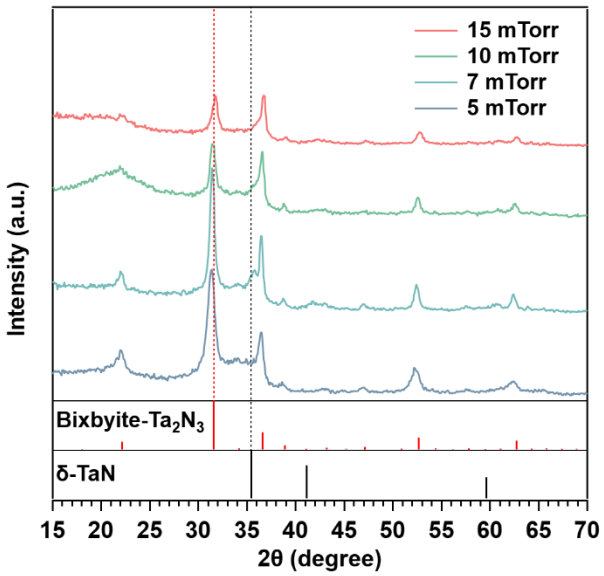

Figure 3.9 The GIXRD patterns measured from TaN_x films deposited with varying process pressure. The reference of δ-TaN was obtained from ICSD-colloid180957.

For samples deposited at a process pressure of 5 mTorr, traces of amorphous domain were still evident, as indicated by the board peak around 2θ = 32.5 - 35° in the GIXRD pattern (**Figure 3.9**). When the process pressure increased from 5 to 15 mTorr, a noticeable decrease in crystallinity was observed, as indicated by the reduced intensity of diffraction peaks. As mentioned previously, an increase in process pressure lowers the kinetic energy of sputtered atoms, leading to decreased crystallinity and less densely packed grains. This decrease in crystallinity was also evident in the cross-section images of samples deposited with different process pressures. In the upper four images of **Figure 3.10**, the columnar growth structure gradually disappeared as the process pressure

doi:10.6342/NTU202403464

increased. At a process pressure of 15 mTorr, the cross-sectional view exhibited an amorphous structure, reflecting reduced crystallinity compared to the GIXRD measurement in **Figure 3.9**. Additionally, the morphology of the as-deposited films changed as predicted, as indicated by the top-view SEM images in the lower four images of **Figure 3.10**. The less effective bombardment of sputtered species resulted in films that were less densely packed, owing to the reduced kinetic energy available for adsorbed atoms to conduct lateral diffusion at the same substrate temperature.

Moreover, a slight impurity of the δ-TaN phase was detected, characterized by a shoulder at the diffraction peak at $2\theta = 38.87°$. This was attributed to the peak of δ-TaN at $2\theta = 35.65°$ but with a slight shift towards a higher angle, suggesting a smaller unit cell size than the typical one. This phenomenon may be attributed to the inevitable bombardment of sputtered atoms on the films.

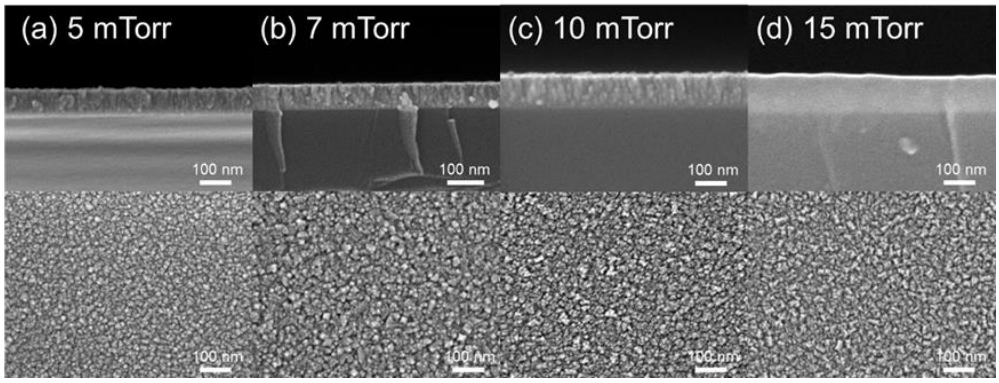

Figure 3.10 SEM images for TaN_x films deposited with different process pressures.

Across different process pressures, the film thickness surprisingly increased significantly, which might originate from the increased amount of sputtering gas introduced into the chamber. The optimized condition for synthesizing metastable Ta_2N_3 was determined by GIXRD and SEM. The former assesses crystallinity while the latter evaluates film thickness and determines growth structure and grain packing density. The detailed parameters for the optimized synthesis condition are listed in **Table 3.1** below.

doi:10.6342/NTU202403464

Table 3.1 Optimized parameters for synthesizing metastable Ta_2N_3, the asterisk sign will be discussed in the next section.

Rotation	Temperature	Gas (sccm)	Process pressure	Power
10 rpm	500°C	Ar (20), N_2 (30)	5 mTorr*	70W
Deposition time	**Mode**	**Frequency**	**Reversed-time**	
7200 s	Pulsed-DC	100 kHz	1 μs	

* When the process pressure was set to 5 mTorr, the as-deposited Ta_2N_3 films suffered from severe reproducibility problems owing to the residual oxygen background in the process chamber, which will be discussed in the next section.

3.2 Reproducibility of Ta_2N_3 Deposition

Maintaining reproducibility in the fabrication process is critical for ensuring the validity and reliability of subsequent experiments. While some parameters can be directly monitored during sputtering, others, such as residual reactive gas adsorbed on the chamber walls after each deposition and the use of different sputtering targets in the same main chamber, can also significantly impact reproducibility.

The presence of residual reactive gas in the chamber, particularly oxygen, can lead to variations in the synthesis of nitride compounds. Even small amounts of oxygen can yield different results, affecting reproducibility. Unfortunately, residual gas analysis (RGA) equipment is not available in the configuration of the presented thesis, making it challenging to ascertain the composition of residual gas in the chamber.

Additionally, the use of different sputtering targets can introduce contamination through alloying of different target atoms or the presence of impurities in the target material. For instance, titanium and tungsten can alloy with tantalum, potentially affecting

doi:10.6342/NTU202403464

the sputter yield and purity of the deposited films. However, contamination from alloying can be mitigated through frequent cleaning of the target or longer cleaning times before use.

In this section, we will focus on how the oxygen content in the main chamber affects the reproducibility of Ta_2N_3 thin film fabrication under optimized conditions.

3.2.1 Reproducibility of Ta_2N_3 Deposition Using 5 mTorr Process Pressure

To evaluate the effect of oxygen content in the main chamber, we utilized three distinct sets of parameters, as detailed in **Table 3.2**, was used. For brevity, the experiments will be referred to as Exp. A, B, and C in the following discussion.

Table 3.2 Different experimental parameters for the experiment of controlling oxygen content in the main chamber. The asterisk sign indicates that the substrate shutter would not open in this experiment configuration.

X	Temperature	Gas (sccm)	pressure	Power	time
Exp. A	500°C	Ar (20), N_2 (30), O_2 (0.7)	5 mTorr	80W	7200 s
Exp. B*	25°C	Ar (40)	9 mTorr	60W	3600 s
Exp. C	500°C	Ar (20), N_2 (30)	5 mTorr	70W	7200 s

*Exp. B is optionally performed between Exp. A and Exp. C for guttering the residual oxygen in the main chamber.

To regulate the background oxygen content, the experiments were conducted in different sequences. Exp. A was performed first, followed by Exp. C, to introduce additional oxygen content, simulating real sputtering conditions. The as-deposited film in

doi:10.6342/NTU202403464

Exp. C under this sequence was denoted as "with oxygen in the previous deposition". In contrast, the control group involved inserting Exp. B between these experiments. The as-deposited film in Exp. C by this sequence was denoted as "without oxygen in the previous deposition". This setup leveraged the ability of Ta atoms to adsorb oxygen molecules.

The resulting films on both quartz and n^+-Si(111) substrates yielded significantly different outcomes. In the GIXRD measurement (**Figure 3.11**), two distinct phases were observed. On the quartz substrate, films deposited with the intended introduction of oxygen background exhibited primarily the bixbyite-Ta_2N_3 phase with minimal impurities. Conversely, samples deposited with the intended elimination of oxygen content showed a mixed Ta_2N_3/δ-TaN phase. Incorporating oxygen has been shown to benefit the synthesis of the bixbyite-Ta_2N_3 phase. Oxygen, with a higher electronegativity than nitrogen, can effectively increase the oxidation state of Ta by being incorporated into the interstitial sites of the Ta_2N_3 lattice.[60]

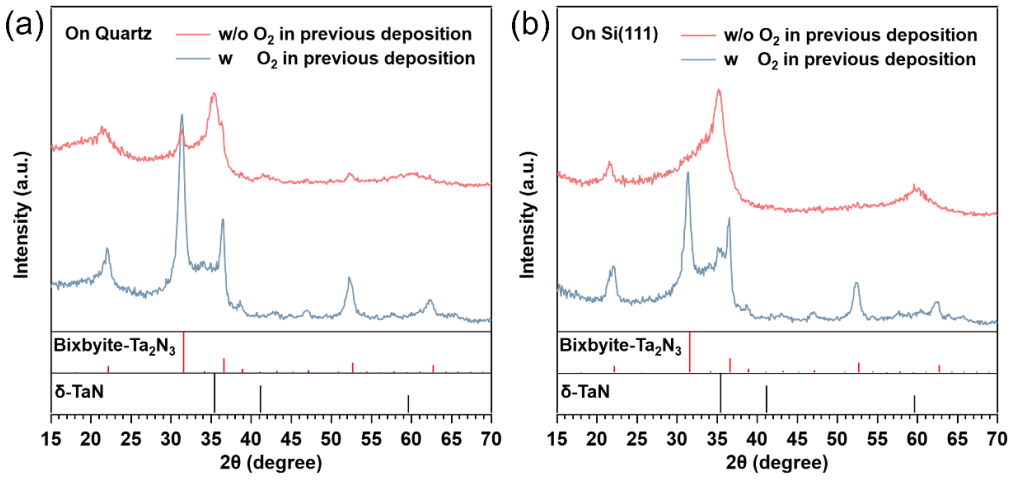

Figure 3.11 The GIXRD patterns measured from TaN_x films deposited on (a) quartz substrate or (b) n^+-Si(111) substrate with or without the intended incorporated oxygen background under optimized conditions. The reference of δ-TaN was obtained from ICSD-colloid180957.

doi:10.6342/NTU202403464

The samples deposited on silicon wafers showed more drastic differences. Regardless of whether an additional oxygen background was added to the main chamber, the films always contained the δ-TaN phase. This discrepancy might have originated from the differences in the substrates used for deposition. The chemical formula of quartz is SiO_2, making it a potential oxygen supplier during deposition through the diffusion of oxygen atoms assisted by substrate heating. However, the native oxide layer on silicon wafers is etched by the Ar plasma during substrate cleaning. This could explain why, in the control experiment with the intended decreased oxygen background, the resulting films exhibited such discrepancies.

3.2.2 Re-examination of Gas Atmosphere with a Low Background Oxygen Level

To replicate the optimal crystallinity of the Ta_2N_3 phase without the influence of oxygen background, a different ratio of N_2 flow was reexamined. In these experiments, the oxygen content was intentionally eliminated using the parameters from Exp. B. Still, no obvious trend was observed as in the previous finding (**Figure 3.2**). As the nitrogen flow rate increased, the chemical potential reached a point where the metastable phase could be accessed. With the intended elimination of the oxygen background, the metastable phase of bixbyite-Ta_2N_3 could be obtained with a nitrogen flow rate of 35 sccm.

When the nitrogen flow rate was increased to 39 sccm, the characteristic peak at $2\theta = 31.53°$, which signifies Ta_2N_3 with the strongest form factor, disappeared. Instead, a peak persisted around $2\theta = 21°$, accompanied by an amorphous background and a slightly crystallized δ-TaN phase, indicating the presence of a mixed phase of bixbyite-Ta_2N_3 and δ-TaN. This outcome was consistent with previous results obtained with a nitrogen flow

doi:10.6342/NTU202403464

rate of 40 sccm (**Figure 3.2**). The thinner thickness of the as-deposited film and relatively poor crystallinity likely contributed to this result.

Despite the change in deposition parameters, as indicated by the GIXRD diffractogram in **Figure 3.12b**, the samples deposited with the new optimized condition with the intended elimination of background oxygen still exhibited a mixed phase of bixbyite-Ta_2N_3 and δ-TaN. As we will discuss in the later sections, this mixed phase character is detrimental to PEC application once converted to Ta_3N_5 via nitridation.

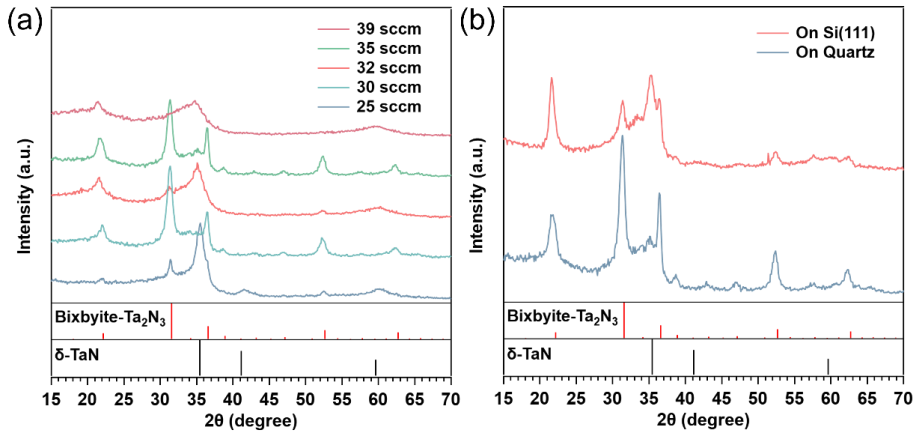

Figure 3.12 The GIXRD patterns measured from TaN_x films (a) deposited with varying N_2 flow rates but with the intended elimination of oxygen background, and (b) deposited with different substrates with a fixed nitrogen flow rate of 35 sccm. The reference of δ-TaN was obtained from ICSD-colloid180957.

3.2.3 Reproducibility of Ta_2N_3 Deposition Using 10 mTorr Process Pressure

The reproducibility within a process pressure of 5 mTorr was found to be invalid, as indicated by the experiments in **Figure 3.11**. The residual oxygen content would severely affect the composition of the resulting films. This failure can be attributed not only to fluctuations in the oxygen background in the main chamber but also to the low process pressure itself. While low process pressures can result in a compact and densely

doi:10.6342/NTU202403464

packed film, the sputtered atoms and clusters would have higher kinetic energies for bombardment. In the case of deposition on a silicon wafer, where there is no native oxide as an oxygen source to stabilize the Ta_2N_3 phase, the severe bombardment due to the low process pressure resulted in partial desorption of nitrogen atoms, leading to the presence of a mixture of the desired bixbyite-Ta_2N_3 phase and the δ-TaN phase, even with the optimized condition (N_2 = 35 sccm) under intended elimination of oxygen background, as indicated by the diffractogram of **Figure 3.12b**.

To resolve this problem, a set of samples was deposited with 10 mTorr process pressure. The same procedure as described in **section 3.3.1** to control the residual oxygen content in the main chamber was also performed. This time, the films deposited on quartz and n^+-Si(111) substrates yielded similar results (**Figure 3.13**). In GIXRD measurement, two phases were observed. On the quartz substrate, films deposited with the intended introduction of oxygen background exhibited primarily the bixbyite-Ta_2N_3 phase with a slight presence of the δ-TaN phase as impurities. On the other hand, samples deposited with the intended elimination of oxygen content showed almost the same dominance of the bixbyite-Ta_2N_3 phase but with a larger amount of δ-TaN phase, indicated by the shoulder at $2\theta = 36.12°$ in the diffractogram. The peak of the δ-TaN phase shifted to a higher angle, indicating a smaller unit cell compared to the theoretical value. Importantly, films deposited on the Si(111) substrates showed similar results to those deposited on quartz substrates. Even though there might always be some impurity phases present in the as-deposited film if oxygen is not intentionally added during deposition. The consistency between the deposition on different substrates with or without controlling oxygen background proved the hypothesis that the key factor in sputtering deposition is the kinetic energy for effective bombardment.

doi:10.6342/NTU202403464

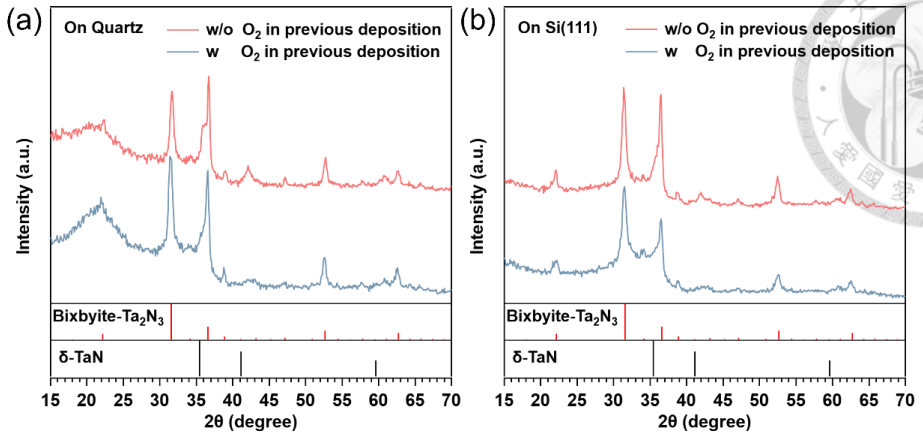

Figure 3.13 The GIXRD patterns measured from Ta_2N_3 films deposited on (a) quartz substrate or (b) n^+-Si(111) substrate with or without the intended incorporated oxygen background with a process pressure of 10 mTorr. The reference of δ-TaN was obtained from ICSD-colloid180957.

Consequently, even though the sample deposited at a nitrogen flow rate of 35 sccm exhibited the best crystallinity due to the discrepancy in deposition between different substrates, for the presented thesis, we have chosen to maintain the nitrogen flow rate at 30 sccm but increase the process pressure to 10 mTorr.

3.3 Characterization of Optimized Ta_2N_3

The optimal deposition parameters for the growth of bixbyite-Ta_2N_3 on both the quartz substrate and the silicon wafer have been established in the previous section, as listed in **Table 3.3**. It is important to note that since the application of the presented thesis is PEC measurement, the composition of the as-deposited film on both types of substrates is equally important. Therefore, even though the pure phase of Ta_2N_3 cannot be obtained within this deposition condition, the consistency between these two different types of substrates is crucial. Herein, the films deposited with optimal conditions on the

doi:10.6342/NTU202403464

transparent quartz substrates were used for optical characterizations, whilst films deposited on the n^+-Si(111) substrates were used for XPS measurements.

Table 3.3 Optimized parameters for the synthesis of Ta_2N_3 thin film.

Rotation	Temperature	Gas (sccm)	Process pressure	Power
10 rpm	500°C	Ar (20), N2 (30)	10 mTorr	70W
Deposition time	Mode	Frequency	Reversed-time	
7200 sec	Pulsed-DC	100 kHz	1 μs	

3.3.1 Structure Characterizations

The GIXRD diffractograms of the as-deposited Ta_2N_3 films on n^+-Si(111) and quartz were consistent, as described in the previous section (**Figure 3.13**). According to the X-ray diffraction data in **Figure 3.14**, Ta_2N_3 can be assigned to a 2×2×2 ordered defect bixbyite superstructure, as reported by Ganin *et al.*[54] The Miller indices associated with each peak are labeled in the diffractogram. Specifically, the order arrangement of nitrogen-vacancy sites is evident by the weak satellite diffraction peak, such as (321), that is otherwise forbidden in the regular cubic FCC structure.

There was also δ-TaN phase presented in the as-deposited films, marked with an asterisk sign in **Figure 3.14**. The peak position of this impurity was shifted to a higher angle, indicating a smaller unit cell than a normal BCC δ-TaN structure. While beyond the scope of this thesis, a possible reason for this formation might originate not only from the defect tolerance properties of nitride species but also from the lack of enough oxygen to stabilize the high oxidation state of Ta, leading to the presence of some low-valence Ta species after sputtering.[26, 27]

doi:10.6342/NTU202403464

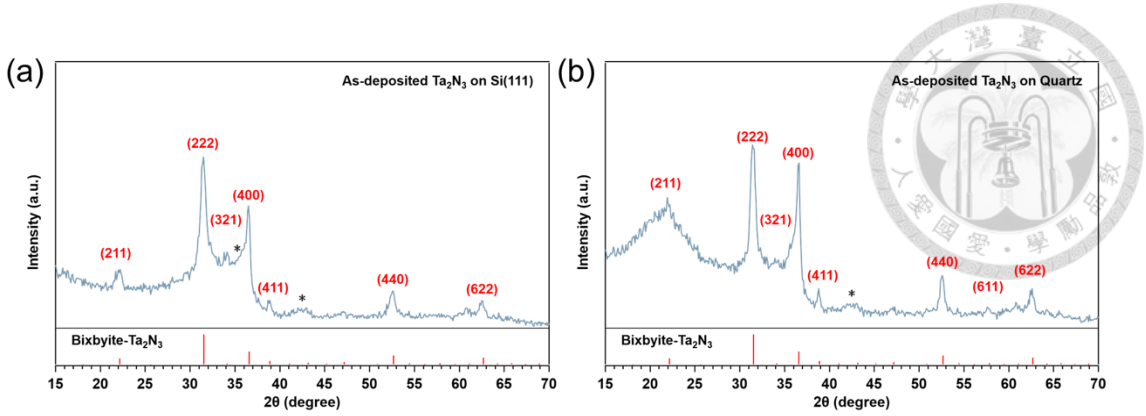

Figure 3.14 The GIXRD patterns measured from Ta_2N_3 films deposited on (a) n^+-Si(111) substrate or (b) quartz substrate with intended elimination of oxygen background with the optimal parameters.

The measured Ta_2N_3 diffraction peaks are slightly shifted to lower angles than the reference peaks originating from the polycrystalline films by Ganin *et al*.[54] This suggests a lattice constant of the Ta_2N_3 unit cell slightly larger than the CVD growth films but smaller than films grown by reactive sputtering with intended oxygen addition, as reported by Jiang *et al*.[60] The expansion of the lattice constant originated from the addition of oxygen, which occupies the interstitial site of the Ta_2N_3 unit cell, expanding the volume. Based on the lattice constants obtained from the GIXRD results of the diffraction peak of (222) and previous research values, the unit cell volume and theoretical density were calculated by considering the mass of the unit cell of a perfect Ta_2N_3 crystal containing 32 Ta and 48 N atoms, and then dividing by the unit cell volume. The results are summarized in **Table 3.4**.

doi:10.6342/NTU202403464

Table 3.4 Summary of Ta_2N_3 lattice constant and density with different synthesis methods.

X	Lattice constant	Unit cell volume	Theoretical density
Ganin *et al.*[54]	9.8205 Å^3	947.311 Å^3	11.33 g/cm^3
Jiang *et al.*[60]	9.89 Å^3	967.362 Å^3	~ 11.09 g/cm^3
This thesis	9.83 Å^3	646.862 Å^3	~ 11.29 g/cm^3

In the presented case, the expansion of unit cells can be attributed to two possible reasons: (1) the oxygen background in the sputtering chamber, which is inevitably incorporated into the sputtering process even with intended elimination, and (2) the excess nitrogen, due to the usage of a nitrogen flow rate of 30 sccm combined with a higher process pressure, which lowers the energy used to rearrange the ordering inside the unit cell. Both cases can be elucidated through the measurement of XPS, which will be addressed in the next section. Nevertheless, the GIXRD analysis of the as-deposited Ta_2N_3 films showed a bixbyite structure with slightly different lattice constants.

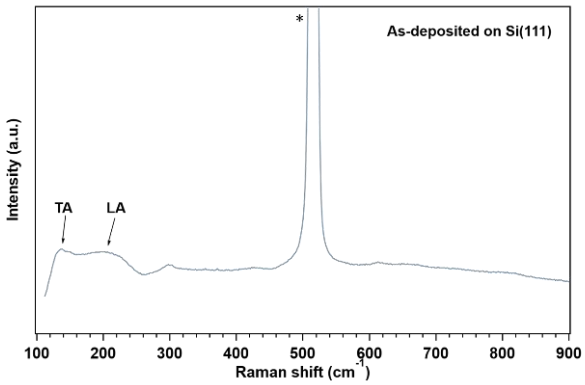

Figure 3.15 (a) The Raman spectrum measured from as-deposited Ta_2N_3 thin films deposited on the n^+-Si(111) substrate with the intended elimination of oxygen background with optimal conditions. The asterisk sign is the Raman signal of the silicon substrate.

doi:10.6342/NTU202403464

The Raman spectrum of as-deposited Ta_2N_3 on n^+-Si(111) substrate using 532 nm excitation yielded limited information (**Figure 3.15a**). The prominent peak at approximately 520 cm^{-1} was the signal of the silicon substrate. A relatively small peak at 136 cm^{-1} and a broad peak centered at 207 cm^{-1} were assigned to the transverse acoustic (TA and the longitudinal acoustic (LA) phonon mode of δ-TaN, respectively, but no signal from the bixbyite Ta_2N_3 phase was observed.[156]

The lack of signal from the bixbyite Ta_2N_3 phase in the Raman spectrum might be attributed to the crowded unit cell of Ta_2N_3, rendering it Raman inactive. The peaks observed in the Raman spectrum corresponding to δ-TaN are consistent with the observations from GIXRD; however, the Raman measurement did not provide useful information about the bixbyite Ta_2N_3 phase itself.

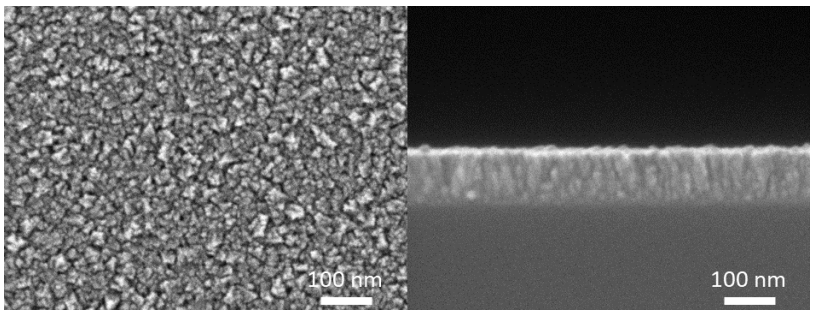

Figure 3.16 SEM images for as-deposited Ta_2N_3 thin films with a cross-sectional view on the right and a top view on the left.

The as-deposited Ta_2N_3 films exhibited a thickness of approximately 100 nm, characterized by a columnar microstructure in the cross-sectional SEM image (**Figure 3.16**). The morphology displayed a relatively uniform distribution with a grain size of about 15-20 nm. However, the surface appeared somewhat rough due to the high process pressure during sputtering.

doi:10.6342/NTU202403464

3.3.2 XPS Measurements

Despite its limited probing depth, XPS was employed to analyze the chemical state of the as-deposited Ta_2N_3 thin films. It is worth noting that XPS provides surface information that may not fully represent the bulk properties of the material. Achieving depth resolution in XPS typically requires ion sputtering, which can introduce false-positive results due to the preferential sputtering of different elements or ion mixing effects. Herein, the nitrogen 1s, oxygen 1s, and tantalum 4f core levels as well as the full spectrum with all binding energy measured were presented in **Figure 3.17**. First, the calibration of all binding energies was done by referencing the C 1s signal to 284.8 eV. This referencing method is usually not encouraged because the C 1s binding energy would change with the work function of the adsorbed material. Auger signals should be used as a reference, instead, to eliminate the shifting of spectrum by charging or other issues. However, acquiring sufficient Auger signals is quite difficult and time-consuming because of the small cross-section of Auger electron formation. As a result, this thesis still references the C 1s peak positions to 284.8 eV.

The survey spectrum provided an overview of all the elements present on the film surface (**Figure 3.17a**). A notable observation was the sharp and intense peak detected around 500 eV binding energy, corresponding to the O 1s signal. This prominent O 1s peak indicated the presence of oxygen in the as-deposited Ta_2N_3 thin film, despite efforts to eliminate oxygen from the main chamber before deposition. It is worth mentioning that this oxygen presence was detected even though the sample was measured shortly after being removed from the sputtering chamber, ruling out the possibility of surface oxidation during prolonged air exposure. Additionally, the survey spectrum revealed noisy O KLL Auger signals, highlighting the challenge of using Auger peaks for energy referencing.

doi:10.6342/NTU202403464

Auger electrons originated from other elements that were not discerned in the survey spectrum.

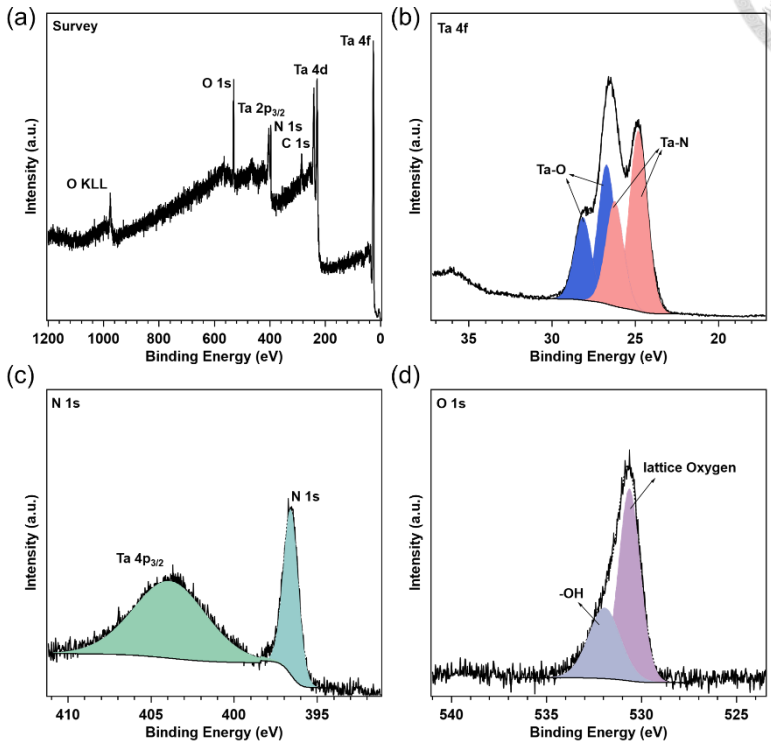

Figure 3.17 XPS (a) survey spectrum and (b)Ta 4f, (c) N 1s, and (d) O 1s core-levels measured from as-deposited Ta_2N_3 thin films. The core-level binding energies were calibrated by referencing the peak in the C 1s spectrum to 284.8 eV.

The Ta 4f core level spectrum in **Figure 3.17b** revealed three distinct peaks at 24.8, 26.6, and 28.0 eV, respectively, which could be deconvoluted into two spin-orbit splitting doublets from Ta-N and Ta-O bonding. These doublets stem from spin-orbit coupling, and the two peaks would have a fixed energy spacing and ratio of integrated area. Specifically, for f orbitals, the two states are denoted as $f_{7/2}$ and $f_{5/2}$, respectively, and the energy spacing between the peaks is 1.91 eV. The ratio of the integrated area under the $f_{7/2}$ and $f_{5/2}$ peaks is fixed at 4:3 for f orbitals. In **Figure 3.17b**, the peak at 24.81 eV corresponded to the Ta $4f_{7/2}$ state associated with Ta-N bonding. Similarly, the peak at 26.6 eV could be fitted into two peaks centered at 26.23 and 26.72 eV, respectively. The

doi:10.6342/NTU202403464

former peak represented the Ta $4f_{5/2}$ state from Ta-N bonding, while the latter peak corresponded to the Ta $4f_{7/2}$ state contributed by Ta-O bonding. Finally, the peak at 28.0 eV indicated the Ta $4f_{5/2}$ state from Ta-O bonding.

The peak at 24.81 eV corresponded to the Ta $4f_{7/2}$ state of the first spin-orbit splitting doublet associated with Ta-N bonding. Similarly, the peak at 26.6 eV could be resolved into two peaks centered at 26.23 eV and 26.72 eV. The former peak represented the Ta $4f_{5/2}$ state of the first spin-orbit splitting doublet from Ta-N bonding, while the latter peak corresponded to the Ta $4f_{7/2}$ state of the second spin-orbit splitting doublet contributed by Ta-O bonding. Finally, the peak at 28.0 eV indicated the Ta $4f_{5/2}$ state of the second spin-orbit splitting doublet from Ta-O bonding.

The difference in binding energies between two sets of doublets was attributed to the electronegativity difference between oxygen and nitrogen, affecting the ability of the compound to stabilize the core hole after photoionization via X-ray absorption. Moreover, the full width at half maximum (FWHM) of these peaks varied due to the different lifetimes of the core-hole excited states, according to Heisenberg's uncertainty principle. The presence of the first doublet at 24.81 eV and 26.23 eV, arising from Ta-N bonding, suggested that the oxidation state of Ta atoms was predominantly in the highest Ta^{5+} state, akin to that of Ta_3N_5.[4] Additionally, the appearance of another doublet at 26.72 eV and 28.14 eV was attributed to oxynitride species.

Interestingly, despite the observation of a few impurities from the δ-TaN phase in both the GIXRD measurement and Raman spectrum, there was no signal indicative of low-valence Ta species, such as Ta^{3+}, typically observed around 23 eV for the Ta $4f_{7/2}$ state.[157]

Figure 3.17c exhibited two distinct peaks at 396.6 and 403.9 eV. The peak at 396.6 eV corresponded to nitrogen involved in Ta-N bonding. As discussed in **Section 3.4.1**,

doi:10.6342/NTU202403464

one possible explanation for the diffraction peak shift of the as-deposited Ta_2N_3 to a lower angle was the occupancy of nitrogen in the interstitial sites of the unit cell. Typically, nitrogen that is not bonded with the metal cations would have a different binding energy, resulting in an additional peak at higher binding energy, around 400 eV.[158] The absence of this signal suggests that nitrogen not bound to tantalum does not occupy the interstitial sites of the Ta_2N_3 unit cell. Another broad peak centered at 403.8 eV was attributed to the Ta $4p_{3/2}$ state and not related to nitrogen. This peak had a large FWHM due to the 4p electron being a core electron in Ta's electron configuration. After the ionization of this core electron, the resulting core hole had a shorter lifetime because of the reduced screening effect of charges in the nucleus. This led to a larger energy spread compared to valence electrons, according to Heisenberg's Uncertainty Principle. Due to the broad nature of this peak and the absence of the Ta $4p_{5/2}$ peak in the spectrum, this peak was not used for analysis. It is important to note that the presence of this broad peak is inevitable when acquiring the N 1s spectrum.

The O 1s spectrum in **Figure 3.17d** revealed an asymmetric peak at 530.6 eV, which could be deconvoluted into two peaks centered at 530.6 and 531.95 eV, respectively. The former peak was attributed to the oxygen incorporated into the lattice, corresponding to the Ta-O bonding observed in the Ta 4f core level spectrum. The presence of lattice oxygen provides insight into the peak shift observed in the GIXRD measurement of the as-deposited Ta_2N_3 to a lower angle. It is conceivable that oxygen may have occupied the interstitial sites of the Ta_2N_3 unit cell. Another peak centered at 531.95 eV was attributed to adsorbed water on the film surface.[60] This finding suggests that despite efforts to eliminate the oxygen background, a significant amount of oxygen can still be incorporated into the lattice, as supported by research by Jiang *et al.*, which indicates that the formation of metastable Ta_2N_3 relies on the stabilization of oxygen in the lattice to

doi:10.6342/NTU202403464

increase the oxidation state of Ta from low valence Ta^{3+} to a higher oxidation state of Ta^{5+}.[60]

Another advantage of using XPS is its capability for quantification. By normalizing the integrated peak area with the photoionization cross-section, the composition of different elements on the surface can be obtained. However, when determining surface stoichiometry with XPS, the binding energies of the analyzed peaks should be on the same scale. This is because differences in binding energy imply variations in the kinetic energy of the photoelectron being analyzed, leading to slight differences in sampling depth. In this case, the binding energy of the Ta 4f level is much smaller than that of N 1s and O 1s, so using these spectra to determine surface stoichiometry is not feasible.

Additionally, as discussed earlier, XPS is a surface-sensitive technique, meaning that the chemical state and stoichiometry observed at the surface may not accurately represent the bulk properties of the material. For more accurate quantification of bulk stoichiometry, techniques such as Rutherford backscattering spectroscopy (RBS) are preferred, though this is beyond the scope of this thesis. The presented XPS results suffice to support the existence of oxygen in the lattice of as-deposited Ta_2N_3 films that increase the cell volume and make the diffraction peak shift to a lower angle.

3.3.3 Optical Properties

The optical characterization utilized the as-deposited Ta_2N_3 thin films on the quartz substrate using UV-Vis spectroscopy. Both transmittances and reflectances were measured to obtain the absorbances. The detailed experimental setup and background are discussed in **Chapter 2**.

doi:10.6342/NTU202403464

The absorption spectrum of the as-deposited Ta_2N_3 film was demonstrated in **Figure 3.18a**. Since this absorption spectrum was derived with reflectance correction, the absorbance in longer wavelengths is more reliable. It would be better to describe the longer wavelengths using diffuse reflectance spectroscopy (DRS), which uses an integration sphere to acquire all the signals. Nevertheless, merely correcting the reflectance for a better description of absorption is acceptable in the presented thesis. The Tauc plots in **Figure 3.18b** were derived from the absorption spectrum in **Figure 3.18a**, and the indirect optical bandgap was found at 1.98 eV while the direct bandgap was located at 2.28 eV. These values are slightly larger than the reported value by Jiang *et al.*, who synthesized a high-quality Ta_2N_3 thin film and observed a strong optical absorption above a ~ 1.9 eV onset.[60] Another group claimed that Ta_2N_3 would have an optical bandgap varying between 1.95 and 2.57 eV.[52] These discrepancies come from the oxygen impurities inside the Ta_2N_3 lattice. The oxygen content inside the films would transform Ta_2N_3 from metallic to semiconducting, which has already proved to be correct.[60] As demonstrated by the XPS results in **Figure 3.17**, oxygen was incorporated into the lattice of the as-deposited Ta_2N_3 film. Consequently, the enlarged bandgap can be attributed to the oxygen content in the as-deposited Ta_2N_3 film.

doi:10.6342/NTU202403464

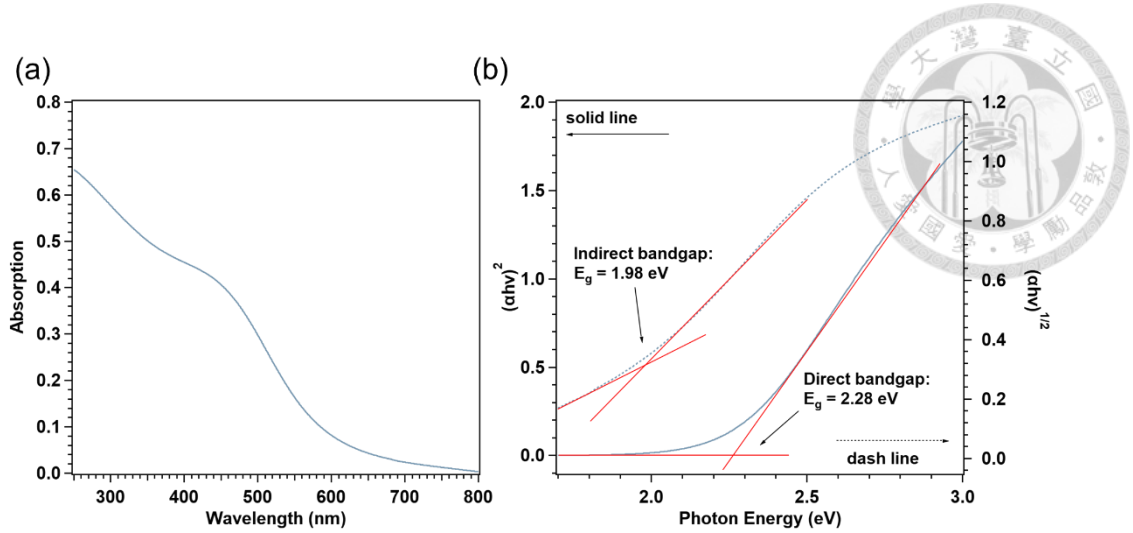

Figure 3.18 (a) Absorption spectrum measured from as-deposited Ta_2N_3 film on quartz. (b) Tauc plots for direct and indirect transitions of as-deposited Ta_2N_3 thin films.

3.4 Converting Ta_2N_3 to Ta_3N_5

The as-deposited Ta_2N_3 films underwent a further nitridation process in a quartz tube furnace. Two samples were placed on a quartz slide as a boat and sent to the center of the tube furnace to ensure a uniform temperature distribution, as indicated by **Figure 3.19**.

Figure 3.19 Image of the position where the samples were placed inside the tube furnace.

doi:10.6342/NTU202403464

The tube was evacuated by a diaphragm pump to about 8 Torr and then refilled with N_2 gas at a 500 sccm flow rate until the atmospheric pressure was reached. This evacuation and refilling process was repeated twice to rid of oxygen and moisture content in the tube furnace. Subsequently, the quartz tube was purged with N_2 gas at a 150 sccm flow rate for approximately 25 minutes, and then ammonia (NH_3) was introduced at a 100 sccm flow rate of 100 sccm (the N_2 gas supply was stopped). The samples were nitridated for 3 hours at different temperatures with a 10°C/min ramp rate, followed by natural cooling to room temperature with the same flow rate of NH_3. After the quartz tube temperature cooled down to room temperature, N_2 gas was introduced into the tube at a flow rate of 150 sccm for 25 minutes to clean up any residual NH_3. Finally, the samples were taken out for further characterization.

Reactive annealing in an ammonia atmosphere is widely used for converting Ta_2O_5 into Ta_3N_5. This process involves carefully controlling various parameters, such as the gas flow rate, annealing temperature, ramp-up and ramp-down rates, annealing duration, and the positioning of the sample. These parameters greatly influence the characteristics of the resulting Ta_3N_5 film, including its phase purity, stoichiometry, and crystallinity.

Most reports use Ta_2O_5 as precursor films when searching for the optimized reactive annealing parameters, and the results are highly varying between different research groups. While the final Ta_3N_5 films exhibit similar photoelectrochemical characteristics, the discrepancies in reactive annealing conditions stem from the precursor films as well as the variations in the annealing setup, such as the sample position within the tube furnace and the ramp-down rate. Therefore, this work follows the work done by Eichhorn *et al.*, which also starts with TaN_x films for Ta_3N_5 synthesis.[159] We also limited each annealing process to two samples to maintain control over the reproducibility.

doi:10.6342/NTU202403464

Furthermore, the ramp-up rate was fixed at 10℃/min, the highest attainable value for our tube furnace. Temperature ramp-down was done by allowing the furnace to naturally cool down to 30℃ without opening the lid of the tube furnace. Finally, the ammonia flow rate was fixed to 100 sccm for the presented thesis. We should note that higher ammonia flow rates may further improve the photoelectrochemical performance of Ta_3N_5, but this goes beyond the scope of this thesis. The annealing duration and temperature were two major annealing parameters that are investigated here. Eventually, the optimal annealing parameters were determined based on the PEC performances of Ta_3N_5, which will be introduced in **Chapter 4**. Herein, XRD measurements, Raman spectroscopy, SEM, and XPS were conducted on the films deposited on n^+-Si(111) substrates and the results are discussed in the next paragraphs.

3.4.1 Effect of Nitridation Duration

The annealing duration serves as a crucial parameter in determining the extent to which the as-deposited Ta_2N_3 films transform into the desired Ta_3N_5 phase. Upon subjecting the films to 1 hour of NH_3 annealing at 820℃, the resulting films exhibited both the diffraction peaks of Ta_3N_5 and Ta_2N_3, as evidenced by the GIXRD data shown in **Figure 3.20**. While the constitution of these films primarily consisted of the pure phase of Ta_3N_5, a minor peak at $2\theta = 22.15°$ and a shoulder at $2\theta = 36.53°$ suggested that the as-deposited Ta_2N_3 did not fully convert to Ta_3N_5 within the 1-hour annealing period under an NH_3 atmosphere. However, the PXRD measurement depicted in **Figure 3.21** revealed a slightly different outcome. Although the dominant phase observed in the PXRD measurement was still Ta_3N_5, there was also evidence of a phase of low-valence Ta_5N_6 and Ta_2N present in the diffractogram. Specifically, the peak at $2\theta = 26.28°$ and a shoulder at $2\theta = 34.63°$ were characteristic signals derived from Ta_5N_6, and the peak at

doi:10.6342/NTU202403464

$2\theta = 36.45°$ was characteristic signals derived from Ta_2N. The inconsistency between the GIXRD and PXRD results stemmed from differences in the information depth obtained from the sample. GIXRD, being relatively surface-sensitive, utilizes an extremely small incident angle of about 0.5°. In contrast, the incident angle of PXRD varies during measurement, leading to the collection of data primarily from the bulk portion of the Ta_3N_5 films.

Combining the GIXRD and PXRD results suggested that the as-deposited Ta_2N_3 film was converted into Ta_3N_5 films almost entirely after 1 hour of reactive annealing, though a small amount of Ta_2N_3 remained on the surface. However, some of the Ta_3N_5 within the bulk of the films had decomposed into low-valence Ta_5N_6.[53]

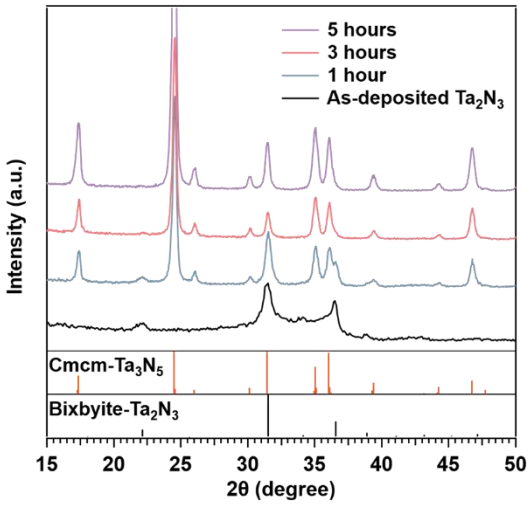

Figure 3.20 GIXRD patterns measured from Ta_3N_5 films annealed at 820°C with different durations. The reference of Cmcm-Ta_3N_5 was obtained from ICSD-colloid66533.

doi:10.6342/NTU202403464

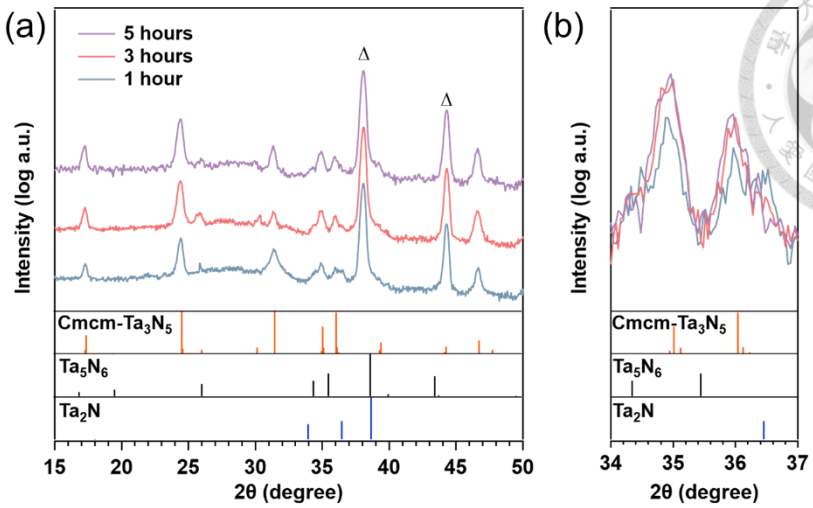

Figure 3.21 PXRD patterns measured from Ta_3N_5 films annealed at 820°C with different durations. The reference of Cmcm-Ta_3N_5 and Ta_5N_6 were obtained from ICSD-colloid66533 and ICSD-colloid644720, respectively. The triangular sign was the diffraction peaks from the substrate holder.

Upon increasing the annealing duration to 3 hours, the films appeared to have converted into pure Ta_3N_5 according to the GIXRD measurements. Moreover, the crystallinity appeared to improve, as indicated by the enhanced intensity of each diffraction peak, particularly the (110) peak at $2\theta = 24.49°$. The absence of the Ta_2N_3 phase in the GIXRD measurement suggested the complete conversion of the as-deposited Ta_2N_3 into the desired Ta_3N_5 on the surface. However, similar to the results obtained after 1 hour of annealing, diffraction peaks characterized as low-valence Ta_5N_6 and Ta_2N were still present. Especially, the Ta_2N content was reduced within increasing annealing dwell times. (**Figure 3.21b**) The decreasing content of Ta_2N suggests that this phase is the intermediate phase when converting from the Ta_2N_3 phase to the Ta_3N_5 phase; while the Ta_5N_6 phase was decomposed from the Ta_3N_5 phase. Consequently, after 3 hours of ammonia annealing, the surface appeared to be converted into pure Ta_3N_5, and the bulk

doi:10.6342/NTU202403464

of the film was predominantly constituted of the Ta_3N_5 phase, albeit with some minor impurities in the form of Ta_5N_6 and Ta_2N. Further increasing the annealing dwell time to 5 hours leads to improved crystallinity in both GIXRD and PXRD measurements. Still, a small amount of Ta_5N_6 and Ta_2N impurities remained in the bulk portion of Ta_3N_5 film.

In summary, the analysis of the surface and bulk layers of the films revealed that extending the annealing duration from 1 hour to 5 hours facilitated a progressive conversion of the Ta_2N_3 phase into the desired Ta_3N_5 phase. This transformation was accompanied by enhanced crystallinity, particularly noticeable on the film's surface. Additionally, the bulk phase predominantly consisted of the desired Ta_3N_5 phase, with crystallinity improving further with longer annealing durations. However, traces of impurities in the form of low-valence Ta_5N_6 and Ta_2N phases persisted in the bulk, with the content of Ta_2N decreased with prolonged annealing times (**Figure 3.21b**).

For our presented thesis, the annealing dwell time was fixed at 3 hours. While longer nitridation times have been shown to improve the crystallinity of the desired Ta_3N_5 films and reduce impurities content, we have chosen this duration based on its potential impact on PEC performance, which will be discussed in **Chapter 4**.

3.4.2 Effect of Nitridation Temperature

When subjected to an annealing temperature of 780℃ for 3 hours, the film primarily exhibited the Ta_2N_3 phase, as evidenced by the GIXRD results in **Figure 3.22a**. This suggests that the annealing temperature was insufficient to fully convert the films to the desired Ta_3N_5 phase.

doi:10.6342/NTU202403464

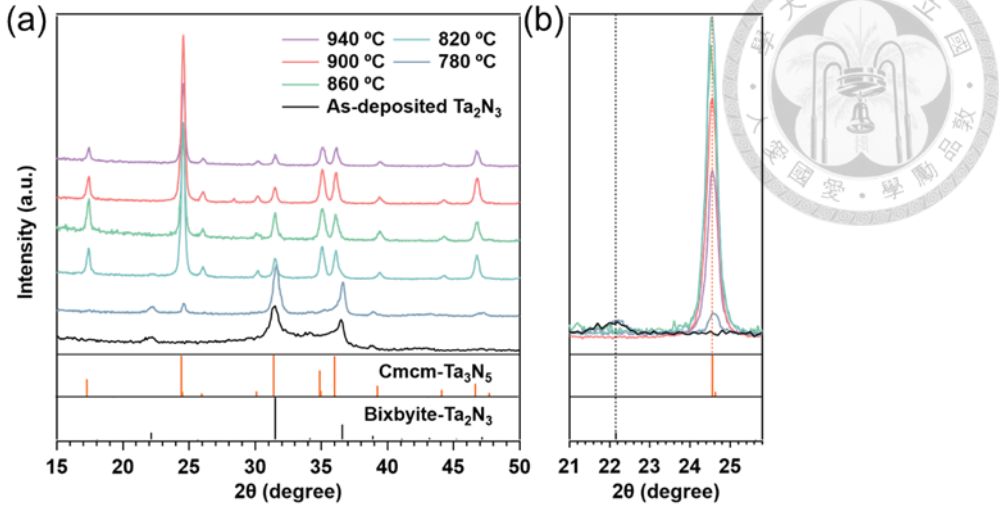

Figure 3.22 GIXRD patterns measured from Ta_3N_5 films annealed at different temperatures for 3 hours. (b) Enlarged diffractograms for 2θ = 21 - 26°. The reference of Cmcm-Ta_3N_5 was obtained from ICSD-colloid66533.

The crystallinity of Ta_2N_3 was found to be better than that of the as-deposited film. A closer examination of the peak at 2θ = 24.60° revealed that the film contained a small amount of converted Ta_3N_5 (**Figure 3.22b**), although its crystallinity was relatively low. Therefore, the films annealed at 780°C were found to be primarily Ta_2N_3 with improved crystallinity and a small amount of Ta_3N_5. In contrast, the bulk phase of the film annealed at 780°C primarily consisted of low-valence Ta_5N_6 and Ta_2N phases. The peak at 2θ = 26.28° and a shoulder at 2θ = 34.63° were characterized as Ta_5N_6 phase, while the peak at 2θ = 36.45° was characteristic signals derived from Ta_2N, as indicated by the PXRD measurement in **Figure 3.23**.

Upon increasing the annealing temperature to 820°C, the film completely converted to the pure phase of Ta_3N_5 on the surface, as observed in the surface-sensitive GIXRD measurement. However, a few impurities phases of Ta_5N_6 and Ta_2N were still present in the bulk phase of the annealed film, as indicated by the diffraction peaks at 2θ = 34.63° and 36.45°, respectively, as shown in the diffractogram of **Figure 3.23**.

doi:10.6342/NTU202403464

Subsequent annealing temperature increases from 820°C to 940°C resulted in the observation of a pure phase of Ta_3N_5 by GIXRD, but with deteriorating film crystallinity, as indicated by the decrease in intensity of the peak at 2θ = 17.27°. Additionally, the bulk phase also appeared to consist mainly of the desired Ta_3N_5 phase, albeit with decreasing crystallinity as the annealing temperature increased. Furthermore, the content of both Ta_5N_6 and Ta_2N phases increased with higher annealing temperature as indicated by the increasing intensity of diffraction peaks at 2θ = 34.63° and 36.45° demonstrated in **Figure 3.23b**. It confirmed the observation that high-temperature treatment of Ta_3N_5 leads to its decomposition into Ta_5N_6 phases.[53]

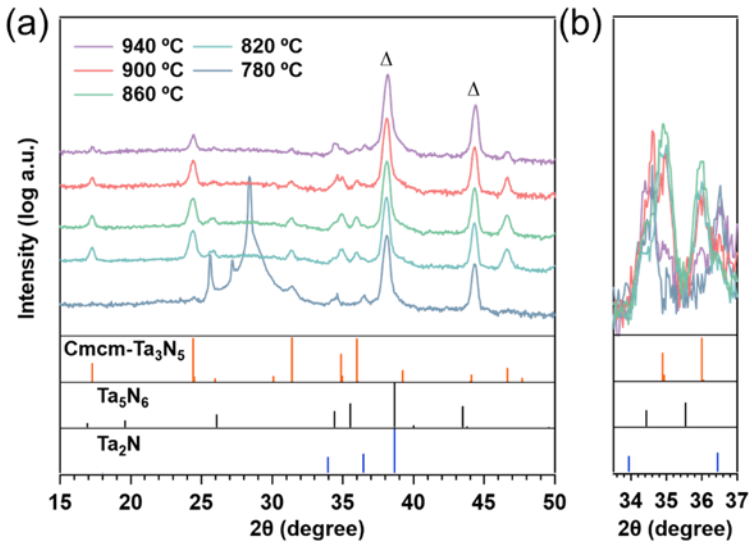

Figure 3.23 (a) PXRD patterns measured from Ta_3N_5 films annealed at different temperatures for 3 hours. (b) Enlarged diffractograms for 2θ = 33 - 37°. The reference of Cmcm-Ta_3N_5 and Ta_5N_6 were obtained from ICSD-colloid66533 and ICSD-colloid644720, respectively. The triangular sign was the diffraction peaks from the substrate holder.

The SEM image in **Figure 3.24** of the NH_3-annealed thin film revealed an increase in film thickness from 100 nm to about 120 nm. This increase can be attributed to the fact

doi:10.6342/NTU202403464

the density of the Ta_2N_3 phase was larger than the Ta_3N_5 phase, leading to volume expansion after phase conversion. Interestingly, the thickness of films annealed at different temperatures remained relatively consistent. Therefore, only the cross-sectional image of Ta_3N_5 annealed at 820°C is presented. It is worth noting that this volume expansion could potentially result in a broken surface morphology if epitaxial Ta_3N_5 films were formed from Ta_2N_3 as the starting phase. However, in this case, the morphology remained intact due to the use of polycrystalline film. The grain size of the thin film annealed at 780°C was approximately the same as that of the as-deposited Ta_2N_3. The post-annealing process using a tube furnace did not lead to a significant increase in grain size within the same crystalline phase. This may be attributed to the uncontrolled cooling process following annealing, which is considered crucial for crystal formation.[160]

However, with increasing annealing temperatures, the grain size increased and more clear grain boundaries were formed. Additionally, pinholes were observed on the surface of the Ta_3N_5 films regardless of the annealing temperature used.

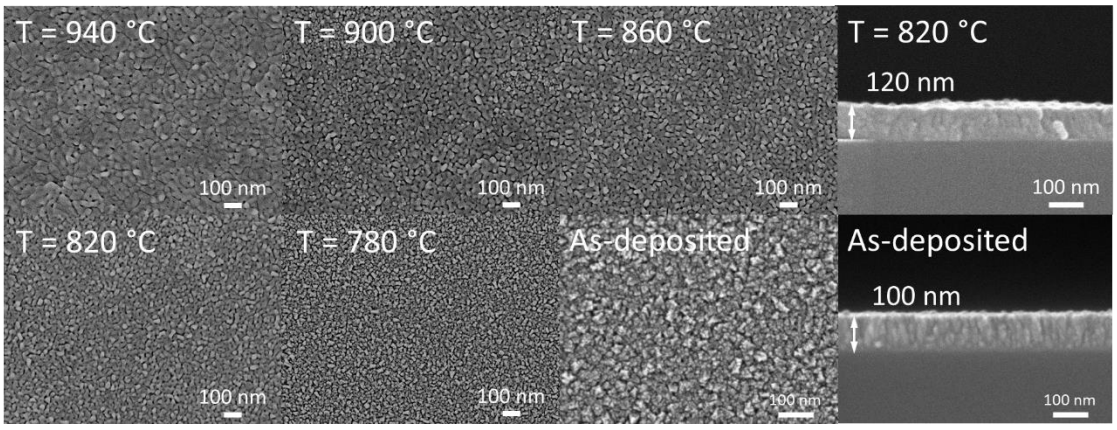

Figure 3.24 SEM images for Ta_3N_5 films annealing at various temperatures and as-deposited Ta_2N_3 films.

The Raman spectrum of Ta_3N_5 annealed at 820°C, illustrated in **Figure 3.25**, reveals distinct vibrational modes classified into two groups, namely A_g and B_g modes.

doi:10.6342/NTU202403464

These assignments were established by referencing theoretical values calculated by Nurleala *et al.*, with all vibrational modes categorized as longitudinal optical phonon modes.[67] Additionally, a broad peak denoted with a triangle symbol was identified as the second overtone of the A_g vibration mode at 266 cm^{-1}.[67] This peak emerges when using an excitation wavelength of 532 nm (~ 2.3 eV) similar to the band gap energy of Ta_3N_5, resulting in resonance excitation. However, the peak at 300 cm^{-1} revealed the presence of an oxynitride phase in the films.

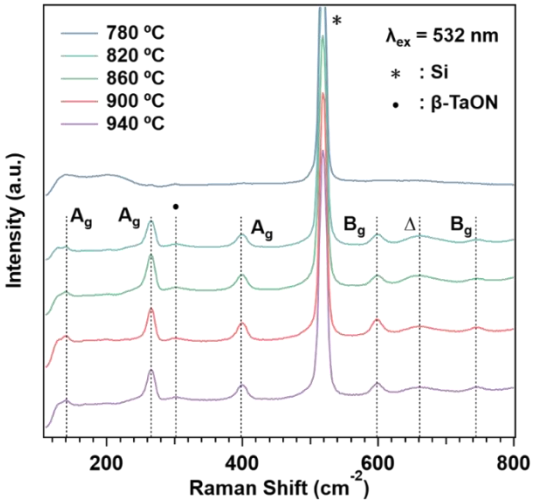

Figure 3.25 Raman spectrum measured from Ta_3N_5 films annealed at different temperatures for 3 hours using 532 nm excitation. The vibration modes of Ta_3N_5 were marked on the figures with the resonance mode marked as the triangle, the peak of the Si substrate was denoted by the asterisk sign, and the oxynitride phase marked as the dot sign.

Examining the Raman spectrum of Ta_3N_5 with annealing temperature increasing from 820°C to 940°C progressively, a notable trend emerges: increasing the annealing temperature gave decease crystallinity, as evidenced by the decreasing intensity of peak centered at 266 cm^{-1}. This trend was observed after calibrating the peak intensity of the Si substrate, marked with an asterisk, to a consistent value. The peak intensity of Raman

doi:10.6342/NTU202403464

spectroscopy can be thought of as the estimation of the degree of disorder since Raman spectrum is a technique used for the measurement of the vibrational modes of material.

However, the Raman spectra of film annealed at 780 °C displayed no characteristic vibrational mode of Ta_3N_5 but only the phonon modes of the δ-TaN phase were observed, consistent with the finding of **Figure 3.15a**. This further confirms the presence of the Ta_2N_3 phase and the low crystallinity of Ta_3N_5, which was only partially converted under these annealing conditions.

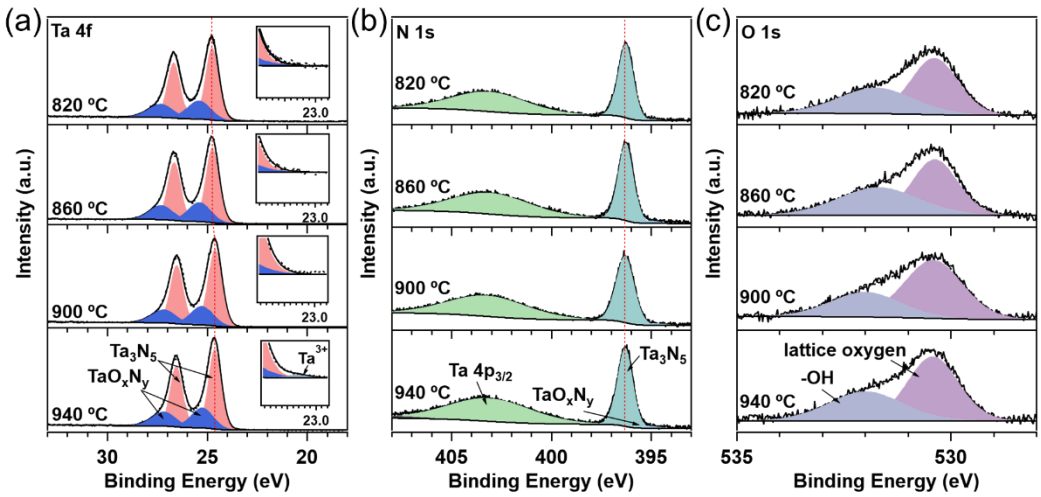

Figure 3.26 XPS (a)Ta 4f, (b) N 1s, and (c) O 1s core-levels measured from Ta_3N_5 thin films annealed at different temperatures for 3 hours. The core-level binding energies were calibrated by referencing the peak in the C 1s spectrum to 284.8 eV.

Surface elemental analysis was conducted using XPS, all the spectra were referenced the C 1s peak position to 284.8 eV. Analysis was performed on samples annealed at 820°C, 860°C, 900°C, and 940°C, excluding the 780°C sample due to incomplete conversion to the desired Ta_3N_5 phase.

The Ta 4f core level spectrum in **Figure 3.26a** revealed two distinct peaks at 24.80, and 26.7 eV, respectively, which could be deconvoluted into two spin-orbit splitting doublets from Ta-N and Ta-O bonding. In **Figure 3.26a**, the peak at 24.80 eV

doi:10.6342/NTU202403464

corresponded to the Ta $4f_{7/2}$ state associated with Ta-N bonding, and the peak at 26.7 eV represented the Ta $4f_{5/2}$ state from Ta-N bonding. The binding energy of the Ta $4f_{7/2}$ state aligned well with that expected for Ta_3N_5, confirming the presence of Ta^{5+} as the highest oxidation state after annealing at 820 °C.[4] While, the peak at 25.4 eV corresponded to the Ta $4f_{7/2}$ state contributed by Ta-O bonding, and the peak at 27.3 eV indicated the Ta $4f_{5/2}$ state from Ta-O bonding. It originated from the presence of the oxynitride phase instead of Ta_2O_5 in the surface composition. Typically, Ta_2O_5 exhibits a binding energy of around 26.6 eV for the Ta $4f_{7/2}$ state, while oxynitride phases tend to have lower binding energy, around 25.8 eV.[4] Consequently, the peak centered at 25.4 eV can be attributed to the Ta $4f_{7/2}$ state of the second spin-orbit doublet, reflecting the presence of oxynitride on the surface. The existence of the oxynitride phase suggests that, even under an anhydrous ammonia atmosphere, the removal of lattice oxygen from the surface was still incomplete.

Upon increasing the annealing temperature, the Ta $4f_{7/2}$ state representing Ta-N bonding shifted to a lower value, from 24.8 eV (820°C) to 24.6 eV (940°C), indicating a more reductive surface bonding environment. This shift suggested that the oxidation state of Ta was slightly lower than the typical Ta^{5+} with increasing annealing temperature. The absence of any tail signals observed at the lower binding energy side of the data, including the Ta 4f, N 1s, and O 1s spectra, ruled out the possibility that the binding energy shift was due to poor charge compensation during XPS measurement.

Furthermore, a peak at 23.40 eV was deconvoluted for Ta_3N_5 film annealed at 940°C, demonstrating the existence of low-valence Ta^{3+} shown in the inset of Figure 3.24a. This presence of Ta^{3+} confirmed that high-temperature treatment resulted in the formation of nitrogen vacancies, combined with the generation of low-valence Ta^{3+} to maintain charge neutralization.[34] The content of low-valence Ta^{3+} was low, as indicated by the small peak area.

doi:10.6342/NTU202403464

Figure 3.26b exhibited two distinct peaks at 396.6 and 403.3 eV. Deconvolution of the peak at 396.6 eV yielded two peaks centered at 396.6 eV and 395 eV. The peak at 396.6 eV corresponded to nitrogen involved in Ta-N bonding; while the peak at around 395 eV was attributed to the Ta-N bonding in the oxynitride phase. Another broad peak centered at 403.8 eV was attributed to the Ta $4p_{3/2}$ state and not related to nitrogen. Upon increasing the annealing temperature, there was no significant shift in the position of the N 1s peak position.

The O 1s spectrum in **Figure 3.26c** revealed an asymmetric peak at 530.4 eV, which could be deconvoluted into two peaks centered at 530.4 and 531.9 eV, respectively. The former peak was attributed to the oxygen incorporated into the lattice, corresponding to the Ta-O bonding observed in the Ta 4f core level spectrum. Another peak centered at 531.9 eV was attributed to adsorbed water on the film surface. The peak position of lattice oxygen didn't shift with increasing annealing temperature, which is consistent with the Ta-O bonding presented in the Ta 4f spectrum.

The optical characterization utilized the Ta_3N_5 thin films on the quartz substrate annealed at different temperatures using UV-Vis spectroscopy. The absorption spectra of Ta_3N_5 annealed at various temperatures were demonstrated in **Figure 3.27**.

Interestingly, no significant difference was observed in the absorption profiles among samples annealed at different temperatures. All spectra exhibited an absorption onset around 580 nm, corresponding to an approximate band gap of 2-2.3 eV for Ta_3N_5. Consequently, for this section we focus on the overall profile of Ta_3N_5 synthesized at different annealing temperatures, reserving detailed optical analysis for further investigation in the next section.

doi:10.6342/NTU202403464

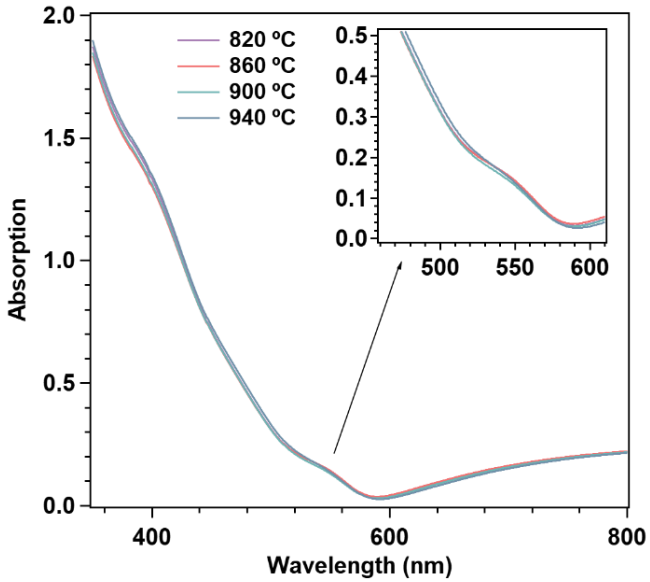

Figure 3.27 Absorption Spectrum measured from Ta_3N_5 films annealed at different temperatures for 3 hours. The inset was the absorption spectrum near the absorption edge within the wavelength from 450 nm to 600 nm.

Based on the comprehensive analysis conducted, particularly the XPS analysis of Ta_3N_5 films subjected to various annealing temperatures, we have determined the optimal conditions for the reactive annealing of as-deposited Ta_2N_3 to achieve the desired Ta_3N_5 phase. These optimal conditions result in films with superior crystallinity and minimal defect content, as characterized by GIXRD, PXRD, and Raman spectroscopy. The XPS analysis revealed the presence of the highest oxidation state, Ta^{5+}, without the formation of lower-valence Ta^{3+}, after annealing at 820°C.

It was observed that the dwell time significantly influenced the phase of the annealed films. While a dwell time of 5 hours yielded Ta_3N_5 films with better crystallinity and lower impurities content, a dwell time of 3 hours was selected for further application, as detailed in **Chapter 4**. The detailed parameters of the annealing condition are listed in **Table 3.5**.

doi:10.6342/NTU202403464

Table 3.5 Parameters for reactive annealing of Ta_3N_5.

Sample position	Temperature	Gas (sccm)	Dwell Time	Ramp up	Ramp down
Figure 3.19	820°C	NH_3 (100)	3 hours	10°C/min	Nature cooling

3.5 Characterization of Optimized Ta_3N_5

In this section, the established optimal conditions for Ta_3N_5 synthesis via reactive annealing of as-deposited Ta_2N_3, as outlined in **Table 3.5**, were utilized. Samples deposited on both n^+-Si(111) substrate and quartz substrate underwent the same reactive annealing conditions for further characterization.

It is worth addressing that there might be some concerns about the discrepancies in the composition of Ta_3N_5 thin films on a n^+-Si(111) substrate or a transparent quartz substrate. However, given that the final application of Ta_3N_5 films was intended for PEC measurement, the characterization in this section primarily focused on Ta_3N_5 films deposited on n^+-Si(111) substrate. In this study, we would treat the Ta_3N_5 on both substrates as having identical compositions, which had been identified by both GIXRD and Raman measurements as shown in **Figure 3.28** and **Figure 3.31**, respectively.

Structural characterizations, including GIXRD, PXRD, Raman, and SEM measurements, were performed on these films. Additionally, elemental analysis and examination of the electronic structure were conducted on films deposited on n^+-Si(111) substrates by XPS and UPS. Meanwhile, Ta_3N_5 films synthesized under optimal conditions on a transparent quartz substrate were specifically used for optical

doi:10.6342/NTU202403464

measurements to extract the bandgap energy of Ta_3N_5, which helps construct a band diagram in **Chapter 4**.

3.5.1 Structural Characterization

The GIXRD measurements of Ta_3N_5 films that underwent reactive NH_3 annealing on n^+-Si(111) and quartz gave consistent results indicating the orthorhombic crystal structure of Ta_3N_5 (**Figure 3.28**). When comparing samples grown on different substrates, some diffraction peaks have different intensities, which is indicative of the preferred orientations of these films. Additionally, the consistent peak position compared to the calculated values of Ta_3N_5 with that of samples deposited on quartz substrate also confirmed the synthesis of Ta_3N_5 through reactive annealing under NH_3 atmosphere.

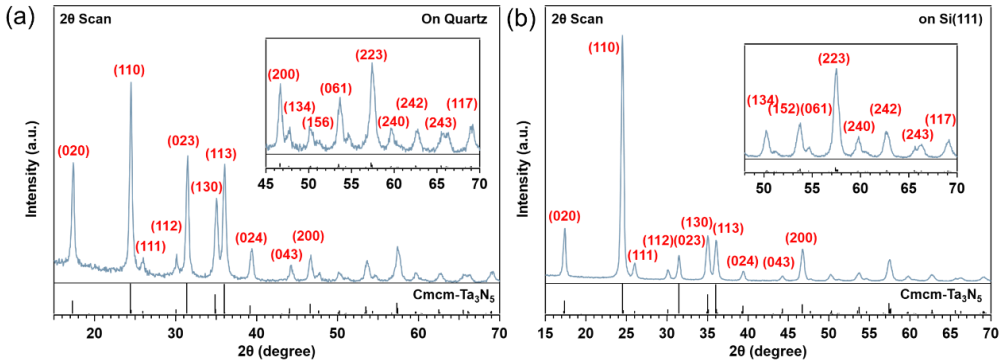

Figure 3.28 The GIXRD diffractograms measured from Ta_3N_5 thin films grown on (a) quartz and (b) n^+-Si(111) and annealed at 820°C for 3 hours. The reference of Cmcm-Ta_3N_5 was obtained from ICSD-colloid66533.

However, the PXRD result demonstrated that the bulk phase of the films still presented some low-valence Ta_5N_6 and Ta_2N phases for the diffraction peaks at $2\theta = 34.1°$ and 36.5°, respectively (**Figure 3.29**). Usually, when preparing Ta_3N_5 from an oxide precursor of Ta_2O_5, the presence of low-valence Ta-N species only happens when using a

doi:10.6342/NTU202403464

metallic substrate such as Ta or Nb.[103, 161, 162] The interdiffusion of nitrogen into the metallic substrate during the reactive annealing under an NH_3 atmosphere would cause the low-valence species to appear. The formation of low-valence Ta-N species is inevitable in these systems. Conversely, using substrates that do not facilitate nitrogen diffusion during annealing, such as quartz or sapphire, wouldn't yield these low-valence species in the final films.

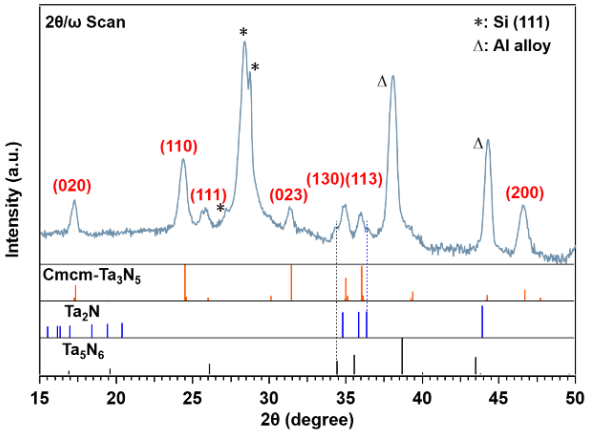

Figure 3.29 The PXRD diffractogram measured from Ta_3N_5 thin films annealed at 820°C on an n^+-Si(111) substrate. The reference of Cmcm-Ta_3N_5 and Ta_5N_6 were obtained from ICSD-colloid66533 and ICSD-colloid644720, respectively. The triangular sign was the diffraction peaks from the substrate holder, and the asterisk sign was the diffraction peals of Si.

In this thesis, we posit that the formation of low-valence Ta-N species is also an unavoidable outcome when utilizing nitride as a precursor film for the synthesis of Ta_3N_5 but not because of the interdiffusion of nitrogen with silicon substrate. The absence of Si_3N_4 in the PXRD measurement supports this claim, indicating that while nitrogen can diffuse into the silicon layer, the dense surface of silicon nitride does not facilitate further diffusion to form a thick layer of silicon nitride. Therefore, we conclude that the possible

doi:10.6342/NTU202403464

reason for the formation of low-valence Ta-N species lies in both the insufficient diffusion of surface nitrogen into the bulk of films and the breakdown of Ta_3N_5 in the bulk phase, which can be demonstrated by the evolution of impurity phase concentration with annealing duration shown in **Figure 3.21**.

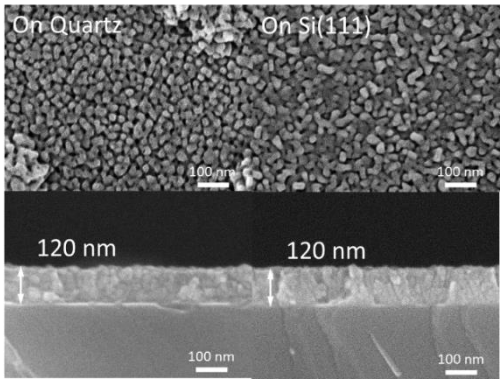

Figure 3.30 SEM measured from Ta_3N_5 films annealed at 820 °C on a quartz substrate (right) and an n^+-Si(111) substrate (left).

The observation of similar grain sizes but differing surface roughness between Ta_3N_5 films on n^+-Si(111) and quartz substrates, as depicted in the SEM images in **Figure 3.30**, is intriguing. Despite the rougher surface of the Ta_3N_5 film on the n^+-Si(111) substrate, both films exhibit a thickness of approximately 120 nm. While the roughness difference might lead to slight deviations in absorption characteristics for the Ta_3N_5 film on the quartz substrate compared to that on n^+-Si(111), the overall thickness consistency and phase purity provide confidence in using the quartz substrate for optical measurements aimed at determining the bandgap of Ta_3N_5.

The presence of peaks at 138, 167, 200, 230, 266, 400, 600, 661, and 744 cm^{-1} in the Raman spectrum of **Figure 3.31** aligns with the analysis of the Ta_3N_5 Raman peak discussed in **Section 3.6.2**, indicating that samples on both substrates consist of a pure

doi:10.6342/NTU202403464

phase of Ta_3N_5. This consistency reaffirms the purity and integrity of the synthesized Ta_3N_5 films.

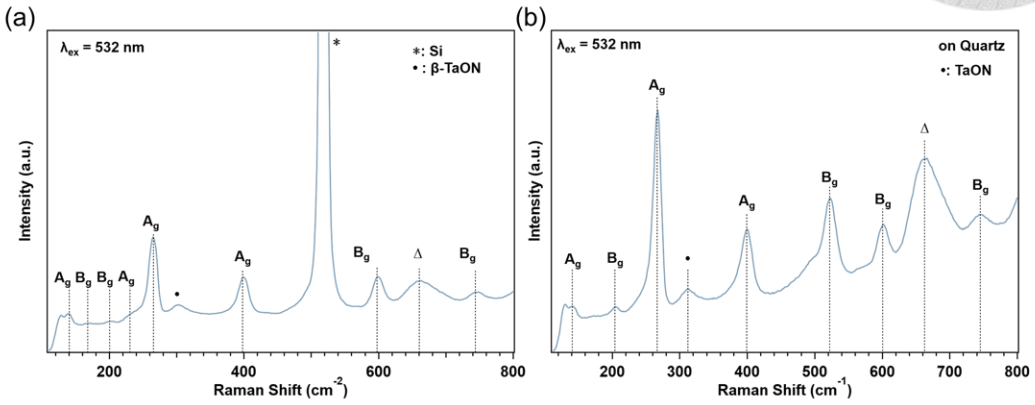

Figure 3.31 The Raman spectrum measured from Ta_3N_5 thin films annealed at 820 °C on (a) the n^+-Si(111) substrate and (b) a transparent quartz substrate. The asterisk sign is the Raman signal of the silicon substrate, the triangle sign represents the resonance Raman peak of Ta_3N_5, and the dot sign represents the TaON phase. The excitation wavelength is from a 532 nm laser.

However, the observation of a tantalum oxynitride phase, as evidenced by the Raman peak at 302 cm^{-1}, is particularly intriguing. This implies the coexistence of oxynitride species alongside Ta_3N_5 in the synthesized films, suggesting a more complex composition than initially anticipated. The absence of characteristic peaks for tantalum nitride in the GIXRD measurement, indicating its amorphous nature, further underscores the dominance of Ta_3N_5 in the film composition. Moreover, the presence of the oxynitride phase is also corroborated by the surface elemental analysis, adding further credence to its existence within the synthesized films. For a more in-depth analysis of the Raman spectrum of Ta_3N_5 refer to **Section 3.6.2** for detailed insights.

doi:10.6342/NTU202403464

3.5.2 XPS Measurements

As discussed in **Section 3.6.2** regarding the elemental composition of Ta_3N_5 films annealed at different temperatures, the surface composition of the sample annealed at 820°C yielded the highest Ta^{5+} oxidation state with slightly oxynitride phase of TaON appeared on the surface. The oxidation state of TaON was also Ta^{5+}. All binding energies were calibrated by referencing the C 1s signal to 284.8 eV. A detailed discussion of the spectrum for each element can refer to **Section 3.6.2** regarding the XPS analysis.

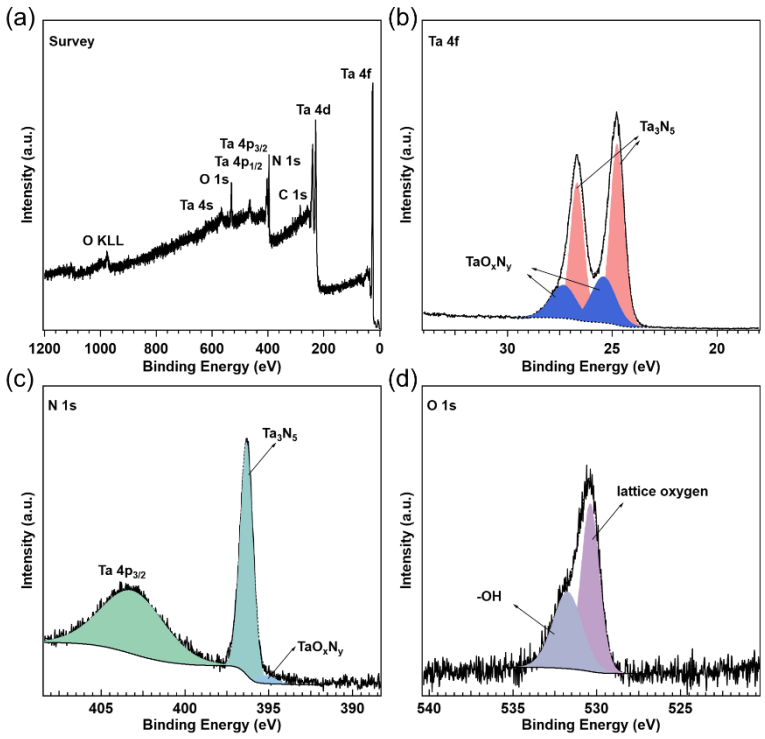

Figure 3.32 XPS (a) survey spectrum and (b)Ta 4f, (c) N 1s, and (d) O 1s core-levels measured from Ta_3N_5 thin films annealed at 820°C for 3 hours. The energy referencing of each spectrum was done by referencing the peak in the C 1s spectrum to 284.8 eV.

The survey spectrum provided an overview of all the elements present on the film surface (**Figure 3.32a**), revealing the composition on the surface is free of contamination from other elements used in the sputtering chamber.

doi:10.6342/NTU202403464

The Ta 4f core level spectrum in **Figure 3.32b** revealed two distinct peaks at 24.8 and 26.7 eV, respectively, which could be deconvoluted into two spin-orbit splitting doublets from Ta-N and Ta-O bonding. In **Figure 3.32b**, the peak at 24.80 eV corresponded to the Ta $4f_{7/2}$ state associated with Ta-N bonding, and the peak at 26.7 eV represented the Ta $4f_{5/2}$ state from Ta-N bonding. While, the peak at 25.4 eV corresponded to the Ta $4f_{7/2}$ state contributed by Ta-O bonding, and the peak at 27.3 eV indicated the Ta $4f_{5/2}$ state from Ta-O bonding.

Figure 3.32c exhibited two distinct peaks at 396.6 and 403.3 eV. Deconvolution of the peak at 396.6 eV yielded two peaks centered at 396.6 eV and 395 eV. The peak at 396.6 eV corresponded to nitrogen involved in Ta-N bonding; while the peak at around 395 eV was attributed to the Ta-N bonding in the oxynitride phase. The presence of oxynitride in the N1s spectrum has been observed in the TiN system which also had a peak appear at lower binding energy.[158, 163, 164] Another broad peak centered at 403.8 eV was attributed to the Ta $4p_{3/2}$ state and not related to nitrogen.

The O 1s spectrum in **Figure 3.32d** revealed an asymmetric peak at 530.4 eV, which could be deconvoluted into two peaks centered at 530.4 and 531.9 eV, respectively. The former peak was attributed to the oxygen incorporated into the lattice, corresponding to the Ta-O bonding observed in the Ta 4f core level spectrum. Another peak centered at 531.9 eV was attributed to adsorbed water on the film surface.

3.5.3 UPS Measurements

To establish the band alignment of Ta_3N_5 relative to the vacuum, UPS was employed to measure both the work function and the VBM position. By combining insights gleaned from the UPS spectrum with the bandgap energy determined through UV-Vis measurements, we could accurately determine the band edge positions of Ta_3N_5

doi:10.6342/NTU202403464

annealed at 820°C. To ensure the extraction of the valance band structure and the work function without mixing information, a sample bias of about 5 eV would be applied to shift the valance band density of states (DoS) to a higher value. Consequently, an energy referencing of the spectrum was performed by shifting the binding energy scale by a 5 eV increment to align the Fermi level position of the analyzer with that of the sample, referencing the binding energy at 0 eV.

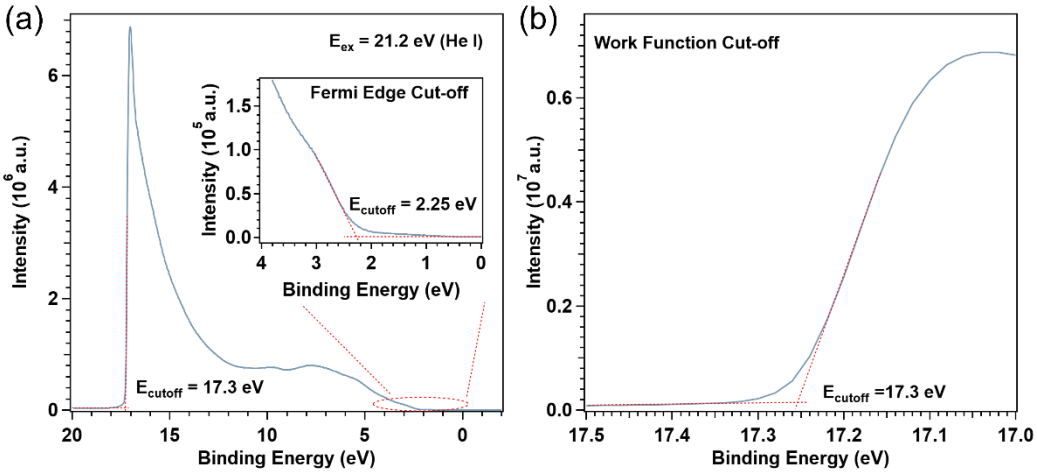

Figure 3.33 (a) UPS spectrum measured from Ta_3N_5 thin films annealed at 820°C for 3 hours with an incident photon energy of 21.2 eV. The inset was the fermi-edge cut-off. (b) The secondary electron scut-off spectrum derived from the high binding energy side of the UPS spectrum. The energy referencing of each spectrum was done by adding back the sample bias to align the fermi level position to 0 eV.

Firstly, the work function of Ta_3N_5 can be resolved by examining the cut-off energy of the secondary electrons at the higher binding energy side, as depicted in **Figure 3.33b**. Utilizing the equation (**2.53**), the work function of Ta_3N_5 was determined to be 3.9 eV below vacuum. Furthermore, the VBM position relative to the Fermi level was determined by assessing the cut-off energy at the lower binding energy side of the UPS spectrum. Since the Fermi level is aligned with the position of zero binding energy, the

doi:10.6342/NTU202403464

cut-off energy at the lower binding energy side indicates that the valence band position is 2.25 eV below the Fermi level.

3.5.4 Optical Properties

The absorption spectrum of Ta_3N_5, obtained after annealing at 820 °C in an NH_3 atmosphere, reveals intriguing insights into its optical behavior. The absorption spectrum was calibrated by both transmittance and reflectance. In **Figure 3.34a**, a peak centered at 540 nm was observed, separating the absorption of Ta_3N_5 into two distinct regions. These absorption features are attributed to the optical characteristics of Ta_3N_5, which exhibits a strong optical anisotropy depending on the polarization vector of incident light.[66, 165, 166] The peak centered at 540 nm is assigned to the absorption when the light is polarized along the a-axis. The absorption at a shorter wavelength than 540 nm is attributed to the absorption of a light polarization along the b- or c-axis of the crystal.[66]

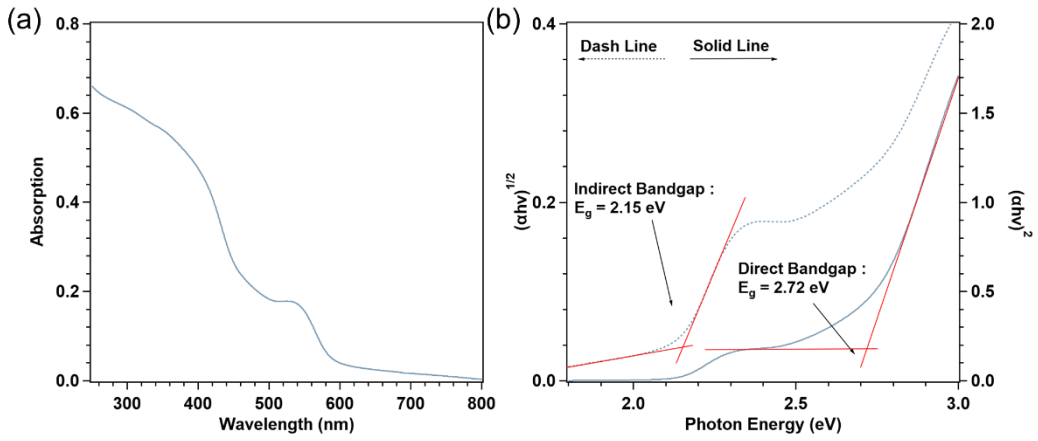

Figure 3.34 (a) Absorption spectrum measured from Ta_3N_5 film annealed at 820°C for 3 hours on quartz. (b) Tauc plots for direct and indirect transitions of Ta_3N_5 film annealed at 820°C for 3 hours.

doi:10.6342/NTU202403464

Traditionally, researchers have associated these absorption transitions with the direct transition of electrons from N 2p to Ta 5d orbitals, implying the presence of two direct optical transitions in Ta_3N_5. However, the observed low absorption region between the two absorption onsets challenges this interpretation, suggesting that the transition may not be direct.[66] This interpretation aligns with the findings of Eichorn *et al.*, who proposed that the first transition is likely indirect rather than direct.[159]

To further analyze the bandgap characteristics, Tauc analysis was performed based on the absorption spectrum (**Figure 3.34c**). This analysis revealed an indirect optical bandgap of 2.15 eV and a direct bandgap of 2.70 eV. These values are consistent with the observed absorption onsets, supporting the proposition that the bandgap of Ta_3N_5 involves an indirect optical transition.

doi:10.6342/NTU202403464

Chapter 4. Photoelectrochemical Performance of Ta_3N_5

This chapter focuses on the photoelectrochemical performance of Ta_3N_5 photoanodes prepared with different nitridation conditions on different conductive substrates. We will construct a comprehensive model for explaining the performance differences in conjunction with the results presented in **Chapter 3.6** and **Chapter 3.7**.

In general, the PEC performance can be deconvoluted into three factors: (1) carrier dynamics at the electrode-electrolyte interface, (2) bulk transport and recombination, and (3) heterojunction between the photoelectrode and the conductive substrate. Unless otherwise specified, a hole scavenger was used in all measurements in this thesis to prevent the rapid deterioration of Ta_3N_5 due to severe photo-corrosion.[88-90, 167] This ensured 100% injection of photogenerated holes into the electrolyte solution, allowing the influences of different annealing treatments on photoanodes to be accurately evaluated. All the electrochemical measurements in **Chapter 4.1** to **Chapter 4.3** were performed in an electrolyte consisting of 0.1 M $K_4[Fe(CN)_6]$ and 0.1 M KPi buffers. In **Chapter 4.1**, we address the importance of nitridation temperatures on the surface-to-sub-surface defect content, which significantly affects the obtained photocurrent densities. In **Chapter 4.2**, we explore how bulk conductivity can be modified by introducing various impurity contents through changes in nitridation duration. In **Chapter 4.3**, we discuss the impact of semiconductor heterojunctions by varying the doping concentrations and crystallographic orientations of commercially available silicon wafers. In **Chapter 4.4**, water oxidation was tested in an electrolyte consisting of 1M KOH with pH = 13.6 for Ta_3N_5 photoanodes with and without the presence of a co-catalyst.

doi:10.6342/NTU202403464

4.1 Effect of Annealing Temperatures

The PEC performance of Ta_3N_5 photoanodes was significantly affected by the annealing temperature. The current-voltage (J-V) curves in **Figure 4.1**. When using 780°C nitridation temperature and 3 hours duration, the resulting photocurrent density was 0.23 mA/cm^2 at 1.23 V vs. RHE, with a larger dark current density compared to other annealing temperatures. This is due to the incomplete transformation of Ta_3N_5, as indicated by the GIXRD results in **Figure 3.22a**. The larger dark current density is attributed to the metallic properties of Ta_2N_3, a degenerate semiconductor with better conductivity than the semiconducting Ta_3N_5 phase.[60]

When the annealing temperature was raised to 820°C, the Ta_3N_5 photoanode achieved the best photocurrent density of about 3.9 mA/cm^2 at 1.23 V vs. RHE. However, the photocurrent density decreased with further increases in annealing temperature, dropping to only 1.3 mA/cm^2 at 1.23 V vs. RHE when annealing at 940°C. **Table 4.1** summarizes the photocurrent densities of Ta_3N_5 photoanodes at the OER potential (1.23 V_{RHE}) for different annealing temperatures.

This phenomenon can be evaluated from several perspectives. First, the crystallinity of Ta_3N_5 photoanodes deteriorates with increasing annealing temperature, as indicated by the GIXRD and PXRD results in **Figure 3.22** and **Figure 3.23**. Second, top-view images in **Figure 3.24** show a lower active surface area for redox reactions with higher annealing temperatures. The most critical factor affecting the PEC performance of Ta_3N_5 photoanodes is the presence of low-valence Ta^{3+} defects. Ta^{3+} defects are known to act as deep traps in Ta_3N_5, serving as recombination centers for electrons and holes, leading to a loss of photocurrent density.[34] As discussed in **Chapter 3.6.2**, surface elemental analysis in **Figure 3.26** revealed a reductive bonding environment with increasing annealing temperature, indicated by a shift to lower Ta 4f binding energy. This

doi:10.6342/NTU202403464

correlates with the decreasing photocurrent density with increasing annealing temperature from 820°C.

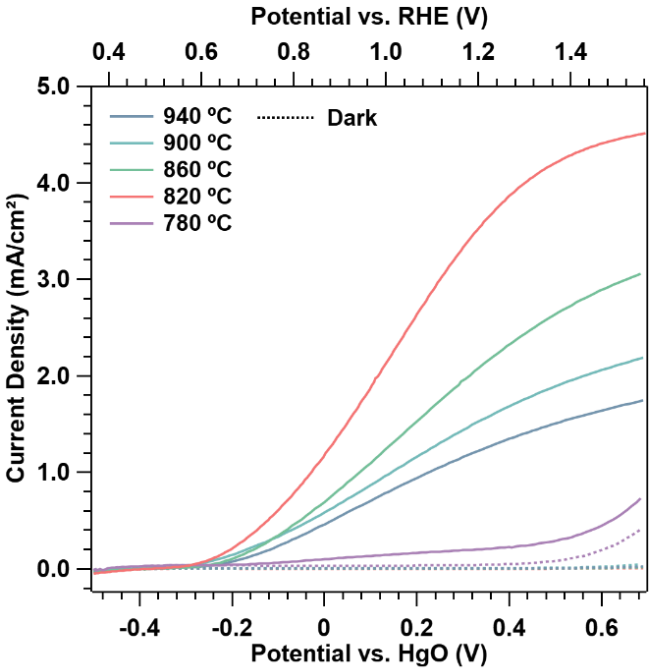

Figure 4.1 LSV plot measured from Ta_3N_5 photoanodes deposited on n^+-Si(111) using different annealing temperatures and 3-hour annealing duration.

Table 4.1 Photocurrent densities of Ta_3N_5 photoanodes annealed at different temperatures recorded at V = 1.23 V vs. RHE.

Temperature (°C)	780	820	860	900	940
J (mA/cm^2) @ 1.23 V_{RHE}	0.23	3.86	2.32	1.70	1.34

As a result, the influence of annealing temperature on the PEC performance is primarily due to its effect on the surface-to-sub-surface defect contents of Ta_3N_5 photoanodes. Increasing the annealing temperature introduces more Ta^{3+} defects in the surface composition of Ta_3N_5 photoanodes, which is highly detrimental to the PEC performance. Thus, annealing temperature can be used to tune the surface defect contents.

doi:10.6342/NTU202403464

Additionally, the crystallinity of the Ta_3N_5 photoanodes is also affected by the annealing temperature, contributing to differences in PEC performance, albeit to a lesser extent. The effects of annealing temperature on PEC performance are summarized in **Figure 4.2**.

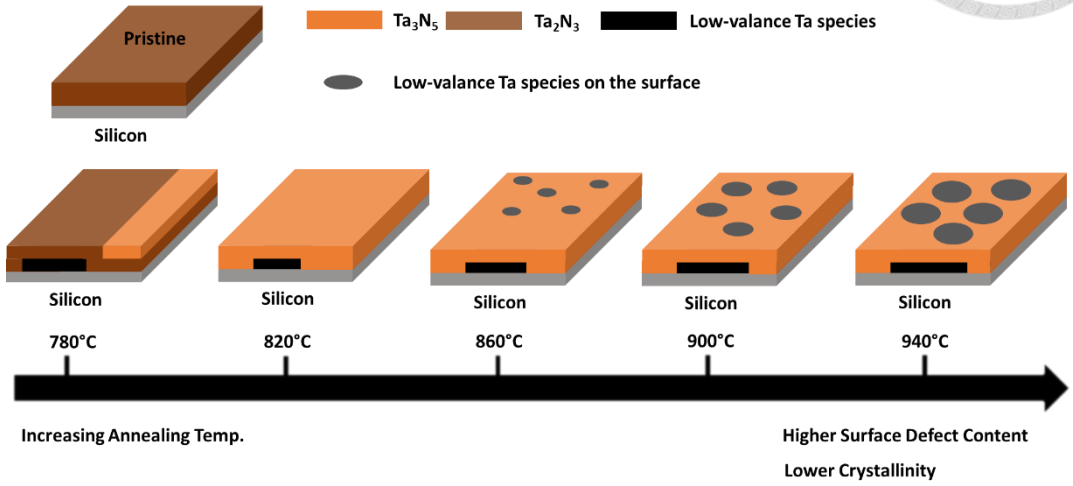

Figure 4.2 Summary of the contribution of annealing temperature to the PEC performance.

4.2 Effect of Annealing Dwell Time

The PEC performance of Ta_3N_5 photoanodes was also investigated under varying nitridation durations, all at the same 820°C annealing temperature, known for producing defect-free surfaces without observable Ta^{3+} on the Ta 4f XPS after 3 hours of annealing (**Figure 3.26**). The J-V curves are presented in **Figure 4.3** and the photocurrent densities of Ta_3N_5 photoanodes at the OER potential (1.23 V_{RHE}) for different annealing durations are summarized in **Table 4.2**.

When the dwell time was set to 1 hour, the photocurrent density was approximately 1.6 mA/cm² at 1.23 V vs. RHE. This relatively low photocurrent density

doi:10.6342/NTU202403464

was attributed to the presence of slight Ta_2N_3 impurities on the surface of Ta_3N_5 photoanodes, as exhibited in the surface-sensitive GIXRD in **Figure 3.20a**.

The presence of these recombination centers is also evident from the J-V curve never reaching a saturated level even at higher bias voltages. This indicates that not all photogenerated holes are utilized in the oxidation reactions at the electrode-electrolyte interface to produce a diffusion-limited current. However, compared to photoanodes annealed at 780°C for 3 hours, the sample annealed at 820°C for 1 hour still exhibited a higher photocurrent density. This improvement is due to the majority phase being the desired Ta_3N_5 phase when annealed at 820°C for 1 hour, despite the presence of some Ta_2N_3 impurities. In contrast, at 780°C for 3 hours, the photo-inactive Ta_2N_3 phase remains predominant, resulting in a lower photocurrent.

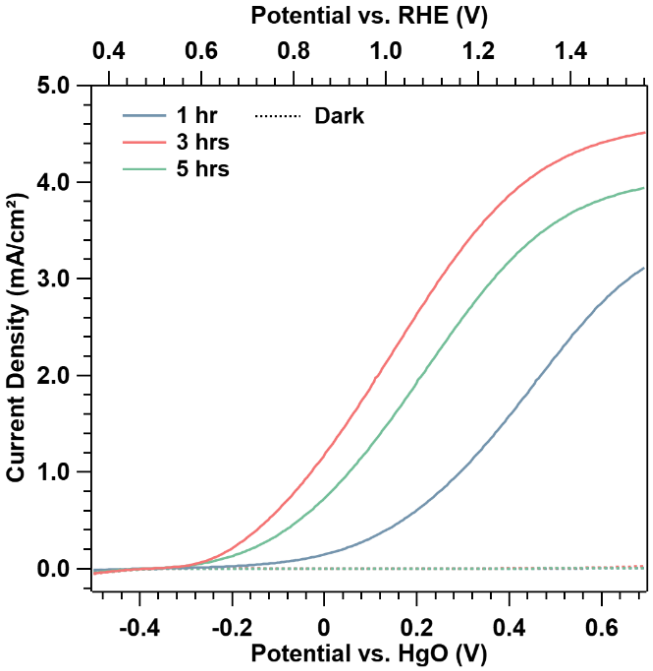

Figure 4.3 LSV plot measured from Ta_3N_5 photoanodes deposited on n^+-Si(111) with different annealing durations.

doi:10.6342/NTU202403464

Table 4.2 PEC performance of Ta_3N_5 photoanodes annealed with different durations recorded at V = 1.23 V vs. RHE.

Dwell Time (hour)	1	3	5
J (mA/cm^2) @ 1.23 V_{RHE}	0.23	3.86	2.32

As discussed in **Chapter 3.6.1**, the crystallinity of Ta_3N_5 improved, and the impurity content, particularly the low-valence Ta_2N phases, decreased with increasing annealing duration from 1 to 5 hours, as indicated by both the GIXRD and PXRD results in **Figure 3.20**. Typically, better crystallinity and lower impurity content are expected to enhance PEC performance. However, contrary to this expectation, the PEC performance worsened as the annealing duration increased from 3 to 5 hours, despite the improved crystallinity and reduced impurity content shown by both GIXRD and PXRD results in **Figure 3.20** and **Figure 3.21**.

This contradiction was attributed to the presence of low-valence Ta-N species in the bulk composition of Ta_3N_5 photoanodes. These low-valence Ta-N species possess intrinsic metallic properties that can enhance n-type conductivity in the photoanode system. These metallic defects facilitate the rapid extraction of photogenerated electrons, which in turn allows photogenerated holes to survive longer during operation. Given that the hole diffusion length in Ta_3N_5 is around 50 nm, the mean free path of the photogenerated hole is short, making it more likely to recombine within a given time.[168] Therefore, the rapid removal of photogenerated electrons can effectively extend the lifetime of photogenerated holes.

To provide more convincing evidence, we plan to perform XPS measurements to analyze the surface and bulk composition of Ta_3N_5 photoanodes with various annealing dwell times. We have scheduled XPS measurements using both Al and Cr sources to

doi:10.6342/NTU202403464

deconvolute the contributions of the surface and bulk composition, taking advantage of the different penetration depths of X-rays with varying energy. It is advisable not to use sputtering depth profiling with soft X-rays, as the preferential sputtering of nitrogen by incoming sputtering ions could produce artifacts of low-valence metal species in the sampling depth of the soft X-ray region. Instead, a hard X-ray source would be a better choice when combined with sputtering for depth profiling, due to its longer penetration depth relative to the damage caused by sputtering.

According to the discussion in previous chapters, we propose a possible explanation for the enhanced performance of our Ta_3N_5 photoanodes. During annealing under ammonia flow, the conversion of Ta_2N_3 to the desired Ta_3N_5 phase begins at the surface. As a result, the surface layer always becomes a perfect layer of Ta_3N_5 once the annealing time is sufficient. However, the bulk conversion of thin films depends on the diffusion of nitrogen from the surface to the bulk composition. With increased annealing time, more thermal energy is available for nitrogen diffusion into the bulk, facilitating the formation of Ta_3N_5 photoanodes with better crystallinity and lower bulk defect content.

Given the moderate diffusion length and lifetime of photogenerated holes, Ta_3N_5 with good crystallinity struggles to extract electrons and allow the photogenerated holes to survive to the surface for heterogeneous redox reactions. In comparison, most research articles fabricated a thick Ta_3N_5 layers layer of about 500 nm or above produced by a Ta_2O_5 as a precursor, which would also show enhanced n-type conductivity due to increasing oxygen defects in the bulk composition, which contributed to the n-type conductivity needed for photogenerated electron extraction.

For our system, the improved performance of Ta_3N_5 photoanodes is primarily due to the presence of low-valence Ta-N species in the bulk composition, originating from the decomposition of Ta_2N_3 and Ta_3N_5 during nitridation, rather than in the surface

doi:10.6342/NTU202403464

composition of the photoanodes. These low-valence Ta-N species, with their intrinsic metallic properties, can rapidly extract photogenerated holes. Consequently, as crystallinity improves and defect content decreases, photogenerated holes have a higher probability of recombining with photogenerated electrons. The effects of annealing dwell times on PEC performance are summarized in **Figure 4.4**.

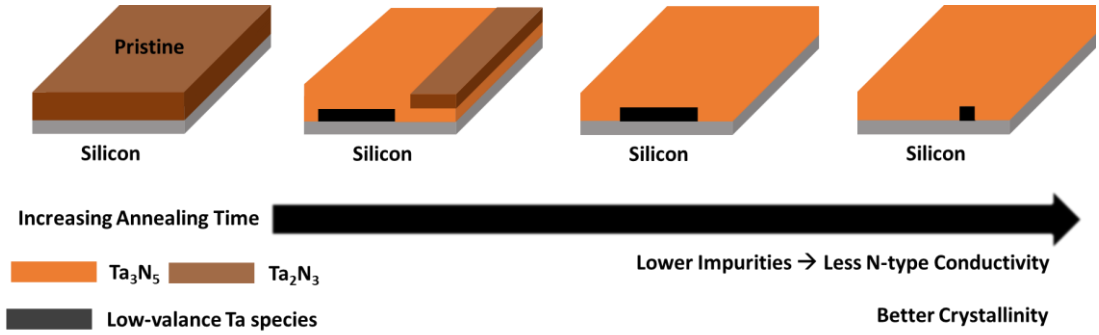

Figure 4.4 Proposed mechanism for the enhanced performance of Ta_3N_5 photoanode.

4.3 Effect of Different Conductive Silicon Substrates

From the discussion in the previous section, we have explored how surface and sub-surface recombination affect PEC performance through defect control managed by ammonia annealing temperature and how bulk transport is influenced by annealing duration, which alters bulk crystallinity and impurity content significantly. Another critical factor impacting PEC performance is the heterojunction between the semiconductor and conductive substrate. The difference in Fermi levels between the two materials causes varying degrees of band bending, affecting the ease with which carriers travel across the junction.

To elucidate the impacts of the heterojunction between Ta_3N_5 and silicon, we used silicon wafers with different out-of-plane orientations and doping concentrations. Different out-of-plane orientations result in different band edge positions, and varying

doi:10.6342/NTU202403464

doping concentrations shift the Fermi level positions. Combined, these factors significantly alter the final heterojunction band bending.

4.3.1 Linear Sweep Voltammetry

The PEC performance was first characterized by linear sweep voltammetry measurements, as indicated by the J-V curve in **Figure 4.5a**. The photocurrent densities at the OER potential (1.23 V_{RHE}) and the onset potential of Ta_3N_5 photoanodes for different substrates are summarized in **Table 4.3**. Herein, we define the onset potential to the point where the cathodic current changes to an anodic current.

The Ta_3N_5 photoanode deposited on n^+-Si(111) achieved the highest photocurrent density of about 3.86 mA/cm^2 at V = 1.23 V vs. RHE and the lowest onset potential of about 0.48 V_{RHE}. In contrast, the Ta_3N_5 photoanode deposited on n-Si(100) got the lowest photocurrent density of about 1.36 mA/cm^2 at V = 1.23 V vs. RHE and the largest onset potential of about 0.72 V_{RHE}. This significant difference is influenced not only by the doping concentration of the silicon substrate but primarily by the heterojunction between the silicon substrate and Ta_3N_5.

Table 4.3 PEC performance of Ta_3N_5 photoanodes deposited on different silicon wafers recorded at V = 1.23 V vs. RHE.

substrate	n-Si(100)	n^+-Si(111)	n^+-Si(100)
J (mA/cm^2) @ 1.23 V_{RHE}	1.36	3.86	2.74
Onset potential (vs. V_{RHE})	0.72	0.48	0.52

doi:10.6342/NTU202403464

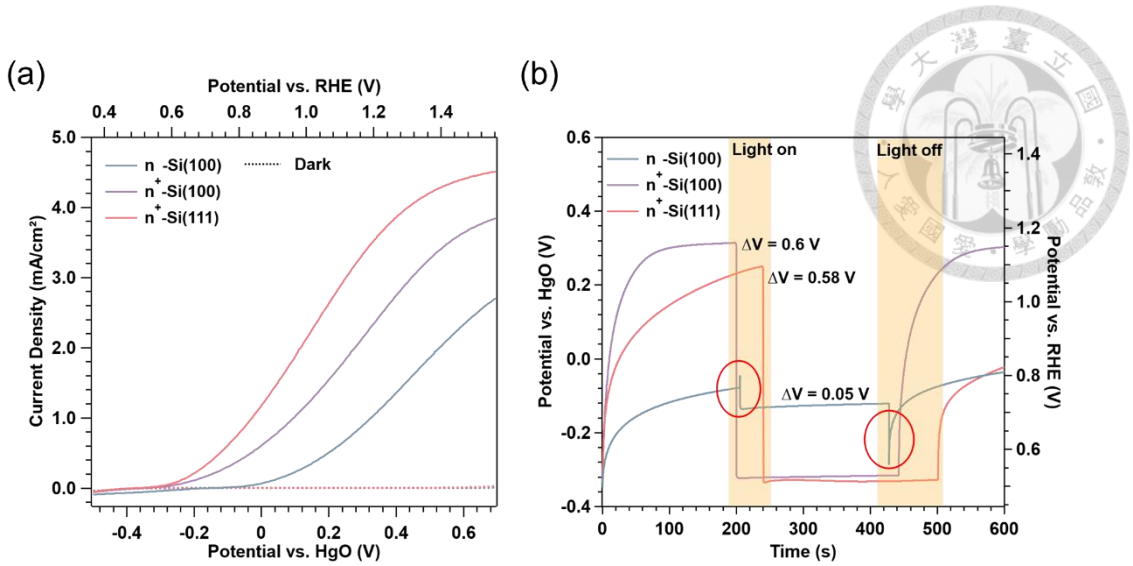

Figure 4.5 (a)LSV plot (b) OCP plot measured from Ta_3N_5 photoanodes deposited on silicon wafers with different orientations and doping concentrations. All Ta_3N_5 photoanodes were annealed at 820°C for 3 hours.

The importance of the heterojunction can also be confirmed by the open-circuit potential (OCP) measurement with or without illumination. The OCP measurements in **Figure 4.5b** for the Ta_3N_5 photoanode deposited on n-Si(100) exhibited protuberance when light is turned on and off. This is a typical phenomenon indicating charge accumulation at the interface between any heterojunction.[169] We rule out the possibility that this protuberance comes from the semiconductor-electrolyte junction for two reasons. First, the Ta_3N_5 photoanodes were characterized to be defect-free at the surface composition by XPS, so there shouldn't be any recombination defects serving as active sites for carrier accumulation. Second, OCP measurements on Ta_3N_5 photoanodes deposited on heavily doped silicon wafers with two different out-of-plane orientations showed no protuberance, confirming that charge accumulation occurred at the heterojunction between the semiconductor and silicon substrate rather than at the semiconductor-electrolyte junction.

doi:10.6342/NTU202403464

4.3.2 Proposed Band Alignment

A band diagram was constructed to understand the heterojunction behavior between Ta_3N_5 photoanodes and silicon wafers. The UPS measurement of Ta_3N_5, discussed in **Chapter 3.7.3** and **Chapter 3.7.4**, provided the necessary data for the Ta_3N_5 band structure. However, conducting UPS measurements for silicon substrates presents challenges due to the native oxide layer that forms on the silicon wafer surface.[170] Typically, sputter cleaning is required to remove this native oxide, but this process creates dangling bonds on the silicon surface, leading to Fermi-level pinning in the energetic structure of silicon.[171, 172] This pinning interferes with accurately determining the real band edge positions and Fermi level in UPS measurements. To resolve this issue, annealing in the UPS chamber would be necessary to heal the defect states and accurately capture the real band positions of the silicon wafer.[172] This experiment was not feasible in our case. Instead, we utilized experimental data for intrinsic silicon with different orientations obtained from research articles. By combining this data with calculations of the Fermi level position based on doping concentration, we determined the band positions for n^+-Si(111), n^+-Si(100), and n-Si(100).[170-173] The detailed calculations can be referred to the textbook of semiconductor physics. The energetic structures of the different silicon wafers and Ta_3N_5 are summarized in **Figure 4.6**.

The band alignment diagram is shown in **Figure 4.7**. For Ta_3N_5 deposited on an n-Si(100) substrate, both n-Si(100) and Ta_3N_5 are semiconducting, resulting in the formation of an n-n heterojunction at the interface.[174] On the n-Si(100) side, there is downward band bending, while on the Ta_3N_5 side, there is upward band bending. Consequently, under light illumination, photogenerated carriers form on both sides: photogenerated electrons accumulate on the n-Si(100) side, and photogenerated holes accumulate on the Ta_3N_5 side due to the opposite band bending across the heterojunction.

doi:10.6342/NTU202403464

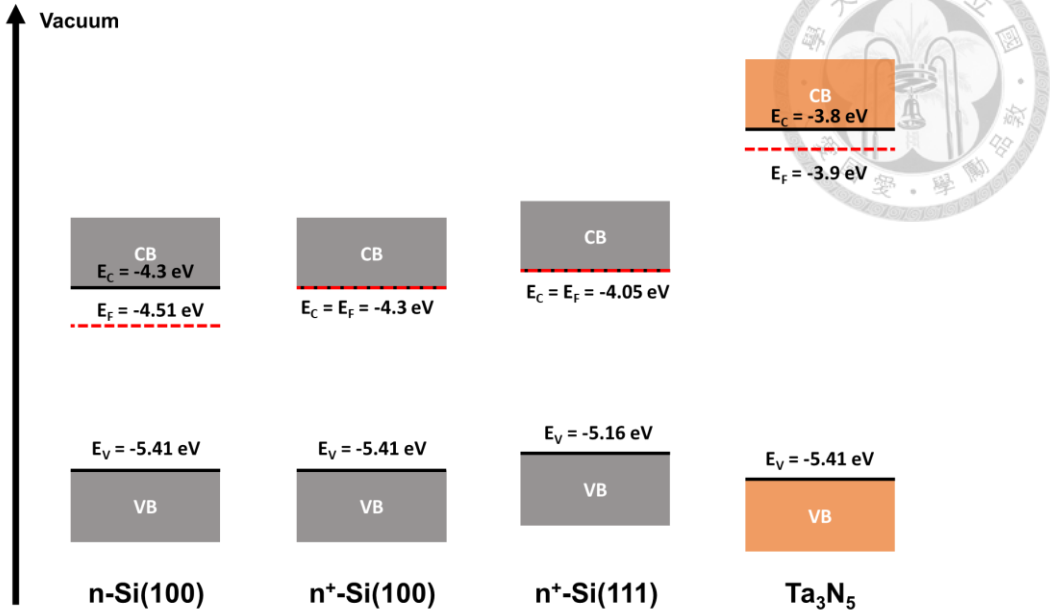

Figure 4.6 Energetic structure of silicon wafer with different out-of-plane orientation and doping concentration, and Ta_3N_5 against vacuum level.

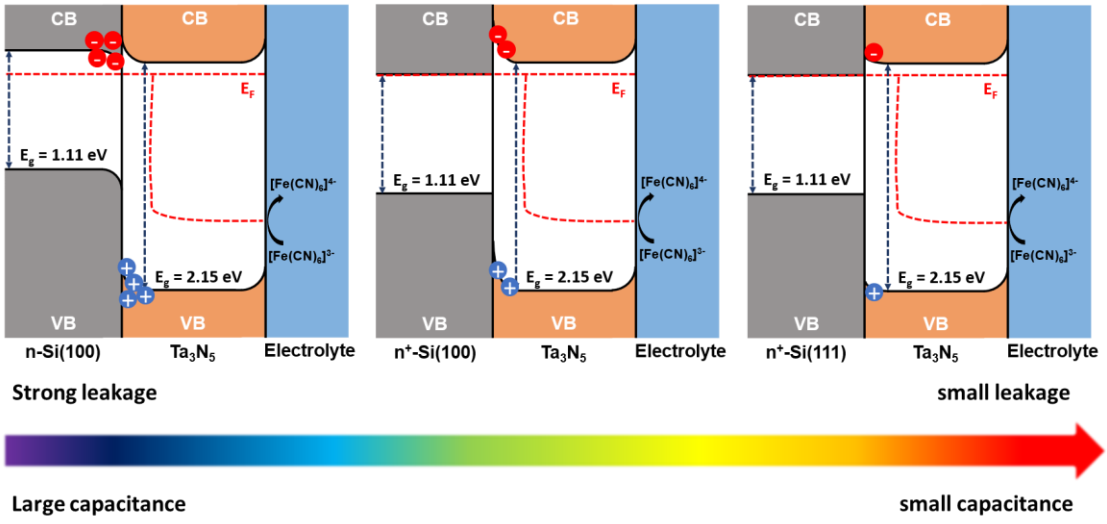

Figure 4.7 Proposed mechanism for the main PEC performance across the heterojunction between Ta_3N_5 and Silicon substrate.

doi:10.6342/NTU202403464

For Ta_3N_5 deposited on heavily doped silicon wafers, the situation is different. Heavily doped silicon wafers can be considered metallic, thus forming a Schottky junction with Ta_3N_5. The performance differences are mainly attributed to the built-in potential difference caused by the band edge position differences of Si(111) and Si(100) substrates. For Ta_3N_5 deposited on n^+-Si(111), the smaller built-in potential difference results in a smaller heterojunction barrier compared to Ta_3N_5 deposited on n^+-Si(100). As a result, under light illumination, photogenerated electrons can more easily be injected into the conductive substrate, leading to fewer charges accumulating at this one-sided junction.

4.3.3 Impedance Analysis for Heterojunction Characterization

To evaluate the contribution of the heterojunction between Ta_3N_5 and silicon substrates with different orientations and doping concentrations, photoelectrochemical impedance spectroscopy (PEIS) was conducted. **Figure 4.8** shows the Nyquist plot of Ta_3N_5 photoanodes deposited on various types of silicon substrates with different applied potentials. Typically, two semi-circles were observed in each Nyquist plot, representing at least two different time constants that can be extracted from these impedance data. The smaller semi-circle, often emphasized in the inset of each plot, corresponds to the high-frequency response in the impedance analysis. We assigned this response to the convolution of the trapping-de-trapping process of carriers in the bulk and the behavior at the heterojunction between Ta_3N_5 and the silicon substrate. On the other hand, the larger semi-circle, which did not form a complete semi-circle at cathodic potentials, formed a complete semi-circle at applied anodic potentials in response to the semiconductor-electrolyte junction.

doi:10.6342/NTU202403464

The advantage of using the Nyquist plot for impedance analysis lies in the ease of predicting the equivalent circuit based on the number of semi-circles presented in each plot. However, it is not straightforward to directly extract detailed information from the Nyquist plot itself. Therefore, fitting the data from impedance analysis is preferred. The equivalent circuit used in **Figure 4.9** was adapted from the equivalent circuit proposed by Bisquert *et al*. and is widely used in research articles on Ta_3N_5 photoanode systems.[70, 129, 175] Additional modifications were made to include heterojunction terms to address the Schottky barrier expected between the semiconductor and the silicon substrate, as well as the interface between the two different materials.

The electrical elements are defined as follows. R_s represents the series resistance, R_{rec} denotes the recombination resistance across the bulk film, CPE_{ss} stands for the capacitance and constant phase element of the surface state, R_{ct} refers to the charge transfer resistance from the semiconductor to the electrolyte, R_{ht} indicates the heterojunction resistance, and CPE_{ht} represents the capacitance and constant phase element of the heterojunction.

doi:10.6342/NTU202403464

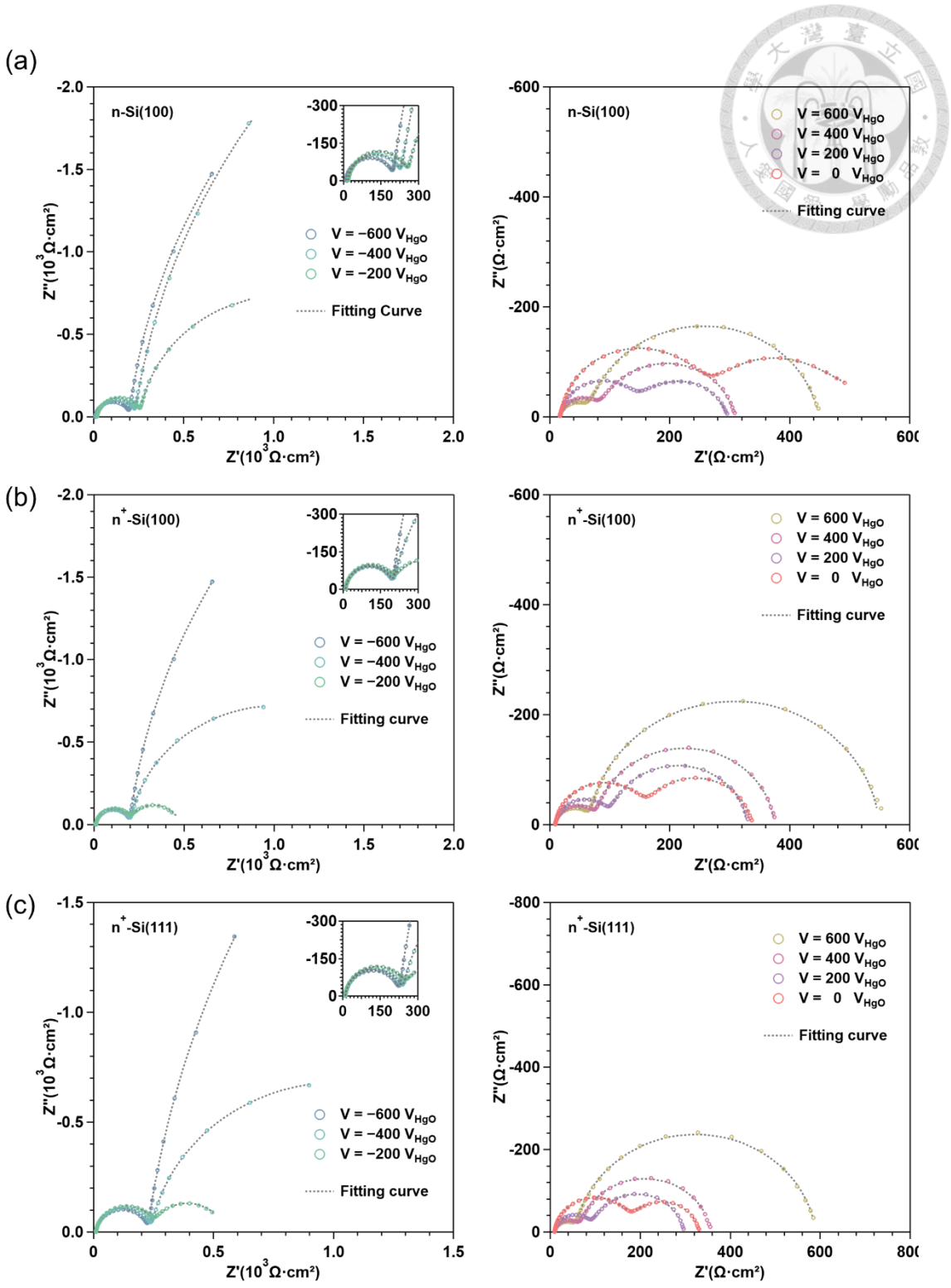

Figure 4.8 PEIS Nyquist plots measured from Ta_3N_5 photoanodes deposited on (a) n-Si(100), (b)n^+-Si(100), and n^+-Si(111). The inset in each figure represented the first semi-circle.

doi:10.6342/NTU202403464

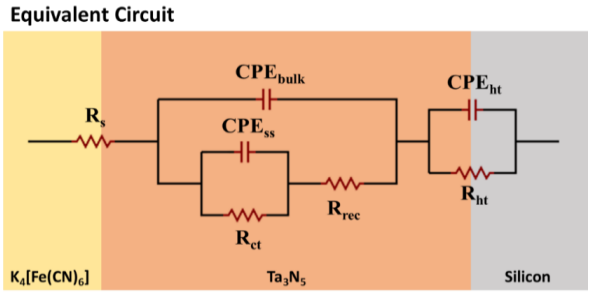

Figure 4.9 The equivalent circuit for the fitting of the PEIS result.

Figure 4.10 summarizes the fitting results for each component in the equivalent circuit at different applied potentials. The series resistance remained relatively stable across the range of applied potentials (**Figure 4.10a**). The differences in series resistance were primarily due to the conductivity variations of the silicon substrates, which were influenced by their doping concentrations. The normally-doped silicon wafers, being less conductive due to lower carrier concentrations even after illumination, exhibited higher series resistance compared to heavily doped silicon wafers. Despite these differences, the similar values of series resistance across various substrates suggest that conductivity differences are not the primary cause of variations in the PEC performance of the Ta_3N_5 photoanodes.

In **Figure 4.10b**, the charge transfer resistance, indicated by solid lines, decreased with increasing potential anodically, reaching its lowest values near the onset potential observed in the J-V curves for Ta_3N_5 photoanodes deposited on different silicon wafers. This decrease occurred because the applied anodic potential facilitated the activation of heterogeneous redox reactions at the semiconductor-electrolyte interface, thus lowering the charge transfer resistance. At even higher anodic potentials, charge transfer resistance started to increase slightly due to the depletion of reactants in the electrolyte, making charge transfer more challenging. Despite this, the similarity in the value of charge transfer resistance across different substrates after the activation of redox reactions

doi:10.6342/NTU202403464

indicates that the charge transfer process, related to surface composition, is not the main factor for the observed performance differences.

On the other hand, the recombination resistance, represented by dashed lines in **Figure 4.10b**, shows variations that are slightly different across the substrates. This recombination is related to the low-valance Ta-N defect presented in the bulk composition of the Ta_3N_5 photoanode system. Each fitting shows recombination resistance increasing and peaking near the onset potential, which was close to the flat band potential of the photoanodes. At the flat band potential, the applied potential flattens the band, reducing the driving force for photogenerated carrier separation and resulting in severe trapping-de-trapping by bulk defects, which causes peak formation at the fitting results. Beyond this point, with increased anodic potential, recombination by bulk defects decreases because more photogenerated carriers are extracted either to the outer circuit or to the surface for redox reactions. While recombination in the bulk phase affects performance, its impact is relatively minor compared to other factors.

The difference between the flat band potential and the onset potential might be a bit difficult to differentiate here for the following reasons. First, the definition of onset potential is relatively ambiguous. Using the traditional electrochemical system definition, which sets the onset potential at the current density of 10 mA/cm^2, results in extremely high values for all photoelectrochemical systems. Therefore, it would be more appropriate to define the onset potential as the potential at which the current density changes from cathodic to anodic. However, this often roughly overlaps with the flat band potential. Second, resolving the flat band potential is challenging due to the difficulties in conducting Mott-Schottky analysis in this system and because the potential steps in these PEIS measurements are relatively large. These larger steps are used to shorten the

doi:10.6342/NTU202403464

operation time to avoid deterioration from long-term measurements, which could cause artifacts in the data analysis.

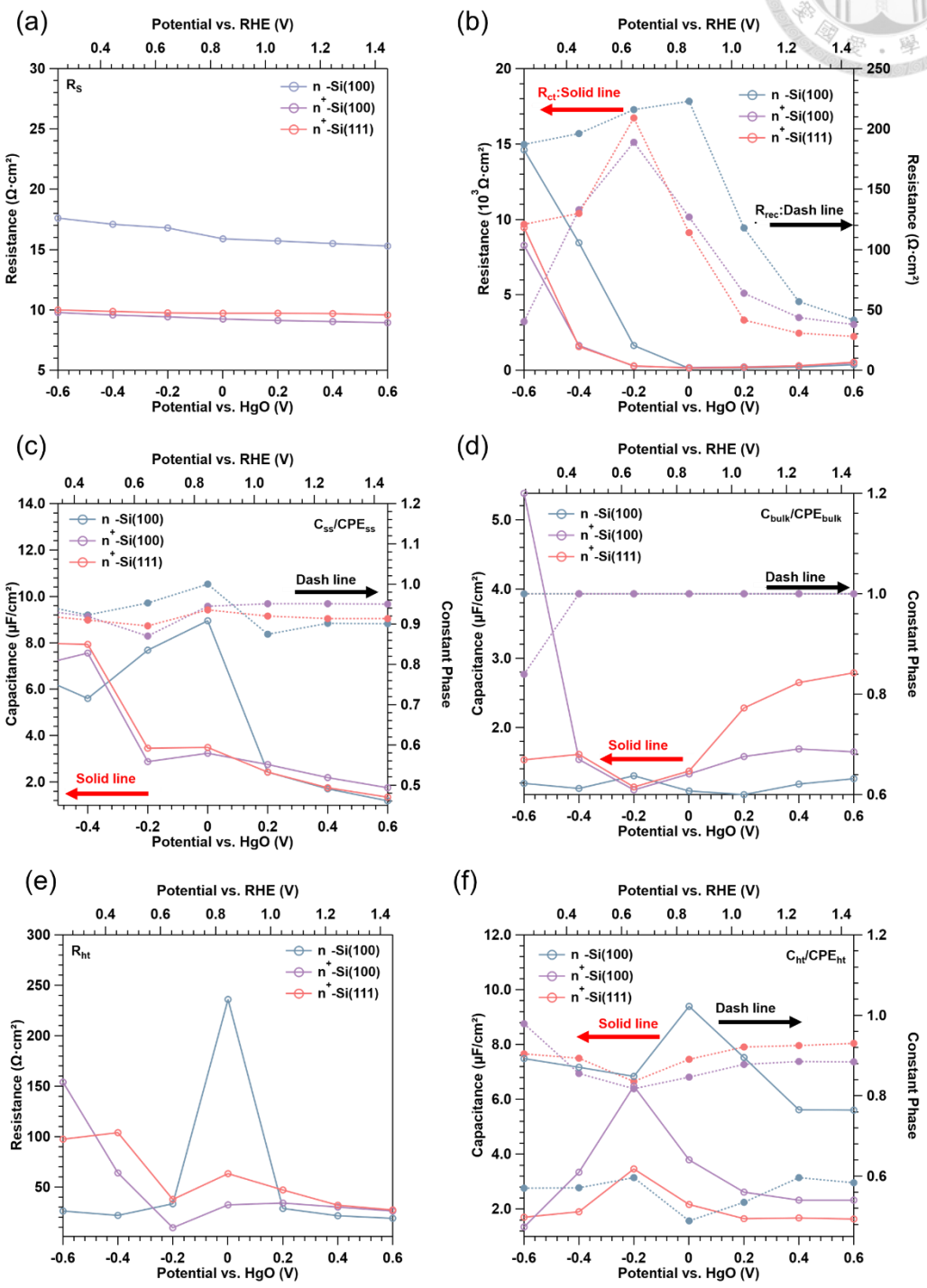

Figure 4.10 The PEIS fitting result for Ta_3N_5 photoanodes deposited on silicon wafers with different orientations and doping concentrations at different applied potential: (a) R_s (b) R_{ct} and R_{rec} (c) CPS_{ss} (d) CPE_{bulk} (e) R_{ht} (f) CPE_{ht}.

doi:10.6342/NTU202403464

In **Figure 4.10c**, the surface state capacitance and its constant phase were examined. The surface state represents the additional active sites on the surface that facilitated charge recombination or transfer to the electrolyte. In the case of Ta_3N_5 photoanodes, the surface state is shown to cause only photogenerated charge recombination, with no charge transfer occurring at the surface state.[176] As a result, the surface state capacitance, indicated by the solid line, decreased as the applied potential shifted anodically. Higher capacitance was observed when a cathodic potential was applied because the surface of Ta_3N_s was unsuitable for reduction reactions. Thus, photogenerated electrons accumulate at the semiconductor-electrolyte interface, resulting in a large constant phase element, as indicated by the dashed line, fitting well with Ta_3N_5 photoanodes deposited on heavily doped silicon wafers.

In **Figure 4.10d**, the bulk capacitance represents the depleted charges, typically ionized donors in the depletion region of the semiconductor-electrolyte junction for n-type semiconductors. For Ta_3N_5 photoanodes deposited on heavily doped silicon wafers, the bulk capacitance should first decrease before the flat band potential and then gradually increase past the flat band potential. When a large cathodic potential was applied, the majority of carriers accumulated at the semiconductor-electrolyte interface, increasing the concentration of ionized donors with negative charges and resulting in a high bulk capacitance. As the applied potential shifted anodically, the concentration of ionized donors diminished, leading to a smaller bulk capacitance. After crossing the flat band potential, the application of anodic potential inverted the carriers, causing the depletion of ionized donors with positive charges and thus increasing the bulk capacitance. Interestingly, the larger bulk capacitance observed for Ta_3N_5 deposited on n^+-Si(111) compared to n^+-Si(100) was due to the higher photocurrent density, which depleted more ionized donors with positive charges, thereby increasing capacitance.

doi:10.6342/NTU202403464

In **Figure 4.10e**, the heterojunction resistance initially decreased with increasing potential anodically from −0.6 V_{HgO} until it reached the flat band potential, then gradually increased with further application of anodic potential for Ta_3N_5 photoanodes deposited on heavily doped silicon wafers. Before reaching the flat band potential, the band bending on the Ta_3N_5 side was downward, making it energetically unfavorable for electrons to pass to the Ta_3N_5 side, resulting in higher heterojunction resistance. After over the flat band potential, the band bending on the Ta_3N_5 side became upward, which was also unfavorable for electron extraction from Ta_3N_5 to the silicon side. However, the applied anodic potential facilitated the rapid extraction of photogenerated electrons through band tilting caused by the electric field, so the resistance remains lower than on the cathodic side. Nonetheless, since the photogenerated electrons can only tunnel to the silicon side, the extraction remained limited.

For Ta_3N_5 photoanodes deposited on n-Si(100) substrates, the behavior differed due to the formation of an n-n heterojunction. The band bending on the silicon side was downward, while on the Ta_3N_5 side, it was upward. Consequently, when a large cathodic potential was applied, the downward band bending on the silicon side facilitated the tunneling of photogenerated electrons from the silicon to the Ta_3N_5 side, resulting in smaller heterojunction resistance. As the cathodic potential decreased and reached the flat band potential, tunneling was no longer possible, leading to the highest resistance across the junction. Once anodic potential is applied, the band bending on the silicon side facilitates the transport of photogenerated electrons from Ta_3N_5 to silicon, causing the heterojunction resistance to decrease. However, after the heterogeneous redox reaction was activated, the heterojunction resistance remained similar across different samples, suggesting that the heterojunction resistance is not the primary cause of the observed performance differences.

doi:10.6342/NTU202403464

In **Figure 4.10f**, the heterojunction capacitance and its constant phase show the most significant differences for Ta_3N_5 photoanodes deposited on different silicon wafers across the applied potentials. The heterojunction capacitance gradually increased with increasing potential anodically until it reached its maximum at the flat band potential. Then, it decreased with further increasing potential anodically, as the photogenerated electrons were successfully extracted to the silicon side and the photogenerated holes were used for redox reactions on the electrode surface, leading to fewer charges accumulating at the heterojunction interface.

The main differences between using different silicon wafers arise from the built-in potential differences between Ta_3N_5 and the silicon substrates, causing varying band bending on the Ta_3N_5 side and resulting in different accumulated charge densities. The formation of an n-n heterojunction between semiconducting silicon and Ta_3N_5 created opposite band bending across the junction, causing all photogenerated charges to accumulate at the interface, resulting in the largest heterojunction capacitance for all applied potentials.

The heterojunction constant phase also shows significant differences. The constant phase can be used to evaluate the degree of leakage current across the capacitance, denoted as the deviation from ideal capacitance. A constant phase closer to one indicates more ideal capacitive behavior with less leakage current, while a smaller constant phase suggests significant leakage current and substantial recombination across the junction. The small constant phase observed for the Ta_3N_5 photoanode deposited on n-Si(100) indicates severe recombination due to the n-n heterojunction formation. For Ta_3N_5 photoanodes deposited on heavily doped silicon wafers, a larger constant phase was observed compared to Ta_3N_5 deposited on n-Si(100) substrates due to the formation of the Schottky junction instead of a n-n heterojunction. As a result, under light

doi:10.6342/NTU202403464

illumination, photogenerated electrons can more easily be injected into the conductive substrate, leading to fewer charges accumulating at this one-sided junction and thus reducing leakage current. More photogenerated holes can then travel to the surface for heterogeneous redox reactions. Ta_3N_5 photoanode deposited on n^+-Si(111), therefore, exhibited the best performance among the three different silicon substrates due to its smaller built-in potential difference compared to Ta_3N_5 photoanode deposited on n^+-Si(100). Consequently, the heterojunction capacitance and leakage current are determined to be the main factors contributing to the performance differences.

The constructed band alignments in **Chapter 4.3.2** confirmed the fitting results for heterojunction behavior. It showed that heterojunction leakage current, due to intrinsic upward band bending on the Ta_3N_5 side, was the primary cause of performance differences when using different silicon substrates.

4.4 Incorporation of NiFeOx for Photoelectrochemical Water Splitting

Almost all research articles to date that use Ta_3N_5 photoanodes for water-splitting reactions incorporated a layer of electrocatalyst to further improve their photocurrent density and stability during long-term operation. One can refer to **Table 1.2** for more detailed information. Several studies have reported that the surface of Ta_3N_5 is not stable for the OER due to severe photo-corrosion on the surface of Ta_3N_5 photoanodes.[88-91, 167] OER involves the transfer of four electrons on the surface of Ta_3N_5, which can lead to severe photo-corrosion and subsequently oxidize the surface back to amorphous TaO_x.[88-91] This phenomenon suggests that the surface of Ta_3N_5 lacks true active sites for OER.[69] As a result, incorporating a co-catalyst can not only protect the surface of Ta_3N_5 but also

doi:10.6342/NTU202403464

provide active sites for heterogeneous reactions. In this study, a $NiFeO_x$ layer was spin-coated onto Ta_3N_5 through a metal-organic precursor sol as an electro-cocatalyst, and several parameters were examined to optimize the performance of Ta_3N_5 under OER conditions.

4.4.1 Spin-Coating Procedure

The Ta_3N_5 photoanodes used for co-catalyst deposition were directly treated with spin-coating procedures after nitridation to ensure the best surface composition of Ta_3N_5 and higher coverage of the coated co-catalyst. First, the Ta_3N_5 photoanodes were cleaned with an N_2 nozzle to remove adhesion contaminants. For the co-catalyst solution, 0.4653 g (1.6 mmol) of nickel (II) nitrate hexahydrate (CAS: 13478-00-7, >99.9%, Sigma-Aldrich) and 0.097 g (0.24 mmol) of iron (III) nitrate nonahydrate (CAS: 13478-00-7, >99.95%, Sigma-Aldrich) were dissolved in 8.0 mL of 2-methoxyethanol (CAS:190-86-4, 98%, ACROS). This solution was sonicated for 5 minutes before being filtered with a hydrophobic PET membrane with 0.2 μm pore size. 100 μL precursor solution was added onto a 2 × 2 cm^2 Ta_3N_5 substrate and spin-coated for 30 seconds; the spin speed was adjusted to 3000 rpm, with a 600 rpm/sec acceleration rate. The as-deposited films were then placed on a 200°C hot plate (MA-1827F, Thermo Scientific) for different durations. Only one layer of the co-catalyst was deposited on the Ta_3N_5 photoanodes.

4.4.2 Optimization of Spin-Coating Procedure

To evaluate the PEC performances of Ta_3N_5 photoanodes integrated with $NiFeO_x$ OER co-catalyst, an electrolyte consisting of 1 M KOH with pH 13.6 was used without the addition of any hole scavengers. The PEC performance of Ta_3N_5 photoanodes converted from metastable Ta_2N_3 with different $NiFeO_x$ pyrolysis conditions was

doi:10.6342/NTU202403464

examined, as shown by the J-V curve in **Figure 4.11**. The photocurrent densities of Ta_3N_5 photoanodes at the OER potential (1.23 V_{RHE}) for different annealing temperatures are summarized in **Table 4.4**.

The pristine sample demonstrated an extremely low photocurrent density of about 0.94 mA/cm² at V = 1.23 V vs. RHE. This can be attributed to the deterioration of surface composition by severe photo-corrosion, where many photogenerated holes stay on the surface of Ta_3N_5 photoanodes due to the sluggish kinetics of oxygen evolution. Even if there are no recombination defects on the surface of Ta_3N_5 photoanodes initially, those photogenerated holes would still experience severe recombination, which can be confirmed by the J-V profile in the low-bias regions.

After the deposition of $NiFeO_x$, the photocurrent density improved to varying extents depending on the pyrolysis time and temperature. This improvement was due to the protection of the Ta_3N_5 surface from severe photo-corrosion via extracting photogenerated holes to the active sites of $NiFeO_x$. The best-performing Ta_3N_5 photoanode was achieved when the pyrolysis temperature was set to 200 °C with a dwell time of 10 minutes, resulting in a photocurrent density of 2.16 mA/cm² at V = 1.23 V vs. RHE. When the pyrolysis time was kept at 10 minutes, increasing the temperature from 200°C to 300°C led to a deterioration of performance. This deterioration can be attributed to the degradation of the Ta_3N_5 surface by the high-temperature treatment under atmospheric conditions. This suggests that if a co-catalyst is to be deposited on the surface of a nitride-based photoelectrode, the solution should be precisely chosen. If the pyrolysis temperature is high, it might deteriorate the surface of the nitride photoelectrode via oxidation in the presence of oxygen.

The reason for choosing 2-methoxyethanol as the solution was due to its moderate boiling point and better film coverage after spin-coating procedures. The optimization of

doi:10.6342/NTU202403464

the solution is beyond the scope of this thesis, but several solutions were tested, including ethanol combined with acetic acid, acetylacetone, isopropanol, and 2-methoxyethanol. The deposition of co-catalysts utilizes high-volatile organic solutions such as hexane combined with metal-organic precursors like Iron(III) 2-ethylhexanoate, nickel(II) 2-ethylhexanoate, and cobalt(III) 2-ethylhexanoate, which has been demonstrated by most research articles.[77, 99, 101]

In our case, a higher temperature is needed to ensure that nitrates do not remain in the co-catalyst layer, which could cause artifacts in the PEC performance. The deterioration of surface composition could also be observed when the pyrolysis time was increased, as indicated by the decline in photocurrent densities with increased pyrolysis duration. Additionally, a broad peak was observed at about 0.8 to 0.9 V_{RHE}. The formation of this broad peak is still unknown, but from the perspective of optimizing photocurrent density, all of these treatments showed deteriorated performance. Therefore, these conditions will not be used.

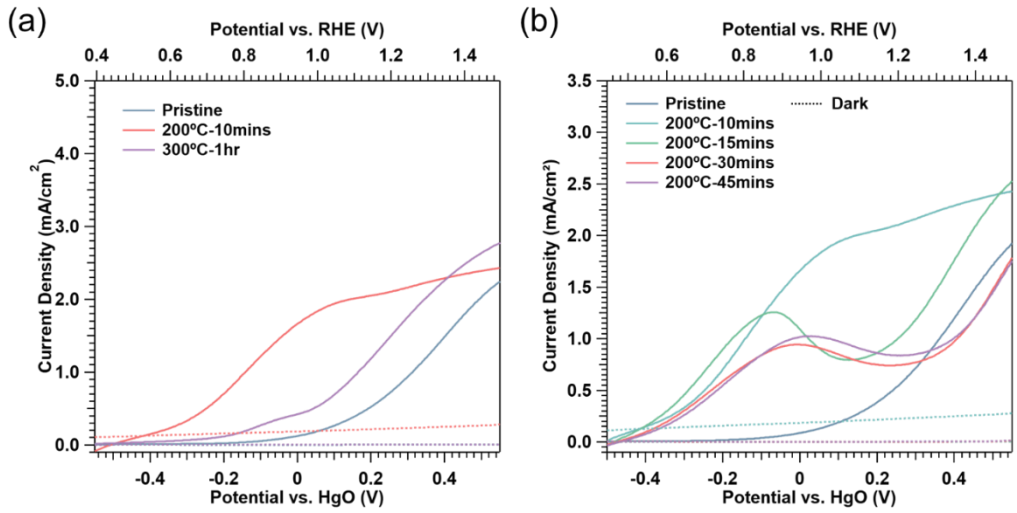

Figure 4.11 LSV plots measured from $NiFeO_x$-coated Ta_3N_5 photoanodes deposited on n^+-Si(111) with (a) different pyrolysis temperatures, (b) different pyrolysis duration at 200°C.

doi:10.6342/NTU202403464

Table 4.4 PEC performance of $NiFeO_x$-coated Ta_3N_5 photoanodes with different spin-coating procedures recorded at V = 1.23 V vs. RHE.

Treatment(°C-min)	Pristine	200-10	200-15	200-30	200-45	300-60
J (mA/cm^2) @ 1.23 V_{RHE}	0.94	2.17	1.19	0.78	0.85	0.94

4.4.3 Stability Test

After optimizing the deposition conditions of $NiFeO_x$, chronoamperometry was conducted at an applied potential of 1.23 V_{RHE} under a 1 M KOH solution with a pH of 13.6 to check the stability. As shown in **Figure 4.12**, the stability of pristine Ta_3N_5 was extremely poor; after the light was turned on, the photocurrent dropped drastically to almost zero within a few minutes, which is due to severe photo-corrosion on the surface of the Ta_3N_5 photoanode.

On the other hand, after the deposition of the co-catalyst, the photocurrent density was three times larger than that of the pristine Ta_3N_5. However, a rapid drop was also observed, with the current density decreasing from 3.5 mA/cm^2 to 2 mA/cm^2 right after the light was turned on. This implies that the initial photocurrent increase was mainly due to charging instead of a true redox reaction. However, after dropping to 2 mA/cm^2, the photocurrent remained stable for half an hour. This suggests that the incorporation of $NiFeO_x$ indeed protected the surface of Ta_3N_5 photoanodes and successfully extracted the photogenerated holes.

doi:10.6342/NTU202403464

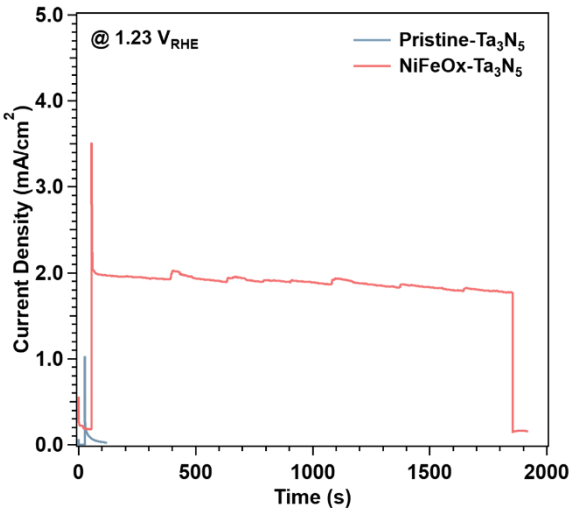

Figure 4.12 CA plot measured from $NiFeO_x$-coated Ta_3N_5 photoanodes with an applied potential of 1.23 V vs. RHE.

From the SEM images of $NiFeO_x/Ta_3N_5$ in **Figure 4.13**, the coverage of $NiFeO_x$ was poor. The improved PEC stability despite the low $NiFeO_x$ coverage implies that the rapid degradation of Ta_3N_5 is mainly due to the accumulation of photogenerated holes. Once a co-catalyst is deposited on the surface of Ta_3N_5 photoanodes, the photogenerated holes will spontaneously transfer to the co-catalysts owing to the preferred band alignment.[88] Therefore, the photogenerated holes accumulated on the surface of Ta_3N_5 can be successfully dissipated. Since $NiFeO_x$ has active sites for performing the OER reaction, those photogenerated holes can then be successfully consumed, achieving good stability for $NiFeO_x/Ta_3N_5$ photoanodes.

However, to ensure that the current density is truly used for the oxygen evolution reactions, product analysis and quantifying the Faradaic efficiency (FE) are still needed. This is a task scheduled for August. For now, in the presented work, we have successfully incorporated a co-catalyst to achieve stable oxygen evolution reactions for the Ta_3N_5 photoanode system.

doi:10.6342/NTU202403464

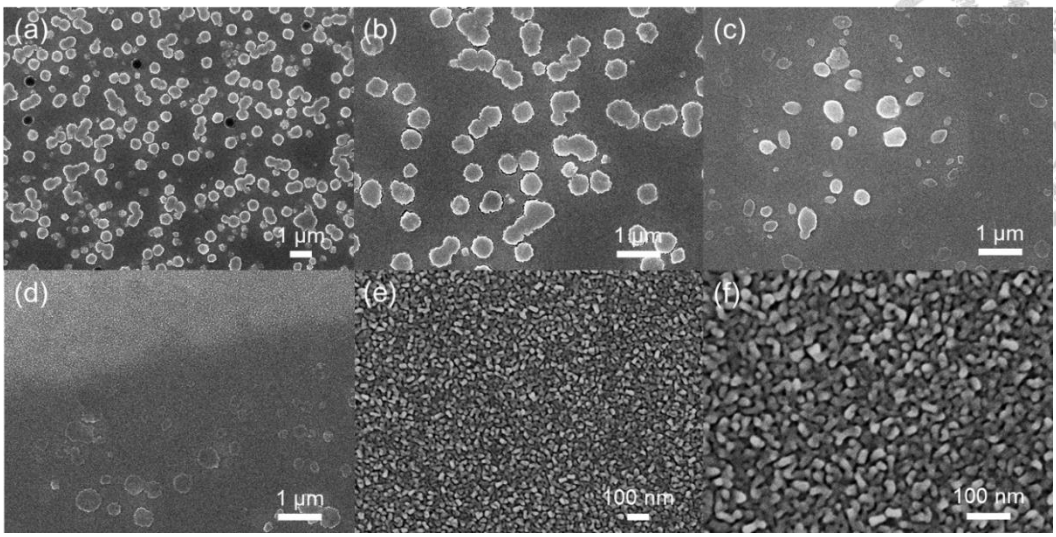

Figure 4.13 SEM images of Ta_3N_5 deposited with NiFeOx co-catalyst.

doi:10.6342/NTU202403464

Chapter 5. Fabrication of Ta_3N_5 Photoanode by Different Precursors

In **Chapter 3**, a new Ta_3N_5 synthesis procedure was developed through the nitridation of high-quality Ta_2N_3 precursor films. This method partially addressed the issue of direct synthesis of nitride species by the reactive sputtering method, which often results in metal cations in their lower oxidation state, i.e., Ta^{3+} in the Ta-N system. **Chapter 4** focused on examining the PEC performance of Ta_3N_5 photoanodes fabricated by the method constructed in **Chapter 3**.

In contrast, most research articles have fabricated Ta_3N_5 by nitridation from tantalum oxide, where all metal cations are already in their highest oxidation states. Additionally, many research articles claim that using oxide as precursors can introduce more oxygen impurities to serve as n-type dopants in Ta_3N_5 photoanode systems.[92, 177-180] In this chapter, reactive magnetron sputtering was utilized for the fabrication of other nitridation precursors by varying the reactive gas atmosphere to change film compositions. **Chapter 5.1** evaluated the potential of incorporating minor oxygen impurities into the Ta_2N_3 precursor films established in **Chapter 3** to improve the performance of Ta_3N_5 photoanodes after nitridation. In **Chapter 5.2**, Ta_3N_5 was fabricated and optimized from tantalum oxide to compare our newly established method with the method commonly used by other research groups.

doi:10.6342/NTU202403464

5.1 Intentional Introduction of Oxygen Impurities in Ta_2N_3 Precursor Films

As discussed at the beginning of this chapter, most research articles assign oxygen impurities to be beneficial defects in Ta_3N_5 photoanode systems. The energetic position of oxygen defects is close to the CBM of Ta_3N_5 so they can serve as n-type dopants to enhance electrical conductivity. Oxygen impurities are easy to incorporate since the common method of Ta_3N_5 fabrication is the nitridation from Ta_2O_5. However, in our newly established method, no oxygen can be intentionally incorporated into the unit cell. Hence, we evaluated the possibility of whether the intentional incorporation of oxygen into the precursor films can further enhance the PEC performance through additional n-type conductivity.

5.1.1 Deposition Procedure

Double sides polished quartz, and n^+-Si(111) were used as the substrate for the deposition. The detailed cleaning procedures of the substrates and the deposition procedures can be referred to in **Chapter 3.1**.

After the cleaning process, the substrate was securely attached to the substrate holder and then introduced into the load lock chamber. The load lock chamber was evacuated until it reached a pressure of 3×10^{-7} Torr, then the substrate holder was transferred into the main chamber for the sputter deposition process. The substrate holder was configured with a rotational speed of 10 rpm and heated at a ramp rate of 10°C/sec until it reached the 500°C target temperature.

For the cleaning of the substrate, Ar gas was introduced into the main chamber at a 40 sccm flow rate, with the process pressure maintained at 9 mTorr. The substrate shutter

doi:10.6342/NTU202403464

was then opened, and a 50W RF power was applied on the substrate to ignite the Ar plasma, aimed at removing organic contaminants and native oxide from the substrate surface. This condition was sustained for 10 minutes.

Following the substrate cleaning, the substrate shutter was closed, and the target shutter was opened. A DC power of 60W was applied to the Ta target to ignite the Ar plasma for target cleaning and chamber conditioning for another 10 minutes. The gas flow and process pressure remained constant as substrate cleaning.

For the pre-deposition, The DC power applied to the Ta target was changed to 80W, and the pulsed DC mode was activated with 100 kHz frequency and a 1 μs reverse time, which is equivalent to a 99% duty cycle. Subsequently, the reactive gas(es) was introduced, with the Ar flow rate adjusted to 20 sccm. The N_2 flow rate was set to 30 sccm, with varying O_2 flow rates from 0.1 sccm to 0.7 sccm. The process pressure was adjusted to 5 mTorr. The target shutter remained open while and the substrate shutter remained closed in the target conditioning phase. This phase would last for 15 minutes, allowing the voltage and current applied to the target to reach a steady state.

The actual deposition period set to 2 hours commenced after the substrate shutter was opened. Upon completion of the deposition, the heater was promptly turned off, followed by discontinuing the supply of oxygen, nitrogen, and then Ar. The substrate shutter would remain open after the deposition. The deposited film would be transferred out for further use once it had cooled down to room temperature.

5.1.2 Effect of Oxygen Flow Rate on the Quality of Ta_2N_3

As discussed in **Chapter 3.2.1**, the gas atmosphere significantly impacts the chemical composition and crystallinity of as-deposited films. Without additional oxygen in the main chamber, typical Ta_2N_3 thin films were characterized by diffraction peaks

doi:10.6342/NTU202403464

centered at 2θ = 31.20° and 36.50°. Introducing O_2 into the process chamber improved the crystallinity of Ta_2N_3, causing the diffraction peaks to shift slightly to lower angles. The amorphous background exhibited at 2θ = 30 - 40° was also reduced; however, the as-deposited films became amorphous when the oxygen flow rate was higher than 0.5 sccm, as shown in **Figure 5.1.** These phenomena were attributed to oxygen incorporation, which stabilized the Ta_2N_3 unit cell by increasing the oxidation state of tantalum cations due to oxygen's higher electronegativity compared to nitrogen. Oxygen was incorporated into the interstitial sites of the Ta_2N_3 unit cell rather than replacing nitrogen atoms, as indicated by the peak shift to lower angles.[60] The ionic radii of oxygen and nitrogen are 124 pm and 132 pm, respectively; if oxygen replaced nitrogen, the unit cell would contract, causing the diffraction peaks to shift to higher angles.[181] Therefore, oxygen occupied interstitial sites, explaining why excessive oxygen led to amorphization of the unit cell due to the introduced disorder.

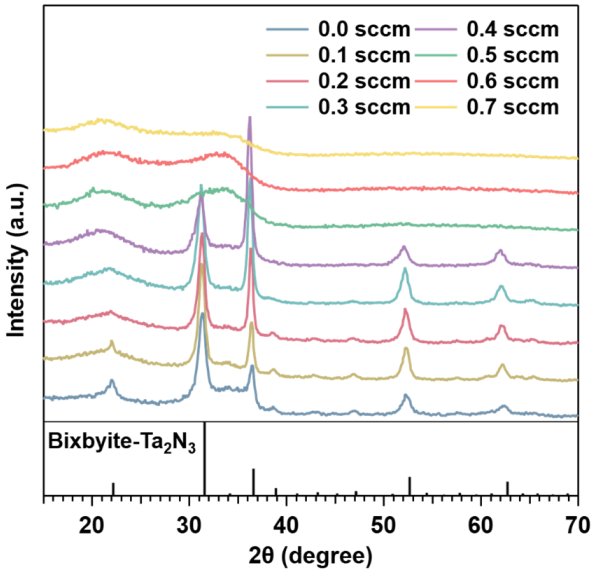

Figure 5.1 GIXRD patterns measured from TaN_x films deposited with varying O_2 flow rates.

doi:10.6342/NTU202403464

A closer examination of the diffraction peaks revealed deviations from the reference intensity, which was owing to the introduction of excess oxygen content into the unit cell of the bixbyite structure. the weaker bixbyite diffraction peak at $2\theta = 31.20°$ with increasing oxygen flow rate suggested the order arrangement of interstitial sites no longer existed.

The grain size and structure of the as-deposited films differed significantly between crystalline and amorphous samples, as shown in the SEM images (**Figure 5.2**). When the oxygen flow rate was 0.1 sccm during deposition, the Ta_2N_3 film was crystalline and the grains were larger and exhibited clear grain boundaries (**Figure 5.2a**). On the other hand, while the oxygen flow rate was set at 0.7 sccm, the TaN_x films were amorphous and had extremely small grain sizes with no obvious features visible in the images. Interestingly, the film thickness remained relatively unchanged after the introduction of oxygen into the process chamber. This suggests that the addition of oxygen does not significantly decrease the sputtering rate. Instead, the primary factor affecting the sputtering rate is the introduction of nitrogen. Consequently, the film thickness for both crystalline and amorphous samples was consistently around 100 nm (**Figure 5.2c - Figure 5.2i**).

doi:10.6342/NTU202403464

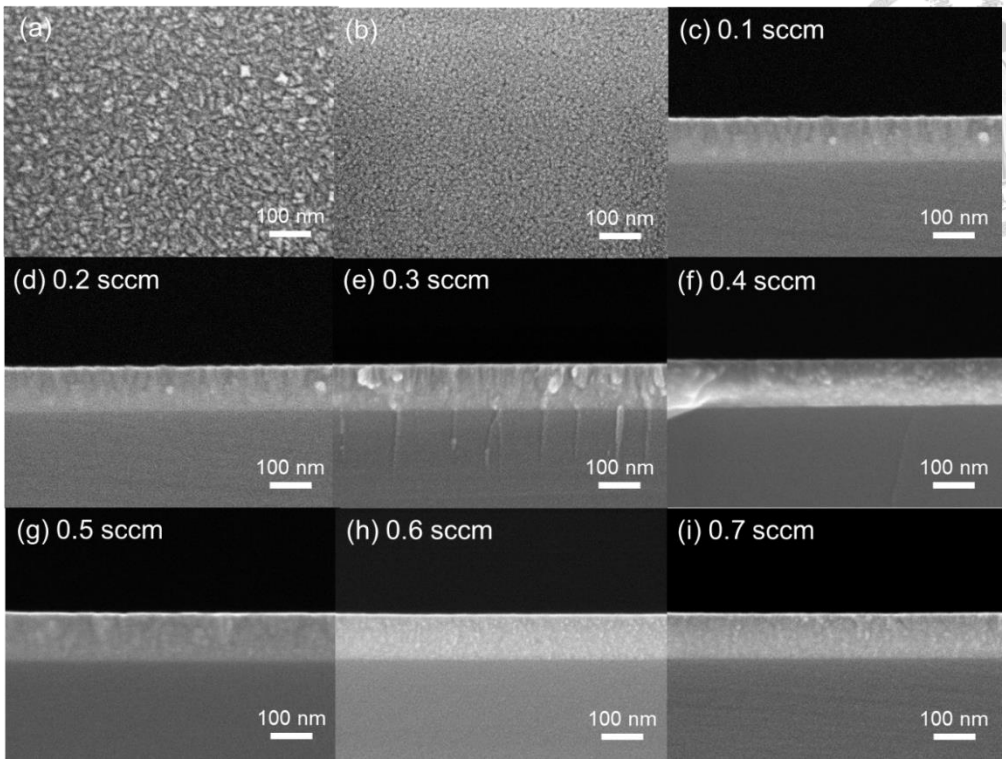

Figure 5.2 SEM top-view images for TaN_x films deposited with (a) 0.1 sccm and (b) 0.2 sccm O_2. (c) - (i) Cross-sectional images taken from TaN_x films deposited with different flow rates of O_2.

5.1.3 Nitridation of Oxygen-Doping Precursor Films

Two series of as-deposited films with oxygen incorporation, including O_2 flow rates of 0.1 sccm and 0.7 sccm, underwent the same annealing conditions as described in **Chapter 3.4**. Detailed annealing procedures can be found in **Chapter 3.4**. The optimized conditions were 820°C for 3 hours with an NH_3 flow rate of 100 sccm. These conditions were examined first to determine if oxygen doping in the precursor films positively affects the PEC performance of Ta_3N_5 photoanodes.

The Ta_2N_3 thin film with 0.1 sccm O_2 incorporation was successfully converted to the desired Ta_3N_5 thin film, as characterized by the GIXRD measurement shown in **Figure 5.3**. However, the surface of the Ta_3N_5 thin film appeared rough even to the naked

doi:10.6342/NTU202403464

eye. SEM top-view and cross-sectional images of this Ta_3N_5 thin film, shown in **Figure 5.4**, revealed the presence of numerous bulging microstructures. One possible origin for this morphology difference includes the film volume expansion due to the density difference between Ta_2N_3 and Ta_3N_5. The density of Ta_3N_5 is about 9.8 g/cm³, while the density of Ta_2N_3 is about 11.29 g/cm³. Consequently, when Ta_2N_3 converts to Ta_3N_5, there must be a volume expansion, as observed and discussed in **Figure 3.24**.

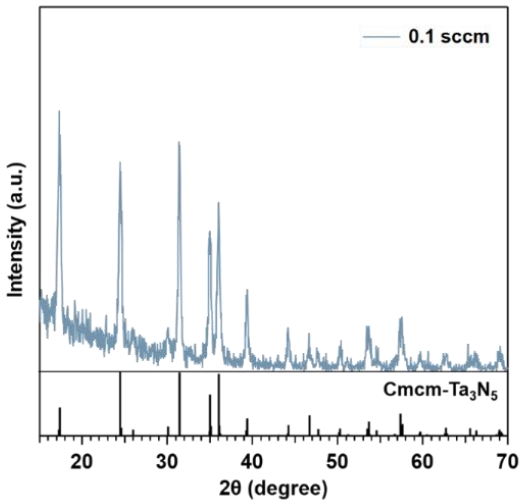

Figure 5.3 GIXRD pattern measured from Ta_3N_5 converted from TaN_x with 0.1 sccm O_2 treatment. The reference of Cmcm-Ta_3N_5 was obtained from ICSD-colloid66533.

Additionally, since oxygen incorporation increases the crystallinity of Ta_2N_3, the conversion to Ta_3N_5 becomes more difficult compared to previous cases. The conversion likely occurs at the grain boundaries, where nitrogen diffusion is easier. Thus, nitrogen diffusion might start from the grain boundaries and diffuse laterally, causing the grain boundary sites to experience volume expansion first. This expansion could lead to the formation of the bulging microstructures observed in the SEM images, with cracking potentially resulting from the exchange of oxygen with nitrogen on the surface.

The surface roughness issue persisted regardless of changes to the nitridation temperature, dwell time, and ammonia flow rate, with a rough surface always being

doi:10.6342/NTU202403464

observed. Therefore, no detailed analysis was conducted for samples that underwent other annealing conditions for Ta_3N_5 thin films converted from Ta_2N_3 thin films with 0.1 sccm oxygen incorporation.

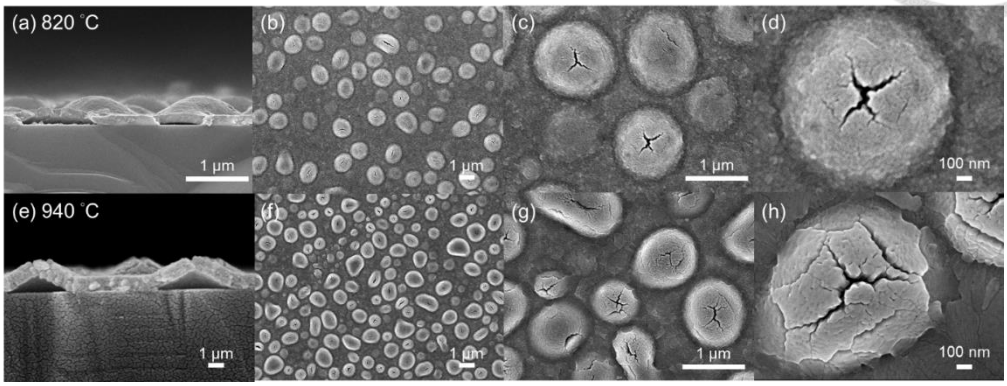

Figure 5.4 SEM images for Ta_3N_5 films converted from TaN_x films with 0.1 sccm O_2 incorporation. (a) - (d) Ta_3N_5 annealed at 820°C, and (e)-(h) Ta_3N_5 annealed at 940°C.

For Ta_3N_5 converted from TaN_x films with 0.7 sccm O_2 incorporation, the desired Ta_3N_5 phase was also successfully obtained after reactive annealing under an ammonia atmosphere, as exhibited by the GIXRD results in **Figure 5.5a**. The surfaces of these Ta_3N_5 thin films obtained from the amorphous precursors did not show observable rough structure when seen by the naked eye. The effect of nitridation temperature was examined for Ta_3N_5 films converted from TaN_x films with 0.7 sccm oxygen incorporated.

When subjected to the optimized annealing temperature of 820℃ for 3 hours, the film completely converted to the pure phase of Ta_3N_5, as observed in the surface-sensitive GIXRD measurement. Besides, no impurities phases of Ta_5N_6 and Ta_2N were observed in the bulk composition of the annealed film, as shown in the diffractogram of **Figure 5.5b**. It might originate from the oxygen in the precursor films that helps to keep the oxidation state of the Tantalum cation at +5. Therefore, after the implication of optimized annealing condition for this amorphous precursor, a pure phase of Ta_3N_5 not only on the surface layer but also on the bulk of the thin films can be obtained. However, the peak

doi:10.6342/NTU202403464

intensity still slightly deviated from the theoretical value, which implies there might be some oxygen still present in the unit cell that changed the atomic form factor of Ta_3N_5.

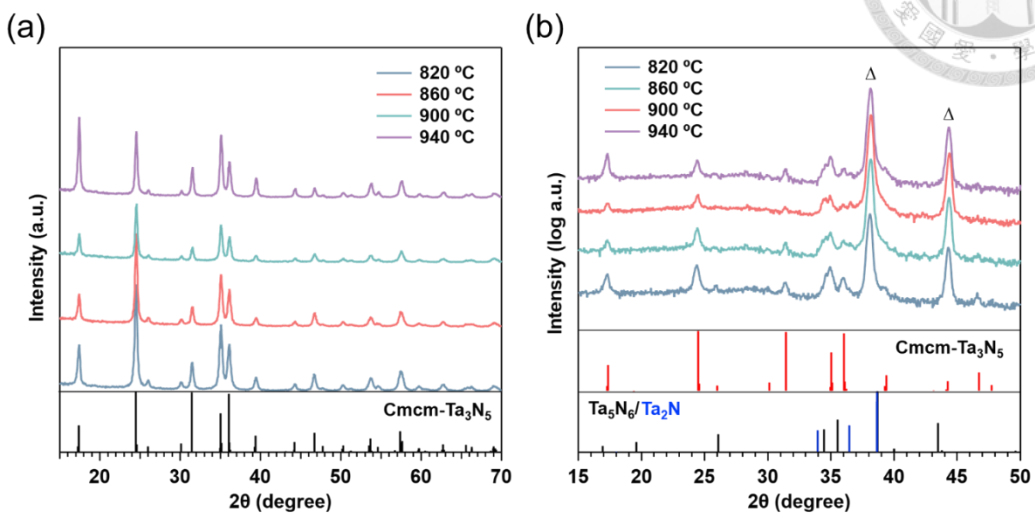

Figure 5.5 (a) GIXRD and (b) PXRD patterns measured from Ta_3N_5 annealed at different temperatures. The Ta_3N_5 films were converted from TaN_x films with 0.7 sccm O_2 incorporation. The reference of Cmcm-Ta_3N_5 and Ta_5N_6 were obtained from ICSD-colloid66533 and ICSD-colloid644720, respectively. The triangular sign was the diffraction peaks from the substrate holder.

Subsequently increasing the annealing temperature from 820°C to 940°C resulted in the observation of a pure phase of Ta_3N_5 by GIXRD, but with deteriorating film crystallinity, as indicated by the decrease in intensity of the peak at 2θ = 24.49°. Additionally, the bulk composition also appeared to consist mainly of the desired Ta_3N_5, albeit with decreasing crystallinity as the annealing temperature increased. Furthermore, the impurities content, especially the Ta_5N_6 content as the shoulder peak at 2θ = 34.51°, increased with higher annealing temperatures, confirming the observation that high-temperature treatment of Ta_3N_5 leads to its decomposition into Ta_5N_6 phases. Besides, the peak intensity also deviated from the theoretical value in the GIXRD results, especially, the ratio between peaks at 2θ = 17.12°, 24.49°, 35.10°, and 36.15°. These results also

doi:10.6342/NTU202403464

imply composition differences that changed the atomic form factor of Ta_3N_5 with increasing annealing temperature. Further characterization is needed to check the composition either by XPS, ERDA, or secondary ion mass spectroscopy (SIMS), but it is already beyond the scope of this thesis.

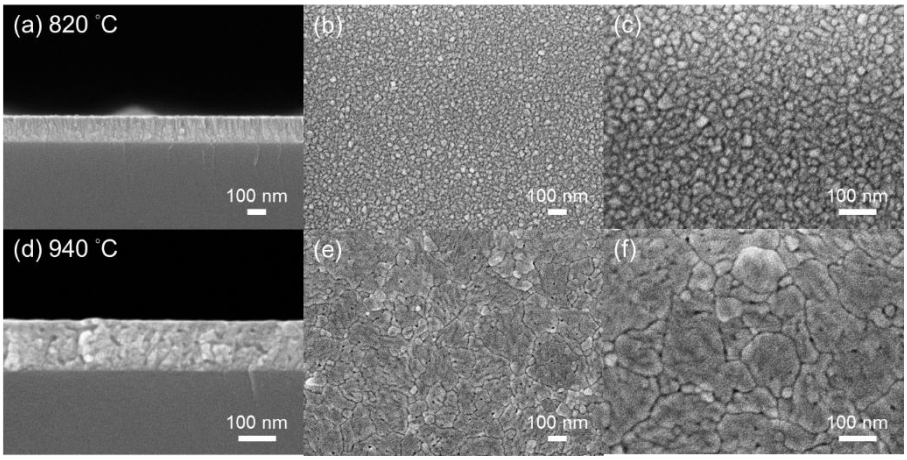

Figure 5.6 SEM images for Ta_3N_5 converted from TaNx films with 0.7 sccm oxygen incorporation. (a) - (c) Ta_3N_5 annealed at 820°C, and (d) - (f) Ta_3N_5 annealed at 940°C.

The SEM image in **Figure 5.6** of the NH_3-annealed thin film revealed an increase in film thickness from the initial 100 nm to about 120 nm. But unlike in Ta_3N_5 thin films obtained from Ta_2N_3 precursor that was treated by the 0.1 sccm oxygen gas, bulging microstructures did not appear (**Figure 5.4**). At higher annealing temperatures, the grain size increased upon reaching the desired phase. Higher temperatures can better fuse the Ta_3N_5 grain with more clear grain boundaries formed. Additionally, pinholes were observed on the surface of the desired Ta_3N_5 thin films for the sample annealed at 940°C.

doi:10.6342/NTU202403464

5.1.4 PEC Performance of Ta_3N_5 Photoanodes Converted from Oxygen-Doping Precursors

The PEC performance of Ta_3N_5 photoanodes converted from TaN_x films with 0.7 sccm incorporation with various annealing temperatures was examined, as shown by the J-V curve in **Figure 5.7**. The photocurrent densities of Ta_3N_5 photoanodes at the OER potential (1.23 V_{RHE}) for different annealing temperatures are summarized in **Table 5.1**. When the annealing temperature was raised from 820°C to 940°C, the photocurrent density of Ta_3N_5 photoanodes decreased from 1.11 to 0.12 mA/cm^2 at V = 1.23 V vs. RHE. The decreasing photocurrent density can be evaluated from several perspectives.

First, the crystallinity of Ta_3N_5 photoanodes deteriorated with increasing annealing temperature, as indicated by the GIXRD and PXRD results in **Figure 5.5**. Second, more impurity phases were incorporated into the Ta_3N_5 as the annealing temperature increased. Although low-valence Ta-N species can improve bulk conductivity, the surface composition significantly impacts the final PEC performance. We propose that higher annealing temperatures result in more Ta^{3+} defects on the surface, leading to increased recombination and a consequent decrease in photocurrent density. The unsaturated profile of the J-V curve in the low-applied bias region can be the clue for severe recombination.

Table 5.1 PEC performance of Ta_3N_5 photoanodes converted from TaN_x films with 0.7 sccm O_2 incorporation annealed at different temperatures recorded at V = 1.23 V vs. RHE.

Temperature (°C)	820	860	900	940
J (mA/cm^2) @ 1.23 V_{RHE}	1.11	0.83	0.47	0.12

doi:10.6342/NTU202403464

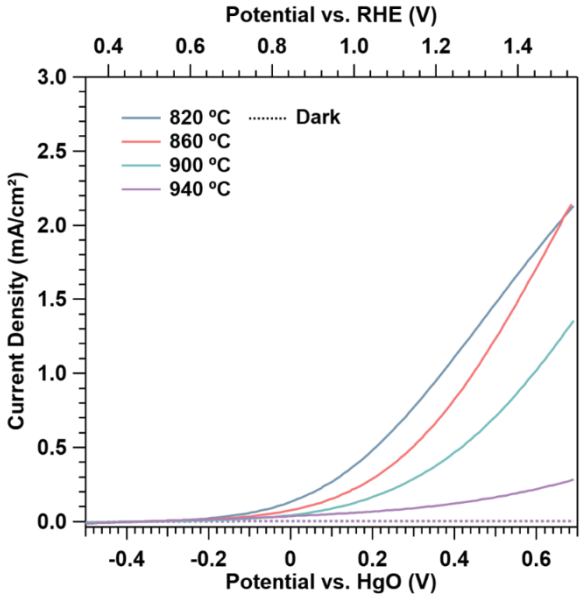

Figure 5.7 LSV plots measured from Ta_3N_5 photoanodes deposited on n^+-Si(111) annealed at various temperatures for 3 hours. The Ta_3N_5 films were converted from TaN_x films with 0.7 sccm O_2 incorporation.

These results partially agree with our conclusions in **Chapter 4.1**. While we cannot confirm this conclusively without XPS measurements, we can qualitatively suggest that annealing temperature can be used to tune the surface defect content, which is most detrimental to the PEC performance of Ta_3N_5 photoanodes.

These results partially agree with our conclusions in **Chapter 4.1**. While we cannot confirm this conclusively without XPS measurements, we can qualitatively suggest that annealing temperature can be used to tune the surface defect content, which is most detrimental to the PEC performance of Ta_3N_5 photoanodes.

The PEC performances of Ta_3N_5 photoanodes converted from TaN_x with 0.1 sccm and 0.7 sccm O_2 incorporation during precursor deposition were examined (**Figure 5.8**). These Ta_3N_5 photoanodes underwent annealing conditions at a temperature of 820°C and a duration of 3 hours. The photocurrent densities of Ta_3N_5 photoanodes at the OER

doi:10.6342/NTU202403464

potential (1.23 V_{RHE}) for different O_2 flow rates during precursor fabrication are summarized in **Table 5.2**.

The photocurrent density of Ta_3N_5 photoanodes converted from Ta_2N_3 films with 0.1 sccm O_2 incorporation was extremely low, around 0.2 mA/cm^2 at V = 1.23 V vs. RHE, which can be attributed to the bulging structure deteriorating the adhesion between Ta_3N_5 and n^+-Si(111). It can be confirmed by the cross-sectional images in **Figure 5.4a**.

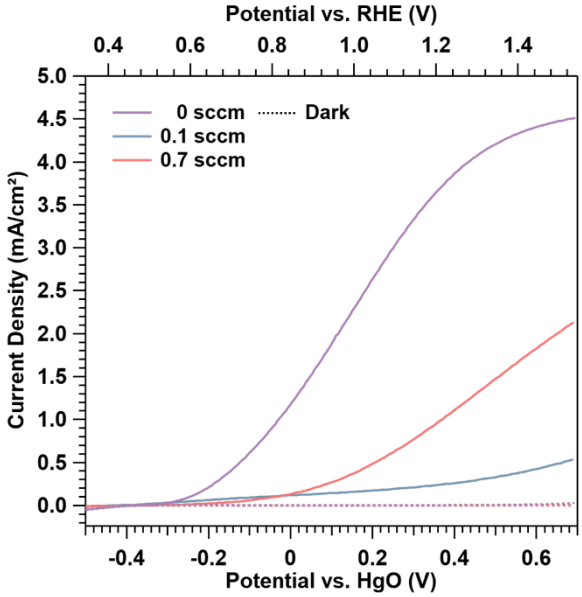

Figure 5.8 LSV plot measured from Ta_3N_5 photoanodes deposited on n^+-Si(111) annealed at 820°C for 3 hours. The Ta_3N_5 films were converted from TaN_x films with different O_2 flow rates.

Table 5.2 PEC performance of Ta_3N_5 photoanodes annealed at 820°C for 3 hours recorded at V = 1.23 V vs. RHE. The Ta_3N_5 films were converted from TaN_x films with different amounts of O_2 during deposition.

Treatment	0 sccm O_2	0.1 sccm O_2	0.7 sccm O_2
J (mA/cm^2) @ 1.23 V_{RHE}	3.89	0.26	1.11

doi:10.6342/NTU202403464

On the other hand, the photocurrent density incorporated was 1.11 mA/cm² at V = 1.23 V vs. RHE. The enhancement of photocurrent density can be attributed to improved contact between Ta_3N_5 and n^+-Si(111). However, when compared to the photocurrent density obtained from Ta_3N_5 films annealed from metastable Ta_2N_3 films without additional oxygen incorporation, that of Ta_3N_5 converted from TaN_x films with 0.7 sccm O_2 was still relatively small. The deteriorated performance might be attributed to the presence of low-valance Ta_5N_6 and Ta_2N in the bulk composition of Ta_3N_5 films when fabricated from TaN_x films with 0.7 sccm O_2 incorporated as shown in **Figure 5.3b**, which further addressed the importance of low-valence Ta-N species in the bulk composition of the films as the metallic properties of Ta_5N_6 and Ta_2N can enhance the photogenerated carrier extraction. The role of oxygen in the composition of Ta_3N_5 photoanodes will be further discussed in the next section using Ta_3N_5 directly converted from Ta_2O_5 films.

5.2 Fabrication of Tantalum Oxide as Nitridation Precursor

As discussed in the preface of this chapter, tantalum oxide was fabricated via reactive magnetron sputtering as the nitridation precursor for comparison with Ta_3N_5 photoanodes constructed in **Chapter 3**, annealed from metastable Ta_2N_3 films.

5.2.1 Deposition Procedure

Double sides polished quartz, and n^+-Si(111) were used as the substrate for the deposition. The detailed cleaning procedures of the substrates and the deposition procedures can be referred to in **Chapter 3.1**.

doi:10.6342/NTU202403464

After the cleaning process, the substrate was securely attached to the substrate holder and then introduced into the load lock chamber. The load lock chamber was evacuated until it reached a pressure of 3×10^{-7} Torr, then the substrate holder was transferred into the main chamber for the sputter deposition process. The substrate holder was configured with a rotational speed of 10 rpm and heated at a ramp rate of 10°C/sec until it reached the 500°C target temperature.

For the cleaning of the substrate, Ar gas was introduced into the main chamber at a 40 sccm flow rate, with the process pressure maintained at 9 mTorr. The substrate shutter was then opened, and a 50W RF power was applied on the substrate to ignite the Ar plasma, aimed at removing organic contaminants and native oxide from the substrate surface. This condition was sustained for 10 minutes.

Following the substrate cleaning, the substrate shutter was closed, and the target shutter was opened. A DC power of 60W was applied to the Ta target to ignite the Ar plasma for target cleaning and chamber conditioning for another 10 minutes. The gas flow and process pressure remained constant as substrate cleaning. For the first 5 minutes, the substrate shutter was open for the deposition of Ta metal on the surface of the n^+-Si(111) substrate, which prevented the direct oxidation of the Si surface after the introduction of O_2 into the process chamber. For the rest of the time, the substrate shutter was closed.

For the pre-deposition, The DC power applied to the Ta target was changed to 70W, and the pulsed DC mode was activated with 100 kHz frequency and a 1 μs reverse time, which is equivalent to a 99% duty cycle. Subsequently, the reactive gas was introduced, with the Ar flow rate adjusted to 37 sccm and the O_2 flow rate set to 4 sccm. The process pressure was adjusted to 5 mTorr. The target shutter remained open while and the substrate shutter remained closed in the target conditioning phase. This phase

doi:10.6342/NTU202403464

would last for 15 minutes, allowing the voltage and current applied to the target to reach a steady state.

The actual deposition period varied from 0.5 - 2 hours commenced after the substrate shutter was opened. Upon completion of the deposition, the heater was promptly turned off, followed by discontinuing the supply of oxygen, nitrogen, and then Ar. The substrate shutter would remain open after the deposition. The deposited film would be transferred out for further use once it had cooled down to room temperature.

5.2.2 Characterization of Tantalum Oxide with Different Deposition Times

The Ta_2O_5 films obtained with different deposition durations all demonstrated an amorphous nature, as indicated by two broad peaks in the 2θ range from 20 - 40°, as shown in **Figure 5.9**. Additionally, the thickness of the as-deposited Ta_2O_5 films increased from 140 nm to 500 nm as the deposition time was prolonged from 0.5 hours to 2 hours. Surprisingly, the tantalum oxide films grew to over 100 nm in just 0.5 hours of deposition. This rapid growth might be due to the high concentration of sputtering gas (Ar) in the atmosphere, leading to an extremely high sputtering yield in this configuration. The thickness of the as-deposited films is shown in **Figure 5.10**. The grain size of Ta_2O_5 was also larger compared to Ta_2N_3 in **Figure 3.16** and TaNx films with different oxygen flow rates incorporated shown in **Figure 5.2**. These precursor films were then subjected to nitridation at various temperatures to optimize the conversion process.

doi:10.6342/NTU202403464

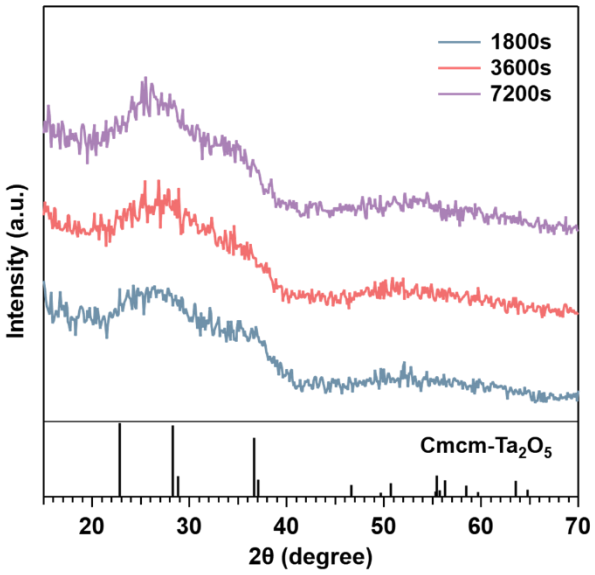

Figure 5.9 GIXRD patterns measured from the TaO_x films deposited with different deposition durations. The reference of Cmcm-Ta_2O_5 was obtained from COD-2102123.

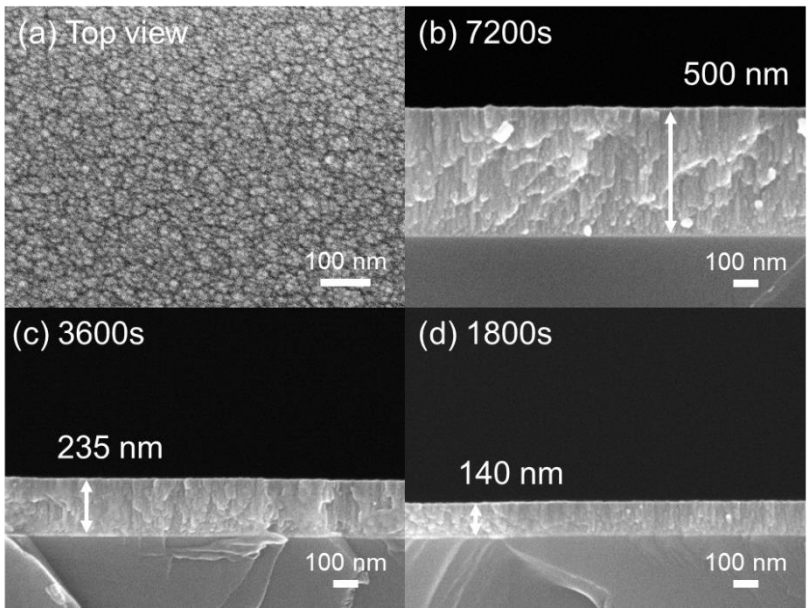

Figure 5.10 SEM images for TaO_x films deposited with different deposition durations.

Herein, the composition of tantalum oxide was not optimized in terms of sputtering parameters for several reasons. First, the crystallinity of Ta_2O_5 can only be improved with substrate heating higher than 800°C, which is beyond the capacity of our

doi:10.6342/NTU202403464

heating unit. Consequently, our Ta_2O_5 exhibited an amorphous nature regardless of which parameters were optimized.[182] Additionally, annealing Ta_2O_5 in a box furnace at 1000°C in atmospheric conditions was not feasible, as this would cause the silicon substrate to form a thick oxide layer, deteriorating the conductivity of our conductive substrate. Second, amorphous Ta_2O_5 serves as a better nitridation precursor since no extra energy is needed to break the ordering inside Ta_2O_5, making it more easily converted to Ta_3N_5 as we hypothesized.

The PEC performance of Ta_3N_5 photoanodes is strongly affected by the thickness of films, a non-monotonically increase in photocurrent density within increasing film thickness was reported by several research articles.[71, 77, 168, 183] Consequently, in the presented thesis, the thickness of TaO_x films was examined to confirm that the PEC performance of Ta_3N_5 constructed in **Chapter 3** can be better than Ta_3N_5 converted from thicker TaO_x film.

5.2.3 PEC Performance of Ta_3N_5 Converted from Various Temperatures

First, the PEC performances of Ta_3N_5 photoanodes converted from 500 nm thick Ta_2O_5 using different nitridation temperatures were examined, the J-V curves are shown in **Figure 5.11** and the photocurrent densities of Ta_3N_5 photoanodes at the OER potential (1.23 V_{RHE}) for different annealing temperatures are summarized in **Table 5.3**.

When the annealing temperature was set to 820°C for 3 hours the photocurrent density was 2.50 mA/cm^2 at V = 1.23 V vs. RHE. The photocurrent density decreased with increasing annealing temperature to 940°C, dropping to 0.57 mA/cm^2 at V = 1.23 V vs. RHE. It might be attributed to the decomposition of Ta_3N_5 at higher annealing temperatures, which introduced reductive environments and low-valence Ta species on the surface of Ta_3N_5 that serve as recombination centers for photogenerated charges.[53]

doi:10.6342/NTU202403464

This can be partially confirmed by the unsaturated profiles of J-V curves measured from Ta_3N_5 photoanodes in the low-applied bias regions, which suggested that significant recombination occurred at the electrode, indirectly indicating the formation of low-valence Ta^{3+} on the surface of Ta_3N_5 photoanodes.

Table 5.3 PEC performance of Ta_3N_5 photoanodes annealed at different temperatures recorded at V = 1.23 V vs. RHE. All the Ta_3N_5 films were converted from TaO_x films with 2 hours deposition duration.

Temperature (°C)	780	800	820	920	940
J (mA/cm^2) @ 1.23 V_{RHE}	2.60	3.25	2.50	0.92	0.57

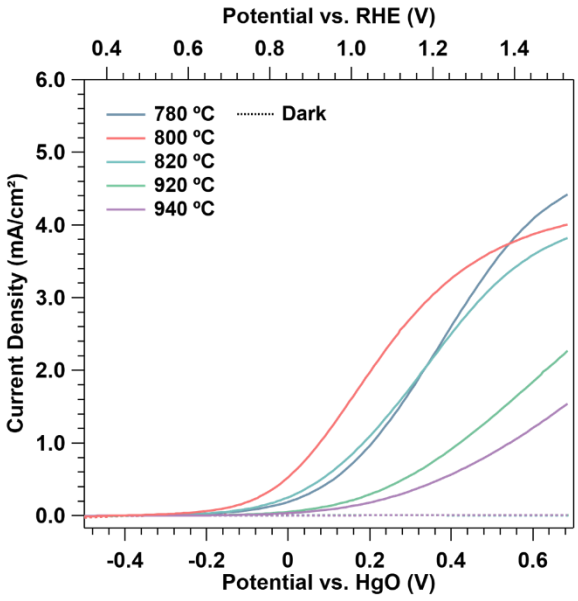

Figure 5.11 LSV plots measured from Ta_3N_5 photoanodes converted from TaO_x films deposited on n^+-Si(111) with different annealing temperatures. The deposition duration of TaOx films was 2 hours.

doi:10.6342/NTU202403464

Temperatures lower than 820°C were also examined since the optimal annealing temperature for Si-based Ta_3N_5 photoanodes was reported to be 800°C.[97, 98] When subjected to an annealing temperature of 800°C for 3 hours, the PEC performance of Ta_3N_5 photoanodes was better than annealing at 820°C, and the photocurrent density was about 3.25 mA/cm^2 at V = 1.23 V vs. RHE. However, further decreasing temperatures to 780°C did not yield better results, instead showing a deteriorated photocurrent density of about 2.6 mA/cm^2 at V = 1.23 V vs. RHE. As a result, the annealing temperature for Ta_3N_5 converted from TaOx films was chosen to 800°C for 3 hours. Next, we characterized the Ta_3N_5 annealed at 800 °C but with different thicknesses, achieved by changing deposition time, and examined their PEC performance.

5.2.4 Ta_3N_5 Photoanodes with Different Thicknesses

The converted films with different thicknesses exhibited the ideal phase of Ta_3N_5, as indicated by both GIXRD and PXRD results in **Figure 5.12**. From the GIXRD results, the crystallinity of Ta_3N_5 appeared to be similar across different thicknesses since the peak intensities and their ratios were almost identical. No impurities were observed on the surface composition of Ta_3N_5 regardless of thickness when the annealing temperature was set to 800°C. Additionally, there was no observation of low-valence Ta_5N_6 and Ta_2N in the bulk composition of Ta_3N_5, suggesting that using TaO_x as a precursor successfully maintains the highest oxidation state of the film after the nitridation process. Compared to using Ta_2N_3 as the precursor, using TaO_x can achieve a purer phase of Ta_3N_5 in terms of crystallinity and phase impurities.

Besides the comparison between different precursors, the PXRD results in **Figure 5.12** for Ta_3N_5 with different thicknesses also exhibited slight differences. Ta_3N_5 films with 150 nm in thickness exhibited the best crystallinity, as indicated by the clear

doi:10.6342/NTU202403464

appearance of peaks with smaller theoretical form factors centered at 2θ = 26° and 30°. When the thickness of Ta_3N_5 increased, the crystallinity slightly decreased, which can be attributed to the incomplete diffusion of nitrogen or exchange of nitrogen with oxygen during the nitridation process. This might also explain why no low-valence Ta-N species were observed in the bulk phase, which was instead replaced by oxygen-doped tantalum nitride that might be intrinsically amorphous. The bulk defect content, which might not be visible in XRD but only in elemental analysis, is unknown also for precursor films since no XPS sputtering depth profile is conducted, it is also the necessary characterization that is scheduled to be conducted in August.

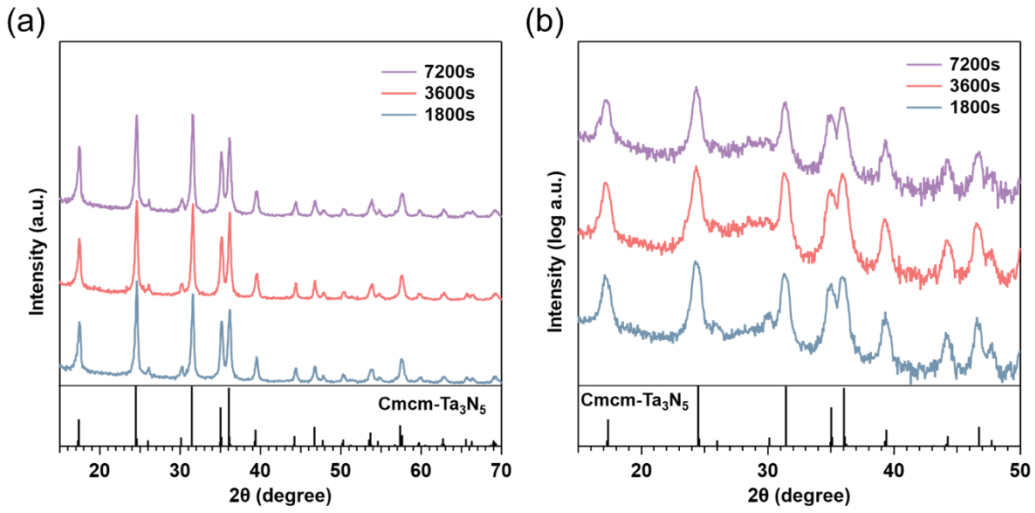

Figure 5.12 (a) GIXRD and (b) PXRD patterned measured from Ta_3N_5 annealed at 800°C for 3 hours. The Ta_3N_5 films were obtained from TaO_x films with different deposition durations.

The SEM images in **Figure 5.13** show no significant difference in the grain size of Ta_3N_5 films with different thicknesses, but larger grains were obtained after nitridation compared to Ta_3N_5 converted from Ta_2N_3. This difference in grain size can be attributed to the reconstruction of the crystalline structure from an amorphous state, as opposed to

doi:10.6342/NTU202403464

the direct conversion from Ta_2N_3, which exhibited smaller grain sizes. For comparison, all the relevant SEM images can be referred to in **Figure 3.24**, **Figure 5.4**, and **Figure 5.6**.

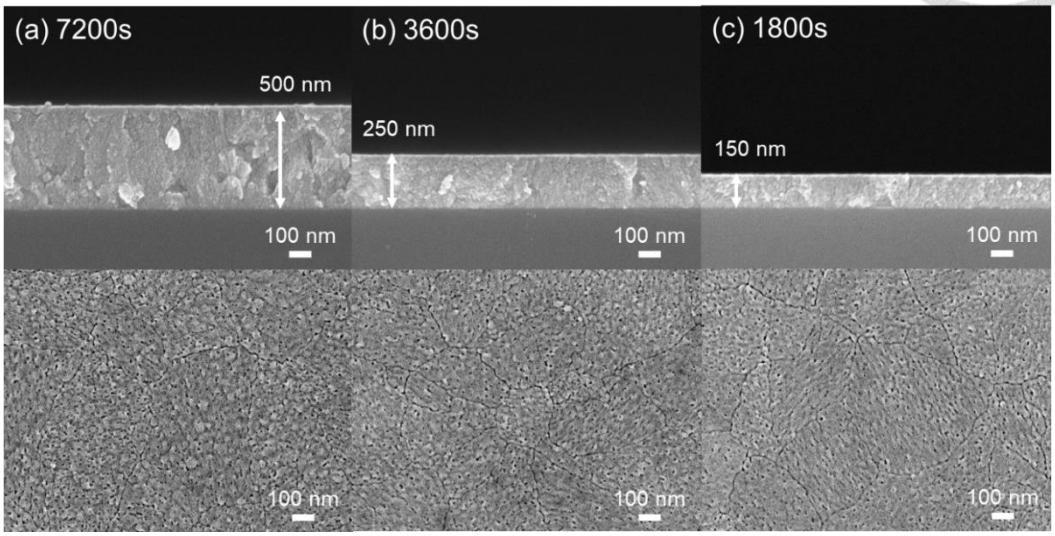

Figure 5.13 SEM images for Ta_3N_5 annealed at 800°C for 3 hours. The Ta_3N_5 films were converted from TaO_x films with different deposition durations.

The J-V curves of Ta_3N_5 photoanodes converted from TaO_x with different thicknesses are shown in **Figure 5.14**, and the photocurrent densities of Ta_3N_5 photoanodes at the OER potential (1.23 V_{RHE}) are summarized in **Table 5.4**. The photocurrent density exhibited non-monotonic growth when the thickness increased. The best-performing thickness was 500 nm, achieving a photocurrent density of about 3.25 mA/cm² at V = 1.23 V vs. RHE. Shrinking the thickness from 500 nm to 150 nm, which was roughly the same scale as our optimized Ta_3N_5 converted from Ta_2N_3, showed a photocurrent density of only about 0.16 mA/cm² at V = 1.23 V vs. RHE. This unique phenomenon has been mentioned in many research articles, but almost no explanation has been provided.[71, 77] Herein, even though not enough characterization was conducted on this set of samples, we attempt to explain this phenomenon according to our knowledge regarding the use of nitride and oxygen-doping precursors in previous sections.

doi:10.6342/NTU202403464

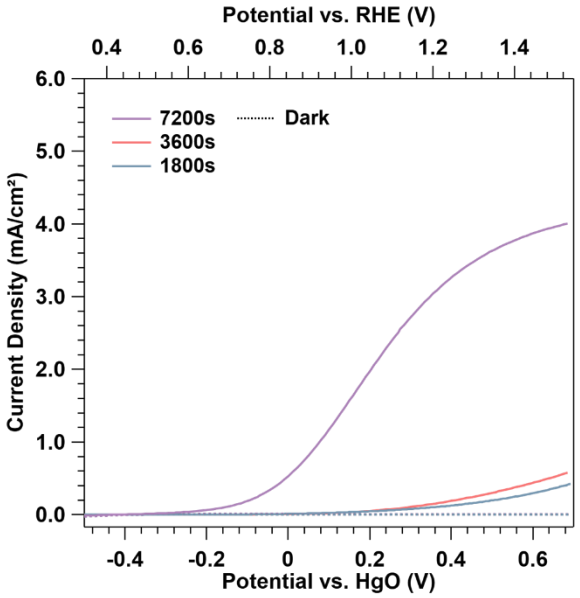

Figure 5.14 LSV plot measured from Ta_3N_5 photoanodes annealed at 800°C for 3 hours. Ta_3N_5 films were deposited on n^+-Si(111) and converted from TaO_x films with different thicknesses.

Table 5.4 PEC performance of Ta_3N_5 photoanodes recorded at V = 1.23 V vs. RHE. Ta_3N_5 films were deposited on n^+-Si(111) and converted from TaO_x films with different thicknesses.

Deposition Dwell (s)	7200	3600	1800
J (mA/cm^2) @ 1.23 V_{RHE}	3.25	0.19	0.13

As we already know, three different defects were characterized in the Ta_3N_5 photoanode system: nitrogen vacancy, low-valence Ta^{3+}, and oxygen impurities.[34] We can observe from the XRD results that no low-valence Ta_5N_6 or Ta_2N was present in the bulk composition regardless of thickness, likely due to the incorporation of oxygen, which helps maintain a high oxidation state of Ta cations during nitridation. However, this also caused the lack of a metallic layer to transport the photogenerated electrons, which is

doi:10.6342/NTU202403464

detrimental in Ta_3N_5 photoanodes due to the short diffusion length (~ 50 nm) and shorter lifetime of photogenerated holes.[168] Hence, when a relatively thin layer of Ta_3N_5 was fabricated from TaO_x, Ta_3N_5 films had better crystallinity, leading to the dominant recombination of photogenerated electron-hole pairs and resulting in extremely low photocurrent density.

When the thickness of Ta_3N_5 increased to about 250 nm, the photocurrent density did not double because the Ta_3N_5 still had better crystallinity, so recombination of electron-hole pairs still dominated the process. However, a slight increase in photocurrent density might be due to insufficient nitrogen diffusion throughout the films causing the formation of amorphous oxynitride presented in the bulk composition of the films, which also bear a better conductivity.

When the thickness was further increased to 500 nm, the photocurrent density increased non-monotonically. As observed from the PXRD in **Figure 5.12b**, the crystallinity decreased but without the formation of low-valence impurities, such as Ta_2N or Ta_5N_6, further supporting that the increase in photocurrent density possibly originated from the oxygen impurities.

In this work, we primarily focused on the development of the Ta_3N_5 photoanode system derived from metastable Ta_2N_3 thin films. To elucidate the origin of the thickness-dependent PEC performance of Ta_3N_5 photoanodes converted from TaOx films, further characterization regarding the bulk composition and detailed electrical measurements should be conducted.

doi:10.6342/NTU202403464

Chapter 6. Outlook and Conclusion

In this work, we constructed a platform for efficient material usage for Ta_3N_5-based photoanode systems grown on Si by reactive magnetron sputtering and post-ammonia annealing. First, we identify parameters, including gas atmosphere, substrate temperature, deposition time, deposition power, and process pressure, for fabricating high-quality Ta_2N_3 films with good reproducibility. The optimized condition was achieved by sputtering the Ta target under a pulsed DC power supply at 70W power, 100 kHz frequency, and 99% duty cycle with a substrate temperature of 500°C, process pressure of 10 mTorr, and a mixed atmosphere of N_2/Ar flow rate ratio of 1.5. The film quality was severely affected by the intrinsic chamber condition, especially the base oxygen content, as proved by control experiments with or without intentionally removing the oxygen background. The optimized Ta_2N_3 thin films served as the nitridation precursor for the synthesis of Ta_3N_5 photoanodes by reactive annealing in ammonia. The performances of Ta_3N_5 photoanodes were evaluated from three different aspects: surface injection and recombination, bulk transport properties, and the junction between the conductive layer and semiconductor. The reactive annealing temperature significantly altered the performance of Ta_3N_5 photoanodes by deteriorating the surface composition with the introduction of deep trap defects to the surface of Ta_3N_5, characterized as Ta^{3+} in XPS results. The optimized annealing temperature was set to 820°C, achieving the highest photocurrent density and providing a defect-free surface.

Annealing duration improved the crystallinity of Ta_3N_5 and significantly decreased defect contents in the bulk composition. However, the presence of low-valence Ta_5N_6 and Ta_2N defects in the bulk composition was characterized to be key to the improvement of PEC performance, as the intrinsic metallic properties can extract photogenerated electrons more efficiently. The bulk composition difference can also

doi:10.6342/NTU202403464

explain why the Ta_3N_5 photoanodes fabricated by Ta_2N_3 have better performance than Ta_3N_5 of similar thickness converted from Ta_2O_5 or oxygen-doped precursor films.

The junction between Ta_3N_5 and the silicon wafers was evaluated with controlled experiments of silicon wafers with different doping concentrations and out-of-plane orientations. Several techniques, including OCP, PEIS, UV-Vis, and UPS, were used to construct the band alignment diagrams between Ta_3N_5 and each silicon substrate. The formation of an n-n heterojunction between semiconducting n-Si(100) and Ta_3N_5 mainly caused the deteriorated PEC performance by the strong heterojunction capacitance and leakage currents, as confirmed by EIS fitting results. Additionally, the protuberance observed in the OCP measurements also confirmed the strong charge accumulation of the heterojunction. For Ta_3N_5 deposited on metallic heavily doped silicon with different substrate orientations, the performance difference was also contributed by the heterojunction capacitance and leakage currents but no formation of n-n heterojunction. This can be treated as a metal-semiconductor junction, where the built-in potential difference between the fermi levels of materials would severely affect the performance.

The pristine Ta_3N_5 photoanode suffered from severe photo-corrosion by the accumulated photogenerated holes due to the sluggish kinetics of the oxygen evolution reaction, a 4-step reaction. As a result, $NiFeO_x$ as an electro-cocatalyst was deposited on the surface of the Ta_3N_5 photoanode by spin-coating the metal-organic sol-gel precursor. The incorporation of $NiFeO_x$ co-catalyst provided a stable surface for at least 30 minutes under an applied potential of 1.23 V vs. RHE. However, whether the photocurrent is used to drive the oxygen evolution reaction or corrosion current should still be examined by calculating the Faradaic efficiency.

In conclusion, this research demonstrated the possibility of more efficient material usage by fabricating high-quality Ta_2N_3 as the nitridation precursor with silicon as a

doi:10.6342/NTU202403464

conductive substrate for the synthesis of Ta_3N_5 photoanodes. This work has also achieved the highest photocurrent density of the planar silicon-based Ta_3N_5 photoanode system to date. By addressing the limitations and optimizing the conditions, this study provides valuable insights for the development of efficient and stable Ta_3N_5 photoanode systems for solar energy conversion applications.

doi:10.6342/NTU202403464

Reference

(1) Eklund, P.; Kerdsongpanya, S.; Alling, B. Transition-metal-nitride-based thin films as novel energy harvesting materials. *J. Mater. Chem. C* **2016**, *4* (18), 3905-3914.
(2) Sun, W.; Bartel, C. J.; Arca, E.; Bauers, S. R.; Matthews, B.; Orvañanos, B.; Chen, B.-R.; Toney, M. F.; Schelhas, L. T.; Tumas, W. A map of the inorganic ternary metal nitrides. *Nat. Mater.* **2019**, *18* (7), 732-739.
(3) Wang, K.; Sheng, C. Application of GaN in 5G technology. 2020, IOP Publishing: Vol. 1699, p 012004.
(4) Chun, W.-J.; Ishikawa, A.; Fujisawa, H.; Takata, T.; Kondo, J. N.; Hara, M.; Kawai, M.; Matsumoto, Y.; Domen, K. Conduction and valence band positions of Ta_2O_5, TaON, and Ta_3N_5 by UPS and electrochemical methods. *J. Phys. Chem. B* **2003**, *107* (8), 1798-1803.
(5) Hisatomi, T.; Kubota, J.; Domen, K. Recent advances in semiconductors for photocatalytic and photoelectrochemical water splitting. *Chem. Soc. Rev.* **2014**, *43* (22), 7520-7535.
(6) Hitoki, G.; Ishikawa, A.; Takata, T.; Kondo, J. N.; Hara, M.; Domen, K. Ta_3N_5 as a novel visible light-driven photocatalyst ($\lambda < 600$ nm). *Chem. Lett.* **2002**, *31* (7), 736-737.
(7) Liu, G.; Ye, S.; Yan, P.; Xiong, F.; Fu, P.; Wang, Z.; Chen, Z.; Shi, J.; Li, C. Enabling an integrated tantalum nitride photoanode to approach the theoretical photocurrent limit for solar water splitting. *Energy Environ. Sci.* **2016**, *9* (4), 1327-1334.
(8) Salamat, A.; Hector, A. L.; Kroll, P.; McMillan, P. F. Nitrogen-rich transition metal nitrides. *Coord. Chem. Rev.* **2013**, *257* (13-14), 2063-2072.
(9) Sun, W.; Holder, A.; Orvañanos, B.; Arca, E.; Zakutayev, A.; Lany, S.; Ceder, G. Thermodynamic routes to novel metastable nitrogen-rich nitrides. *Chem. Mater.* **2017**, *29* (16), 6936-6946.
(10) Ghani, S. S. The development of ternary nitride chemistry during the last few decades. *J. Mod. Mater.* **2017**, *4* (1), 10-15.
(11) Hinuma, Y.; Hatakeyama, T.; Kumagai, Y.; Burton, L. A.; Sato, H.; Muraba, Y.; Iimura, S.; Hiramatsu, H.; Tanaka, I.; Hosono, H. Discovery of earth-abundant nitride semiconductors by computational screening and high-pressure synthesis. *Nat. Commun.* **2016**, *7* (1), 11962.
(12) Ross, M. B.; De Luna, P.; Li, Y.; Dinh, C.-T.; Kim, D.; Yang, P.; Sargent, E. H. Designing materials for electrochemical carbon dioxide recycling. *Nat. Catal.* **2019**, *2* (8), 648-658.
(13) Yan, Y.; Xia, B. Y.; Zhao, B.; Wang, X. A review on noble-metal-free bifunctional heterogeneous catalysts for overall electrochemical water splitting. *J. Mater. Chem. A* **2016**, *4* (45), 17587-17603.
(14) Jerkiewicz, G. Standard and reversible hydrogen electrodes: Theory, design, operation, and applications. *ACS Catal.* **2020**, *10* (15), 8409-8417.
(15) Chen, S.; Wang, L.-W. Thermodynamic oxidation and reduction potentials of photocatalytic semiconductors in aqueous solution. *Chem. Mater.* **2012**, *24* (18), 3659-3666.
(16) Shockley, W. The Shockley-Queisser limit. *J. Appl. Phys.* **1961**, *32* (3), 510-519.
(17) *Solar Radiation Spectrum* https://en.m.wikipedia.org/wiki/File:Solar_Spectrum.png. (accessed 2024 0709).
(18) Jafari, T.; Moharreri, E.; Amin, A. S.; Miao, R.; Song, W.; Suib, S. L. Photocatalytic water splitting—the untamed dream: a review of recent advances. *Molecules* **2016**, *21* (7), 900.

doi:10.6342/NTU202403464

(19) Wheeler, D. A.; Wang, G.; Ling, Y.; Li, Y.; Zhang, J. Z. Nanostructured hematite: synthesis, characterization, charge carrier dynamics, and photoelectrochemical properties. *Energy Environ. Sci.* **2012**, *5* (5), 6682-6702.
(20) Ziwritsch, M.; Müller, S.; Hempel, H.; Unold, T.; Abdi, F. F.; van de Krol, R.; Friedrich, D.; Eichberger, R. Direct time-resolved observation of carrier trapping and polaron conductivity in $BiVO_4$. *ACS Energy Lett.* **2016**, *1* (5), 888-894.
(21) Butler, K. T.; Dringoli, B. J.; Zhou, L.; Rao, P. M.; Walsh, A.; Titova, L. V. Ultrafast carrier dynamics in $BiVO_4$ thin film photoanode material: interplay between free carriers, trapped carriers and low-frequency lattice vibrations. *J. Mater. Chem. A* **2016**, *4* (47), 18516-18523.
(22) Jiang, C.-M.; Reyes-Lillo, S. E.; Liang, Y.; Liu, Y.-S.; Liu, G.; Toma, F. M.; Prendergast, D.; Sharp, I. D.; Cooper, J. K. Electronic structure and performance bottlenecks of $CuFeO_2$ photocathodes. *Chem. Mater.* **2019**, *31* (7), 2524-2534.
(23) Prévot, M. S.; Jeanbourquin, X. A.; Bourée, W. S.; Abdi, F.; Friedrich, D.; van de Krol, R.; Guijarro, N.; Le Formal, F.; Sivula, K. Evaluating charge carrier transport and surface states in $CuFeO_2$ photocathodes. *Chem. Mater.* **2017**, *29* (11), 4952-4962.
(24) Are metal chalcogenides, nitrides, and phosphides oxygen evolution catalysts or bifunctional catalysts? *ACS Energy Lett.* **2017**, *2* (8), 1937-1938.
(25) Nurlaela, E.; Ziani, A.; Takanabe, K. Tantalum nitride for photocatalytic water splitting: concept and applications. *Mater. Renew. Sustain. Energy* **2016**, *5*, 1-21.
(26) Zakutayev, A. Design of nitride semiconductors for solar energy conversion. *J. Mater. Chem. A* **2016**, *4* (18), 6742-6754.
(27) Zakutayev, A.; Caskey, C. M.; Fioretti, A. N.; Ginley, D. S.; Vidal, J.; Stevanovic, V.; Tea, E.; Lany, S. Defect tolerant semiconductors for solar energy conversion. *J. Phys. Chem. Lett.* **2014**, *5* (7), 1117-1125.
(28) Ponce, F. A.; Bour, D. P. Nitride-based semiconductors for blue and green light-emitting devices. *Nature* **1997**, *386* (6623), 351-359.
(29) Asif Khan, M.; Bhattarai, A.; Kuznia, J. N.; Olson, D. T. High electron mobility transistor based on a GaN-$Al_xGa_{1-x}N$ heterojunction. *Appl. Phys. Lett.* **1993**, *63* (9), 1214-1215.
(30) Feng, Y.; Witkoske, E.; Bell, E. S.; Wang, Y.; Tzempelikos, A.; Ferguson, I. T.; Lu, N. Advanced metal oxides and nitrides thermoelectric materials for energy harvesting. *ES Mater. Manuf.* **2018**, *1* (4), 13-20.
(31) Yamanaka, S. High-Tc superconductivity in electron-doped layer structured nitrides. *Annu. Rev. Mater. Sci.* **2000**, *30* (1), 53-82.
(32) Chu, S.; Vanka, S.; Wang, Y.; Gim, J.; Wang, Y.; Ra, Y.-H.; Hovden, R.; Guo, H.; Shih, I.; Mi, Z. Solar water oxidation by an InGaN nanowire photoanode with a bandgap of 1.7 eV. *ACS Energy Lett.* **2018**, *3* (2), 307-314.
(33) Higashi, T.; Nishiyama, H.; Suzuki, Y.; Sasaki, Y.; Hisatomi, T.; Katayama, M.; Minegishi, T.; Seki, K.; Yamada, T.; Domen, K. Transparent Ta_3N_5 photoanodes for efficient oxygen evolution toward the development of tandem cells. *Angew. Chem. Int. Ed.* **2019**, *58* (8), 2300-2304.
(34) Fu, J.; Wang, F.; Xiao, Y.; Yao, Y.; Feng, C.; Chang, L.; Jiang, C.-M.; Kunzelmann, V. F.; Wang, Z. M.; Govorov, A. O. Identifying performance-limiting deep traps in Ta_3N_5 for solar water splitting. *ACS Catal.* **2020**, *10* (18), 10316-10324.
(35) Sarmiento-Perez, R.; Cerqueira, T. F. T.; Körbel, S.; Botti, S.; Marques, M. A. L. Prediction of stable nitride perovskites. *Chem. Mater.* **2015**, *27* (17), 5957-5963.
(36) Flores-Livas, J. A.; Sarmiento-Pérez, R.; Botti, S.; Goedecker, S.; Marques, M. A. L. Rare-earth magnetic nitride perovskites. *J. Phys. Mater.* **2019**, *2* (2), 025003.

doi:10.6342/NTU202403464

(37) Mochizuki, Y.; Sung, H.-J.; Takahashi, A.; Kumagai, Y.; Oba, F. Theoretical exploration of mixed-anion antiperovskite semiconductors M_3XN (M= Mg, Ca, Sr, Ba; X= P, As, Sb, Bi). *Phys. Rev. Mater.* **2020**, *4* (4), 044601.
(38) Elder, S. H.; DiSalvo, F. J.; Topor, L.; Navrotsky, A. Thermodynamics of ternary nitride formation by ammonolysis: application to lithium molybdenum nitride ($LiMoN_2$), sodium tungsten nitride (Na_3WN_3), and sodium tungsten oxide nitride (Na_3WO_3N). *Chem. Mater.* **1993**, *5* (10), 1545-1553.
(39) Li, Y.; Takata, T.; Cha, D.; Takanabe, K.; Minegishi, T.; Kubota, J.; Domen, K. Vertically aligned Ta_3N_5 nanorod arrays for solar-driven photoelectrochemical water splitting. *Adv. Mater.* **2013**, *25* (1), 125-131.
(40) Choi, J.; Gillan, E. G. Solvothermal metal azide decomposition routes to nanocrystalline metastable nickel, iron, and manganese nitrides. *Inorg. Chem.* **2009**, *48* (10), 4470-4477.
(41) Kroll, P.; Schröter, T.; Peters, M. Prediction of novel phases of tantalum (V) nitride and tungsten (VI) nitride that can be synthesized under high pressure and high temperature. *Angew. Chem. Int. Ed.* **2005**, *44* (27), 4249-4254.
(42) Bailey, E.; Ray, N. M. T.; Hector, A. L.; Crozier, P.; Petuskey, W. T.; McMillan, P. F. Mechanical properties of titanium nitride nanocomposites produced by chemical precursor synthesis followed by high-P, T treatment. *Materials* **2011**, *4* (10), 1747-1762.
(43) Taniguchi, T.; Dzivenko, D.; Riedel, R.; Chauveau, T.; Zerr, A. Synthesis of cubic zirconium (IV) nitride, c-Zr_3N_4, in the 6–8 GPa pressure region. *Ceram. Int.* **2019**, *45* (16), 20028-20032.
(44) PalDey, S.; Deevi, S. C. Single layer and multilayer wear resistant coatings of (Ti, Al) N: a review. *Mater. Sci. Eng. A* **2003**, *342* (1-2), 58-79.
(45) Fischer, D.; Jansen, M. Synthesis and structure of Na_3N. *Angew. Chem. Int. Ed.* **2002**, *41* (10), 1755-1756.
(46) Vajenine, G. V. Plasma-assisted synthesis and properties of Na_3N. *Inorg. Chem.* **2007**, *46* (13), 5146-5148.
(47) Talley, K. R.; Perkins, C. L.; Diercks, D. R.; Brennecka, G. L.; Zakutayev, A. Synthesis of $LaWN_3$ nitride perovskite with polar symmetry. *Science* **2021**, *374* (6574), 1488-1491.
(48) Sherbondy, R.; Smaha, R. W.; Bartel, C. J.; Holtz, M. E.; Talley, K. R.; Levy-Wendt, B.; Perkins, C. L.; Eley, S.; Zakutayev, A.; Brennecka, G. L. High-throughput selection and experimental realization of two new Ce-based nitride perovskites: $CeMoN_3$ and $CeWN_3$. *Chem. Mater.* **2022**, *34* (15), 6883-6893.
(49) Greenaway, A. L.; Ke, S.; Culman, T.; Talley, K. R.; Mangum, J. S.; Heinselman, K. N.; Kingsbury, R. S.; Smaha, R. W.; Gish, M. K.; Miller, E. M. Zinc titanium nitride semiconductor toward durable photoelectrochemical applications. *J. Am. Chem. Soc.* **2022**, *144* (30), 13673-13687.
(50) Sun, W.; Ceder, G. Induction time of a polymorphic transformation. *CrystEngComm* **2017**, *19* (31), 4576-4585.
(51) Salamon, K.; Radić, N.; Radović, I. B.; Očko, M. Phase map, composition and resistivity of reactively magnetron sputtered and annealed Ta–N films. *J. Phys. D: Appl. Phys.* **2016**, *49* (19), 195301.
(52) Coyne, H. J., Jr.; Tauber, R. N. Preparation, structure, and properties of sputtered, highly nitrided tantalum films. *J. Appl. Phys.* **1968**, *39* (12), 5585-5593.
(53) Terao, N. Structure of tantalum nitrides. *Jpn. J. Appl. Phys.* **1971**, *10* (2), 248.
(54) Ganin, Alexei Y.; Kienle, L.; Vajenine, Grigori V. Plasma-enhanced CVD synthesis and structural characterization of Ta_2N_3. *Eur. J. Inorg. Chem.* **2004**, *2004* (16), 3233-3239.

doi:10.6342/NTU202403464

(55) Zerr, A.; Miehe, G.; Li, J.; Dzivenko, D. A.; Bulatov, V. K.; Höfer, H.; Bolfan-Casanova, N.; Fialin, M.; Brey, G.; Watanabe, T.; et al. High-pressure synthesis of tantalum nitride having orthorhombic U_2S_3 structure. *Adv. Funct. Mater.* **2009**, *19* (14), 2282-2288.
(56) Zhao, Y.; Lu, G. First-principles simulations of copper diffusion in tantalum and tantalum nitride. *Phys. Rev. B* **2009**, *79* (21), 214104.
(57) Min, K. H.; Chun, K. C.; Kim, K. B. Comparative study of tantalum and tantalum nitrides (Ta_2N and TaN) as a diffusion barrier for Cu metallization. *J. Vac. Sci. Technol. B: Nanotechnol. Microelectron.* **1996**, *14* (5), 3263-3269.
(58) Lüdtke, T.; Orthmann, S.; Lerch, M. Bixbyite-type phases in the system Ta-Zr-O-N. **2017**, *72* (4), 305-311.
(59) Grundmann, M. *Physics of semiconductors*; Springer, 2010.
(60) Jiang, C.-M.; Wagner, L. I.; Horton, M. K.; Eichhorn, J.; Rieth, T.; Kunzelmann, V. F.; Kraut, M.; Li, Y.; Persson, K. A.; Sharp, I. D. Metastable Ta_2N_3 with highly tunable electrical conductivity via oxygen incorporation. *Mater. Horiz.* **2021**, *8* (6), 1744-1755.
(61) Jiang, C.; Lin, Z.; Zhao, Y. Thermodynamic and mechanical stabilities of tantalum nitride. *Phys. Rev. Lett.* **2009**, *103* (18), 185501.
(62) Du, X. P.; Wang, Y. X.; Lo, V. C. Vacancy and oxygen substitution for nitrogen-induced structural stability of Ta_2N_3. *J. Phys. Chem. C* **2011**, *115* (7), 3129-3135.
(63) Kawase, Y.; Higashi, T.; Katayama, M.; Domen, K.; Takanabe, K. Maximizing oxygen evolution performance on a transparent $NiFeO_x/Ta_3N_5$ photoelectrode fabricated on an insulator. *ACS Appl. Mater. Interfaces* **2021**, *13* (14), 16317-16325.
(64) Brauer, G.; Weidlein, J.; Strähle, J. Über das tantalnitrid Ta_3N_5 und das tantaloxidnitrid TaON. *Z. fur Anorg. Allg. Chem.* **1966**, *348* (5-6), 298-308.
(65) Brese, N. E.; O'Keeffe, M.; Rauch, P.; DiSalvo, F. J. Structure of Ta_3N_5 at 16 K by time-of-flight neutron diffraction. *Acta Crystallogr., Sect. C: Struct. Chem.* **1991**, *47* (11), 2291-2294.
(66) Morbec, J. M.; Narkeviciute, I.; Jaramillo, T. F.; Galli, G. Optoelectronic properties of Ta3N5: a joint theoretical and experimental study. *Phys. Rev. B* **2014**, *90* (15), 155204.
(67) Nurlaela, E.; Harb, M.; Del Gobbo, S.; Vashishta, M.; Takanabe, K. Combined experimental and theoretical assessments of the lattice dynamics and optoelectronics of TaON and Ta_3N_5. *J. Solid State Chem.* **2015**, *229*, 219-227.
(68) Cui, Z.-H.; Jiang, H. Theoretical investigation of Ta_2O_5, TaON, and Ta_3N_5: electronic band structures and absolute band edges. *J. Phys. Chem. C* **2017**, *121* (6), 3241-3251.
(69) Kwon, H. R.; Yang, J. W.; Choi, S.; Cheon, W. S.; Im, I. H.; Kim, Y.; Park, J.; Lee, G. H.; Jang, H. W. Low onset-potential Z-scheme Ta_3N_5-based photoanode with enhanced light harvesting and charge transport. *Adv. Energy Mater.* **2024**, *14* (5), 2303342.
(70) Fu, J.; Fan, Z.; Nakabayashi, M.; Ju, H.; Pastukhova, N.; Xiao, Y.; Feng, C.; Shibata, N.; Domen, K.; Li, Y. Interface engineering of Ta_3N_5 thin film photoanode for highly efficient photoelectrochemical water splitting. *Nat. Commun.* **2022**, *13* (1), 729.
(71) Xiao, Y.; Fan, Z.; Nakabayashi, M.; Li, Q.; Zhou, L.; Wang, Q.; Li, C.; Shibata, N.; Domen, K.; Li, Y. Decoupling light absorption and carrier transport via heterogeneous doping in Ta_3N_5 thin film photoanode. *Nat. Commun.* **2022**, *13* (1), 7769.
(72) Xiao, Y.; Feng, C.; Fu, J.; Wang, F.; Li, C.; Kunzelmann, V. F.; Jiang, C.-M.; Nakabayashi, M.; Shibata, N.; Sharp, I. D. Band structure engineering and defect control of Ta_3N_5 for efficient photoelectrochemical water oxidation. *Nat. Catal.* **2020**, *3* (11), 932-940.
(73) Zhong, M.; Hisatomi, T.; Sasaki, Y.; Suzuki, S.; Teshima, K.; Nakabayashi, M.; Shibata, N.; Nishiyama, H.; Katayama, M.; Yamada, T. Highly active GaN-stabilized

doi:10.6342/NTU202403464

Ta_3N_5 thin-film photoanode for solar water oxidation. *Angew. Chem.* **2017**, *129* (17), 4817-4821.
(74) Wang, L.; Zhou, X.; Nguyen, N. T.; Hwang, I.; Schmuki, P. Strongly enhanced water splitting performance of Ta_3N_5 nanotube photoanodes with subnitrides. *Adv. Mater.* **2016**, *28* (12), 2432-2438.
(75) Li, Y.; Zhang, L.; Torres-Pardo, A.; González-Calbet, J. M.; Ma, Y.; Oleynikov, P.; Terasaki, O.; Asahina, S.; Shima, M.; Cha, D. Cobalt phosphate-modified barium-doped tantalum nitride nanorod photoanode with 1.5% solar energy conversion efficiency. *Nat. Commun.* **2013**, *4* (1), 2566.
(76) Higashi, T.; Nishiyama, H.; Otsuka, Y.; Kawase, Y.; Sasaki, Y.; Nakabayashi, M.; Katayama, M.; Minegishi, T.; Shibata, N.; Takanabe, K. Efficient water oxidation using Ta_3N_5 thin film photoelectrodes prepared on insulating transparent substrates. *ChemSusChem* **2020**, *13* (8), 1974-1978.
(77) Higashi, T.; Sasaki, Y.; Kawase, Y.; Nishiyama, H.; Katayama, M.; Takanabe, K.; Domen, K. Surface-modified Ta_3N_5 photoanodes for sunlight-driven overall water splitting by photoelectrochemical cells. *Catalysts* **2021**, *11* (5), 584.
(78) Higashi, T.; Nishiyama, H.; Nandal, V.; Pihosh, Y.; Kawase, Y.; Shoji, R.; Nakabayashi, M.; Sasaki, Y.; Shibata, N.; Matsuzaki, H. Design of semitransparent tantalum nitride photoanode for efficient and durable solar water splitting. *Energy Environ. Sci.* **2022**, *15* (11), 4761-4775.
(79) Kawase, Y.; Higashi, T.; Obata, K.; Sasaki, Y.; Katayama, M.; Domen, K.; Takanabe, K. Interfacial design of a Ta_3N_5 thin-film photoanode for highly stable oxygen evolution over a wide pH range. *ACS Sustain. Chem. Eng.* **2022**, *10* (45), 14705-14714.
(80) Higashi, T.; Nishiyama, H.; Pihosh, Y.; Wakishima, K.; Kawase, Y.; Sasaki, Y.; Nagaoka, A.; Yoshino, K.; Takanabe, K.; Domen, K. Physicochemical insights into semiconductor properties of a semitransparent tantalum nitride photoanode for solar water splitting. *Phy. Chem. Chem. Phys.* **2023**, *25* (30), 20737-20748.
(81) Chang, J.-C.; Eriksson, F.; Sortica, M. A.; Greczynski, G.; Bakhit, B.; Hu, Z.; Primetzhofer, D.; Hultman, L.; Birch, J.; Hsiao, C.-L. Orthorhombic $Ta_{3-x}N_{5-y}O_y$ thin films grown by unbalanced magnetron sputtering: the role of oxygen on structure, composition, and optical properties. *Surf. Coat. Technol.* **2021**, *406*, 126665.
(82) Rudolph, M.; Vickridge, I.; Foy, E.; Alvarez, J.; Kleider, J. P.; Stanescu, D.; Magnan, H.; Herlin-Boime, N.; Bouchet-Fabre, B.; Minea, T. Oxygen incorporated during deposition determines the crystallinity of magnetron-sputtered Ta_3N_5 films. *Thin Solid Films* **2019**, *685*, 204-209.
(83) Rudolph, M.; Stanescu, D.; Alvarez, J.; Foy, E.; Kleider, J. P.; Magnan, H.; Minea, T.; Herlin-Boime, N.; Bouchet-Fabre, B.; Hugon, M. C. The role of oxygen in magnetron-sputtered Ta_3N_5 thin films for the photoelectrolysis of water. *Surf. Coat. Technol.* **2017**, *324*, 620-625.
(84) Chang, J.-C.; Birch, J.; Gueorguiev, G. K.; Bakhit, B.; Greczynski, G.; Eriksson, F.; Sandström, P.; Hultman, L.; Hsiao, C.-L. Domain epitaxial growth of Ta_3N_5 film on c-plane sapphire substrate. *Surf. Coat. Technol.* **2022**, *443*, 128581.
(85) Maeda, K.; Nishimura, N.; Domen, K. A precursor route to prepare tantalum (V) nitride nanoparticles with enhanced photocatalytic activity for hydrogen evolution under visible light. *Appl. Catal. A: Gen.* **2009**, *370* (1), 88-92.
(86) Tabata, M.; Maeda, K.; Higashi, M.; Lu, D.; Takata, T.; Abe, R.; Domen, K. Modified Ta3N5 powder as a photocatalyst for O_2 evolution in a two-step water splitting system with an iodate/iodide shuttle redox mediator under visible light. *Langmuir* **2010**, *26* (12), 9161-9165.

doi:10.6342/NTU202403464

(87) Yuliati, L.; Yang, J.-H.; Wang, X.; Maeda, K.; Takata, T.; Antonietti, M.; Domen, K. Highly active tantalum(v) nitride nanoparticles prepared from a mesoporous carbon nitride template for photocatalytic hydrogen evolution under visible light irradiation. *J. Mater. Chem.* **2010**, *20* (21), 4295-4298.
(88) Dahl, Ø.; Sunding, M. F.; Killi, V.; Svenum, I.-H.; Grandcolas, M.; Andreassen, M.; Nilsen, O.; Thøgersen, A.; Jensen, I. J. T.; Chatzitakis, A. Interrogation of the interfacial energetics at a tantalum nitride/electrolyte heterojunction during photoelectrochemical water splitting by Operando ambient pressure X-ray photoelectron spectroscopy. *ACS Catal.* **2023**, *13* (17), 11762-11770.
(89) Seki, K.; Higashi, T.; Kawase, Y.; Takanabe, K.; Domen, K. Exploring the photocorrosion mechanism of a photocatalyst. *J. Phys. Chem. Lett.* **2022**, *13* (44), 10356-10363.
(90) He, Y.; Thorne, James E.; Wu, Cheng H.; Ma, P.; Du, C.; Dong, Q.; Guo, J.; Wang, D. What Limits the Performance of Ta_3N_5 for Solar Water Splitting? *Chem* **2016**, *1* (4), 640-655.
(91) Li, K.; Miao, B.; Fa, W.; Chen, R.; Jin, J.; Bevan, K. H.; Wang, D. Evolution of surface oxidation on Ta_3N_5 as probed by a photoelectrochemical method. *ACS Appl. Mater. Interfaces* **2021**, *13* (15), 17420-17428.
(92) Xie, Y.; Wang, Y.; Chen, Z.; Xu, X. Role of oxygen defects on the photocatalytic properties of Mg-doped mesoporous Ta_3N_5. *ChemSusChem* **2016**, *9* (12), 1403-1412.
(93) Pei, L.; Lv, B.; Wang, S.; Yu, Z.; Yan, S.; Abe, R.; Zou, Z. Oriented growth of Sc-doped Ta_3N_5 nanorod photoanode achieving low-onset-potential for photoelectrochemical water oxidation. *ACS Appl. Energy Mater.* **2018**, *1* (8), 4150-4157.
(94) Zou, X.; Han, X.; Wang, C.; Zhao, Y.; Du, C.; Shan, B. Carrier engineering of Zr-doped Ta_3N_5 film as an efficient photoanode for solar water splitting. *Sustain. Energy Fuels* **2021**, *5* (11), 2877-2883.
(95) Wang, Y.; Zhu, D.; Xu, X. Zr-doped mesoporous Ta_3N_5 microspheres for efficient photocatalytic water oxidation. *ACS Appl. Mater. Interfaces* **2016**, *8* (51), 35407-35418.
(96) Wagner, L. I.; Sirotti, E.; Brune, O.; Grötzner, G.; Eichhorn, J.; Santra, S.; Munnik, F.; Olivi, L.; Pollastri, S.; Streibel, V.; et al. Defect engineering of Ta_3N_5 photoanodes: enhancing charge transport and photoconversion efficiencies via Ti doping. *Adv. Funct. Mater.* **2024**, *34* (4), 2306539.
(97) Narkeviciute, I.; Chakthranont, P.; Mackus, A. J. M.; Hahn, C.; Pinaud, B. A.; Bent, S. F.; Jaramillo, T. F. Tandem core–shell Si–Ta_3N_5 photoanodes for photoelectrochemical water splitting. *Nano Lett.* **2016**, *16* (12), 7565-7572.
(98) Narkeviciute, I.; Jaramillo, T. F. Effects of Ta_3N_5 morphology and composition on the performance of Si-Ta_3N_5 photoanodes. *Sol. RRL* **2017**, *1* (11), 1700121.
(99) Kawase, Y.; Higashi, T.; Obata, K.; Kishimoto, F.; Pihosh, Y.; Domen, K.; Takanabe, K. Simple immersing method of nanocoating on uneven surfaces applicable to highly durable Ta_3N_5 nanorod photoelectrode for water splitting. *Chem. Mater.* **2024**, *36* (5), 2390-2401.
(100) Pihosh, Y.; Nandal, V.; Shoji, R.; Bekarevich, R.; Higashi, T.; Nicolosi, V.; Matsuzaki, H.; Seki, K.; Domen, K. Nanostructured tantalum nitride for enhanced solar water splitting. *ACS Energy Lett.* **2023**, *8* (5), 2106-2112.
(101) Pihosh, Y.; Nandal, V.; Higashi, T.; Shoji, R.; Bekarevich, R.; Nishiyama, H.; Yamada, T.; Nicolosi, V.; Hisatomi, T.; Matsuzaki, H. Tantalum nitride-enabled solar water splitting with efficiency above 10%. *Adv. Energy Mater.* **2023**, *13* (36), 2301327.
(102) Wang, P.; Ding, C.; Deng, Y.; Chi, H.; Zheng, H.; Liu, L.; Li, H.; Wu, Y.; Liu, X.; Shi, J. Simultaneous improvement in hole storage and interfacial catalysis over Ni–Fe

doi:10.6342/NTU202403464

oxyhydroxide-modified tantalum nitride photoanodes. *ACS Catal.* **2023**, *13* (4), 2647-2656.
(103) Nurlaela, E.; Nakabayashi, M.; Kobayashi, Y.; Shibata, N.; Yamada, T.; Domen, K. Plasma-enhanced chemical vapor deposition Ta_3N_5 synthesis leading to high current density during PEC oxygen evolution. *Sustain. Energy Fuels* **2020**, *4* (5), 2293-2300.
(104) Abdel Haleem, A.; Perumandla, N.; Naruta, Y. Preparation of nanostructured Ta_3N_5 electrodes by alkaline hydrothermal treatment followed by NH_3 annealing and their improved water oxidation performance. *ACS omega* **2019**, *4* (4), 7815-7821.
(105) Prévot, M. S.; Sivula, K. Photoelectrochemical tandem cells for solar water splitting. *J. Phys. Chem. C* **2013**, *117* (35), 17879-17893.
(106) Tamirat, A. G.; Rick, J.; Dubale, A. A.; Su, W.-N.; Hwang, B.-J. Using hematite for photoelectrochemical water splitting: a review of current progress and challenges. *Nanoscale Horiz.* **2016**, *1* (4), 243-267.
(107) Li, C.; Luo, Z.; Wang, T.; Gong, J. Surface, bulk, and interface: rational design of hematite architecture toward efficient photo-electrochemical water splitting. *Adv. Mater.* **2018**, *30* (30), 1707502.
(108) Rettie, A. J. E.; Lee, H. C.; Marshall, L. G.; Lin, J.-F.; Capan, C.; Lindemuth, J.; McCloy, J. S.; Zhou, J.; Bard, A. J.; Mullins, C. B. Combined charge carrier transport and photoelectrochemical characterization of $BiVO_4$ single crystals: intrinsic behavior of a complex metal oxide. *J. Am. Chem. Soc.* **2013**, *135* (30), 11389-11396.
(109) Kweon, K. E.; Hwang, G. S.; Kim, J.; Kim, S.; Kim, S. Electron small polarons and their transport in bismuth vanadate: a first principles study. *Phys. Chem. Chem. Phys.* **2015**, *17* (1), 256-260.
(110) Rettie, A. J. E.; Chemelewski, W. D.; Emin, D.; Mullins, C. B. Unravelling small-polaron transport in metal oxide photoelectrodes. *J. Phys. Chem. Lett.* **2016**, *7* (3), 471-479.
(111) Zhang, S.; Ahmet, I.; Kim, S.-H.; Kasian, O.; Mingers, A. M.; Schnell, P.; Kölbach, M.; Lim, J.; Fischer, A.; Mayrhofer, K. J. J.; et al. Different photostability of $BiVO_4$ in near-pH-neutral electrolytes. *ACS Appl. Energy Mater.* **2020**, *3* (10), 9523-9527.
(112) Liu, X.; Wang, F.; Wang, Q. Nanostructure-based WO_3 photoanodes for photoelectrochemical water splitting. *Phys. Chem. Chem. Phys.* **2012**, *14* (22), 7894-7911.
(113) Li, W.; Da, P.; Zhang, Y.; Wang, Y.; Lin, X.; Gong, X.; Zheng, G. WO3 nanoflakes for enhanced photoelectrochemical conversion. *ACS Nano* **2014**, *8* (11), 11770-11777.
(114) Wang, Y.; Tian, W.; Chen, C.; Xu, W.; Li, L. Tungsten trioxide nanostructures for photoelectrochemical water splitting: material engineering and charge carrier dynamic manipulation. *Adv. Funct. Mater.* **2019**, *29* (23), 1809036.
(115) Kim, W.; Tachikawa, T.; Monllor-Satoca, D.; Kim, H.-i.; Majima, T.; Choi, W. Promoting water photooxidation on transparent WO_3 thin films using an alumina overlayer. *Energy Environ. Sci.* **2013**, *6* (12), 3732-3739.
(116) Bai, S.; Yang, X.; Liu, C.; Xiang, X.; Luo, R.; He, J.; Chen, A. An integrating photoanode of WO_3/Fe_2O_3 heterojunction decorated with NiFe-LDH to improve PEC water splitting efficiency. *ACS Sustain. Chem. Eng.* **2018**, *6* (10), 12906-12913.
(117) Ma, M.; Zhang, K.; Li, P.; Jung, M. S.; Jeong, M. J.; Park, J. H. Dual oxygen and tungsten vacancies on a WO_3 photoanode for enhanced water oxidation. *Angew. Chem.* **2016**, *128* (39), 11998-12002.
(118) Zhou, Y.; Zhang, L.; Lin, L.; Wygant, B. R.; Liu, Y.; Zhu, Y.; Zheng, Y.; Mullins, C. B.; Zhao, Y.; Zhang, X.; et al. Highly efficient photoelectrochemical water splitting from hierarchical $WO_3/BiVO_4$ nanoporous sphere arrays. *Nano Lett.* **2017**, *17* (12), 8012-8017.

doi:10.6342/NTU202403464

(119) Liu, Y.; Li, J.; Li, W.; Yang, Y.; Li, Y.; Chen, Q. Enhancement of the photoelectrochemical performance of WO_3 vertical arrays film for solar water splitting by gadolinium doping. *J. Phys. Chem. C* **2015**, *119* (27), 14834-14842.
(120) Liu, Y.; Zhang, Z.; Wang, K.; Tan, X.; Chen, J.; Ren, X.; Jiang, F. Efficient $BiVO_4$ photoanode with an excellent hole transport layer of CuSCN for solar water oxidation. *Adv. Energy Mater.* **2024**, *14* (17), 2304223.
(121) Pei, H.; Peng, L.; Jiang, Z.; Zhang, Y.; Li, R.; Peng, T. Gradient-tuned VO_4 vacancies in $BiVO_4$ photoanode for boosting bulk hole transport and oxygen evolution reaction performance. *Adv. Funct. Mater.* **2024**, *34* (30), 2401122.
(122) Zhang, Y.; Xu, L.; Liu, B.; Wang, X.; Wang, T.; Xiao, X.; Wang, S.; Huang, W. Engineering $BiVO_4$ and oxygen evolution cocatalyst interfaces with rapid hole extraction for photoelectrochemical water splitting. *ACS Catal.* **2023**, *13* (9), 5938-5948.
(123) Liu, B.; Wang, X.; Zhang, Y.; Xu, L.; Wang, T.; Xiao, X.; Wang, S.; Wang, L.; Huang, W. A $BiVO_4$ photoanode with a VO_x layer bearing oxygen vacancies offers improved charge transfer and oxygen evolution kinetics in photoelectrochemical water splitting. *Angew. Chem.* **2023**, *135* (10), e202217346.
(124) Zhang, B.; Yu, S.; Dai, Y.; Huang, X.; Chou, L.; Lu, G.; Dong, G.; Bi, Y. Nitrogen-incorporation activates $NiFeO_x$ catalysts for efficiently boosting oxygen evolution activity and stability of $BiVO_4$ photoanodes. *Nat. Commun.* **2021**, *12* (1), 6969.
(125) Park, J.; Yoon, K.-Y.; Ghule, B. G.; Kim, H.; Jang, J.-H. Morphology-engineered hematite photoanode for photoelectrochemical water splitting. *ACS Energy Lett.* **2024**, *9* (6), 3169-3176.
(126) Chaule, S.; Kang, J.; Ghule, B. G.; Kim, H.; Jang, J.-H. An approach to enhance PEC water splitting performance through Al:Ti codoping in hematite (α-Fe_2O_3) photoanode: the effect of Al^{3+} as a codopant. *ACS Materials Lett.* **2024**, *6* (7), 2897-2904.
(127) Kang, J.; Ghule, B. G.; Gyeong, S. G.; Ha, S.-J.; Jang, J.-H. Alleviating charge recombination caused by unfavorable interaction of P and Sn in hematite for photoelectrochemical water oxidation. *ACS Catal.* **2024**, *14* (13), 10355-10364.
(128) Yoon, K.-Y.; Park, J.; Lee, H.; Seo, J. H.; Kwak, M.-J.; Lee, J. H.; Jang, J.-H. Unveiling the role of the Ti dopant and viable Si doping of hematite for practically efficient solar water splitting. *ACS Catal.* **2022**, *12* (9), 5112-5122.
(129) Zhang, H.; Li, D.; Byun, W. J.; Wang, X.; Shin, T. J.; Jeong, H. Y.; Han, H.; Li, C.; Lee, J. S. Gradient tantalum-doped hematite homojunction photoanode improves both photocurrents and turn-on voltage for solar water splitting. *Nat. Commun.* **2020**, *11* (1), 4622.
(130) Kong, H.; Yang, H.; Park, J.-S.; Chae, W.-S.; Kim, H. Y.; Park, J.; Lee, J. H.; Choi, S. Y.; Park, M.; Kim, H.; et al. Spatial control of oxygen vacancy concentration in monoclinic WO_3 photoanodes for enhanced solar water splitting. *Adv. Funct. Mater.* **2022**, *32* (36), 2204106.
(131) Nomellini, C.; Polo, A.; Mesa, C. A.; Pastor, E.; Marra, G.; Grigioni, I.; Dozzi, M. V.; Giménez, S.; Selli, E. Improved photoelectrochemical performance of WO_3/$BiVO_4$ heterojunction photoanodes via WO_3 nanostructuring. *ACS Appl. Mater. Interfaces* **2023**, *15* (45), 52436-52447.
(132) Wang, A.; Cao, D.; Zhang, F.; Chen, Y.; Feng, J.; Fang, D.; Mi, B.; Gao, Z.; Li, Z. Ultrathin and conformal TiO_x overlayers on WO_3 photoelectrodes for simultaneous surface trap passivation and heterojunction formation. *ACS Catal.* **2024**, *14* (5), 3446-3456.
(133) Chen, F. F. *Introduction to plasma physics*; Springer Science & Business Media, 2012.

doi:10.6342/NTU202403464

(134) Conrads, H.; Schmidt, M. Plasma generation and plasma sources. *Plasma Sources Sci. Technol.* **2000**, *9* (4), 441.
(135) Murty, M. V. R. Sputtering: the material erosion tool. *Surf. Sci.* **2002**, *500* (1-3), 523-544.
(136) Kelly, P. J.; Arnell, R. D. Magnetron sputtering: a review of recent developments and applications. *Vacuum* **2000**, *56* (3), 159-172.
(137) Berg, S.; Nyberg, T. Fundamental understanding and modeling of reactive sputtering processes. *Thin Solid Films* **2005**, *476* (2), 215-230.
(138) Anders, A. Physics of arcing, and implications to sputter deposition. *Thin Solid Films* **2006**, *502* (1-2), 22-28.
(139) Mattox, D. M.; Mattox, V. H. *Vacuum coating technology*; Springer, 2003.
(140) Schiller, S.; Goedicke, K.; Reschke, J.; Kirchhoff, V.; Schneider, S.; Milde, F. Pulsed magnetron sputter technology. *Surf. Coat. Technol.* **1993**, *61* (1), 331-337.
(141) Kittel, C.; McEuen, P. *Introduction to solid state physics*; John Wiley & Sons, 2018.
(142) Klein, J.; Kampermann, L.; Mockenhaupt, B.; Behrens, M.; Strunk, J.; Bacher, G. Limitations of the Tauc plot method. *Adv. Funct. Mater.* **2023**, *33* (47), 2304523.
(143) Hüfner, S. *Photoelectron spectroscopy: principles and applications*; Springer Science & Business Media, 2013.
(144) Chastain, J.; King Jr, R. C. Handbook of X-ray photoelectron spectroscopy. *Perkin-Elmer Corporation* **1992**, *40*, 221.
(145) Stevie, F. A.; Donley, C. L. Introduction to x-ray photoelectron spectroscopy. *J. Vac. Sci. Technol. A* **2020**, *38* (6).
(146) Eland, J. H. D. *Photoelectron spectroscopy: an introduction to ultraviolet photoelectron spectroscopy in the gas phase*; Elsevier, 2013.
(147) Zangwill, A. *Physics at surfaces*; Cambridge university press, 1988.
(148) Greczynski, G.; Hultman, L. C 1s Peak of Adventitious Carbon Aligns to the Vacuum Level: Dire Consequences for Material's Bonding Assignment by Photoelectron Spectroscopy. *ChemPhysChem* **2017**, *18* (12), 1507-1512.
(149) Wagner, C. D.; Joshi, A. The auger parameter, its utility and advantages: a review. *J. Electron Spectros. Relat. Phenomena* **1988**, *47*, 283-313.
(150) Moretti, G. Auger parameter and Wagner plot in the characterization of chemical states by X-ray photoelectron spectroscopy: a review. *J. Electron Spectros. Relat. Phenomena* **1998**, *95* (2-3), 95-144.
(151) Lazanas, A. C.; Prodromidis, M. I. Electrochemical impedance spectroscopy─ a tutorial. *ACS Meas. Sci. Au* **2023**, *3* (3), 162-193.
(152) Kang, C. S.; Cho, H. J.; Kim, Y. H.; Choi, R.; Onishi, K.; Shahriar, A.; Lee, J. C. Characterization of resistivity and work function of sputtered-TaN film for gate electrode applications. *J. Vac. Sci. Technol. B: Nanotechnol. Microelectron.* **2003**, *21* (5), 2026-2028.
(153) Reuter, K.; Scheffler, M. Composition, structure, and stability of RuO2 (110) as a function of oxygen pressure. *Phys. Rev. B* **2001**, *65* (3), 035406.
(154) Kusano, E. Structure-zone modeling of sputter-deposited thin films: a brief review. *Appl. Sci. Converg. Technol.* **2019**, *28* (6), 179-185.
(155) Barna, P. B.; Adamik, M. Fundamental structure forming phenomena of polycrystalline films and the structure zone models. *Thin Solid Films* **1998**, *317* (1-2), 27-33.
(156) Stoehr, M.; Shin, C. S.; Petrov, I.; Greene, J. E. Raman scattering from epitaxial TaN_x ($0.94 \leq x \leq 1.37$) layers grown on MgO (001). *J. Appl. Phys.* **2007**, *101* (12).

doi:10.6342/NTU202403464

(157) Sasaki, K.; Noya, A.; Umezawa, T. Stoichiometry of Ta–N film and its application for diffusion barrier in the Al_3Ta/Ta–N/Si contact system. *Jpn. J. Appl. Phys.* **1990**, *29* (6R), 1043.
(158) Greczynski, G.; Hultman, L. Self-consistent modelling of X-ray photoelectron spectra from air-exposed polycrystalline TiN thin films. *Appl. Surf. Sci.* **2016**, *387*, 294-300.
(159) Eichhorn, J.; Lechner, S. P.; Jiang, C.-M.; Heunecke, G. F.; Munnik, F.; Sharp, I. D. Indirect bandgap, optoelectronic properties, and photoelectrochemical characteristics of high-purity Ta 3 N 5 photoelectrodes. *J. Mater. Chem. A* **2021**, *9* (36), 20653-20663.
(160) Aysal, N.; Kurt, Y.; Öztürk, H.; Ildiz, G. O.; Yesiltas, M.; Laçin, D.; Öngen, S.; Nikitin, T.; Fausto, R. Crystallization kinetics: relationship between crystal morphology and the cooling rate—applications for different geological materials. *Crystals* **2023**, *13* (7), 1130.
(161) Pinaud, B. A.; Vailionis, A.; Jaramillo, T. F. Controlling the structural and optical properties of Ta_3N_5 films through nitridation temperature and the nature of the Ta metal. *Chem. Mater.* **2014**, *26* (4), 1576-1582.
(162) Wang, C.; Hisatomi, T.; Minegishi, T.; Nakabayashi, M.; Shibata, N.; Katayama, M.; Domen, K. Effects of interfacial layers on the photoelectrochemical properties of tantalum nitride photoanodes for solar water splitting. *J. Mater. Chem. A* **2016**, *4* (36), 13837-13843.
(163) Prieto, P.; Kirby, R. E. X-ray photoelectron spectroscopy study of the difference between reactively evaporated and direct sputter-deposited TiN films and their oxidation properties. *J. Vac. Sci. Technol. A: Vac. Surf. Films* **1995**, *13* (6), 2819-2826.
(164) Esaka, F.; Furuya, K.; Shimada, H.; Imamura, M.; Matsubayashi, N.; Sato, H.; Nishijima, A.; Kawana, A.; Ichimura, H.; Kikuchi, T. Comparison of surface oxidation of titanium nitride and chromium nitride films studied by x-ray absorption and photoelectron spectroscopy. *J. Vac. Sci. Technol. A: Vac. Surf. Films* **1997**, *15* (5), 2521-2528.
(165) Yin, H.; Shao, C.; Wang, H.; Zhang, H.; Li, D.; Zong, X.; Wang, X.; Li, C. Shallow oxygen substitution defect to deeper defect transformation mechanism in Ta_3N_5 under light irradiation. *J. Phys. Chem. Lett.* **2021**, *12* (15), 3698-3704.
(166) Fu, G.; Yan, S.; Yu, T.; Zou, Z. Oxygen related recombination defects in Ta_3N_5 water splitting photoanode. *Appl. Phys. Lett.* **2015**, *107* (17).
(167) Suen, N.-T.; Hung, S.-F.; Quan, Q.; Zhang, N.; Xu, Y.-J.; Chen, H. M. Electrocatalysis for the oxygen evolution reaction: recent development and future perspectives. *Chem. Soc. Rev.* **2017**, *46* (2), 337-365.
(168) Hajibabaei, H.; Little, D. J.; Pandey, A.; Wang, D.; Mi, Z.; Hamann, T. W. Direct deposition of crystalline Ta_3N_5 thin films on FTO for PEC water splitting. *ACS Appl. Mater. Interfaces* **2019**, *11* (17), 15457-15466.
(169) Xing, Z.; Ren, F.; Wu, H.; Wu, L.; Wang, X.; Wang, J.; Wan, D.; Zhang, G.; Jiang, C. Enhanced PEC performance of nanoporous Si photoelectrodes by covering HfO_2 and TiO_2 passivation layers. *Sci. Rep.* **2017**, *7* (1), 43901.
(170) Shao, G. Work function and electron affinity of semiconductors: Doping effect and complication due to fermi level pinning. *Energy Environ. Mater.* **2021**, *4* (3), 273-276.
(171) Himpsel, F. J.; Hollinger, G.; Pollak, R. A. Determination of the Fermi-level pinning position at Si (111) surfaces. *Phys. Rev. B* **1983**, *28* (12), 7014.
(172) Allen, F. G.; Gobeli, G. W. Comparison of the photoelectric properties of cleaved, heated, and sputtered silicon surfaces. *J. Appl. Phys.* **1964**, *35* (3), 597-605.
(173) Neamen, D. A. An introduction to semiconductor devices. **2006**.
(174) Oldham, W. G.; Milnes, A. G. nn Semiconductor heterojunctions. *Solid State Electron.* **1963**, *6* (2), 121-132.

doi:10.6342/NTU202403464

(175) Klahr, B.; Gimenez, S.; Fabregat-Santiago, F.; Hamann, T.; Bisquert, J. Water oxidation at hematite photoelectrodes: the role of surface states. *J. Am. Chem. Soc.* **2012**, *134* (9), 4294-4302.
(176) Shao, C.; Chen, R.; Zhao, Y.; Li, Z.; Zong, X.; Li, C. Reducing the surface defects of Ta_3N_5 photoanode towards enhanced photoelectrochemical water oxidation. *J. Mater. Chem. A* **2020**, *8* (44), 23274-23283.
(177) Wang, J.; Ma, A.; Li, Z.; Jiang, J.; Feng, J.; Zou, Z. Unraveling the mechanism of 720 nm sub-band-gap optical absorption of a Ta_3N_5 semiconductor photocatalyst: a hybrid-DFT calculation. *Phy. Chem. Chem. Phys.* **2015**, *17* (12), 8166-8171.
(178) Cui, L.; Wang, M.; Wang, Y. X. Nitrogen vacancies and oxygen substitution of Ta_3N_5: first-principles investigation. *J. Phys. Soc. Jpn.* **2014**, *83* (11), 114707.
(179) Jing, T.; Dai, Y.; Ma, X.; Wei, W.; Huang, B. Effects of intrinsic defects and extrinsic doping on the electronic and photocatalytic properties of Ta_3N_5. *RSC Adv.* **2015**, *5* (73), 59390-59397.
(180) Rudd, P. N.; Tereniak, S. J.; Lopez, R. Characterizing density and spatial distribution of trap states in Ta_3N_5 thin films for rational defect passivation. *ACS Appl. Mater. Interfaces* **2023**, *15* (6), 7969-7977.
(181) Rahm, M.; Hoffmann, R.; Ashcroft, N. W. Atomic and ionic radii of elements 1–96. *Chem. Eur. J.* **2016**, *22* (41), 14625-14632.
(182) Xu, C.; Xiao, Q.; Ma, J.; Jin, Y.; Shao, J.; Fan, Z. High temperature annealing effect on structure, optical property and laser-induced damage threshold of Ta_2O_5 films. *Appl. Surf. Sci.* **2008**, *254* (20), 6554-6559.
(183) Pinaud, B. A.; Vesborg, P. C. K.; Jaramillo, T. F. Effect of film morphology and thickness on charge transport in Ta_3N_5/Ta photoanodes for solar water splitting. *J. Phys. Chem. C* **2012**, *116* (30), 15918-15924.

doi:10.6342/NTU202403464

doi:10.6342/NTU202403464